Title

A New Modality for High Resolution Diffuse Optical Imaging: Temperature Modulated Fluorescence Tomography

Author

Kwong, Tiffany Chelsea

Publication Date

2017

UNIVERSITY OF CALIFORNIA,
IRVINE

A New Modality for High Resolution Diffuse Optical Imaging: Temperature Modulated Fluorescence Tomography

DISSERTATION

submitted in partial satisfaction of the requirements
for the degree of

DOCTOR OF PHILOSOPHY

in Physics

by

Tiffany C. Kwong

Dissertation Committee:
Associate Professor Gultekin Gulsen, Chair
Professor Min-Ying (Lydia) Su
Assistant Professor Jered Haun

2017

DEDICATION

To

my mentors

in recognition of their worth

for their dedication, support, caring, and encouragement,

for starting me on my path

and

believing in my future.

"A mentor empowers a person to see a possible future and believe it can be obtained."

—*Shawn Hitchcock*

"I almost wish I hadn't gone down that rabbit-hole — and yet — and yet — it's rather curious, you know, this sort of life!"

– Lewis Carroll, *Alice in Wonderland*

Table of Contents

LIST OF FIGURES

CHAPTER 1: INTRODUCTION

CHAPTER 2: BACKGROUND

CHAPTER 3: MATHEMATICAL FRAMEWORK FOR OPTICAL TOMOGRAPHY

CHAPTER 4: VALIDATION WITH SIMULATION STUDIES

CHAPTER 5: THERMODOTS

CHAPTER 6: SYSTEM SET UP AND EXPERIMENTAL DETAILS

CHAPTER 7: EXPERIMENTAL RESULTS

CHAPTER 8: SUMMARY AND FUTURE WORK

LIST OF TABLES

CHAPTER 1: INTRODUCTION

CHAPTER 2: BACKGROUND

CHAPTER 4: VALIDATION WITH SIMULATION STUDIES

CHAPTER 5: THERMODOTS

CHAPTER 7: EXPERIMENTAL RESULTS

ACKNOWLEDGMENTS

In the words of Issac Newton, "*If I have seen further it is by standing on the shoulders of giants.*" This project would not have been possible with the support and contributions from a number of people. First of all, I would like to acknowledge the core team members of TM-FT and recognize their contributions. Namely, Dr. Gultekin Gulsen and Dr. Yuting Lin for starting TM-FT and Dr. Farouk Nouizi for his contributions in implementing the continuous scanning method.

I am very thankful for all the years I have spent working at the Center for Functional Onco-Imaging. I feel extremely grateful to have met and worked with so many incredible people and would like to thank all the lab members for helping, training, teaching, and guiding me all these years. There is no way that this project would have been possible without the help of many people.

I owe some much to my amazing advisor and mentor Dr. Gultekin Gulsen. I am so grateful to have met you and count myself lucky to be your student. I don't know many other professors who care about their students as much as their research, and I am grateful for your help, mentorship, and leadership in creating such a supportive, collaborative, and fun research environment. Thank you for being so open and communicative, always making time to discuss problems with us no matter how busy you are. Thank you for being so optimistic and encouraging me when I encountered a problem, but especially for teaching me how to be resourceful and creative when solving problems. I truly appreciate all your help from all the time you spent training me in lab, to your help with grant proposals and papers, and your insightful advice on careers and life. Thank you for being such a kind, funny, and generous person who taught me many important things not just in research but in life.

I would also like to thank my mentor and role model Dr. Yuting Lin for all the help and support she has provided. She was the first person to train me when I first started in this lab and taught me so much. Thank you for your patience and kindness and for encouraging and pushing me to try harder and go further then I dared. I would also like to thank Dr. Farouk Nouizi for all his help. Thank you for being so patient teaching me about the DOT and FEM, reviewing my papers, helping out whenever I had problems, and giving good advice. Thank you for being so encouraging, supportive, and always making time to answer my questions in your busy schedule. Thank you for all the fun times, I am so lucky to have you as a mentor.

I would also like to thank Dr. Min-Ying Lydia Su, center director of CFOI. Thank you for all your help, advice, training and leadership. Thank you for being such a kind and generous mentor and sharing your insights on clinical applications of imaging techniques. You have been an inspiration and role model.

I don't know how I would have managed with two of my lab mates Dr. Alex Luk and Dr. Jaedu Cho, I count myself lucky to be able to call you my friends. A big thanks to Alex for being such a generous and kind lab mate and for your help with the MR thermometry and program debugging. Thank you for always helping me or listening to me when I had a problem, and for all the fun times and good food. And thanks to Jaedu for being such a calming and knowledgeable presence in the lab and helping out with all my hardware related problems. Also, a big thanks to Lena Qin for all her help with the animal preparation and studies. Thank you for being so cheerful and helpful and checking on me when I got spooked of being alone in the dark with the animals.

I would also like to thank my office mates. These years staying in UCI would not have been fun and memorable without you. Dr. Jessica Ruiz, my unrelated cousin, thanks so much for all the fun times, advice, and conversation. Dr. Hakan Erkol, my health and fitness guru, thanks so much for your help, friendship, and your daily attempts to convert me to coffee. Yang Zhang, my late-night office buddy, thank you for the conversation and friendship that allowed me to survive those 12+ hour days. I would also like to thank all the center members, past and present and give a special shout out to Jie Zheng, Joe Chen, Rushi Rajyaguru, Yuwen Chan, Kenji Ikemura, and Dr. Hon Yu. Also, a big thanks to Dr. Chen for his support and advice over these past years. In addition, I would like to also thank Jodi Macgregor and Mei-Hui Wang for their organizational and management skills making sure I got the supplies I needed, and most importantly, paid.

I would also like to thank my committee member and collaborator Dr. Jered Haun who has been a huge help. When we stepped out on a limb and decided to work on the ThermoDots, he graciously offered his advice, guidance, and resources which allowed this project to progress. Thank you for your expertise and guidance and serving on my committee.

This project could not have been completed without the help of our wonderful collaborators. First I would like to thank Dr. Uma Sampathkumaran, Dr. Linden Bolisay, Dr. Maksudul Alam, Dr. Kishology Goswanmi, Shaaz Ahmed, and Sally Zhu at InnoSense, LLC for their work on the ThermoDots. A special thanks to Uma, Shaaz, and Sally, it has been a pleasure collaborating with you all these years. I would also like to thank our UCI collaborators who have generously offered their help and resources including Dr. Amiee Edinger and Dr. Saurabh Ghosh Roy for their help with the targeting studies, Dr. Robert Edwards for his help with the histology report, Drs. Xiaolin Zi and Noriko Yokoyama for the cell lines, and Chung-Ho Sun for the microplate reader. In addition, a big thanks to Dr. Jered Haun and lab, especially Dr. Maha Rahim and Dr. Sumi Lee, for their help with the ThermoDots studies.

I would like to thank the Optical Society of America for permission to include Chapter Four and portions of chapters 2 and 7 in my dissertation which were originally published in Applied Optics and for a portion of Chapter Six which was originally published in Optic Letters. I would also like to thank the SPIE for their permission to include a portion of Chapter Seven of my thesis which was originally published in the Journal of Biomedical Optics and Figure 6.5 originally published in SPIE BIOS conference proceedings. Another thanks to AIP Publishing for their permission to include a portion of Chapter Seven of my thesis which was originally published in Applied Physics Letters. In addition, I also thank World Scientific Publishing Co., Inc., John Wiley and Sons, Elsevier, and the Focused Ultrasound Foundation for permission to include copyrighted figures as part of my dissertation.

This research would not have been possible without the generous funding support provided by UCI, the Eugene Cota Robles Fellowship, and a special thanks to the National

Institute of Health (NIH) for the Ruth L. Kirschstein National Research Service Awards for Individual Pre-Doctoral Fellows F31 (F31CA171915-01A1). In addition, financial support for this work was also provided NIH Grants: P3R01EB008716, R33 CA120175, SBIR HHSN261201300068C.

Lastly, I would like to give a big thanks to my family and friends for all their support and encouragement. I owe so much to my incredible parents: Dr. Phillip and Nancy Kwong for letting me find my own path and encouraging me to pursue my dreams. Thank you for teaching me how to be strong and showing me the value of hard-work, integrity, and empathy. I would also like to give a big shout out to my amazing siblings: Derek, Jillian, and Kelsey for being such kind, funny, and supportive people who always encourage me in all my endeavors. In addition, a big thanks to my uncle Paul for keeping me well fed and my late grandparents John and Mary Nakaji for their sacrifices, love, and support. And to my good friends Drs. Liuyi Pei and Jennifer Shitanishi many thanks for helping not only helping me survive grad school, but enjoying it as well. I would also like to thank my teacher Mr. Paul Shirota for laying the foundation to get me where I am today. And finally, I would like to thank my mentor and undergraduate advisor Dr. William Taylor who took me under his wing and opened up the world of physics to a young teenager. None of this would have been possible without you, and I am so grateful for all your help, advice, and encouragement these past years. Finally, to all the wonderful people who are not listed, but have helped me, mentored me, and inspired me along the way, there are not enough words to express my gratitude. Thank you all, from the bottom of my heart.

“Show me a successful individual and I’ll show you someone who had real positive influences in his or her life. I don’t care what you do for a living—if you do it well I’m sure there was someone cheering you on or showing the way. A mentor.”

— Denzel Washington

CURRICULUM VITAE

Tiffany C Kwong

EDUCATION

2007	B.S. in Physics, California State University, Los Angeles
2011	M.S in Physics, University of California, Irvine
2017	Ph.D. in Physics, University of California, Irvine

HONORS AND AWARDS

2002-2007	Early Entrance Program California State University, Los Angeles
2006	National GE Honors Society Scholarship California State University, Los Angeles
2009-2010	National Science Foundation (NSF) GK-12 Fellowship California State University, Los Angeles
2010-2012	UCI Regents' Fellowship University of California, Irvine
2012	Ford Fellowship Honorable Mention University of California, Irvine
2012	Graduate Assistance in Areas of National Need (GAANN) Fellowship (declined) University of California, Irvine
2014	Association of Graduate Students (AGS) Travel Grant University of California, Irvine
2010-2015	Eugene Cota Robles Fellowship University of California, Irvine

2012-2015	Ruth L. Kirschstein National Research Service Awards for Individual Pre-Doctoral Fellows F31 (NIH) University of California, Irvine
2014, 2015, 2016	Physical Science Travel Award University of California, Irvine

PEER REVIEWED PUBLICATIONS

Lin, Y., Bolisay, L., Ghijsen, M., **Kwong, T. C.**, & Gulsen, G. (2012). Temperature-modulated fluorescence tomography in a turbid media. *Applied physics letters*, *100*(7), pp. 073702.

Lin, Y., **Kwong, T. C.**, Bolisay, L., & Gulsen, G. (2012). Temperature-modulated fluorescence tomography based on both concentration and lifetime contrast. *Journal of biomedical optics*, *17*(5), pp. 0560071-0560074.

Lin, Y., Nouizi, F., **Kwong, T. C.**, & Gulsen, G. (2015). Simulation-based evaluation of the resolution and quantitative accuracy of temperature-modulated fluorescence tomography. *Applied optics*, *54*(25), pp. 7612-7621.

Nouizi, F., **Kwong, T. C.,** Cho, J., Lin, Y., Sampathkumaran, U., & Gulsen, G. (2015). Implementation of a new scanning method for high-resolution fluorescence tomography using thermo-sensitive fluorescent agents. *Optics letters*, *40*(21), pp. 4991-4994.

Kwong, T. C., Hsing, M., Lin, Y., Thayer, D., Unlu, M. B., Su, M. Y., & Gulsen, G. (2016). Differentiation of tumor vasculature heterogeneity levels in small animals based on total hemoglobin concentration using magnetic resonance-guided diffuse optical tomography in vivo. *Applied Optics*, *55*(21), pp. 5479-5487.

Kwong, T. C., Nouizi, F., Lin, Y., Cho, J., Zhu, Y., Sampathkumaran, U., Gulsen, G. (2017) "Experimental evaluation of the resolution and quantitative accuracy of temperature-modulated fluorescence tomography." *Applied Optics,* **56**(3), pp. 521-529.

Kwong, T. C., Nouizi, F., Lin, Y., et al., "Feasibility study of high spatial resolution multimodality fluorescence tomography in *ex vivo* biological tissue" (*Applied Optics* under review)

CONFERENCE PROCEEDINGS

Lin, Y., Bolinsay, L., Ghijsen, M., **Kwong, T. C.**, & Gulsen, G. (2012). "Fluorescence Tomography using Temperature Modulation" In *Biomedical Optics*. Optical Society of America. pp. BTu4A-8

Kwong, T.C., Nouizi, F., Lin, Y., Sampathkumaran, U., Ahmed, S. and Gulsen, G. (2013). "Temperature-Modulated Fluorescence Tomography: Modulating Tissue Temperature Using HIFU for High-Resolution *in vivo* Fluorescence Tomography" In Multimodal Biomedical Imaging VIII *(Proc*. SPIE 8574)

Nouizi, F., **Kwong, T.**, Lin, Y., Sampathkumaran, U., Shaaz, A., & Gulsen, G. (2013). "A combined HIFU-Fluorescence Tomography high-resolution imaging technique using temperature-modulated thermodots" In *Novel Techniques in Microscopy*. Optical Society of America. pp. JW3B-8

Kwong, T.C., Nouizi, F., Lin, Y., Rajyaguru, R., Nguyen, T., Alptekin, L., Sampathkumaran, U., Zhu, Y., Ahmed, S. and Gulsen, G. (2014). "Validation of temperature-modulated fluorescence tomography in vivo" In *SPIE BiOS*. International Society for Optics and Photonics. pp. 89370H

Nouizi, F., **Kwong, T.C.,** Kwong, J., Cho, J., Chan, Y., Sampathkumaran, U., Zhu, Y., Alam, M.M. and Gulsen, G. (2015). "Excitation light leakage suppression using temperature sensitive fluorescent agents" In *SPIE BiOS*. International Society for Optics and Photonics. pp. 93190Y

Kwong, T. C., Nouizi, F., Sampathkumaran, U., Zhu, Y., Alam, M. M., & Gulsen, G. (2015). "Activatable thermo-sensitive ICG encapsulated pluronic nanocapsules for temperature sensitive fluorescence tomography" In *SPIE BiOS*. International Society for Optics and Photonics. pp. 93390C

Kwong, T. C., Lo, P. A., Cho, J., Nouizi, F., Chiang, H. K., Kim, C. S., & Gulsen, G. (2016). "Multi-wavelength fluorescence tomography" In *SPIE BiOS.* International Society for Optics and Photonics. pp. 97001A

Kwong, T. C., Nouizi, F., Lin, Y., Zhu, Y., Sampathkumaran, U., & Gulsen, G. (2016). "Thermal outlining using focused ultrasound (TOFU) with reversible temperature sensitive fluorescent probes" In *SPIE BiOS.* International Society for Optics and Photonics. pp. 97010L

ABSTRACT OF THE DISSERTATION

A NEW MODALITY FOR HIGH RESOLUTION DIFFUSE OPTICAL IMAGING: TEMPERATURE MODULATED FLUORESCENCE TOMOGRAPHY

By

Tiffany C Kwong

Doctor of Philosophy in Physics

University of California, Irvine, 2017

Professor Gultekin Gulsen, Chair

As one of the most sensitive *in vivo* molecular imaging modalities, fluorescence imaging has great potential to play an important role in preclinical and clinical studies. Indeed, *in vivo* fluorescence optical imaging extends across a wide range of applications, from cellular to organ levels. Unfortunately, in organ level applications, fluorescence imaging suffers from low spatial resolution due to the high scattering nature of biological tissue, especially in deep tissue (>1cm). Extensive effort has been spent to improve the spatial resolution of fluorescence tomography (FT). However, approaches such as integrating FT with other anatomic imaging modalities such as Magnetic Resonance Imaging (MRI) or computed tomography (CT) do not perform well if the fluorescent agent distribution within the medium cannot be defined in the anatomical image. There are also several techniques that attempt to modulate fluorescence signals using ultrasound to achieve higher spatial resolution. However, low modulation efficiency and extremely low signal to noise ratio (SNR) are the two primary factors that make the implementation of these techniques difficult.

Consequently, the poor spatial resolution and subsequent low quantitative accuracy are the main obstacles preventing the widespread use of this powerful technique in pre-clinical and clinical settings. To overcome these limitations, the goal of this thesis is to develop an entirely new approach termed, “Temperature-modulated fluorescence tomography (TM-FT)”, that can provide high resolution images at depths up to 6 cm without sacrificing the exceptional sensitivity of FT. In this innovative approach, FT is combined with temperature activatable fluorescence molecular probes (ThermoDots) and high intensity focused ultrasound (HIFU) which can provide localized heating of the tissue (only 3-5 ˚C) with high spatial resolution. The small size of the focal spot (~1.4 mm) allows imaging the distribution of these temperature sensitive agents with not only high spatial resolution but also high quantitative accuracy.

This thesis will present the development of the first TM-FT system prototype including the instrumentation and system design, image reconstruction algorithm, and ThermoDots probe development. The feasibility of this method to provide superior spatial resolution and high quantitative accuracy is validated using simulations and experimentally demonstrated in phantom and *ex vivo* tissue.

Chapter 1: Introduction

"The future belongs to those who see possibilities before they become obvious."

– John Sculley

1.1 Medical Imaging

1.1.1 History/purpose

Since the birth of medical imaging with the first X-ray image in 1895 by Wilhelm Conrod Roentgen, medical imaging has revolutionized the medical field (1) The ability to noninvasively look inside the body revealing internal structures, processes, and functions has become an integral and standard clinical practice for many medical fields including cardiology, orthopedics, oncology, dentistry, and optometry. Indeed, medical imaging plays a critical role in all aspects of treatment from screening and diagnosis to treatment guidance and monitoring.

1.1.2 Medical imaging modalities

1.1.2.1 Energy

Medical imaging uses different types of energy to noninvasively or less invasively probe the body and reveal information that can help in the diagnosis and treatment of a disease. Besides X-rays, other energy forms include those from ultrasound and electromagnetic (EM) fields. Figure 1.1 shows some imaging modalities that uses energy from different parts of the EM spectrum to probe the body for specific applications by interacting with different components of the body.

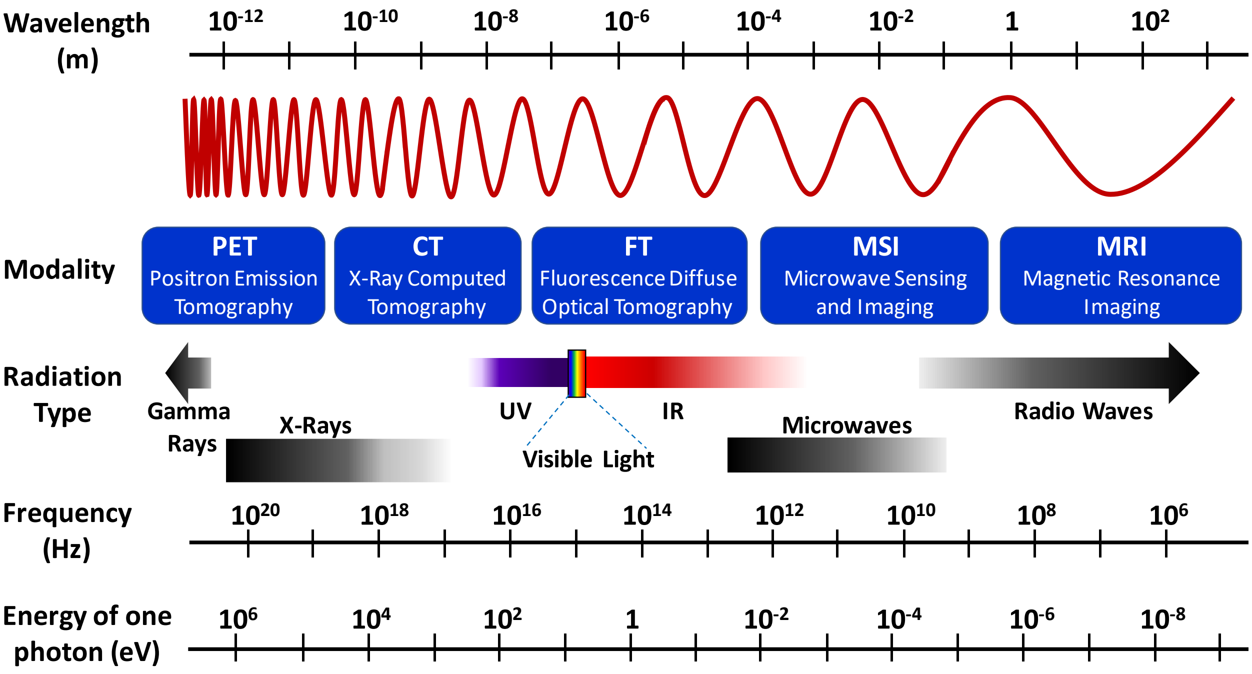

Figure 1. 1 Electromagnetic spectrum of medical imaging.

1.1.2.2 Functional vs anatomical imaging

The development of imaging modalities such as X-Ray Computed Tomography (CT), Ultrasound, and Magnetic Resonance Imaging (MRI) have shown great promise in anatomical or structural imaging. Anatomical imaging is the most common and established imaging type in clinical medicine as it can provide structural information by visualizing internal structures and physical abnormalities (bone fractures, foreign objects, blood clots, solid cancer tumors) with high resolution. Projection radiography was the first use of medical imaging, and remains a cornerstone of modern medical imaging today (1, 2). However, new techniques such as fluoroscopy and CT have allowed x-ray imaging of soft tissue. Angiography, a fluoroscopy technique using an iodine-based contrast agent injected into the bloodstream, can visualize the location and blood vessels and organs of the body which is extremely useful in diagnosing aneurysms, leaks, and blockages. CT is an invaluable tool in clinical medicine as it can provide detailed three-dimensional images of the areas of the body with high spatial resolution and discriminate soft tissue. On the other hand, MRI is a technique that has even higher soft tissue contrast than CT without the ionizing radiation, making it extremely popular in neuroimaging. Additionally, ultrasound has become a standard practice in prenatal care as it can safely provide real-time images of a fetus *in vivo*.

However, more recently, functional imaging has become extremely popular with the advancement of new technologies for MRI, nuclear, and optical imaging. Figure 1.2 shows the relative sensitivity and spatial resolution of popular anatomical and functional imaging modalities. Unlike anatomical imaging which provides information about the location of physical structures, functional imaging is much more sensitive and can provide information on biological processes and physiological and metabolic activities within the body. Functional MRI (fMRI) is a functional neuroimaging technique that detects changes associated with blood flow to measure brain activity. This functional imaging technique has become a popular tool in research to help shed light on understanding how the brain works. In addition, positron emission tomography (PET), a nuclear imaging technique, has become increasing popular in oncology as it can provide information about the location and metabolism of a tumor. Indeed, a whole body PET scan can provide the location(s) of cancer tumors identified by the elevated metabolic activity of the malignant cells using a given radiopharmaceutical isotope (3). Diffuse optical tomography (DOT) is an optical imaging modality that can derive functional information such as total hemoglobin concentration (HbT) and oxygen saturation from endogeneous contrast using near-infrared light and can be used to differentiate between healthy and cancerous tissue. For example, malignant tumors have been shown to have higher HbT compared to benign tumors (4-6).

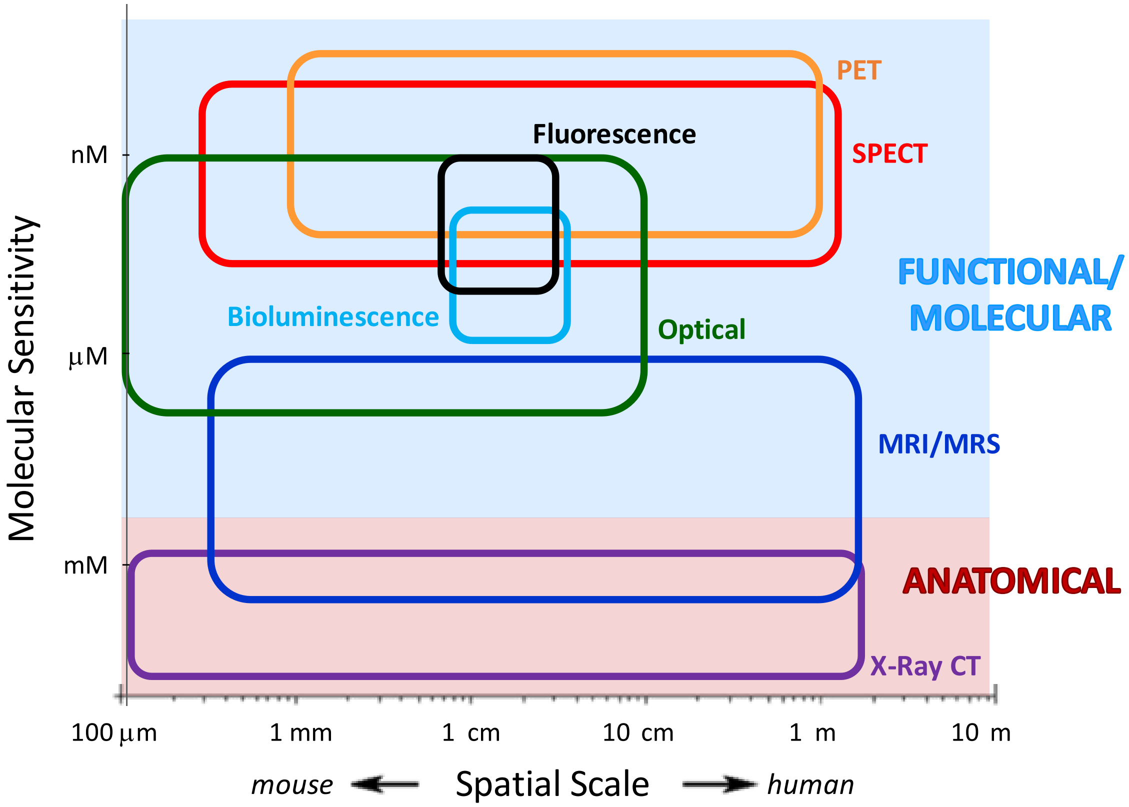

Figure 1. 2 Sensitivity and resolution of different imaging modalities. Schematic showing sensitivity and spatial resolution of different imaging modalities of different functional and anatomical imaging techniques. Figure is adapted from Frontiers in Physics, Vol 1, Townsend, D., et al., Grand challenges in biomedical physics, Page No 1. Copyright (2013) under the Creative Commons Attribution License.(7)

1.1.3 Molecular imaging

1.1.3.1 Introduction

In the last few decades, molecular imaging has exploded onto the scene with the advancement of molecular and cell biology techniques, imaging technologies (nuclear, optical, and MR), transgenic animal models, and specific imaging probes and drugs (8). Molecular imaging can non-invasively image cellular and molecular events *in vivo* to study biological processes and pathways, and diagnosis and manage diseases. The use of molecular probes engineered to respond to specific biological attributes as image contrast represents a significant change and unlocked new potential to enrich our understanding of biology and advanced the field of medicine. It is now more clear than ever that molecular imaging will have a great impact in personalized medicine by providing patient-specific diagnosis and individually tailored treatment based on specific biological attributes identified by molecular probes. Indeed, targeted patient specific treatment using molecular approaches are already a reality rather than a promise for several cancer types (9-12).

1.1.3.2 Fluorescence imaging

Recently, there has been an explosion in the availability of new technologies to noninvasively detect biological processes in preclinical models. One such modality, fluorescence optical imaging, uses fluorescent reporters and probes to repetitively interrogate molecular events and monitor disease progression, therapeutic efficacy, and molecular processes such as proliferation, apoptosis, and angiogenesis in animal models. Fluorescence imaging has great potential to provide new insights into biological research and accelerate the propagation of new knowledge towards pre-clinical and clinical stages with the ultimate goal of improving healthcare.

In this technique, tissue is illuminated with laser light to excite the molecular probes, which in turn emit light at a different wavelength. Fluorescence imaging aims to recover the distribution of the molecular probes inside the tissue by detecting the emitted light that reaches the surface of the tissue. The fact that these probes can target molecular pathways specific to particular diseases is expected to revolutionize the practice of clinical imaging. Although fluorescence imaging technology is slowly moving into the clinical arena, it has already found its niche in small animal imaging research (13-34). Extensively used by academic and industrial research groups to visualize biological processes and molecular events, small animal fluorescent imaging has expanded our knowledge of the fundamental molecular biologic and biochemical nature of various diseases.

In vivo fluorescence imaging has also become popular in pharmaceutical research not only for drug development, but also for the development of new contrast agents and cellular pathway-specific imaging probes (13, 16, 35-39). Small animal *in vivo* fluorescence imaging provides better statistics and reduces the number of animals used by monitoring the entire disease progression at each stage using the same animal *in vivo* as opposed to sacrificing multiple animals at each stage to determine the disease progression. Although there are a number of commercially available optical imaging systems, the majority of the systems can only provide 2D projection images (40-43). Extensive effort has been spent by many research labs to develop 3D tomographic whole-body animal imaging systems (13, 44). While several commercial FT systems have become available in recent years, the main barrier of wide-spread use of 3D fluorescence tomography (FT) systems that provides depth information has been their low spatial resolution and quantitative accuracy (13, 44-47).

As seen in Table 1, compared to other *in vivo* imaging modalities, the main advantages of fluorescence imaging and optical imaging in general is the high sensitivity, safety, low cost, portability, and fast acquisition time (35-39, 48). Optical imaging uses non-ionizing near infrared (NIR) light to probe tissue. This is a major advantage compared to nuclear imaging as it lacks the harmful radiation, complications, and expense that arise from the use of radiopharmaceuticals. However, NIR light has a poor imaging depth compared to nuclear imaging as it lacks the high energy rays that can easily penetrate biological tissue.

Table 1. 1 Comparison of *in vivo* imaging techniques currently used in biomedical research and/or medical diagnosis.***

	CT	**MRI**	**US**	**Diffuse Optics**	**SPECT/PET**
Relative Cost	Medium	High	Low	Low	High
Portability	No	No	Yes	Yes	No
Radiation Burden	Yes	No	No	No	Yes
Spatial Resolution	Excellent (50-100 μm)	Excellent (80-100 μm)	Good (50 μm)	Poor (1-10 mm)	Poor (1-2 mm)
Imaging Depth	Excellent (< 1 m)	Excellent (< 1 m)	Good (<10 cm)	Poor* (<10 cm)	Excellent (< 1 m)
Data Acquisition	min	sec to hours	min	sec to min	min
Clinical Imaging	Yes	Yes	Yes	No	Yes
Application	Anatomical	Anatomical, Functional, Molecular	Anatomical, Functional	Metabolic, Functional, Molecular	Metabolic, Functional, Molecular

*Spatial resolution decreases with imaging depth
**Abbreviations: CT computed tomography, MRI magnetic resonance imaging, US ultrasound, SPECT single photon emission tomography, PET positron emission tomography
***Table is adapted from Brazilian Journal of Physics, Vol 36, Number 1a, Beckmann, N., *In Vivo* magnetic resonance techniques and drug discovery, Page No 16-22. Copyright (2006) under the Creative Commons Attribution License.(59)

The major obstacle preventing the widespread use of diffuse optical imaging in clinical medicine is the high scattering nature of light in biological tissue which results in poor depth penetration and low spatial resolution and limited quantitative accuracy. Indeed, the spatial resolution degrades with imaging depth and is extremely poor in deep tissue (more than 1 cm deep) (49). Combining diffuse optical imaging with other anatomic imaging modalities such as x-ray, MRI and ultrasound have been successful in improving the spatial resolution and quantitative accuracy (13, 50-57). However, the weakness of this approach is that it does not perform well if the fluorescent target cannot be localized in the anatomical image, or when the fluorescence contrast does not correlate with the anatomical imaging modality contrast (58).

1.2 Aim of thesis

Although optical fluorescence imaging is becoming a powerful tool, its low quantitative accuracy and spatial resolution prevents its wide-spread for preclinical studies as well as its translation to the clinical arena. To overcome the high scattering nature of biological tissue, the main goal in this proposal is to develop an entirely new approach termed "Temperature-modulated fluorescence tomography (TM-FT)" that can provide high spatial resolution images at depths up to 6 cm without sacrificing the exceptional sensitivity of fluorescence light-based detection. The proposed technique is a unique and novel platform that brings two modalities together: high intensity focused ultrasound (HIFU) and FT. These two modalities will work synergistically to provide high-quality images that cannot be obtained by either alone. There are two key components to this innovative approach: a) Temperature sensitive florescent molecular probes (ThermoDots) and b) HIFU based modulation of tissue temperature (only 3-5^{0}C) with high spatial resolution. The major innovation is to utilize the HIFU for localized heating of temperature-sensitive molecular probes to achieve higher spatial resolution than conventional FT. The small size of the focal spot of the HIFU (~1.4 mm) allows imaging the distribution of these temperature sensitive agents with not only high spatial resolution but also high quantitative accuracy. This study is geared toward the first TM-FT system and *ex vivo* feasibility studies of this novel imaging modality. The outcome could be a radiation free, cost-effective, and portable tumor imaging system that will enable the utilization of fluorescence tomography (FT) in preclinical settings more effectively, it also has potential for translation to the clinical setting, particularly in image guided HIFU therapy.

Development of this novel system will include: development and optimization of the TM-FT reconstruction algorithm, development of ThermoDots and the TM-FT system, and validation with phantom studies and *ex vivo* animal tissue. The proposed technique will help alleviate the inherent limitation of *in vivo* optical imaging, namely the high scattering of light in biological tissue which results in low quantitative accuracy and spatial resolution.

1.3 Dissertation Organization

The organization of this dissertation is listed as follows:

<u>Chapter 2</u> serves as an introduction to TM-FT. This chapter gives a brief background on the important concepts and current imaging strategies as well as their limitations which serve as the motivation for this work.

<u>Chapter 3</u> describes the mathematical framework for this work. This includes modeling the photon propagation in tissue, the inverse problem, and the incorporation of functional and structural *a priori* information for DOT, FT, and TM-FT. A finite element method (FEM) based numerical solver was implemented to solve the diffusion equation.

Chapter 4 shows a wide range of simulation studies to validate the TM-FT reconstruction algorithm and demonstrate that this technique is capable of recovering the fluorescent agent parameters with high spatial resolution and accuracy.

Chapter 5 starts with a general review of fluorescent contrast agents and then focuses on ThermoDots. The characterization and development of the ThermoDots are described in terms of their dependence on temperature, stability, and size. Later, the pharmacokinetics of the ThermoDots are investigated *in vivo*. Finally, the targeting ThermoDots are introduced and their performance investigated *in vitro*.

Chapter 6 describes the development of the benchtop TM-FT system and TM-FT data acquisition method from the first prototype to optimizing the system parameters for *in vivo* imaging. Details on the TM-FT components, system design, and TM-FT experimental procedure are described. In addition, a general review about the tissue-mimicking multi-modality phantoms used in this work were included.

Chapter 7 presents the experimental results of our TM-FT system. A number of experimental studies were completed to validate the feasibility of this technique and investigate the performance of the system using agarose phantoms and in *ex vivo* animal tissue.

Chapter 8 concludes this thesis work and gives directions for further improvement.

1.4 Innovations and contributions

A number of innovative contributions have been achieved during this work:

1. New molecular diffuse optical imaging modality: TM-FT

The main innovation is the novel imaging technique proposed in this work. The proposed technique is a unique and novel platform that brings two modalities together: HIFU and FT using temperature activatable fluorescent molecular probes to achieve higher spatial resolution and quantitative accuracy than conventional FT. This multimodality method uses acoustic waves from the HIFU to heat the thermo-activatable fluorescent probes (ThermoDots) to directly map their spatial distribution in thick tissue. Acoustic waves are not subject to the same absorption and scattering limitations as optical waves and therefore can be used to improve the spatial resolution of FT.

2. First TM-FT System

To the best of our knowledge, this is the first temperature-modulated fluorescence tomography (TM-FT) system capable of both highly accurate qualitative and quantitative fluorescence studies. The frequency domain TM-FT system was developed by integrating HIFU with a PMT-based FT system. Unlike other hybrid modalities which operate independently and must be co-registered, with TM-FT, perfect co-registration is achieved as HIFU and FT work together in the same system to directly map the fluorescence distribution. Since the spatial resolution is mainly determined by the HIFU spot size, ~1.4 mm spatial resolution can be expected, even for thick tissue (up to 6 cm).

3. First TM-FT Quantitative Studies

We also were the first research group to validate the feasibility of this technique to provide high resolution FT images beyond the diffusion limit in phantom and *ex vivo* tissue studies. While other groups have performed qualitative studies to localize the position of the temperature dependent fluorescence probes alone, our method is the only one which uses this spatial information to recovers the concentration of the temperature dependent fluorescence probes as well (60-62). This is important because fluorophore concentration can reveal valuable information about the functional status of the target tissue and molecular environment especially when using targeted and activatable probes (36).

In addition, the second parameter that FT can provide, fluorescence lifetime, was also investigated (63). In general, fluorescence lifetime can provide additional functional information about the tissue under investigation, however, only a few studies have reported the reconstruction of lifetime (25, 68-75). In this work, we performed the first phantom studies to investigate the feasibility of TM-FT to recover fluorescence lifetime as well as concentration (63).

4. First TM-FT/DOT system

In addition, the first-of-its-kind TM-FT/DOT system was developed to integrate the three modalities in one setting thus resulting in perfect co-registration. DOT can recover the unknown background optical parameters to perform a better modeling of the light propagation within the imaged medium by correcting for the heterogeneity in the optical parameters. This is can be used as functional *a priori* information and combined with the spatial *a priori* information derived from the HIFU scan to guide and constrain the TM-FT image reconstruction algorithm. In this work, a study was performed to investigate the feasibility of TM-FT in *ex vivo* animal tissue. This is the first study to investigate the improvement of TM-FT images with DOT functional *a priori* information. Although not investigated in this work, the addition of DOT to the TM-FT system enhances its capabilities by being able to provide important functional information such as hemoglobin concentration and oxygen saturation for future applications.

5. Development of ThermoDots for *in vivo* small animal studies

   TM-FT relies on the thermo-responsive property of the ThermoDots to produce high spatial resolution FT images. Consequently, included in this work is the development of the unique temperature activatable fluorescent molecular probes (64). The ThermoDots were optimized to improve their fluorescence signal change and tune their temperature reversibility for different temperature ranges (65). In addition, the first *in vivo* studies are reported to investigate the ThermoDots' pharmacokinetics, temperature activation ability, and toxicity *in vivo*. Furthermore, the first *in vitro* studies to test the targeting ability of these novel probes are also reported.

6. TM-FT image reconstruction algorithm

   A frequency domain TM-FT image reconstruction algorithm was developed using a temperature dependent diffusion equation to model the propagation of the photons in the medium. This algorithm generates quantitatively correct fluorescence concentration and/or lifetime images. In addition, the reconstruction algorithm can incorporate *spatial a priori* information from the HIFU scan as well as the background optical parameters provided by DOT as *functional a priori* data to guide and constrain the TM-FT reconstruction algorithm. Included in this work are the programs developed to obtain the *spatial* and *functional a priori* information.

Chapter 2: Background

"The important thing in science is not so much to obtain new facts as to discover new ways of thinking about them." – Sir William Bragg

2.1 Fluorescent Tomography

2.1.1 Interaction of light and tissue

There are two important interactions that can occur as photons travel through biological tissue: absorption and scattering (55). This section outlines the main optical properties of the medium that describe its interaction with light: index of refraction, absorption, and scattering.

2.1.1.1 Index of Refraction (n)

The refractive index (index of refraction) is a dimensionless parameter that describes the effect the propagating medium has on the speed of light. The speed (v) at which light at a particular wavelength (λ) travels within a medium is dependent the refractive index:

$$v(\lambda) = \frac{c}{n(\lambda)} \tag{2.1}$$

where *n* is the refractive index of the medium. The higher the index, the lower the velocity of light in the medium. *c* is the speed of light in a vacuum ($\sim 3.00 \times 10^{11}$ mm/s). Biological tissue consists predominantly of water which has an index of 1.33. Although each tissue type is different (structure, composition, etc.), the commonly accepted value for the refractive index for biological tissue is 1.4 (66).

The index of refraction also determines the interaction of light at an interface. The index of refraction determines the amount of light that is reflected at the interface as well as the extent light is refracted. As light travels between media with different refractive indices, this causes a change in direction. The extent to which light is bent can be described by Snell's law of refraction:

$$n_1 sin\theta_1 = n_2 sin\theta_2$$

[2.2]

where θ_1 and θ_2 are the angles of incidence and refraction as seen in Figure 2.1.

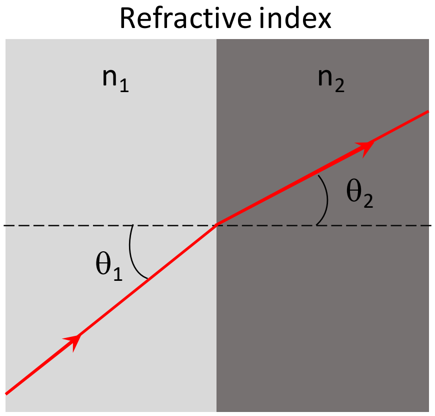

Figure 2. 1 Refraction between two media with different indices of refraction.

2.1.1.2 Absorption

When traveling through tissue, photons can be absorbed by the medium (67). In this event, the photon is extinguished and its energy is commonly converted to heat. This attenuation or reduction of light as it propagates through a non-scattering medium can be described by the Beer-Lambert law which relates the amount of light attenuation to the properties of the material (68):

$$I = I_o e^{-\mu_a(\lambda)x}$$

[2.3]

where I_0 is the incident intensity of light, I is the measured intensity after propagation through a tissue of thickness x, and $\mu_a(\lambda)$ is the absorption coefficient of the medium as seen in Figure 2.2. The absorption coefficient $\mu_a(\lambda)$, represents the probability of a photon being absorbed per unit length in a particular medium. Its reciprocal, the free path of absorption $1/\mu_a(\lambda)$, can also be understood as the distance a photon can travel in a medium before being absorbed (69). The absorption coefficient characterizes a type of absorber (chromophore) and is dependent on the chromophore concentration, C[M], and wavelength (λ) of light used:

$$\mu_a(\lambda) = ln\,10 \cdot \varepsilon(\lambda) \cdot C \tag{2.4}$$

where $\varepsilon_n(\lambda)$ is the wavelength dependent extinction coefficient which represents the absorption of a specific chromophore at a particular wavelength. The absorption coefficient can be due to a single chromophore or a mixture of multiple chromophores. In this case, the total absorption coefficient can be described by the summation of the absorption coefficient of each chromophore.

$$\mu_a(\lambda) = ln\,10 \cdot \sum_n \varepsilon_n(\lambda) \cdot C_n \tag{2.5}$$

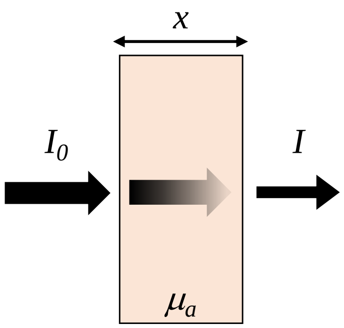

Figure 2. 2 Attenuation of light through an absorbent medium

Absorption is wavelength dependent. The near infrared (NIR) region from around 650-1000 nm is often called the optical or therapeutic window as many imaging modalities have taken advantage of the fact that in this region, both absorption and scattering, which will be described in the next section, are minimized allowing for photons to travel deep into the tissue. The most important absorbing chromophores found within the therapeutic window are water, lipid, deoxy- and oxyhemoglobin, all of which have their own unique absorption spectrums, Figure 2.3 (69, 70). By taking measurements and estimating the μ_a at multiple wavelengths, equation [2.5] can be used to recover the concentration of individual chromophores.

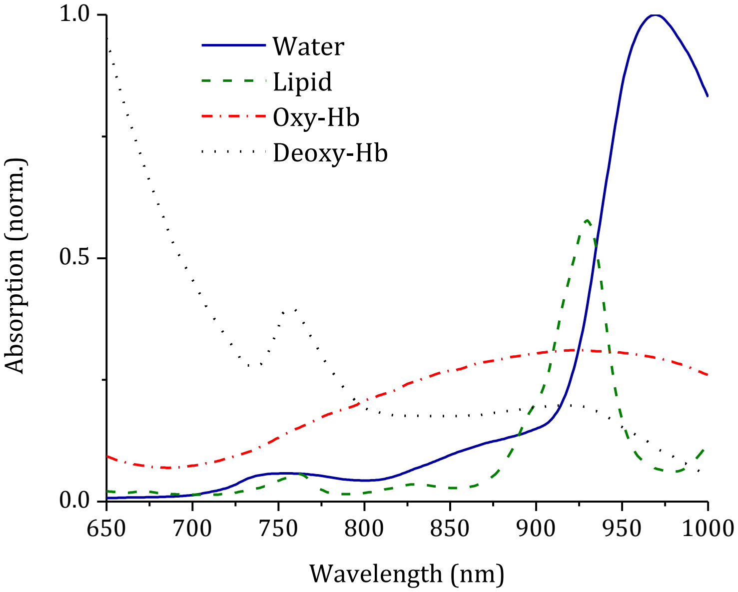

Figure 2. 3 Absorption spectrum in the NIR therapeutic window are shown for water, lipid, oxy- and deoxyhemoglobin. Reprinted from Ruiz, Jessica. Breast Density Quantification Using Structured-Light Diffuse Optical Tomography, Dissertation, UC Irvine, 2016. Page No 18. (71)

2.1.1.3 Scattering

In addition to absorption, a photon can also undergo scattering while propagating through biological tissue. Scattering is caused by a mismatch in the refractive index at microscopic boundaries such as cell membranes. In this event, the photon is not extinguished but undergoes a change in direction from its original path due to interaction with tissue constituents, Figure 2.4.

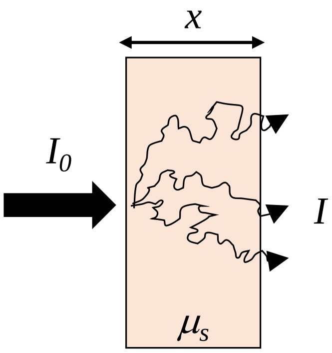

Figure 2. 4 Attenuation of light through a scattering medium

The scattering of a medium is described by its scattering coefficient μ_s, which is the probability of a photon being scattered per unit length. The free path of scattering, $1/\mu_s$, represents the distance a photon can travel in a medium before being scattered. If the medium is highly scattering, this will result in high diffusion of light throughout the medium as the paths taken by the photons are no longer straight lines as for X-rays, Figure 2.4. Due to the different photon paths, the photons emerge from the medium at different positions and directions and cannot be detected by a single photodetector. This results in a lower detected signal. In addition, as the distance each photon travels is different, determining the attenuation of light is extremely challenging when a medium is both absorbing and scattering such as biological tissue. Therefore, the diffusion approximation to the radiative transfer equation is used to describe the light propagation in more complicated media such as biological tissue. This is described in more detail in Chapter 3.

2.1.1.3.1 Anisotropy

In tissue, light is generally scattered in a preferential direction relative to its incident angle. Biological tissue is highly scattering in the forward direction which means the direction of the scattering favors the direction of the incident light (72-74). A measure of this parameter of scattering is given by the anisotropy factor, g, which is the average of the cosine of the scattering or deflection angle θ when a photon is scattered as seen in Figure 2.5 (75). Anisotropy (g) can be understood as the measure of forward direction retained after a single scattering event. The value of g approaching 1, 0, and -1 describe extremely forward, isotropic, and highly backward scattering, respectively. Biological tissue is forward scattering and typically values for g is between 0.8 and 1 (72-74) .

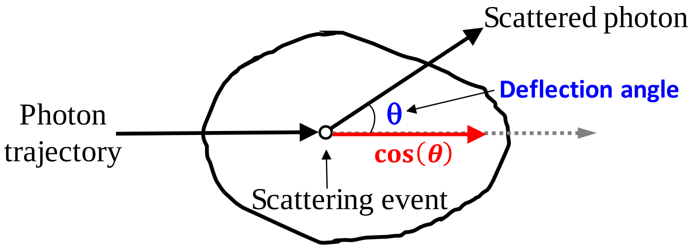

Figure 2. 5 Scattering anisotropy

Scattering in tissues is commonly expressed in terms of the reduced scattering coefficient, μ_s'.

$$\mu_s' = \mu_s(1 - g) \tag{2.6}$$

The reduced scattering coefficient represents the effective equivalent number of isotropic scatters per unit of length, or equivalent isotropic scattering coefficient. It can also be described in terms of its inverse. The inverse of the reduced scattering coefficient is also known as the transport-mean-free pathlength and describes the distance a photon will travel before becoming fully isotropic, where it has equal probability of moving in any direction (69).

In tissue, scattering is complex and the type and intensity of the scattering depends on the properties of the biological scatterer relative to the optical wavelength (~0.6-1 μm)(74). The extent to which a tissue will scatter light depends on the size and spatial distribution of molecules present in the medium:

$$\mu_s'(\lambda) = a \cdot \lambda^{-b} \tag{2.7}$$

with a and b as tissue-specific parameters (74). Mie scattering describes the scattering of electromagnetic radiation by a sphere. From Figure 2.6, we can see that Mie scattering tends to dominate when using NIR light as photons are scattered most strongly by structures whose size match the optical wavelength (~0.6-1μm). Mie scattering is also forward scattering which means the direction of the scattering favors the direction of the incident light compared to Rayleigh scattering which is isotropic (76). Mie theory is valid for all sizes of spherical particles, and the intensity of the scattering is not as wavelength dependent as Rayleigh scattering which dominates when the size of the structure is small, 0.1λ (76).

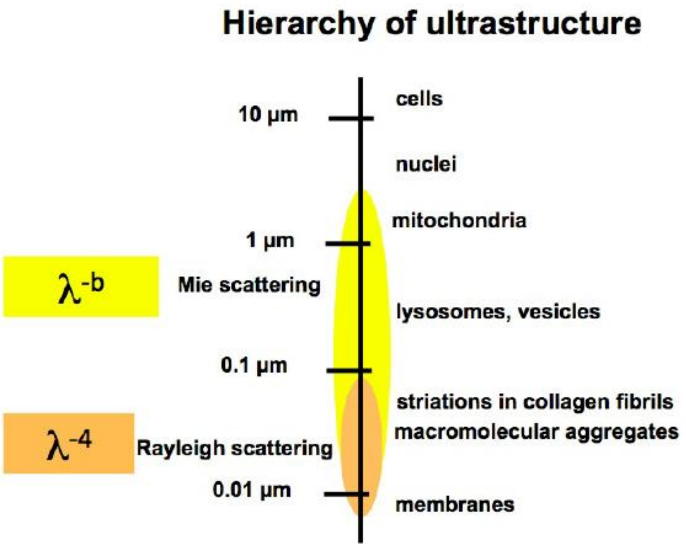

Figure 2. 6 Sources of common biological structures for photon scattering and type of scattering. Reprinted from the Journal of Innovative Optical Health Sciences, Vol 04 Issue 1, Jacques, Steven L., Fractal Nature of Light Scattering in Tissues, Page No 1-7. Copyright (2011) by World Scientific Publishing Co., Inc. (77)

2.1.2 Fluorescence

2.1.2.1 Photophysics of fluorescence

Fluorescence is a form of luminescence. Luminescence is the property of some atoms and molecules to absorb light of a specific wavelength and after a brief period of time emit light of a longer wavelength (photoluminescence)(78). The Jablonski diagram is an energy diagram that describes the relationship between absorption and the photoluminescence processes (fluorescence and phosphorescence) in terms of the electronic and vibrational energy levels, Figure 2.7. Although the Jablonski diagram shows the possible transitions in a particular molecule, the probability of these processes occurring is dependent on the time scale of each transition. The faster the transition, the more likely the process will occur (79). Consequently, the average time for each process is shown in Figure 2.7.

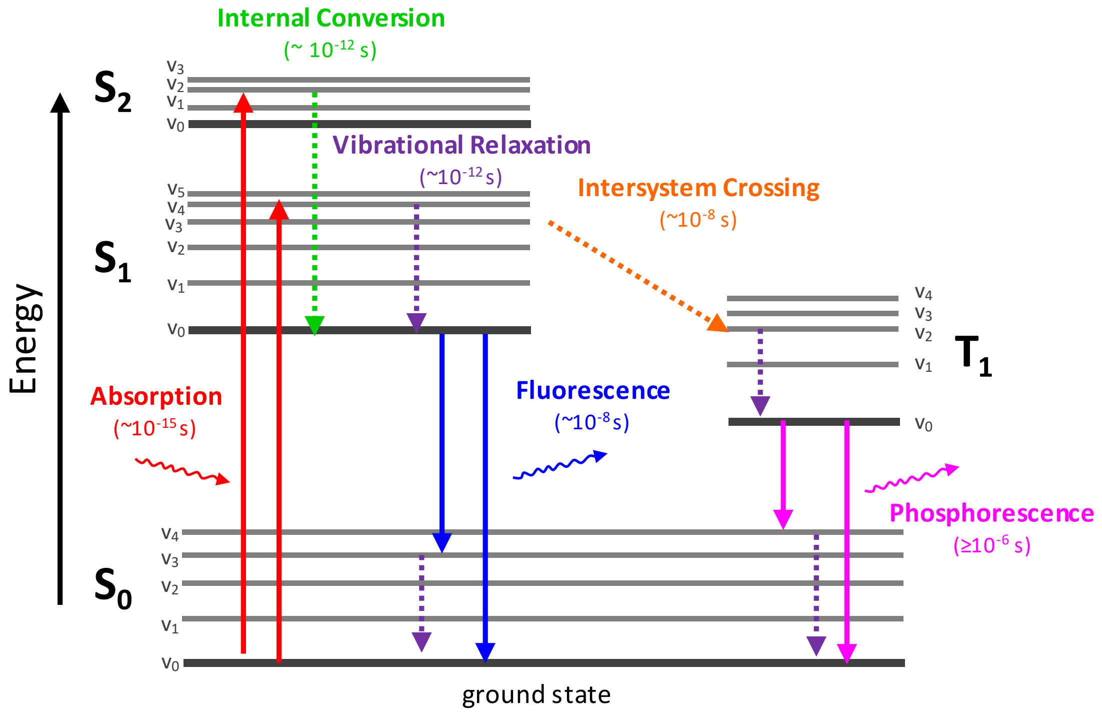

Figure 2. 7 Jablonski diagram. Typical pathways of a fluorophore following excitation by a single photon are shown. S_0, S_1, and S_2 represent the (ground, first excited, and second excited) singlet electronic states. T_1 represents the triplet state. The gray lines at each electronic state represent the vibrational energy levels. Radiative processes are denoted by the solid arrows, while nonradiative processes are described by the dotted arrows. The various processes are shown along with their average times. (80, 81)

2.1.2.2 Absorption

The first step in the luminescence process is the absorption of a photon which is also the fastest step (~10^{-15} s) (80). In this process, a molecule or atom can absorb a photon of a particular energy. This energy is transferred to an electron causing its transition from a lower energy level to an excited singlet electronic state (i.e. $S_0 \rightarrow S_1$) as well as some vibrational states in some cases, as seen by the red arrows in Figure 2.7. Only wavelengths of light that match the energy difference between two different energy levels of a particular molecule can be absorbed. The energy of photon absorbed is directly responsible for the electron excitation and matches the energy difference between the excited and original energy level. Therefore, the minimum energy required for fluorescence is for the photon to cause a transition to a higher electronic excited state.

2.1.2.3 Internal conversion and vibrational relaxation

Once the electron is in its excited state, there are several processes that can occur for the electron to relax back to the more stable ground state (S_0). The most likely scenario will be the relaxation to the lowest vibrational energy level of the first excited state (S_1). This usually occurs through a nonradiative process, vibrational relaxation, in which the electron decays to lower vibrational energy levels in the same electronic state, $v_4 \rightarrow v_0$, (purple dotted arrow in Figure 2.7). If the electron transitions to a lower vibrational energy level in a different electronic state, this process is known as internal conversion (green arrow in Figure 2.7). Both these processes are nonradiative as energy is usually dissipated as heat and occur on the order of a picosecond (10^{-12}) (80).

2.1.2.4 Fluorescence

Another way the electron can dissipate energy is by fluorescence. Fluorescence is the emission of a photon usually upon decay from the first electronically excited state to the ground state, $S_1 \rightarrow S_0$, (blue arrow in Figure 2.7). The energy of the photon, or wavelength of light directly matches the difference in energy between the two energy levels of the transition. This radiative process is relatively slow ($\sim 10^{-8}$ s) compared to vibrational relaxation and internal conversion. Consequently, fluorescence will most often occur between the first excited electron state to the ground state as internal conversion becomes less efficient at this larger energy gap (78).

2.1.2.4.1 Stokes shift

Because energy is dissipated through internal conversion and vibrational relaxation, the emitted fluorescence light is typically of lower energy and longer wavelength than the excitation light absorbed ($E_{exciation}>E_{emission}$, or $\lambda_{excitation}<\lambda_{emission}$), this wavelength shift is known as the Stokes shift, Figure 2.8 (78). For fluorescence imaging, we take advantage of this redshift to separate the emission light from the excitation signal using optical filters. In addition, the degree to which the emission wavelength is shifted depends on the fluorophore and the local environment. For example, the peak emission wavelength of indocyanine green (ICG), the main NIR fluorophore, changes from 810 nm in water to 830 nm in plasma (82, 83).

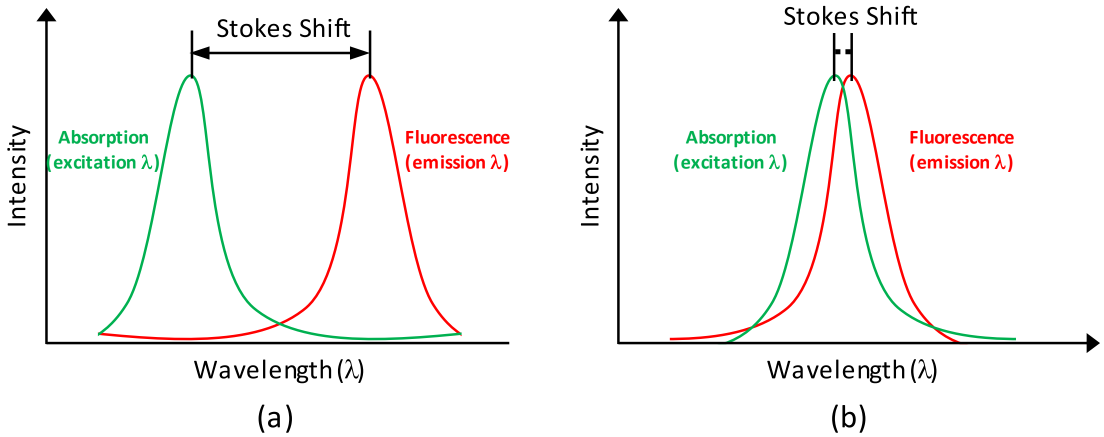

Figure 2. 8 Stokes shift of the excitation and emission spectra of a fluorophore. The size of the Stokes shift determines the usability of the fluorophore. (a) Large Stokes shifts with clear distinction of the excitation and emission light is desired compared to fluorophores with a (b) small Stokes shift in which the spectra overlap leading to low SNR.

2.1.2.4.2 Quantum yield

The Jablonski diagram shows the number of process to dissipate energy (internal conversion, vibrational relaxation, fluorescence, intersystem crossing, phosphorescence).

However, the likelihood of each process occurring is not the same. The probability for a process to occur depends on the radiative and nonradiative decay rates which in turn depends on the fluorophore and the local environment in addition to other factors such as concentration, temperature, pH, and polarity (78). For example, the fluorophore 1-anilinonaphthalene-8-sulfonate (1,8-ANS) has a 200-fold enhancement in fluorescence signal when bound to serum albumin versus aqueous buffer (84). Quantum yield or quantum efficiency describes the efficiency in which light is absorbed and converted to fluorescence. The quantum yield, η, is the ratio of the number of photons emitted $I_{emitted}$ and absorbed $I_{absorbed}$:

$$\eta = \frac{number\ of\ photons\ emitted}{number\ of\ photons\ absorbed} = \frac{I_{emitted}}{I_{absorbed}} \tag{2.7}$$

Consequently, molecules which highly fluoresce will have a quantum yield of 1 as opposed to molecules which do not fluoresce whose quantum yield will be 0. Higher quantum yields increase the fluorescence intensity. Green fluorescent protein (GFP) and the fluorophore fluorescein have rather high quantum yields ~0.8 and ~ 0.9, respectively (80). On the other hand, ICG has a quantum yield of 0.016 (85).

2.1.2.4.3 Lifetime

The fluorescence lifetime, τ, refers to the average time a molecule stays in its excited state before emitting a photon (78). Although this includes the time for processes vibrational relaxation and internal conversion, the majority of this time is dominated by the period of time the electron spends in the lowest excited singlet electronic level (S_1, v_0) prior to emission (80). Because fluorescence is a spontaneous emission, the electron typically spends several nanoseconds before spontaneous decay to the ground state. Therefore, lifetime is important because it describes the amount of time in which the fluorophore can interact with its environment (84). Generally, fluorescence lifetimes are on the order of nanoseconds. In contrast to fluorescence intensity, fluorescence lifetime is very sensitive to changes in the microenvironment of the fluorophore such as local PH, blood supply and temperature (58, 83, 86). Thus, fluorescence lifetime can be a useful tool to probe changes in the fluorophore microenvironment. Fluorescence lifetime can also distinguish between exogenous and endogenous sources of fluorescence increasing the SNR and sensitivity (87). Furthermore, lifetime measurements can also be used to distinguish multiple sources of fluorescence, even if their emission and excitation spectrum overlap (87).

2.1.2.5 Phosphorescence

The second radiative process that can also occur is phosphorescence. Phosphorescence is the emission of light upon the transition from an excited triplet state to a singlet ground state, $T_1 \rightarrow S_0$ (pink arrow in Figure 2.7). This is possible through intersystem crossing, where the electron changes spin multiplicity from an excited singlet state to an excited triplet state, $S_1 \rightarrow T_1$ (orange dotted arrow in Figure 2.7). These processes are relatively rare as transitions between the singlet and triplet states are forbidden. Indeed, although intersystem crossing is comparable to fluorescence ($\sim 10^{-8}$ s), phosphorescence is much slower ($\geq 10^{-6}$ s). Delayed fluorescence, which is the transition of the electron from the triplet state back to the singlet state before radiative transition to the ground singlet state($T_1 \rightarrow S_1 \rightarrow S_0$), is another possible process although it is quite rare.

2.1.2.6 Photobleaching

In theory, the fluorescence cycle can continue indefinitely with the molecule cycling between the ground and excited states. However, in reality, between 10,000-40,000 cycles is the estimated limit before permanent photobleaching occurs for good fluorophores (80). Photobleaching is the destruction of the fluorophore resulting in loss of fluorescence caused by light exposure (84, 88). Photobleaching leads to the permanent loss of fluorescence signal and is different that quenching which is a reversible loss due to the noncovalent interactions between the fluorophore and molecular environment (80). Although the exact process for photobleaching is unclear, it is usually associated with irreversible covalent modifications due to interaction with another molecule (i.e. oxygen) in the triplet state after intersystem conversion (78). The time the fluorophore spends in the excited triplet state is relatively long compared to the excited singlet state allowing more time for the fluorophore to interact with other molecules and undergo chemical reactions in the environment. Thus, the number of excitation and emissions cycles before photobleaching depends on the molecular structure of the fluorophore and its local environment. However, not all photobleaching is undesired, such as in fluorescence recovery after photobleaching (FRAP) to study the diffusion rates of the fluorophore(89). In this process, fluorophore molecules within a target region is intentionally bleached in order to observe the diffusion of new fluorophore molecules into the target region. However, in cases where photobleaching is not desired, it is important to minimize photobleaching to avoid abnormal intensity measurements and sample toxicity.

2.1.3 Contrast

For biomedical imaging, the sources of fluorescence contrast can be separated into two types: endogenous and exogenous fluorophores. Endogenous fluorophores are internal sources of contrast found naturally within the body, while exogenous fluorophores are external sources of contrast not naturally occurring in the body that must be administered externally prior to imaging.

2.1.3.1 Endogenous

Autofluorescence is the natural emission of light by endogenous fluorophores intrinsic to the body upon excitation from an external light source. Common endogenous fluorophores include amino acids, structural proteins, enzymes, vitamins to name a few. A small list of common contributors to autofluorescence are included in Table 2.1. Endogenous fluorophores are biological significant and play important roles in processes such as cellular metabolism or tissue structure (90). Consequently, changes in autofluorescence (intensity and lifetime) could provide important information about diseases such as cancer and ischemia (90). Indeed, several studies have correlated changes in tissue fluorescence during disease onset to changes in the endogenous fluorophore concentration, microenvironment, morphology, and composition (80, 90).

A major benefit of autofluorescence is the lack of external contrast agents and resultant complications that arise such as fluorophore toxicity. However, as seen in Figure 2.9, the excitation and emission spectra of common endogenous fluorophores tend to overlap making it difficult to discriminate individual chromophores. Lifetime measurements can help discriminate individual chromophores as well as provide information about the changes in the microenvironment. In addition, the majority of endogenous fluorophores have a peak absorbance in the UV region and emit in the UV-visible range where absorbance by chromophores: water, melanin, proteins, and hemoglobin is high (91). Consequently, autofluorescence imaging is mostly used for surface or shallow imaging applications as the depth penetration of light is quite low in this region.

Table 2. 1 List of common endogenous fluorophores.**

Endogenous fluorophores	**Excitation maxima (nm)**	**Emission maxima (nm)**
Amino Acids		
Tryptophan	280	350
Phenylalanine	260	280
Structural proteins		
Collagen	325, 360	400, 405
Elastin	290, 325	340, 400
Enzymes and coenzymes		
FAD, Flavins	450	535
NADH	290, 351	440, 460
NADPH	336	464
Vitamins		
Vitamin A	327	510
Vitamin D	390	480
Lipids		
Phospholipids	436	540, 560
Lipofuscin	340–395	540, 430–460
Porphyrins	400–450	630, 690

**NADH*, reduced nicotinamide dinucelotide; *NAD(P)H*, reduced nicotinamide dinucleotide phosphate; *FAD*, flavin adenine dinucleotide.

**Reference: Adapted from Neoplasia, Vol 2, Issue 1-2, Ramanujam, Nirmala. Fluorescence Spectroscopy of Neoplastic and Non-Neoplastic Tissues, Page No 89-117. Copyright (2000) under a Creative Common license. (92)

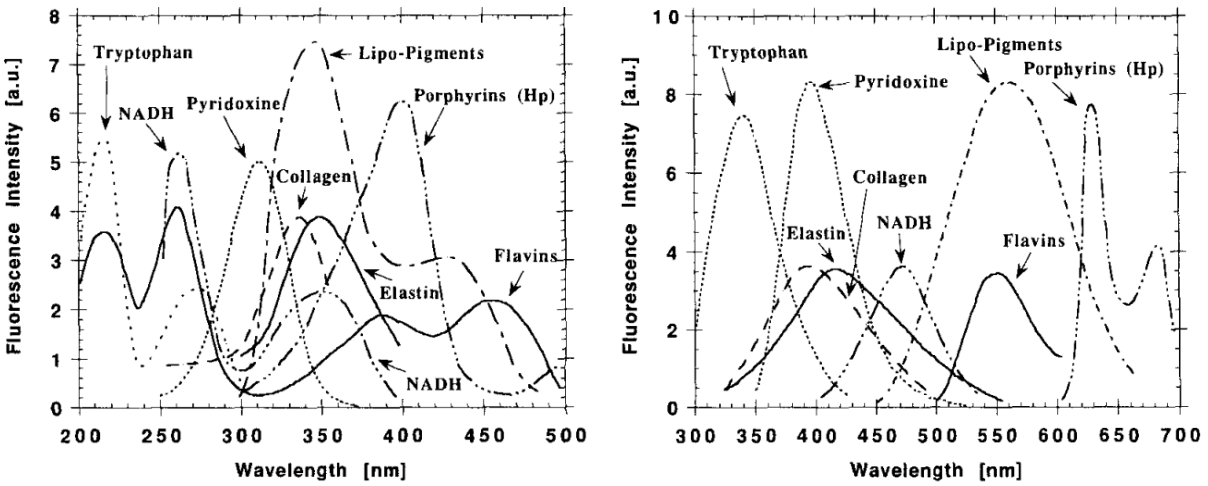

(a) (b)

Figure 2. 9. Endogenous fluorophores. (a) Excitation and (b) emission spectra of several endogenous tissue fluorophores. Excitation and emission spectra for endogenous tissue fluorophores are within UV-vis region (200-700 nm) of the EM spectrum and mostly outside the NIR therapeutic window (650 -1000 nm). Reprinted with permission from Photochemistry and Photobiology, Vol 68 Issue 5, Wagnieres, George A., *In vivo* fluorescence spectroscopy and imaging for oncological applications, Page No 603-632. Copyright (1998) by John Wiley and Sons. (93)

2.1.3.1 Exogenous

The recent advances in exogenous fluorophores have open up the possibility of labelled or targeted fluorescence contrast agents. Exogenous fluorophores can be used to narrow down the focus and highlight specific structural features or monitor the local environment or presence of a biomolecule to answer specific biological questions (84). Indeed, the major advantage of exogenous fluorophores is that they are not native to the body so the contrast agent can be manipulated and engineered to optimize the imaging properties (fluorescence signal, stokes shift, wavelength region, quantum yield, etc) for a particular application (92). Indeed, the fluorophore can be chosen from a broad list of commercially available exogenous fluorophores by selecting the desired photophysical and pharmacokinetic properties depending on the application. In addition, exogenous fluorophores are often brighter than endogenous fluorophores and not limited to the UV and visible spectrum, but can be engineered to span the range from UV to NIR. NIR fluorophores are of a particular interest as in the therapeutic window, photons can penetrate the deepest which is important for *in vivo* molecular imaging. In addition, fluorescent imaging in this region is very sensitive to the NIR fluorophore's signal and has a high signal to background noise ratio (SNR) as the background fluorescence is low due to the fact that autofluorescence from endogenous fluorophores in the tissue are minimized in the NIR region.

2.1.3.1.1 Types of fluorescent probes

The three main categories of exogenous fluorescent probes are organic dyes, proteins and quantum dots. Quantum dots (QDs) are inorganic nanocrystals that fluoresce at sharp and discreet wavelengths depending on their size. QDs benefits include high quantum yields and increased photostability but are difficult to target (94). The discovery of the green fluorescent protein (GFP) opened up a new type of contrast to the fluorophore "toolbox". Fluorescent proteins can be used as reporter genes to impart important information on gene expression, protein trafficking, and other dynamic biochemical signals by transfection of GFP labeled cells (94). In recent years, there has been much work to improve the spectral performance and expand the spectral properties of fluorescent proteins to span a range of excitation and emission wavelengths from blue to NIR (94).

Although there has been a recent surge in the number of fluorescent probes, currently there are only three fluorophores approved for clinical use in the United States of America: ICG, fluorescein, and methylene blue (MB). The majority of the biomedical fluorescent probes developed are in preliminary stages or utilized in preclinical research. These three fluorophores are examples of organic dyes. ICG is of particular interest due to the fact that is the most used NIR fluorophore in clinical imaging. Most organic fluorophores are water-soluble and carry reactive groups that allow the fluorophore to be targeted. Although the three commercially available fluorophores approved by the United States Food and Drug Administration (FDA) for clinical imaging are not molecular specific, there has been a lot of interest in improving the photostability, quantum yield, and targeting ability of ICG in particular by combining it with effective delivery systems (91). More information can be found in Chapter 5.

2.2 Introduction to diffuse optical imaging

2.2.1 DOT

2.2.1.1 Description

Within the therapeutic window, scattering is dominant over absorption, and the propagation of light becomes diffuse. In diffuse optical imaging (DOI), the medium is illuminated with an external light source. These photons propagate through the tissue and exit the medium where they collected by a photodetector. As the photons travel through the tissue, they undergo numerous absorption and scattering events which result in a reduction of signal compared to the intensity of incident light. This attenuation, or the amount of absorption and scattering, is biologically significant as it is dependent on the molecular composition of the tissue due to the interaction of light with the tissue chromophores. Consequently, DOI can infer the internal molecular composition of the tissue from the attenuation of light measured at the boundary of the tissue (69, 95, 96).

Diffuse optical tomography (DOT) is a diffuse optical imaging technique that measures the attenuation of light at multiple positions at the surface boundary. This allows the tomographic recovery of the internal distribution and concentration of tissue chromophores. DOT is safe and inexpensive as it uses NIR light to probe tissue properties based on endogenous contrast. DOT can noninvasively recover chromophore concentration by generating a 3D map of the optical properties of the tissue, absorption and scattering, which can then be used to derive functional information such as total hemoglobin concentration (HbT), oxygen saturation and water content.

2.2.1.2 Applications of DOT [1]

DOT has great potential for cancer imaging (97, 98). HbT can provide much needed insight on tissue metabolism and tumor malignancy (4). For example, malignant tumors have been shown to have a higher HbT than benign tumors (5, 6). DOT can provide information on the tumor microenvironment as changes in the hemoglobin and oxygen content are directly related to the angiogenesis, metabolism, and hypoxia in the tumor (99). Studies have shown that the HbT in the tumor is directly related to the tumor angiogenesis (100). The oxygen saturation of the tumor can also provide valuable information on the tumor metabolism and hypoxia (101). Such information could impact treatment strategies by helping clinicians provide personalized patient treatment. For example, decreases in the tumor hemoglobin and oxygen content following a chemotherapy treatment have been

---

[1] This section (2.2.1.2 Applications of DOT) was reproduced from Applied Optics, Vol 55 Issue 21, Kwong, Tiffany C., et al., Differentiation of tumor vasculature heterogeneity levels in small animals based on total hemoglobin concentration using magnetic resonance-guided diffuse optical tomography in vivo. Page No 5479-5487 Copyright (2016) with permission from Optical Society of America. (66)

associated with a better treatment response and outcome (102, 103). In addition, studies have shown that the tumor metabolic response can predate anatomical changes, such as the size obtained from traditional imaging modalities during neoadjuvant chemotherapy, making DOT a promising imaging modality to monitor the early treatment response (104).

Despite its high sensitivity, DOT renders images at a low spatial resolution due to the high scattering of light in tissue. Tumor background contrast can be enhanced through external stimulation, such as gas inhalation and contrast agent injection, to improve the image quality (105, 106). However, stand-alone diffuse optical imaging systems still suffer from degraded spatial resolution and low quantitative accuracy (107, 108). To overcome these limitations, extensive effort has been spent to develop multimodality techniques that combine DOT with higher resolution imaging modalities, such as MRI, x ray, and ultrasound (106, 109-111). This multimodality approach has successfully been used to overcome the optical resolution limit of DOT for a number of applications such as determining tumor malignancy and monitoring tumor metabolic response to therapy (102, 112, 113).

While multi-modality DOT is still in the research phase, it has primarily been used in human studies. There is a lack of multi-modality small animal DOT systems for preclinical research (102). As the optical properties are very heterogeneous in small animals, most preclinical multimodality imaging systems utilize fluorescent contrast for increased sensitivity and signal separation from background noise. Although DOT lacks the sensitivity of fluorescence imaging, it is much simpler to perform experimentally and computationally, has a higher signal-to-noise ratio (SNR), and does not require administered contrast agents. This can add an additional variable to consider for longitudinal studies, and increase the time during and in between imaging sessions (109, 114). With the growing number of cancer therapy drugs, specifically antiangiogenic drugs that inhibit tumor growth, there is a need for small animal imaging systems to detect tumor microenvironment changes in pharmaceutical research for drug development and the study of hemodynamics. Indeed, with the progress of transgenic manipulation of small animals, there is no denying the key role animal models play in biomedical research to study disease and biological processes (98, 109).

2.2.2 FDOT

2.2.2.1 Description

Recently, fluorescence optical imaging has become increasing popular due to the major advancements in fluorescent molecular probes. As one of the main molecular imaging techniques, fluorescence tomography (FT) can provide the spatial distribution of endogenous fluorescent contrast (i.e. fluorescent proteins) or labeled molecular probes using non-ionizing radiation and low cost instrumentation in contrast to nuclear imaging. Unlike DOT which detects differences in absorption, FT measures fluorescence signal which is unique and only emitted from the specific probe or endogenous source. Consequently, FT is extremely sensitive due to the high signal-to-background contrast.

FT utilizes laser light to excite the fluorescence sources located deep in a medium. Once excited, these sources relax to their ground state in nanoseconds by emitting lower energy photons. While propagating towards the surface of the medium, these photons are subjected to a vast amount of scattering events along the way. This makes the FT inverse problem exceptionally difficult, which is defined as the problem of recovering the fluorescence source distribution from the measured light intensities on the tissue surface. Accordingly, the resolution and quantitative accuracy of the reconstructed images are very low (13). In contrast to DOT which measure the intensity changes of transmitted light through the tissue, FT uses filters to separate the excitation signal from the emitted fluorescence signal when detected at the surface of the tissue. The measured fluorescent light intensities are analyzed using a reconstruction program which is based on the Diffusion Approximation to model photon propagation in tissue to generate an image.

There are two main challenges in quantitative fluorescence tomography. The fluorescence parameters depend on the depth and size of the lesions due to the ill-posedness of the FT inverse problem to determine the distribution of the fluorophore inside the medium from a limited number of measured light intensities on the surface (13). Thus, distinguishing between a small fluorescent inclusion located close to the surface as opposed to a large fluorescent inclusion deep inside the tissue is hard to differentiate. The second challenge is the accuracy of the FT reconstruction is affected by the distribution of the background optical properties. Without proper modeling of emission and excitation light propagation between the boundary of the medium and fluorophores, it is difficult to obtain accurate results (115).

2.2.2.2 Imaging geometries

Imaging geometry is important because it ultimately determines the information content of the images (13). The different imaging geometries used for collecting fluorescent light can be divided in two categories: epi-illumination and trans-illumination.

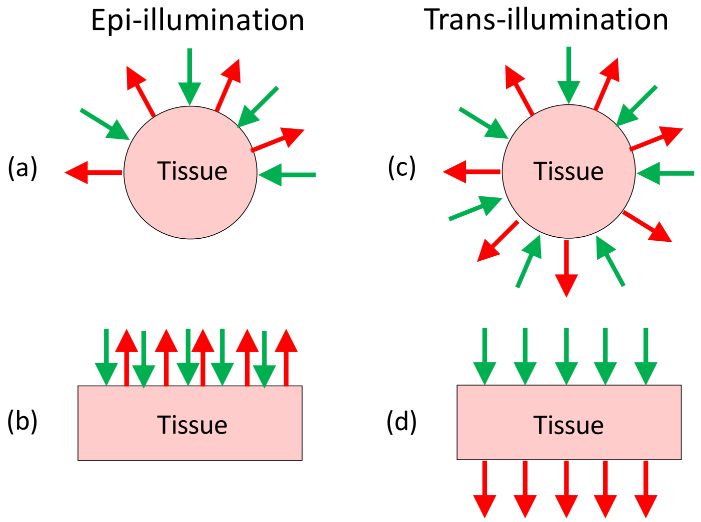

Figure 2. 10 Imaging geometries of common DOT and FT configurations. Green inward arrows indicate sources and the red outward arrows indicate the detector locations. Epi-illumination configurations are shown for (a) circular and (b) slab geometries. Trans-illumination configurations are shown for (a) circular and (b) slab geometries.

2.2.2.2.1 Epi-illumination

Epi-illumination also known as reflectance mode places the source and detector on the same side of the tissue as seen in Figure 2.10 (a) and (b). Wide-field or point illumination and detection schemes can be utilized to achieve various spatial resolution and tissue information. For example, wide-field illumination schemes are noted for this ease of use and fast measurement acquisition as the whole animal can be imaged with a single exposure, and are commonly used in commercial preclinical optical imaging systems. On the other hand, point illumination and detection can be used to provide limited depth information by changing the distance between the source and detector fibers. However, in general, epi-illumination geometry is plagued by the poor depth sensitivity (~ 1-3 cm) and surface-weighted imaging (13).

2.2.2.2.2 Trans-illumination

Trans-illumination geometry (transmission mode) measures the transmission of light through the tissue by positioning the source and detector on opposite sides of the tissue as seen in Figure 2.10 (c) and (d). Consequently, light must pass through the bulk of the tissue to be detected. This limits the number of applications, as a trans-illumination cannot be used when the tissue is too thick (> 10 cm). However, trans-illumination images are more accurate as they can provide more information and are more sensitive to deep seated fluorophores compared to epi-illumination whose sensitivity is surface weighted. Conversely, trans-illumination imaging is usually performed in a raster-scan configuration which much slower than wide-field epi-illumination systems. In addition, as seen in Figure 2.10, the tissue can be compressed to a slab form to reduce the thickness of the tissue. However, the rectangular or slab geometry lacks the symmetry of the circular geometry which results in an uneven response from the imaging field with position (116). The TM-FT system developed in this thesis uses a slab geometry in transmission mode.

2.2.2.3 Optical tomography measurement methods

There are three distinct methods for measuring the propagation of NIR light in tissue: continuous wave (CW), frequency domain photon migration (FD), and time domain photon migration (TD). A brief summary of the three optical tomography methods are included.

2.2.2.3.1 Continuous wave

The CW method is the simplest and easiest to implement. CW methods are based on measuring the intensity of light which can be used to determine the concentration or quantum yield of an exogenous fluorescent contrast agent (FT), or absorption of the tissue (DOT). In general, the tissue is illuminated with a constant intensity light source and detection of the transmitted or fluorescent light involves measuring the spatial distribution of light intensity at the surface of the tissue. As seen in Figure 2.11, this method is the least expensive of the three as virtually any type of light source and detector can be used. Most commercial small animal imaging systems employ the continuous wave strategy due to its ease of use, availability and simplicity of instrumentation and hardware, and low cost (13). However, the weakness of this approach is that CW methods only measure intensity, and cannot provide temporal information from which fluorescence lifetime is derived (87, 117).

2.2.2.3.2 Time domain

TD methods and systems are often considered to be the most expensive and complicated to develop and use as it requires the utilization of very expensive and specialized equipment to measure the temporal distribution of the detected photons (118, 119). However, TD techniques are also considered to be the most sensitive and can supply the most comprehensive information (87). TD illuminates the tissue using a short, sub-nanosecond pulsed laser source and fast time-gated detection system to measure the arrival of individual photons as a function of time. This broadened pulse is called the Temporal Point Spread Function (TPSF) and represents a histogram of the time each individual photon took to travel through the tissue. Basically, TD looks at the amplitude attenuation and broadening of a light pulse due to absorption and scattering of the medium. For FT, a fluorescent light pulse is emitted after excitation from the laser pulse. The position, broadening, and attenuation of the TPSF is characteristic of the fluorophore and its spatial location within the medium (120).

2.2.2.3.3 Frequency domain

FD uses a light source whose intensity is sinusoidally modulated at radio-frequencies to illuminate the tissue (87). Photons are absorbed and scattered as they propagate through the tissue, and the level of amplitude attenuation and phase delay accumulates with distance. For FT, a fluorophore excited with modulated light will emit light at the same modulation frequency. Thus, FD methods measure the amplitude and phase shift of the measured transmitted or fluorescent light relative to the reference signal which contain absorption and scattering information and can be used to find the fluorophore concentration and lifetime. This technique is more complicated than CW and necessitated the use of specialized instrumentation, namely a frequency modulated source and a homo or heterodyned detector (13).

Comparison of the three optical tomography techniques can be found in Figure 2.11. Although FD and TD methods are more expensive and complicated than CW techniques, they can provide temporal information which can be used to derive fluorescence lifetime. In addition, they can potentially provide more accurate information to calculate the fluorophore concentration and location than CW as the addition of the phase measurement allows decoupling of the absorption and scattering coefficients (121). Compared to TD systems, FD systems are cheaper, easier to use and develop, and can provide shorter time scans (87, 122). TD systems tend to use photon counting detectors which are highly sensitive but slow (87).

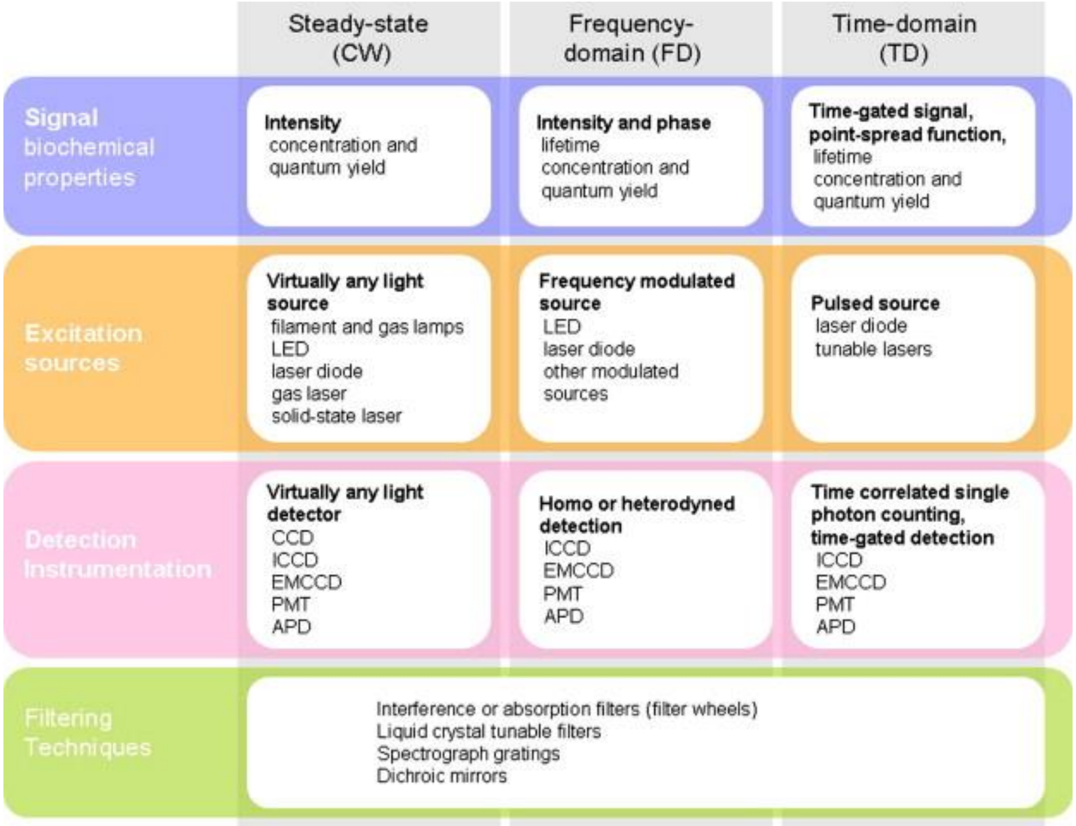

	Steady-state (CW)	Frequency-domain (FD)	Time-domain (TD)
Signal biochemical properties	**Intensity** concentration and quantum yield	**Intensity and phase** lifetime concentration and quantum yield	**Time-gated signal, point-spread function,** lifetime concentration and quantum yield
Excitation sources	**Virtually any light source** filament and gas lamps LED laser diode gas laser solid-state laser	**Frequency modulated source** LED laser diode other modulated sources	**Pulsed source** laser diode tunable lasers
Detection Instrumentation	**Virtually any light detector** CCD ICCD EMCCD PMT APD	**Homo or heterodyned detection** ICCD EMCCD PMT APD	**Time correlated single photon counting, time-gated detection** ICCD EMCCD PMT APD
Filtering Techniques	Interference or absorption filters (filter wheels) Liquid crystal tunable filters Spectrograph gratings Dichroic mirrors		

Figure 2. 11 Comparison of the three measurement methods for DOT and FT: continuous wave (CW), frequency domain (FD), and time domain (TD). Methods are compared in terms of measurement parameters and corresponding biological significance, light source and detector instrumentation, and filtering techniques. Reprinted from the Journal of Photochemistry and Photobiology B: Biology, Vol 98 Issue 1, Leblond, F. *et al.*, Pre-clinical whole-body fluorescence imaging: Review of instruments, methods and applications, Page No 77-94. Copyright (2010), with permission from Elsevier.(13)

In general, out of the three optical tomography methods, TD is considered to be the most comprehensive as it can provide the most information about the tissue since a short laser pulse implicitly contains all the modulation frequencies for FD (118). However, FD has the potential to provide the same information as TD when measured at multiple intensity modulation frequencies as they are related via the Fourier Transforms. Consequently, FD was chosen for TM-FT as it provides a good balance between CW and TD due to its ability to provide temporal information at a relatively low cost. In addition, the instrumentation and reconstructions algorithms tend to be less complicated than TD (119, 123). In this thesis, the TM-FT was first developed using CW methods and then progressed to the frequency domain in order to measure absorption and scattering independently and offer fluorescence lifetime information.

2.2.2.4 Hybrid/multi-modality imaging

2.2.2.4.1 Limitations of stand-alone DOT or FDOT

The ill-posed and underdetermined nature of the inverse problem does not permit optical imaging in thick tissue (more than 1 cm deep) with high resolution. The main reason is the strong tissue scattering, making direct light focusing infeasible beyond one transport mean free path (< 1 mm) (49). This results in poor spatial resolution and low quantitative accuracy for FT, especially in deep tissue. The recovered fluorescence parameters highly depend on the size, depth, and location of the fluorescence source.

2.2.2.4.2 Description/goals

In order to improve the resolution of FT, extensive effort has been spent toward the image-guided approach, which is to integrate FT with other anatomic imaging modalities such as x-ray CT, MRI, and ultrasound (51, 54, 57, 124-126). In image-guided FT, prior information about the location and structure of a specific region of interest, such as a tumor, is obtained using a high-resolution anatomical imaging modality. This structural template is then applied in the FT reconstruction model to acquire region-based fluorescence parameters. For this purpose, both hard *a priori* and soft *a priori* approaches have been utilized by numerous research groups (126-129). In hard *a priori*, all the pixels in a segmented region are forced to be the same value, while in soft *a priori*, the pixels are loosely grouped into regions, but independent update is still permitted. The addition of structural *a priori* information obtained from an anatomical imaging modality to guide and constrain the optical image reconstruction algorithm has been shown to significantly improve the quantitative accuracy of FT (51, 53, 57, 127).

2.2.2.4.3 Types of multimodality/ current systems

Indeed, MRI co-registered FT has been used to quantify cathepsin B activity in glioma tumors and epidermal growth factor receptor (EGFR) activity in murine brain tumors *in vivo (130, 131)*. Additionally, ultrasound-guided FT has also showed promise and has been used to image the Protoporphyrin IX production of subcutaneous tumors *in vivo* in mice (53). Beside utilization of *structural a priori* information, FT accuracy can also be improved if the tissue optical heterogeneity is taken into account instead of treating the tissue as a homogenous medium (115, 128, 132, 133). Lin et al. saw a significant increase in accuracy (87% to 2% error) by combining FT with both DOT functional *a priori* and X-ray CT structural *a priori* when recovering the concentration of a surgically embedded fluorescent inclusion (52).

2.2.2.4.4 Limitations of current hybrid

Although combining FT with anatomical imaging modalities such as x-ray, MRI, and ultrasound have been shown to improve the FT accuracy significantly, complications can arise with co-registration. Typically, these hybrid imaging methods operate independently and then co-registered with FT to guide and constrain the reconstruction algorithm. The weakness of this method occurs due to the fact the structural imaging modalities do not measure fluorescence. Therefore, a major assumption must be made when the anatomical image is co-registered with FT as fluorescence contrast is assumed to correlate with the anatomical contrast. Thus, errors can occur when the structural boundaries provided by the anatomical imaging modality do not exactly coincide with the true fluorescent distribution as seen with necrotic tumors with heterogenous vasculature. Consequently, instead of assuming the fluorophore distribution is confined homogeneously within the structural boundary identified by the separate anatomical imaging modality, an ideal method would be directly mapping the fluorophore distribution to provide *functional a priori* information.

2.3 Introduction to TMFT

2.3.1 Description/goals

In this thesis, we introduce a novel imaging modality termed, "temperature-modulated fluorescence tomography" (TM-FT) to provide remarkable high spatial resolution and quantitatively accurate images of thermo-sensitive fluorophores in deep tissue (≤ 6 cm). TM-FT will provide high resolution images without sacrificing the exceptional sensitivity of fluorescence-based detection by bringing two modalities together: high intensity focused ultrasound (HIFU) and FT. Instead of working independently, both modalities will work in synergy to offer images that not obtainable by either one alone. The sensitivity of this technique relies on the responsiveness of the activatable thermo-reversible fluorescent probes we termed "ThermoDots." The quantum efficiency and lifetime of these ThermoDots are extremely sensitive to slight temperature variations, such that they act as a fluorescence switch activated by heat. Focused ultrasound is used to provide localized heating of the tissue with high resolution by focusing the ultrasound into a small focal zone (~1.33 mm) to heat the medium approximately 4°C. TM-FT is based on the monitoring of the temperature dependence of these ThermoDots during the low power HIFU scanning throughout the medium. TM-FT first uses focused ultrasound to locate the distribution of temperature-sensitive fluorescence probes. Afterward, this *a priori* information is utilized to improve the performance of the inverse solver for conventional fluorescence tomography and reveal quantitatively accurate fluorophore concentration maps. Accordingly, TM-FT provides fluorescence images with much higher spatial resolution than conventional FT by using the *a priori* binary location information provided by the temperature modulation of the ThermoDots (i.e., using them as binary switches). The small size of the focal spot of the HIFU (~1.33 mm) allows imaging the distribution of these temperature sensitive agents with not only high spatial resolution but also high quantitative accuracy. Moreover, the HIFU transducer can generate these hot spots up to a depth of 6 cm. Due to the fact that the spatial resolution is mainly determined by the spot size of the HIFU, high spatial resolution (~1.4 mm) can be achieved, even for thick tissue (6 cm).

2.3.2 How it works

The sensitivity of TM-FT relies on the responsiveness of the ThermoDots. The ThermoDots are based on recently reported temperature-sensitive fluorescence contrast agents using ICG loaded pluronic nanocapsules (134). The unique thermo-reversible behavior of polymers such as Pluronic-F127 has been reported as a promising drug carrier for cancer therapy (135). Pluronic-F127 polymer consists of an amphiphilic tri-block copolymer of ethylene and propylene oxide that can self-assemble into a micelle in aqueous solution. The thermo-responsiveness of the ThermoDots is based on the temperature-dependent hydrophobic/hydrophilic property of the Pluronic polymer micelles. As the temperature changes, this affects the bonding strength of the nanocapsule as it induces a change in the hydrophobicity/hyrophilicity of the Pluronic-F127 polymer. This in turn changes the micelle size, which affects the environment and concentration of the ICG encapsulated inside the micelle and is responsible for the variations in the fluorescence quantum yield (136). In summary, the ThermoDots can act as a fluorescent switch as an increase in temperature induces a variation in the solvent polarity, resulting in an ICG fluorescence signal and lifetime change (63). The temperature dependence of these contrast agents provides an opportunity to overcome the spatial resolution limitation of conventional FT by using temperature modulation.

TM-FT is based on the modulation of the fluorescence quantum efficiency and lifetime of the temperature-sensitive ThermoDots with temperature. The medium is irradiated with both fluorescence excitation light and a focused ultrasound wave generated by the HIFU in low power mode. As the HIFU scans through the medium, it generates a hot spot, which elevates the temperature of this small area several degrees. When the temperature-sensitive fluorescence agents are present within this HIFU focal zone, the fluorescence quantum efficiency increases due to the elevated local temperature. As a result, the emitted fluorescence light intensity has a detectable change only when ThermoDots are present within the focal zone. This temperature modulation via the HIFU allows separate fluorescence measurement for each pixel in a region of interest (ROI), which is not available with conventional FT. Furthermore, the location and size obtained from the HIFU scan specifically indicates the location of the fluorescence source, which can potentially overcome the challenges of the traditional anatomical image guided FT approach.

TM-FT allows fluorescence imaging with high spatial resolution by scanning focused ultrasound column over the medium while detecting the variation in the emitted fluorescence signal. In this approach, first a conventional low resolution FT image is reconstructed to define a region of interest (ROI) around the target. Then, a focused ultrasound column is scanned over this ROI while monitoring the change in the fluorescence signal using selected FT source-detector pairs. This procedure localizes the ThermoDots at focused ultrasound resolution (~1.33 mm) and creates a binary map of the fluorophore distribution. Finally, the boundary of the fluorescent target outlined by this procedure is used as *a priori* information to recover quantitatively accurate concentration and lifetime images using the conventional FT data. Unlike structural *a priori* information which reveals the boundaries of anatomic structures, this method directly delineates the boundary of the fluorescent target. Therefore, it is important to note that the TM-FT binary mask alone reveals a high-resolution image of the fluorescent agent distribution prior to any complex reconstruction process. However, recovering quantitative fluorescence concentration and lifetime parameters requires solving the inverse problem of FT.

2.3.3 Comparison to other optical imaging methods

As mentioned earlier, although multimodality techniques which use anatomical imaging techniques to guide FT have been shown to improve the FT accuracy significantly, the major weakness of the conventional image-guided FT approach is that it loses the accuracy when a) the fluorescence target is not visible on the anatomical image and b) the fluorescence contrast does not correlate with anatomical contrast. In contrast, TM-FT directly maps the fluorescence distribution, eliminating co-registration complications that arise from separate imaging modalities working independently. There are other emerging modalities that also combine optical and ultrasound techniques for imaging of fluorescence agents. Two intriguing techniques are ultrasound modulated fluorescence tomography (UMFT) and photoacoustic imaging (PAI).

2.3.3.1 UMFT

UMFT is an alternative technique that combines fluorescence contrast and ultrasound resolution (137, 138). UMFT utilizes the direct ultrasound modulation of optical signal in the focal zone in contrast with TM-FT, which modulates the local temperature (139). However, the low modulation efficiency and extremely low signal to noise ratio (SNR) are the two main factors that make its implementation difficult. Recently, micro-bubbles that are surface-loaded with self-quenching fluorophores are used to enhance the contrast of UMFT (140, 141). Preliminary phantom results have revealed much improved SNR. However, the main disadvantage of using microbubbles are their instability, low circulation residence times, low binding efficiency to the area of interest especially in the fast-flow conditions and possible side effects of their destruction during the imaging session (142, 143). Additionally, TM-FT does not rely on the ultrasound modulation of the fluorescence in the focal zone but detects and accepts all the photons at detector site. Therefore, superior SNR can be achieved, which will lead to fast and accurate data acquisition.

2.3.3.2 PAI

Another example is PAI, which is also an intriguing combination of optical and ultrasound techniques. PAI can provide the optical absorption maps with high spatial resolution and a depth penetration of several centimeters based on ultrasonic detection of pressure waves generated by the absorption of pulsed light in elastic media (49, 144). By using multiple-wavelength measurements, PAI can reveal the distribution of exogenous contrast agents (145, 146). An interesting PAI application, which uses fluorescence agents, is achieved through fluorescence quenching (147). The idea is that, a lower fluorescence quantum yield of dyes within the perfluorocarbon nanoparticles would improve PAI contrast due to higher heat yield, which in turn would generate a stronger ultrasound signal (thermal expansion) (148). Moreover, non-quenched nanoparticles are expected to produce higher fluorescence intensity but poor PAI signal compared with quenched nanoparticles. However, PAI is inherently sensitive to absorption and detects a differential increase in absorption due to molecular probes compared with background absorption rather than the fluorescence signal generated by these agents. In contrast, TM-FT detects fluorescence signal that is emitted only by the fluorescence probe, hence its sensitivity should be superior due to the high target to background contrast.

2.3.4 Preclinical and Clinical relevance/advantage of TM-FT

TMFT has many potential applications from preclinical small animal imaging to clinical treatment of cancer. The future lies in targeting these Thermodots to provide tumor specific imaging. Optical devices have become the highest growth area in pre-clinical imaging research due in large part to their use in the development and assessment of new drugs for pharmaceutical companies (13). As a small animal imaging device, TMFT has the potential to provide fluorescent *in vivo* images with spatial resolution and quantum accuracy that is competitive with PAT and higher than commercial fluorescent systems.

High intensity focused ultrasound (HIFU) is an emerging and promising minimum invasive treatment option for prostate cancer patients. HIFU can provide a minimally invasive, radiation free, quick recovery treatment option with a low incidence of treatment complications (149, 150). In fact, it has been demonstrated that higher success rates can be achieved if HIFU procedure is guided with imaging (151, 152). Currently MRI and ultrasound are the only clinically available imaging modality for HIFU treatment (153). Recently, MRI has emerged as the gold-standard for HIFU guidance in many applications (uterine fibroid, breast cancer, brain cancer and head and neck cancer) due to its superior soft-tissue contrast, real-time feedback of thermal effects (151, 154-156). For instance, the success rate for MR-guided HIFU ablation for breast tumor is generally high (between 80-100% achieved complete necrosis) due to the high sensitivity of MRI to diagnose breast cancer

Unfortunately, this high cost anatomical imaging modality has limited sensitivity in detecting targeted biomarkers and does not work well for prostate cancer, which tends to be multifocal and/or infiltrative (157-159). Being unreliable in detecting and localizing the small diffused lesions, MRI cannot effectively guide prostate cancer HIFU therapy that leads to low success rates (160). There are two commercially available clinical HIFU devices currently available for prostate cancer treatment: Ablathem (France) and Sonablate (USA). Although these two devices were recently FDA approved, they were approved as a tool to ablate prostate tissue and not treat prostate cancer. The fact that both devices use ultrasound imaging as treatment guidance, which has poor resolution of prostate gland is a contributing factor (151). Indeed, many International Associations (EAU, AUA, National Comprehensive Cancer Network and the National Institute for Health and Clinical Excellence) do not recommend the routine use of HIFU with clinically localized prostate cancer. Therefore, there is a great need for a cost-effective, accurate, and high resolution imaging guidance for prostate cancer treatment.

Chapter 3: Mathematical framework of optical tomography

"In mathematics, you don't understand things. You just get used to them."

– Johann von Neumann

3.1 Modelling the light propagation in tissue

In tomography, cross-sectional images of the body can be generated by analyzing data acquired over multiple projection angles. For example, in x-ray CT, the internal structure can be deduced by looking at the attenuation of signal due to absorbing structures in the x-ray projection path over multiple angles. Since x-rays are assumed to travel in straight paths in tissue, reconstruction algorithms such as the Radon transform can be used to form an image (161). However, diffuse optical tomography is much more complicated as the high scattering of light in biological tissue prevents the majority of photons from travelling through the tissue in a straight path. Furthermore, each photon will not take the same path as this is dependent on the absorption and scattering properties of the tissue. Consequently, simple back-projection methods will not suffice, and it is imperative to understand how the photons propagate through tissue. Thus, before we can talk about image reconstruction, we need to first know how to model the behavior of light in tissue.

3.1.1 Photon migration model and diffusion approximation

3.1.1.1 Radiative transfer equation (RTE)

Photon propagation in tissue can be described by the radiative transport equation (RTE) or Boltzmann transport equation (162-164):

$$\frac{1}{c_n}\frac{\partial L(\vec{r},\hat{s},t)}{\partial t} + \hat{s}\cdot\nabla L(\vec{r},\hat{s},t) + \left[\mu_a(r) + \mu_s(r)\right]L(\vec{r},\hat{s},t)$$
$$= \mu_s \iint\limits_{4\pi} L(\vec{r},\hat{s}',t) f(\hat{s}\cdot\hat{s}')d\Omega' + q(\vec{r},\hat{s},t) \qquad [3.1]$$

where $L\ (r,\hat{s},t)$ ($\mathrm{W{\cdot}mm^{-2}sr^{-1}}$) is the radiance of light, and c_n is the speed of light in tissue (typical value for tissue is 1.4 c_0) (165). In the RTE, light is lost by divergence and extinction through the absorption of the photon and scattering of the photon away from the propagation direction $\hat{s}$. Scattering and absorption coefficients of the medium are represented by μ_s ($\mathrm{mm^{-1}}$) and μ_a ($\mathrm{mm^{-1}}$), respectively. The light gained in the medium from internal light sources and scattering is described by the light source term, $q(\vec{r},\hat{s},t)$, and the phase function $f(\hat{s}\cdot\hat{s}')$.

The phase function, $f(\hat{s}\cdot\hat{s}')$ is a probability density function that represents the probability of light with propagation direction $\hat{s}'$ being scattered in direction $\hat{s}$ within solid angle $d\Omega$.. In most cases, this only depends on the angle between the scattering $\hat{s}'$and incident $\hat{s}$ directions, and the scattering anisotropy, g, can be described as the average cosine of the phase function:

$$g = \int\limits_{4\pi} (\hat{s}\cdot\hat{s}') f(\hat{s}\cdot\hat{s}')d\Omega \qquad [3.2]$$

Scattering and degree of anisotropy in biological tissue is commonly expressed in terms of the reduced scattering coefficient, μ_s', with the typical value for $g = 0.9$ in biological tissue (67):

$$\mu_s' = \mu_s(1-g) \qquad [3.3]$$

The photon density or intensity of light, Φ [W·mm^{-2}], and photon current, J [W·mm^{-2}], can be written respectively as:

$$\Phi(\vec{r},t) = \iint_{4\pi} L(\vec{r},\hat{s},t)d\hat{\Omega} \qquad [3.4]$$

and

$$\vec{J}(\vec{r},t) = \iint_{4\pi} \hat{s}\, L(\vec{r},\hat{s},t)d\hat{\Omega} \qquad [3.5]$$

3.1.1.2 Diffusion Approximation

Resolution of the RTE is complex due to the number of independent variables and directionality of the photons. Nevertheless, an approximation can be made when the radiance can be considered isotropic as in the case where scattering is dominant over absorption, $\mu_s' >> \mu_a$, such as biological tissue in the NIR window. In this regime, photon's propagation in the medium is isotropic (direction independent) and the RTE can be reduced to the diffusion equation:

$$\nabla \cdot [D(\vec{r})\nabla\Phi(\vec{r},t)] - \mu_a(r)\ \Phi(\vec{r},t) - \frac{1}{c_n}\frac{\partial\Phi(\vec{r},t)}{\partial t} = -q_0(\vec{r},t) \qquad [3.6]$$

where $\Phi(\vec{r},t)$ (W·mm^{-2}) is the angle independent photon density, $D(r)$ (mm^{-1}) denotes the diffusion coefficient (defined by $D=1/3(\mu_a+\mu_s')$); and $q_0(\vec{r},t)$ is an isotropic light source. The diffusion approximation makes two assumptions (49):

1. Source term is isotropic.
2. Photon current is temporally broaden relative to the transport mean free time.

Both assumptions require $\mu_s' >> \mu_a$ so that a photon must undergo a sufficient number of scattering events before being absorbed. The first assumption states that the radiance is angle independent. Thus, in order for the radiance to be considered isotropic, the medium must be of a minimum thickness as the photon must travel a longer distance than the diffusion transport length ($1/\mu_s'$) to undergo a sufficient number of scattering events to omit the directionality information. The second assumption implies that the distribution of light in the medium is instantaneous which is incorrect for time dependent cases but justified when assuming $\mu_s' >> \mu_a$ (166). Thus, the diffusion equation models the photon propagation as a diffuse wave and is the most widely used approximation in DOT due to the fact that it has shown good agreement with experimental data and to reduce the computational cost and complexity compared to the RTE (163, 167).

The diffusion equation can be converted to frequency domain by the relationship $\frac{\partial}{\partial t} = i\omega$, using Fourier transformation:

$$\nabla \cdot [D(r) \nabla \Phi(\vec{r}, t)] - [\mu_a(r) + \frac{i\omega}{c_n}]\ \Phi(\vec{r}, t) = -q_0(\vec{r}, t) \tag{3.7}$$

where ω is the modulation angular frequency. The continuous wave case can be considered a simplification of the frequency domain format by setting the modulation frequency to 0.

2.1.1.3 Boundary conditions

The Robin boundary condition relates the photon density to photon flux at the boundary and is generally utilized to model the photon behavior at the biological tissue surface:

$$\Phi(r,\omega) + 2AD(r)\frac{\partial \Phi(r,\omega)}{\partial n}=0 \qquad [3.8]$$

where $\hat{n}$ is the direction perpendicular to the surface. The Robin boundary condition specifies that the total inward directed photon current is zero except for the source term. A is the boundary mismatch parameter and accounts for light reflection at the boundary surface, based on Fresnel's reflections (162). Consequently, the photon flux measurement at the boundary is

$$J = -D(r)\frac{\partial \Phi}{\partial n} = \frac{\Phi}{2A} \qquad \textbf{[3.9]}$$

A point source $q_0(\vec{r},\omega) = \delta(\vec{r}-\overrightarrow{rs})$ is used, with the extrapolated-boundary condition used to model the position of the source.

3.2 Mathematical framework for diffuse optical tomography

DOT image reconstruction requires solving the inverse problem in which the internal optical properties (μ_a, μ_s) are obtained from the measured photon signal at the boundary or surface of the tissue. A non-linear image reconstruction algorithm is used to obtain the optical properties in an iterative fashion by minimizing the difference between the forward and inverse problem, Figure 3.1. In this method, simulated boundary measurements are obtained from the forward problem by assuming a specific distribution of optical properties and comparing the simulated measurements to the experimentally obtained values. The estimated or simulated optical properties are updated iteratively until the difference between the predicted and measured data is minimized.

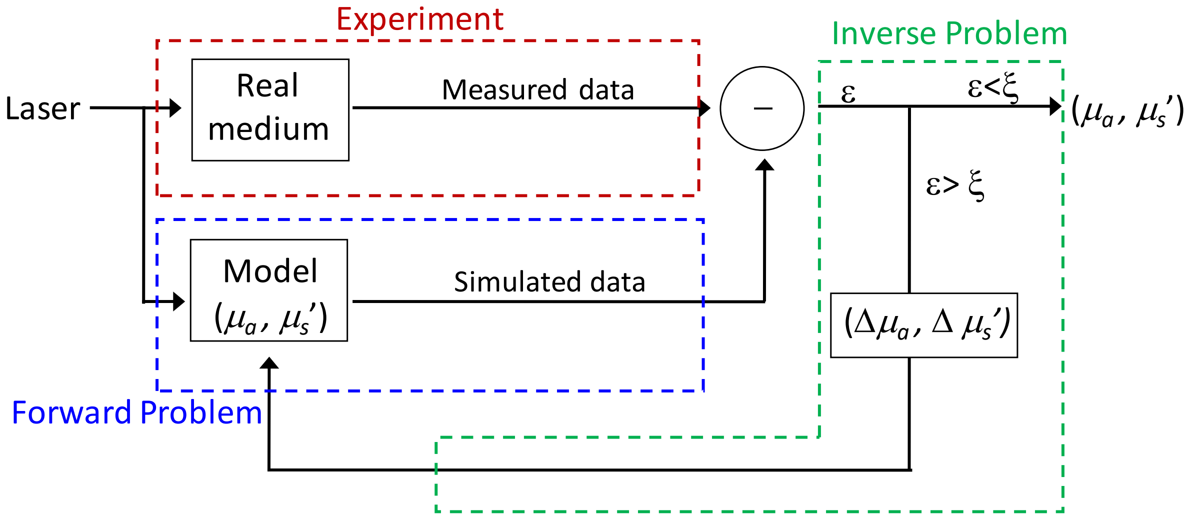

Figure 3. 1 Diagram of the image reconstruction algorithm

3.2.1 Numerical solution of diffusion approximation equation

The diffusion equation which is an elliptical type partial differential equation (PDE) can be solved using various analytical or numerical approaches. Although analytical methods can yield fast and more accurate results compared to numerical methods for regular geometries with homogenous optical properties, numerical methods can be used for realistic situations with complex geometries and heterogeneous optical properties such as *in vivo* animal imaging. The Monte Carlo method and finite element method (FEM) are two common numerical methods. In our approach, FEM was chosen to solve the diffusion equation due to the fact that it is simpler to implement but can offer accurate results comparable to Monte Carlo on a faster timescale (164). The FEM is based on creating a mesh by dividing the volume into a finite number of small tetrahedrals or elements (Figure 3.2) connected by vertices known as nodes and then solving the diffusion equation over the small distance between these nodes throughout the mesh (168).

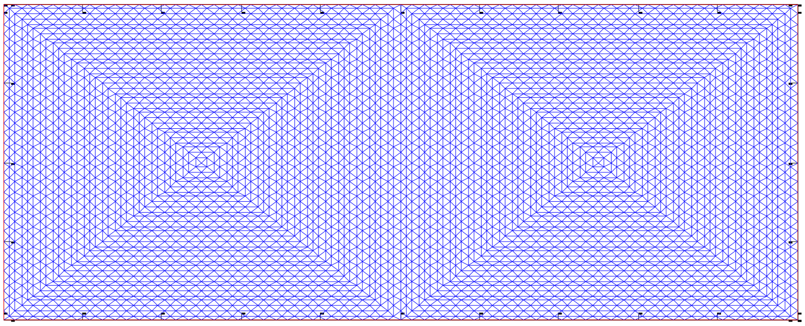

Figure 3. 2 FEM mesh. Example of a typical mesh used for FEM modelling of light propagation through a rectangular domain. Each triangle is an element and each vertex is a node. This node consists of 4193 nodes and 8192 triangular elements. Although the node density is relatively homogeneous in this mesh, improved modelling can be obtained by increasing the node density in certain areas without significantly affecting the computational burden.

In FEM, the diffusion equation is solved in its weak form by multiplying both sides by an arbitrary test function, φ, and integrating over $d\Omega$:

$$\int_{\Omega} \nabla\varphi \cdot (D\nabla\Phi)d\Omega + \int_{\Omega} \mu_a \varphi\Phi\, d\Omega + \frac{i\omega}{c}\int_{\Omega} \varphi\, \Phi\, d\Omega + \frac{1}{2A}\oint_{\partial\Omega} \varphi\, \Phi\, d(\partial\Omega) = \int_{\Omega} \varphi\, q_0 d\Omega \tag{3.10}$$

The solution to the PDE is assumed to be a linear combination of basis function for each node j within the FEM mesh (N=total number of nodes). The function Φ can be expressed as $\Phi = \sum_{j=1}^{N} \xi_j \varphi_j$, where ξ_j and φ_j are the nodal solution vector and a basis function for the j^{th} node, respectively. Furthermore, the distributions for the diffusion coefficient and absorption coefficient can also be represented as $D = \sum_{k=1}^{N} D_k \varphi_k$ and $\mu_a = \sum_{k=1}^{N} \mu_{ak} \varphi_k$. Thus, when the arbitrary test function is also rewritten as $\varphi = \sum_{x=1}^{N} \varphi_x$, the diffusion equation in the FEM framework is:

$$\left(A + B + C + \frac{i\omega}{c} D\right) \xi = Q \qquad [3.11]$$

where

$$A_{ij} = \sum_{k=1}^{N} D_k \int_{\Omega} \varphi_k \left(\nabla\varphi_i \cdot \nabla\varphi_j\right) d\Omega$$

$$B_{ij} = \sum_{k=1}^{N} \mu_{a,k} \int_{\Omega} \varphi_k \left(\varphi_i \varphi_j\right) d\Omega$$

$$C_{ij} = \frac{1}{2\,A} \oint_{\partial\Omega} \left(\varphi_i \varphi_j\right) d(\partial\Omega)$$

$$D_{ij} = \int_{\Omega} \left(\varphi_i \varphi_j\right) d\Omega$$

$$Q_i = \int_{\Omega} \left(\varphi_i q_0\right) d\Omega$$

$$\xi = [\xi_1 \quad \xi_2 \quad \xi_3 \quad \cdots \quad \xi_N] \qquad [3.12]$$

By solving these linear equations, the photon density distribution in the whole medium can be found. Then the measured photon flux on the boundary is $\Phi/2\text{A}$ as described in equation [3.9]. The solution of FEM is often referred to as the solution to the forward problem.

3.2.2 Inverse problem

The inverse problem is solved by a least-square minimization method which consists of iteratively minimizing the difference between the measured and simulated data by the following error function:

$$\varepsilon^2(\mu_a, \mu_s') = \sum_{i=1}^{N_s} \sum_{j=1}^{N_d} (\phi_{ij}^m - P_{ij}(\mu_a, \mu_s'))^2$$

[3.13]

where *i* and *j* represent the number of sources and detectors respectively. ϕ_{ij}^m is the measured data on the detector j due to the source I and P_{ij} is the simulated flux at the measured point calculated by the forward solver from the spatial distribution of μ_a and μ_s'.

Solving the inverse problem requires the creation of a matrix that relates the absorption and scattering at each position within the medium to their induced perturbations in the measurements for each source-detector pair. This sensitivity matrix is known as the Jacobian matrix and is based on perturbation theory which makes the assumption that variations of μ_a and μ_s' will induce changes in measurements $P_{ij}(x_k)$ and can be expressed by a Taylor series (167).

$$P_{ij}(x_{k1}) = P_{ij}(x_{k0}) + \frac{\partial P_{ij}(x_{k0})}{\partial x_k}[x_{k1} - x_{k0}] + \frac{1}{2!}\frac{\partial^2 P_{ij}(x_{k0})}{\partial {x_k}^2}[x_{k1} - x_{k0}]^2 + \cdots$$

[3.14]

in which x_k denotes μ_a and μ_s'. Thus, the coefficients x_{k0} and x_{k1} represent the initial and perturbed state of the internal absorption or reduced scattering coefficient μ_a and μ_s'.

Considering only the first order term in the Taylor series expansion, the Jacobian can be defined as:

$$J_{ij}(x_{k0}) = \frac{\partial P_{ij}(x_{k0})}{\partial x_k} = \frac{P_{ij}(x_{k1}) - P_{ij}(x_{k0})}{x_{k1} - x_{k0}}$$

[3.16]

This Jacobian matrix describes the degree of variation in the measurement $P_{ij}(x_k)$ caused by a small variation in the internal absorption μ_a or scattering μ_s' at each node when the source *s* and detector *d* are used. In frequency domain, amplitude and phase are measured to obtain both μ_a and μ_s'. Thus, the full Jacobian describing all the variations in the amplitude and phase measurements for the whole set of source-detector pairs can be obtained by assembling all the individual Jacobians J_{ij} for both absorption and scattering.

$$J = \begin{vmatrix} \frac{\partial P_{A1}}{\partial \mu_{a1}} & \frac{\partial P_{A1}}{\partial \mu_{a2}} & \cdots & \frac{\partial P_{A1}}{\partial \mu_{aN}} & \frac{\partial P_{A1}}{\partial \mu_{s1}} & \frac{\partial P_{A1}}{\partial \mu_{s2}} & \cdots & \frac{\partial P_{A1}}{\partial \mu_{sN}} \\ \cdots & \cdots & \cdots & \cdots & \cdots & \cdots & \cdots & \cdots \\ \frac{\partial P_{AM}}{\partial \mu_{a1}} & \frac{\partial P_{AM}}{\partial \mu_{a2}} & \cdots & \frac{\partial P_{AM}}{\partial \mu_{aN}} & \frac{\partial P_{AM}}{\partial \mu_{s1}} & \frac{\partial P_{AM}}{\partial \mu_{s2}} & \cdots & \frac{\partial P_{AM}}{\partial \mu_{sN}} \\ \frac{\partial P_{P1}}{\partial \mu_{a1}} & \frac{\partial P_{P1}}{\partial \mu_{a2}} & \cdots & \frac{\partial P_{P1}}{\partial \mu_{aN}} & \frac{\partial P_{P1}}{\partial \mu_{s1}} & \frac{\partial P_{P1}}{\partial \mu_{s2}} & \cdots & \frac{\partial P_{P1}}{\partial \mu_{sN}} \\ \cdots & \cdots & \cdots & \cdots & \cdots & \cdots & \cdots & \cdots \\ \frac{\partial P_{PM}}{\partial \mu_{a1}} & \frac{\partial P_{PM}}{\partial \mu_{a2}} & \cdots & \frac{\partial P_{PM}}{\partial \mu_{aN}} & \frac{\partial P_{PM}}{\partial \mu_{s1}} & \frac{\partial P_{PM}}{\partial \mu_{s2}} & \cdots & \frac{\partial P_{PM}}{\partial \mu_{sN}} \end{vmatrix} . \qquad [3.17]$$

where $P_{A,P}$ are the amplitude and phase measurements. M is the number of measurements and N is the number of mesh nodes or unknowns. The size of the Jacobian in frequency domain is 2M x 2N as both μ_a and μ_s' are unknown and both amplitude and phase are measured.

Therefore, making the substation from equation [3.16], equation [3.15] can be rewritten as:

$$P_{ij}(x_{k1}) - P_{ij}(x_{k0}) = J_{ij}(x_{k0})[x_{k1} - x_{k0}] \qquad [3.18]$$

From this equation, we can see that the updates can be obtained by simply inversing the Jacobian J_{ij}. However, the Jacobian is a singular and non-square matrix as the number of unknowns, *N,* is much larger than the number of measurements *M*. Consequently, the inversion process is not straight forward as the inverse problem of DOT is underdetermined and strongly ill-posed. Therefore, a special technique, the pseudo inversion iterative algorithm of Levenberg-Marquardt (LM), is used to solve this problem (169, 170). In this method, the unknown μ_a and μ_s' are iteratively updated by:

$$\Delta X_k = X_{k+1} - X_k = (J^T J + \lambda I)^{-1}(J^T \varepsilon) \tag{3.19}$$

where $\varepsilon_{ij} = (\phi_{ij}^m - P_{ij})$ and ΔX represents the unknown matrix of μ_a and μ_s'. The dimension of X in frequency domain is [2N×1], which is twice the number of nodes in the FEM mesh when determining both absorption and scattering. I is the identity matrix. $J^T J$ $[2N \times 2N]$ is the Hessian matrix which is known to be ill-conditioned (171). Consequently, there are various techniques to reverse this type of matrix, such as adding a term to the diagonal for stabilization (171). In our method, a regularization factor, $\tilde{\lambda} = \lambda \cdot \max(diag(J^T J))$, is added to improve the stability of the inversion of the Hessian matrix ($J^T J$) by making it diagonally dominant (129, 172-176). For every iteration, ΔX_k is iteratively calculated and added to the current estimate of the absorption and/or reduced scattering coefficient. In addition, the residual error is also calculated for every iteration to check for convergence. Thus, the iteration with the lowest residual is chosen as the correct μ_a and/or μ_s'. The maximum iteration number was chosen as 25. However, if the residual had less than a 5% change in the last 5 iterations (convergence), the algorithm would terminate and the solution would be accepted.

3.2.3 Construction of the Jacobian matrix

To solve the inverse problem, the estimated optical properties are updated iteratively until the simulated and measured data converge and the difference is minimized. As the updates to the optical properties (equation 3.19) are calculated using the Jacobian matrix, this requires the forward problem to be solved a maximum of $2(N_s\times N_d)\times 2(N+1)$ times per iteration. N refers to the number of nodes in the mesh, and N_s and N_d represent the number of sources and detectors respectively. Initially, to start the program, the optical properties of the medium, $x = [\mu_a, \ \mu_s']$, are assumed to be homogeneous, requiring the forward program to be solved $2(N_s\times N_d)$ times to obtain the measurements P_{ij} (x_{k0}) in equation 3.16. Then, in each iteration, the forward program is solved after the sequential perturbations of x at every node of the mesh, $2(N_s\times N_d)\times 2N$ times, to obtain P_{ij} (x_{k1}). Consequently, this method is extremely time consuming as the typical meshes used in this thesis are over 4000 nodes requiring the forward problem to be solved over 1 million times per iteration using eight individual sources and detectors, see Figure 3.2.

Therefore, to speed up this process, the adjoint method was utilized to compute the Jacobian. The adjoint method is based on the reciprocity of the source and detector. This reciprocity principle states that the photon flux measured at point A from an isotropic source positioned at point B would be equal to the photon flux measured at point B if the isotropic source was moved to point A (177). In other words, the attenuation of light is dependent on the path length and optical properties of the medium, not the direction between the two points. Therefore, instead of performing the forward process $2(N_s\times N_d)\times 2N$ times, and retaining only the measurement at the specific node of interest, we can now perform the forward problem just one time for each source and detector position and retain all the nodes in the mesh (177). Using this formulation, the Jacobian is obtained by solving the forward problem $2(N_s + N_d)$ times, reduces the required number of times the forward problem is solved from over 1 million to 32. As you can imagine, this significantly reduces the Jacobian assembly time and overall computation burden.

3.2.4 Incorporation of a priori information

As the inverse problem of DOT is very ill-posed, solution is not unique and extremely sensitive to measurement noise, this results in images with poor spatial resolution and quantitative accuracy. Thus, as mentioned in section 2.2.1.1, much effort has been made to improve DOT reconstruction by incorporating structural information from a high spatial resolution imaging modality (106, 109-111, 129). Indeed, hybrid or multimodality systems have been shown to achieve superior performance by using the structural *a priori* information as anatomical guidance for the DOT inverse problem while preserving the functional information from optical imaging (102, 112, 113).

In general, there are two methods to incorporate structural *a priori* information: hard *a priori* and soft *a priori*. These methods consist of segmenting the mesh into pre-defined regions, based on the high resolution imaging modality.

3.2.4.1 Hard *a priori*

The hard *a priori* method simplifies the mathematical and computational complexity of the inverse problem by greatly reducing the number of unknown parameters and dimensionality of the inversion by assuming all the nodes in a limited number of predetermined regions are optically homogeneous (108). The hard *a priori* method is implemented by applying matrix K (178):

$$K = \begin{array}{c} \begin{matrix} R1 & R2 & \dots & Rn \end{matrix} \\ \left[\begin{array}{cccc} k_{1,1} & k_{1,2} & \dots & k_{1,n} \\ k_{2,1} & k_{2,1} & \dots & k_{2,n} \\ \vdots & \vdots & \ddots & \vdots \\ k_{j,1} & k_{j,1} & \dots & k_{j,n} \\ \hline k_{1,1} & k_{1,2} & \dots & k_{1,n} \\ k_{2,1} & k_{2,1} & \dots & k_{2,n} \\ \vdots & \vdots & \ddots & \vdots \\ k_{j,1} & k_{j,1} & \dots & k_{j,n} \end{array}\right] \end{array} \quad \text{where, } k_{\zeta,\eta} = \begin{Bmatrix} 1, & \zeta \in R_{\eta} \\ 0, & \zeta \notin R_{\eta} \end{Bmatrix} \qquad [3.20]$$

to the Jacobian so that the dimensions of the new Jacobian $\tilde{J} = JK$, is the number of measurements, *j*, by number of segmented regions. *R* refers to the specific segmented region and *n* is the number of segmented regions. As the number of unknowns is now equal to the number of segmented regions which is much less than the number of measurements, the Hessian is a small well-conditioned matrix, thus regularization is not typically required (179). Although the hard *a priori* method greatly reduces the number of unknown parameters, a major drawback of this method is that there is a loss of spatial information within the segmented regions and only bulk homogeneous values can be constructed (108). The spatial resolution is limited by the size of the defined regions and the accuracy of this method is highly dependent on the accuracy of the structural *a priori* information.

3.2.4.2 Soft *a priori*

While hard *a priori*, forces all the pixels in a segmented region to be the same value, soft *a priori*, on the other hand, loosely groups the pixels into regions, but permits updates of independent pixels which allows for optical property variation within the segmented region by penalizing the variations within regions assumed to have similar optical properties (129). This method is performed by applying a Laplacian-type regularization method developed by Yalavarthy et. al (129). In this method, a filter matrix, L, is applied to smooth out the reconstructed parameters within the segmented regions according to the structural information, but allows separate regularization between different tissue types permitting sharp boundaries to exist between different regions (108, 129, 180). Consequently, compared to hard *a priori*, this method is more flexible and more robust to the errors caused by imperfect segmentation (180, 181).

In this method, each node in the mesh is assigned a region number based on the region identified by the high resolution imaging modality. The L regularization matrix links all the nodes within a region such that a second differential operator, L^TL can be approximated for each region (181). The L matrix can be written as:

$$L_{ij} = \begin{cases} 0 & if\ i\ and\ j\ are\ not\ in\ the\ same\ region \\ \dfrac{1}{N_r} & if\ i\ and\ j\ are\ in\ the\ same\ region\ and\ not\ equal \\ 1 & if\ i = j \end{cases}$$

[3.21]

to describe the relationship between two nodes i and j and their respective regions. N_r represents the number of nodes included in one region. Consequently, the update equation can be expressed as:

$$\Delta X_k = X_{k+1} - X_k = (J^TJ + \lambda L^TL)^{-1}(J^T\varepsilon)$$

[3.22]

This method is more computationally efficient than equation 3.19 since the structure of the tissue remains unchanged during the iterative process, the regularization matrix L and the smoothing operator are only calculated once (182). In this thesis, soft *a priori* is preferable as it reduces the likelihood of spatial bias during the inversion process (108).

3.3 Mathematical framework for fluorescence diffuse optical tomography

3.3.1 Forward problem of fluorescence diffuse optical tomography

The forward and inverse problems of FT can be considered as extension of DOT. However, in FT, there is an additional source term due to the fluorophores in the medium. Thus, there are two steps to FT. The first step is to model the light propagation from the external source on the surface of the tissue to the internal fluorophore inside the medium. Secondly, the propagation of the fluorescent emitted light from the internal fluorophore to the detectors located at the tissue boundary is modelled. The solution to the diffusion equation is expected to differ between the excitation and emission wavelengths as the absorption and scattering properties of biological tissue are spectrally dependent (183, 184).

Thus, for this two-step process, a coupled diffusion equation is used to model the photon migration for FT where the solution to the first term equation is the driving source term of the second. In frequency domain, this equation is written as:

$$\nabla \cdot [D_x(r)\nabla \Phi_x(r,\omega)] - \left[\mu_{ax}(r) + \frac{i\omega}{c_n(r)}\right] \Phi_x(r,\omega) = -q_0(r,\omega) \tag{3.23}$$

$$\nabla \cdot [D_m(r)\nabla \Phi_m(r,\omega)] - \left[\mu_{am}(r) + \frac{i\omega}{c_n(r)}\right] \Phi_m(r,\omega) = -\Phi_x(r,\omega)\,\eta\mu_{af}(r)\,\frac{1 - i\omega\tau(r)}{1 + [\omega\tau(r)]^2} \tag{3.24}$$

where $q_0(r,\omega)$ is an isotropic source, $c_n(r)$ is the speed of light in the medium at any point, $\Phi(r,\ \omega)$ is the photon density, $\mu_a(r)$ is the absorption coefficient, and $D(r)$ is the diffusion coefficient (defined by $D=1/3(\mu_a + \mu_s')$). The first equation [3.23] is identical to DOT light propagation as it simply models the light propagation for the excitation light (subscript x) and describes the excitation photon density at the location of the fluorophore. The second equation 3.24 models the light propagation of the emitted fluorescent light (subscript m) from the fluorescent source due to the intrinsic properties of the fluorophore and the excitation photon density, derived from the first equation. The parameters of the fluorescent source are the lifetime $\tau(r)$ and fluorescence yield $\eta\,\mu_{af}(r)$. The fluorescent signal intensity depends on the availability of excitations photons at the location of the fluorophore (excitation photon fluence rate $\Phi_x(r,\omega)$), the fluorophore ability to absorb photons of the excitation energy/wavelength (fluorophore absorption coefficient $\mu_{af}(r)$), and the efficiency of the fluorophores fluorescent process to produce a fluorescent photon, also known as the quantum efficiency η = *(number of photons absorbed/number of photons emitted)*. The absorption coefficient is directly related to the concentration of the fluorophore by the formula $\mu_{af}=2.303 \cdot \varepsilon \cdot C$, where ε is the extinction coefficient of the specific fluorophore with unit of Molar^{-1}·mm^{-1} and C is the concentration of the fluorophore.

A single-exponential fluorescence decay was assumed in the source term of equation 3.24, $\frac{1-i\omega\tau(r)}{1+[\omega\tau(r)]^2}$. This can be better explained in time-domain which is just the Fourier transformation of frequency domain. As described in Chapter 2, fluorescence is only one of the many decay processes from the excited electronic state S_1 to the ground state S_0, with each process associated with their own rate constant k. Thus, in time domain, the concentration of excited state molecules at time t, can be described by:

$$[S_1] = [S_1]_0 e^{-(\sum k)t} \tag{3.25}$$

However, in FT, we are only interested in fluorescence decay and thus assume a single decay process, $\sum k = k_{fluorescence}$. Therefore, assuming fluorescence intensity is proportional to the excited state population, [S1], the intensity decay can be written as:

$$I(t) = I_0 e^{-\frac{1}{\tau}t}$$

[3.26]

where *I* is the intensity at time *t*, *I0* is the intensity at *t*=0, and *τ,* which is the reciprocal of the sum of all the decay processes, now refers to the fluorescence lifetime only, or the average time the fluorophore stays in its excited state before emitting a photon.

At the boundary or surface of tissue, the emission photon flux can be written as:

$$J_m = -D_m(r)\frac{\partial \Phi_m}{\partial n} = \frac{\Phi_m}{2A}$$

[3.27]

Just like DOT, in FEM, the coupled diffusion equation is solved in its weak form as:

$$\int_{\Omega} \nabla\varphi \cdot (D_x \nabla \Phi_x) d\Omega + \int_{\Omega} (\mu_{ax}) \varphi \Phi_x d\Omega + \frac{i\omega}{c} \int_{\Omega} \varphi\, \Phi_x d\Omega + \frac{1}{2A} \int_{\partial\Omega} \varphi\, \Phi_x\, d(\partial\Omega) = \int_{\Omega} \varphi\, q_0 d\Omega$$

[3.28]

$$\int_{\Omega} \nabla\varphi \cdot (D_m \nabla \Phi_m) d\Omega + \int_{\Omega} (\mu_{am}) \varphi \Phi_m d\Omega + \frac{i\omega}{c} \int_{\Omega} \varphi\, \Phi_m d\Omega + \frac{1}{2A} \int_{\partial\Omega} \varphi\, \Phi_m\, d(\partial\Omega) = \int_{\Omega} \varphi \eta \mu_{af} \Phi_x d\Omega$$

[3.29]

and the distributions $D_{x,m}$, $\mu_{ax,am}$, μ_{af}, and τ can also be represented as, $D_{x,m} = \sum_{k=1}^{N} D_{x,m_k} \varphi_k$, $(\mu_a)_{x,m,f_k} = \sum_{k=1}^{N} (\mu_a)_{x,m,f_k} \varphi_k$, and $\tau = \sum_{k=1}^{N} \tau_k \varphi_k$. When the test function is written as $\varphi = \sum_{x=1}^{N} \varphi_x$, the coupled diffusion equations (1) and (2) in the FEM framework are:

$$\begin{cases} \left(A_x + B_x + \frac{i\omega}{c} C_x + \frac{1}{2A} D_x\right) \xi_x = Q_x \\ \left(\left(A_m + B_m + \frac{i\omega}{c} C_m + \frac{1}{2A} D_m\right) \xi_m = Q_m \xi_x \end{cases}$$

[3.30]

where

$$\begin{aligned} (A_x)_{ij} &= \sum_{k=1}^{N} D_{x,k} \int_{\Omega} \varphi_k \left(\nabla\varphi_i \cdot \nabla\varphi_j\right) d\Omega & \qquad (A_m)_{ij} &= \sum_{k=1}^{N} D_{m,k} \int_{\Omega} \varphi_k \left(\nabla\varphi_i \cdot \nabla\varphi_j\right) d\Omega \\ (B_x)_{ij} &= \sum_{k=1}^{N} \mu_{ax,k} \int_{\Omega} \varphi_k \left(\varphi_i \varphi_j\right) d\Omega & \qquad (B_m)_{ij} &= \sum_{k=1}^{N} \mu_{am,k} \int_{\Omega} \varphi_k \left(\varphi_i \varphi_j\right) d\Omega \\ (C_x)_{ij} &= \int_{\Omega} \left(\varphi_i \varphi_j\right) d\Omega & \qquad (C_m)_{ij} &= \int_{\Omega} \left(\varphi_i \varphi_j\right) d\Omega \\ (D_x)_{ij} &= \int_{\partial\Omega} \left(\varphi_i \varphi_j\right) d(\partial\Omega) & \qquad (D_m)_{ij} &= \int_{\partial\Omega} \left(\varphi_i \varphi_j\right) d(\partial\Omega) \end{aligned}$$

[3.31]

and the excitation source term is:

$$(Q_x)_i = \int_{\Omega} \left(\varphi_i q_0\right) d\Omega$$

[3.32]

For the fluorescent source, Q_m, an approximation is made under the assumption that $\omega\tau$<<1. This is usually satisfied as the modulation frequency is in MHz and the lifetime of the fluorophore is on the order of nanoseconds:

$$
\begin{aligned}
(Q_m)_{ij} &= \sum_{k=1}^{N} \mu_{af,k} \int_{\Omega} d\Omega \ \eta \, \varphi_k \left(\varphi_i \varphi_j\right) \frac{1}{1 + i\omega \sum_{l=1}^{N} \tau_l \varphi_l} \\
&= \sum_{k=1}^{N} \mu_{af,k} \int_{\Omega} d\Omega \ \eta \, \varphi_k \left(\varphi_i \varphi_j\right) \frac{1 - i\omega \sum_{l=1}^{N} \tau_l \varphi_l}{1 + (\omega \sum_{l=1}^{N} \tau_l \varphi_l)^2} \\
&\approx \sum_{k=1}^{N} \mu_{af,k} \int_{\Omega} d\Omega \ \eta \, \varphi_k \left(\varphi_i \varphi_j\right) (1 - i\omega \sum_{l=1}^{N} \tau_l \, \varphi_l)
\end{aligned}
$$

[3.33]

In the FEM forward problem, first the excitation photon distribution Φ_x, is obtained by solving the first part of equation [3.30]. Then the emission photon distribution in the whole medium Φ_m, is obtained by solving the second part. Finally, the measured photon flux on the boundaries is calculated as $\Phi_m/2A$.

3.3.2 Inverse problem of FT

A least-square minimization method is used to solve the FT inverse problem. This method is just like the method used in DOT except for the fact that we now are minimizing the difference between the measurements ϕ_{ij}^{m} and data simulated, $P_{ij}(\mu_{af}, \tau)$, from the coupled diffusion equation to find the fluorophore absorption coefficient μ_{af} and lifetime τ. Thus, the objective error function for FT is:

$$
\varepsilon^2 \left(\mu_{af}, \tau\right) = \sum_{i=1}^{N_s} \sum_{j=1}^{N_d} (\phi_{ij}^{m} - P_{ij}(\mu_{af}, \tau))^2
$$

[3.34]

The Jacobian matrix *J* for FT is defined as:

$$J = \begin{vmatrix} \frac{\partial P_{A1}}{\partial \mu_{af1}} & \frac{\partial P_{A1}}{\partial \mu_{af2}} & \cdots & \frac{\partial P_{A1}}{\partial \mu_{afN}} & \frac{\partial P_{A1}}{\partial \tau_1} & \frac{\partial P_{A1}}{\partial \tau_2} & \cdots & \frac{\partial P_{A1}}{\partial \tau_N} \\ \cdots & \cdots & \cdots & \cdots & \cdots & \cdots & \cdots & \cdots \\ \frac{\partial P_{AM}}{\partial \mu_{af1}} & \frac{\partial P_{AM}}{\partial \mu_{af2}} & \cdots & \frac{\partial P_{AM}}{\partial \mu_{afN}} & \frac{\partial P_{AM}}{\partial \tau_1} & \frac{\partial P_{AM}}{\partial \tau_2} & \cdots & \frac{\partial P_{AM}}{\partial \tau_N} \\ \frac{\partial P_{P1}}{\partial \mu_{af1}} & \frac{\partial P_{P1}}{\partial \mu_{af2}} & \cdots & \frac{\partial P_{P1}}{\partial \mu_{afN}} & \frac{\partial P_{P1}}{\partial \tau_1} & \frac{\partial P_{P1}}{\partial \tau_2} & \cdots & \frac{\partial P_{P1}}{\partial \tau_N} \\ \cdots & \cdots & \cdots & \cdots & \cdots & \cdots & \cdots & \cdots \\ \frac{\partial P_{PM}}{\partial \mu_{af1}} & \frac{\partial P_{PM}}{\partial \mu_{af2}} & \cdots & \frac{\partial P_{PM}}{\partial \mu_{afN}} & \frac{\partial P_{PM}}{\partial \tau_1} & \frac{\partial P_{PM}}{\partial \partial \tau_2} & \cdots & \frac{\partial P_{PM}}{\partial \tau_N} \end{vmatrix} \qquad [3.35]$$

where $P_{A,P}$ are the fluorescence amplitude and phase measurements. The number of measurements is M, and the number of unknowns is N, which is also the number of nodes. Similarly, the Jacobian is also calculated analytically with the adjoint method (167).

The unknown μ_{af} and $\tau$are also found by iteratively updating the simulated data using the Levenberg-Marquardt method until convergence or the maximum number of iterations is reached:

$$\Delta X_k = X_{k+1} - X_k = (J^T J + \lambda I)^{-1}(J^T \varepsilon) \qquad [3.36]$$

where $\varepsilon_{ij} = (\phi_{ij}^m - P_{ij})$ and ΔX represents the unknown matrix of μ_{af} and τ.

3.3.3 Incorporation of a priori information for FT

Conventionally, there are two types of *a priori* data for FT: functional *a priori* and structural *a priori.*

3.3.3.1 Functional *a priori*

Proper modelling of the excitation and emission light using a coupled diffusion equation requires the background optical properties of the medium, μ_a and μ_s' to be known. As a result, the absorption and scattering properties of the medium need to be obtained prior to reconstruction of the fluorescence parameters. These parameters can be obtained using DOT prior to FT reconstruction. In this method, DOT measurements are first taken with the excitation and emission wavelengths. Second the optical properties, μ_{ax} and μ_{sx}' are reconstructed for the excitation wavelength and used to calculate the excitation photon distribution Φ_x. Then the optical properties, μ_{am} and μ_{sm}' are reconstructed for the emission wavelength. Finally, the optical background properties obtained from DOT measurements (which include Φ_x, μ_{am} and μ_{sm}'), are used as the functional *a priori* information for FT reconstruction.

3.3.3.2 Structural *a priori*

However, even with the correct optical properties, the accuracy of the recovered fluorescence parameters is highly dependent on the size, location, and concentration of the fluorophore. Just like DOT, FT is also plagued by the poor spatial resolution due to the high scattering of light in tissue. Consequently, FT has also been integrated with other high spatial resolution imaging modalities by incorporating anatomical information as structural *a priori* information to improve the FT reconstruction. In this method, the fluorescence distribution is attributed to a specific region in the FEM mesh identified by the high resolution imaging modality. The implementation of this method for FT is the same as the method described in DOT. However, as the fluorescent contrast is not usually seen by the other imaging modality, error can arise when the prescribed fluorescent region does not match the true distribution (185).

3.4 Introduction to mathematical framework for TM-FT

The mathematical framework for TM-FT is very similar to FT. The difference between the two methods is that TM-FT used a temperature sensitive fluorescent fluorophore whose quantum efficiency depends on temperature. Consequently, the fluorescence light propagation in tissue for TM-FT is described by a temperature dependent coupled diffusion equation:

$$\nabla \cdot [D_x(r)\nabla \Phi_x(r,\omega)] - \left[\mu_{ax}(r) + \frac{i\omega}{c_n(r)}\right] \Phi_x(r,\omega) = -q_0(r,\omega) \tag{3.37}$$

$$\nabla \cdot [D_m(r)\nabla \Phi_m(r,\omega)] - \left[\mu_{am}(r) + \frac{i\omega}{c_n(r)}\right] \Phi_m(r,\omega) = -\Phi_x(r,\omega)\,\eta(T)\mu_{af}(r)\frac{1 - i\omega\tau(r)}{1 + [\omega\tau(r)]^2} \tag{3.38}$$

where T is the temperature of the medium, and the quantum efficiency is now dependent on temperature $\eta(T)$. In addition, the thermo-sensitive fluorescent probes also make it possible to provide high resolution spatial information as the HIFU scan can be used to directly outline the fluorescent distribution boundary and can be incorporated into the FT program as soft *a priori*. From a procedural and computational viewpoint, the method to solve the forward and inverse problem for TM-FT is implemented in the same manner as described for FT using structural *a priori* information. This will be described in greater detail in the next chapter and validated with simulation studies.

Chapter Four: Validation with simulation studies[2]

"Experimental investigation, to borrow a phrase employed by Kepler respecting the testing of hypotheses, is "a very great thief of time." Sometimes it costs many days to determine a fact that can be stated in a line."
– John William Draper, *Scientific Memoirs (1878)*

4.1 Introduction

Conventional fluorescence tomography (FT) can recover the distribution of fluorescent agents within a highly scattering medium. However, poor spatial resolution remains its foremost limitation. In this chapter, we investigate the feasibility of combining HIFU and FT to provide high spatial resolution fluorescent imaging beyond the diffusion limit. TM-FT is a multimodality technique that combines fluorescence imaging with focused ultrasound to locate thermo-sensitive fluorescence probes using *a priori* spatial information to drastically improve the resolution of conventional FT. The idea is to irradiate the medium with excitation light and a focused ultrasound wave generated by high intensity focused ultrasound (HIFU) in low power mode. As the HIFU scans through the medium, it sequentially generates a hot spot, which elevates the temperature of this small area several degrees. When the temperature-sensitive fluorescence agents are present within this HIFU focal zone, the fluorescence quantum efficiency increases due to the elevated local

---

[2] This chapter (4 Simulation study) was reproduced with modifications from Applied Optics, Vol 54 Issue 25, Lin, Y., et al., Simulation-based evaluation of the resolution and quantitative accuracy of temperature-modulated fluorescence tomography. Page No 7612-7621. Copyright (2015) with permission from Optical Society of America. (160)

temperature. As a result, the emitted fluorescence light intensity has a detectable change only when the agent is present within the focal zone. This temperature modulation via the HIFU allows us to now have a separate fluorescence measurement for each pixel in a region of interest (ROI), which is not available with conventional FT. Furthermore, the location and size obtained from the HIFU scan specifically indicates the location of the fluorescence source, which can potentially overcome the challenges of the traditional anatomical image guided FT approach.

Simulation studies were undertaken to evaluate the performance of the TM-FT technique. In this chapter, we demonstrate the theoretical framework for TM-FT and test the algorithm using simulations to study a number of different cases, including size and depth dependence, the presence of multiple fluorescence sources, and the effect of background fluorescence. For each case, the performance of TM-FT is compared with conventional FT. The results show that, in all cases, TM-FT provides higher spatial resolution and superior quantitative accuracy. These simulation studies presented here confirm that TM-FT, which combines FT and HIFU, is able to acquire high-resolution fluorescence images of temperature-sensitive molecular probes in deep tissue.

4.2 Mathematical framework of TM-FT

Simulation studies are carried out to demonstrate the feasibility of this approach. These studies are performed on a synthetic phantom with slab geometry (D:40 mm × W:100 mm). Eight sources and eight detectors are utilized in transmission mode on opposite sides of the phantom. The background optical properties are set to μ_a=0.01 mm^{-1}

and μ'_s=1.0 mm^{-1}, respectively. Synthetic FT data is generated by solving the forward problem using the finite element method. Conventional FT reconstruction is first performed for each case to recover the spatial distribution of the fluorophore concentration, which is directly related to the absorption coefficient $\mu_{af}(r)$. Unfortunately, on its own, conventional FT delivers a low-resolution map with poor quantitative accuracy. However, this low-resolution map can be used to determine the ROI for the TM-FT HIFU scan. Then, the TM-FT forward solver is used to recover a binary map that reveals the spatial distribution of temperature-sensitive fluorophores with high resolution. As the final step of TM-FT, this high-resolution binary map is used to constrain and guide a conventional FT reconstruction algorithm to obtain quantitatively correct high-resolution fluorophore concentration maps. For each case, the conventional FT and TM-FT reconstruction results are compared side by side in terms of the recovered fluorescence object size and concentration. To be able to perform these simulations, several steps have been followed:

1. Modeling of the temperature distribution in the medium due to HIFU.
2. Modeling of excitation and fluorescence emission light propagation in turbid medium (forward solver) and reconstruction of the images from synthetic data (inverse solver).
3. Generation of TM-FT binary *a priori* information.
4. Reconstruction of fluorescence images with TM-FT *a priori*.

These steps are described as follows.

4.2.1 Modeling of temperature distribution in the medium due to HIFU heating

The ultrasound energy deposit is calculated from HIFU heating based on the Rayleigh–Sommerfeld radiation integral equation (186, 187). In this work, the specification of a commercial device is used for simulation studies, Figure 4.1a. The pressure field induced by the Sonic Concepts H102 transducer can be approximated as a Gaussian kernel with a 1.26 mm full width at half-maximum (FWHM) (for first harmonic resonance) in the lateral direction of the focal plane, Figure 4.1b. This approximation can be adapted to different HIFU devices by modifying the focal spot size.

The transport of temperature induced by HIFU heating can be modeled by the Pennes' bioheat transfer equation (187, 188):

$$\rho \cdot c \cdot \frac{\partial T(\vec{r},t)}{\partial t} = \nabla k \nabla T(\vec{r},t) - c_b \omega (T(\vec{r},t) - T_a) + Q(\vec{r},t) \tag{4.1}$$

where T is the temperature of the medium at position $\vec{r}$ and time t. The density, specific heat, and thermal conductivity of the medium are represented by ρ, c, and κ, respectively. T_a is the temperature of blood flow. The last term on the right-hand side, Q, is the heat sink term, which takes into account the heat loss due to blood perfusion. The specific heat and perfusion rate of the blood are represented by c_b and ω. In our simulations, the transducer power is turned on for 2 seconds at each scanning step. Thus, the heat-sink term is neglected due to the short heating time.

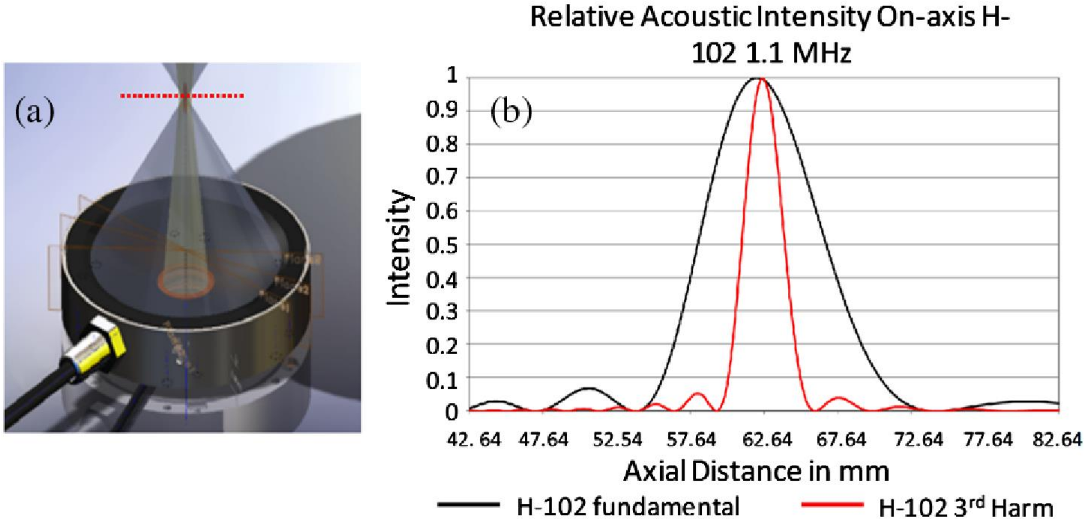

Figure 4. 1 HIFU. (a) Commercial HIFU device (H102 transducer). (b) Its on-axis pressure profile temperature. (189)

4.2.2 Modeling of light propagation in tissue and the forward problem of TM-FT

Since the quantum efficiency of the ThermoDots is temperature dependent, the fluorescence light propagation in tissue for TM-FT is described by the coupled diffusion equation in the continuous wave domain which is modified at the emission wavelength to account for this behavior:

$$\nabla \cdot [D_x \nabla \Phi_x] - [\mu_{ax} + \mu_{af}]\Phi_x = -q_0 \qquad [4.2]$$

$$-\nabla \cdot [D_m \nabla \Phi_m[\eta(T)]] - \mu_{am}\Phi_m[\eta(T)] = -\Phi_x \eta(T)\mu_{af} \qquad [4.3]$$

where $\Phi_x(r)$ and $\Phi_m(r)$ ($W \cdot mm^{-2}$) represent the photon densities for the excitation and emission light, respectively. The diffusion coefficient, $D_{x,m}(r)$ (mm^{-1}), is defined by $D_{x,m}=1/3(\mu_{ax,m} + \mu'_{sx,m})$ where $\mu'_{sx,m}$(mm^{-1}) is the reduced scattering coefficient and $\mu_{ax,m}$ (mm^{-1}) is the absorption coefficient of the medium. The absorption coefficients are assumed to be the same at the excitation and emission wavelengths. The absorption coefficient due to the fluorophore, $\mu_{af}(r)$, is directly related to its concentration. T is the temperature of the medium. The fluorescence quantum efficiency, $\eta(T)$, is the intrinsic property of the fluorophore, which is defined as the ratio of the number of fluorescence photons emitted to the number of excitation photons absorbed. Using our thermo-sensitive agents, the fluorescence quantum efficiency is a temperature-dependent parameter. The Robin boundary condition is applied to the diffusion model.

After applying the finite element method, equation [4.3] can be rewritten in an assembled matrix form:

$$G\zeta_m = Q_m\zeta_x\eta(T) \tag{4.4}$$

where ξ_m and ξ_x are the nodal representation of the emission and excitation photon distribution, respectively. More details on the matrix assembly and computation have been explained in Chapter 3 (49, 128, 133).

4.2.3 Inverse Problem of TM-FT

The inverse problem is solved by minimizing the difference between the measured and calculated data according to the following objective function:

$$O\left(\mu_{af}\right) = \varepsilon^2\left(\mu_{af}\right) = \sum_{i=1}^{N_S}\sum_{j=1}^{N_d}\left(\phi_{ij}^{m} - P_{ij}\left(\mu_{af}\right)\right)^2 \tag{4.5}$$

Where ε is the error to be minimized, and N_s and N_d represent the number of sources and detectors, respectively. ϕ_{ij}^{m} is the set of fluorescence measurements. $P_{ij}(\mu_{af})$ are the flux on the measured point calculated by the forward solver from the spatial distribution of μ_{af}. We iteratively update the unknown μ_{af} to be reconstructed with the Levenberg–Marquardt method by

$$X_{m+1} = X_m + (J^T J + \lambda I)^{-1}(J^T \varepsilon) \tag{4.6}$$

where X represents the unknown matrix of μ_{af}. The Jacobian matrix J is calculated with an adjoint method (167).

Unfortunately, the reconstructed μ_{af} map at the end of this process is not quantitatively accurate and cannot recover the fluorescence targets with high resolution. This justifies the importance of incorporation of another high spatial resolution imaging modality into FT. For conventional FT, eight sources and detectors in transmission configuration are used to acquire full tomographic synthetic measurements, as shown in Figure 4.2a. This configuration produces 64 measurements and allows reconstruction of a fluorescence concentration map. In this example, a 3 mm diameter fluorescent target is placed at the center of the synthetic phantom, 20 mm away from each boundary. The reconstructed conventional FT image is presented in Figure 4.2b.

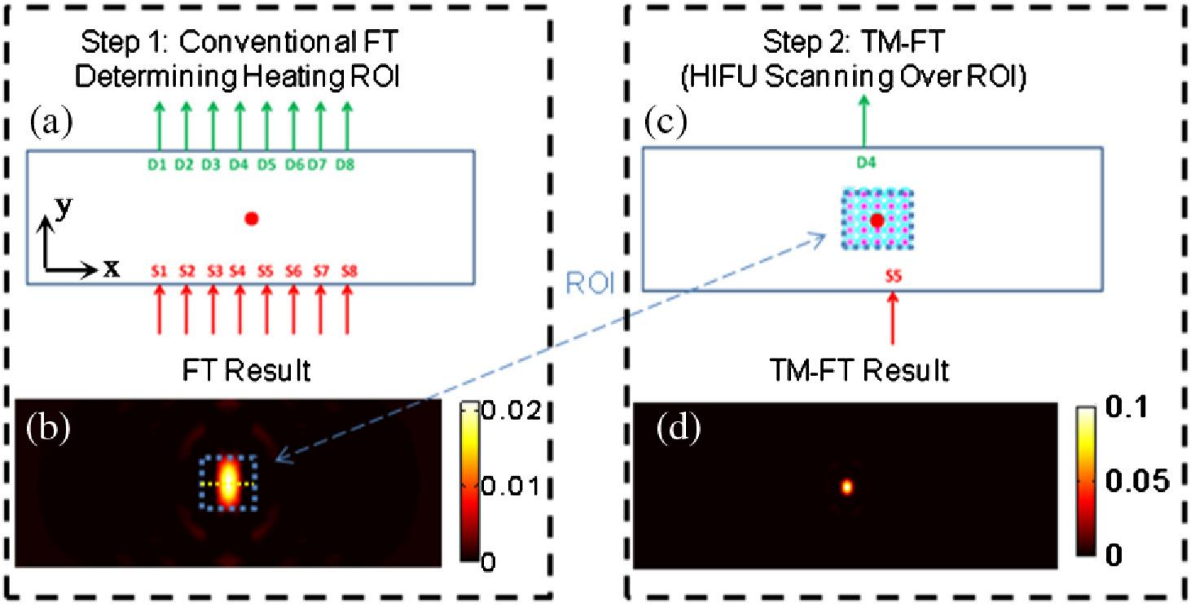

Figure 4. 2 TM-FT image procedure. (a) During step 1, conventional FT is performed using an eight-source and eight-detector configuration. (b) Low-resolution map of μ_{af} is then obtained using the standard FT reconstruction algorithm. This low-resolution map is used to determine the ROI for the HIFU heating in the second step. (c) A specific source-detector pair is selected with the best fluorescence signal in terms of SNR and sensitivity. The HIFU beam scans through the ROI determined from the previous step. This step provides a spatial *a priori* on the localization of the fluorescent source μ_{af}. (d) This *a priori* information is then used in the TM-FT image reconstruction algorithm to obtain a high-resolution image with superior quantitative accuracy.(189)

4.2.4 Generation of TM-FT a priori Information

Once the ROI is determined by the low-resolution conventional FT images reconstructed in the previous step, the HIFU beam is scanned over this ROI (Figure 4.2c). Meanwhile, a particular source-detector pair, which has the highest sensitivity around this ROI (S5/D4 for this case), is monitored continuously. It is only when the temperature-sensitive contrast agent is present within the focal spot, the emitted fluorescence light intensity changes drastically due to the change in quantum efficiency which results in a change in the measured signal. Thus, a well-defined description of the contrast agent distribution in the form of a binary mask is obtained. Here the resolution of TM-FT is closely related to the spot size of HIFU (~1.26 mm for the presented results in our simulation).

Please note that the obtained binary mask already represents a high-resolution fluorescence image even without any reconstruction process. However, a final TM-FT reconstruction process is required in order to achieve a quantitatively accurate contrast agent concentration map.

4.2.4 Reconstruction of fluorescence images with TM-FT a priori information

Since the TM-FT *a priori* information is available in the form of a binary map, the FT reconstruction process is performed a second time utilizing the *a priori* information to guide and constrain the solution. Again, we iteratively update the unknown μ_{af} to be reconstructed with the Levenberg–Marquardt method; however, this time a penalty matrix obtained from the *a priori* information generated with TMFT is used:

$$X_{m+1} = X_m + (J^T J + \lambda L^T L)^{-1}(J^T \varepsilon) \quad \textbf{[4.7]}$$

where X represents the unknown matrix of μ_{af}. The Jacobian matrix J is calculated with the adjoint method (167). Here, the non-unitary matrix L is the penalty matrix describing the *a priori* information obtained using temperature modulation as described below (62). This final step reveals a much higher-resolution fluorescence image with superior quantitative accuracy as it is guided by the TM-FT *priori*, Figure 4.2d.

4.3 Results

The ultrasound pressure field was assumed to be generated from an H102 HIFU transducer, and is approximated by a Gaussian shape with a 1.26 mm FWHM (Figure 4.3).

The specific heat, density, and thermal conductivity of the tissue are set to 4186[J/(kg·°C)], 1000(kg/m^3), and 0.7[W/(m·°C)], respectively. The HIFU is turned on for 2 seconds with the maximum temperature rise below 5°C. Figure 4.3a shows the Gaussian-shaped pressure field from HIFU, and the resulting temperature rise at 2 seconds of heating is shown in Figure 4.3.b. The profile for the pressure field and temperature increase are plotted in Figure 4.3.c. It shows that the size of the heating spot is slightly larger than that of the ultrasound pressure field due to the heat diffusion.

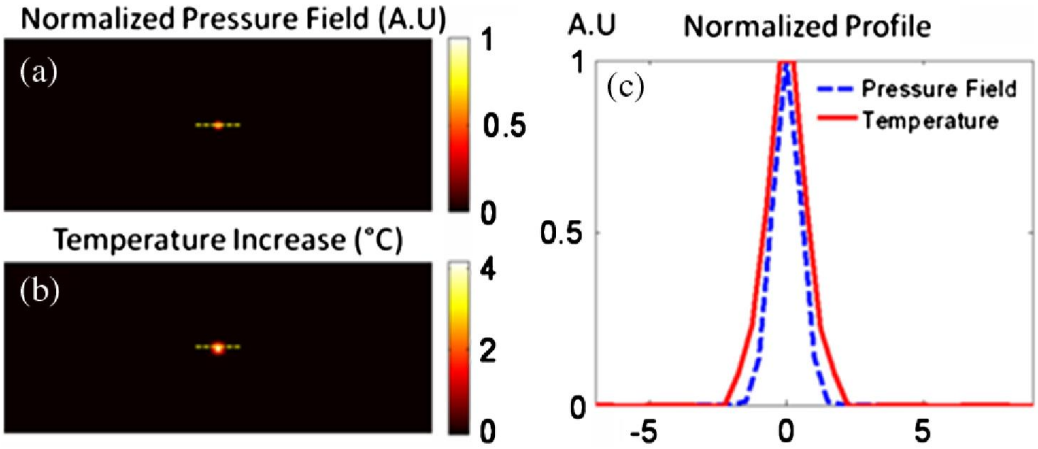

Figure 4. 3 Simulation result 1. (a) 2D pressure field on the focal plane. (b) Corresponding temperature increase due to the HIFU heating at the end of 2 second. (c) Normalized profile for the pressure field and temperature increase.(189)

The temperature-dependent profile of the quantum efficiency is computed from the heating profile and is used in the simulation studies. The quantum efficiency is assumed to increase 50% at the heating spot. For each study, the fluorescence source is reconstructed using conventional FT and TM-FT, and then the results are compared. To evaluate the performance of the TM-FT extensively, the following simulation studies are carried out.

4.3.1 Size and Position Dependence

Due to the ill-posedness of the FT inverse problem, the reconstructed fluorescence concentration is expected to depend on the size and location of the inclusion (126, 190, 191). We evaluate this effect for conventional FT and TM-FT in this study. The size and location of the inclusion are varied, as listed in Table 4.1. Here, the parameter depth refers to the distance from detectors. However, the absorption coefficient due to the contrast agent, μ_{af}= 0.01 mm^{-1}, is kept the same for all the cases.

Table 4. 1 Recovered μ_{af} for First Simulation Study.(189)

				Conventional FT		**TM-FT**	
Case No.	**Inclusion Size (mm)**	**Depth (mm)**	**True μ_{af} (mm^{-1})**	**μ_{af} (mm^{-1})**	**FWHM (mm) *x* / *y***	**μ_{af} (mm^{-1})**	**FWHM (mm) *x* / *y***
1	4	5	0.01	0.0031	3.9/7.1	0.0077	4.0/4.8
2	4	10	0.01	0.0024	4.2/8.0	0.0079	4.0/4.4
3	4	20	0.01	0.0017	4.5/10.4	0.0078	3.8/4.6
4	3	20	0.01	0.0014	4.3/10.4	0.0094	3.0/4.2
5	7	20	0.01	0.0048	5.4/10.8	0.0090	7.0/7.2

The reconstructed absorption map due to the fluorescence contrast agent is shown in Figure 4.4, and the recovered absorption coefficient and fluorescence source size are listed in Table 4.1.

The first three cases (1–3) allowed us to investigate the depth dependence of the results for a 4 mm diameter object. Due to the slab geometry and transmission mode measurements, the spatial resolution in the horizontal and vertical directions are different. The FWHM of the recovered fluorescence source is calculated in both directions, as shown in Table 4.1. For conventional FT, the 4 mm inclusion is recovered with more than 70% error for all three depths (cases 1–3). The accuracy of the recovered fluorescence source strength and size decreases as the inclusion is embedded deeper into the scattering medium. For example, for the very same 4 mm diameter object, the recovered μ_{af} is reduced from 0.0031 mm^{-1} down to 0.0017 mm^{-1} as its depth increases from 5 to 20 mm.

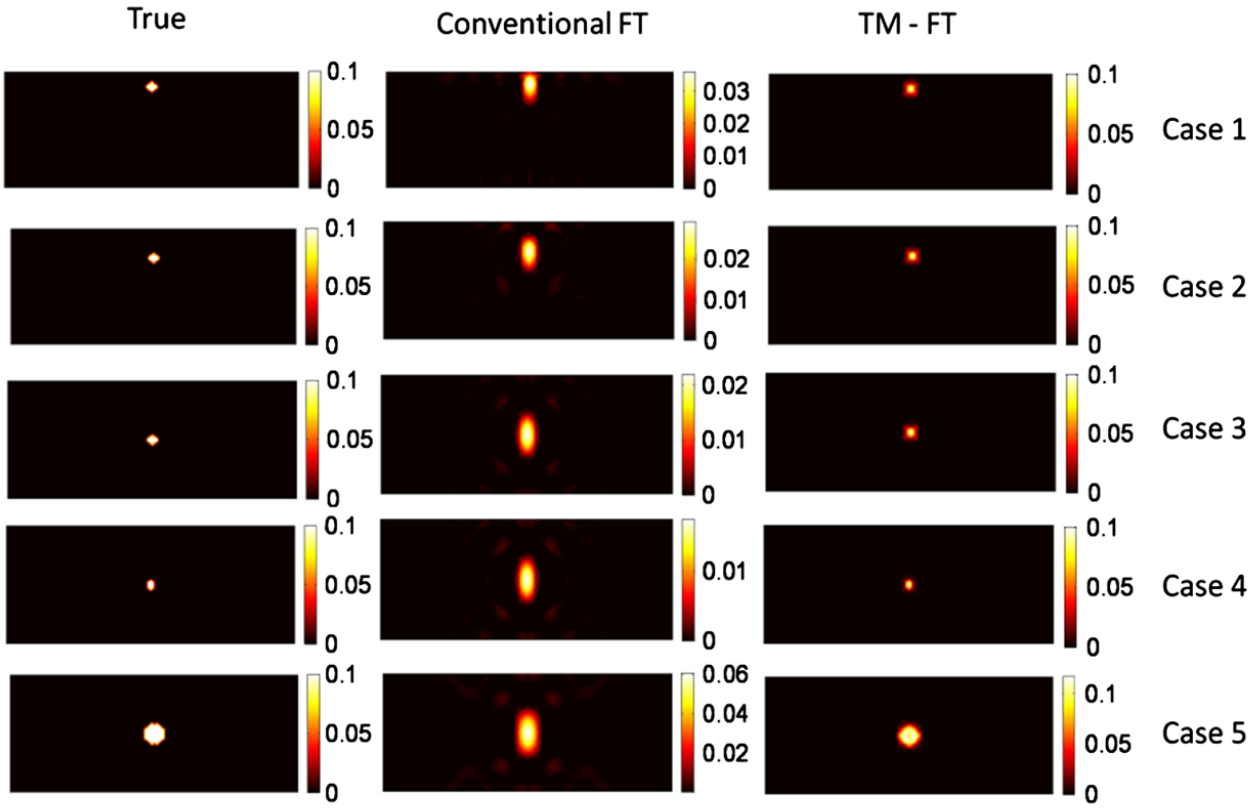

Figure 4. 4. Results for the first simulation study using inclusions of various sizes buried at different depths.(189)

However, when using TM-FT, the size and strength of the fluorescence source are recovered more accurately. Indeed, the quantitative accuracy of TM-FT is not affected by the depth of the inclusion. Regardless of its location, the recovered μaf of the 4mm inclusion is nearly the same, 0.0078 mm^{-1}. Meanwhile, TM-FT recovers the size more accurately, i.e., with less than 20% error in both directions, while the error can go as high as 150% for the conventional FT, especially for the y direction. In summary, the recovered fluorescence size is not affected by the source-detector geometry for the TM-FT compared with the elongated shape obtained with conventional FT.

Meanwhile, the last three cases (3–5) allowed us to investigate the size dependence of the results for different inclusions located at the center of the slab phantom. For these inclusions located at the center, the error of the recovered source strength reduces as the true fluorescence size increases from 3 to 7 mm for conventional FT. For instance, the source strength recovered has an error of almost 50% for the 7mm inclusion and 86% for the 3 mm inclusion. Consequently, the recovered fluorescence strength is indeed highly dependent on the size of the inclusion for conventional FT. When TM-FT is used, the accuracy of the recovered fluorescence source strength is much improved, i.e., the error is less than 20% for all objects, as shown in Table 4.1. When it comes to the recovered size of the object, the performance of TM-FT is superior, with less than 15% error for all three inclusions with different sizes. The error reduces with the size of the object. For example, it is only around 3% for the largest object with 7 mm diameter. The variation in the recovered size of these small inclusions is most probably due to the spatial resolution limitation of the TM-FT, which directly depends on the size of the HIFU beam (~1.26 mm). As it is investigated in the next sections, the other critical factor for the spatial resolution of the TM-FT is the HIFU scanning pattern.

4.3.2 Multiple Inclusions

To further explore the spatial resolution limit of the TM-FT method for imaging temperature-sensitive probes, simulation studies were performed using multiple inclusions. Again, the same slab geometry simulation phantom with similar background optical properties is used. Four cases with various sizes and contrasts are tested. For the first three cases, the two inclusions are separated edge to edge 2 mm apart and are parallel to the source-detector plane, while, for the fourth case, the two inclusions were placed 4 mm apart and are perpendicular to the source-detector plane.

The reconstructed absorption maps due to fluorescence contrast agent are shown in Figure 4.5, and the recovered absorption coefficients are listed in Table 4.2 together with the fluorescence source size for each inclusion. The results show that conventional FT cannot resolve the two objects successfully for any case due to the intrinsic limited spatial resolution; thus, the source strength and size are calculated as one inclusion (Table 4.2). Figure 4.6 shows the plot of the profiles along the yellow dashed lines, as indicated in the first column of Figure 4.5, for the true inclusion and the reconstructed inclusions from conventional FT and TM-FT.

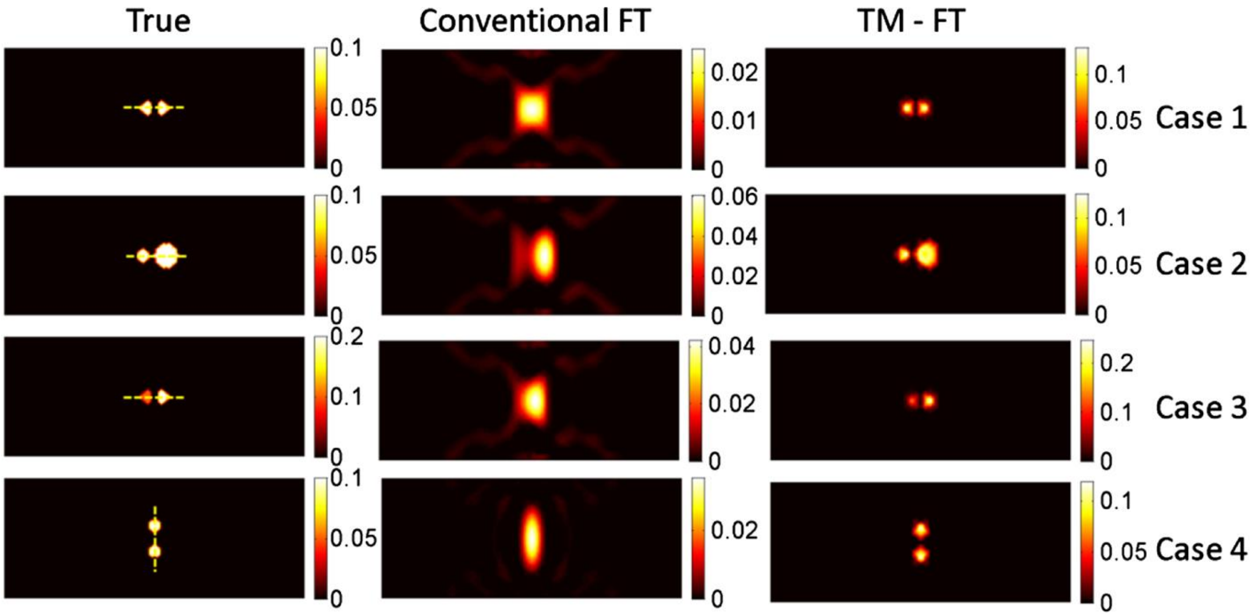

Figure 4. 5 Results for the second simulation study using multiple inclusions.(189)

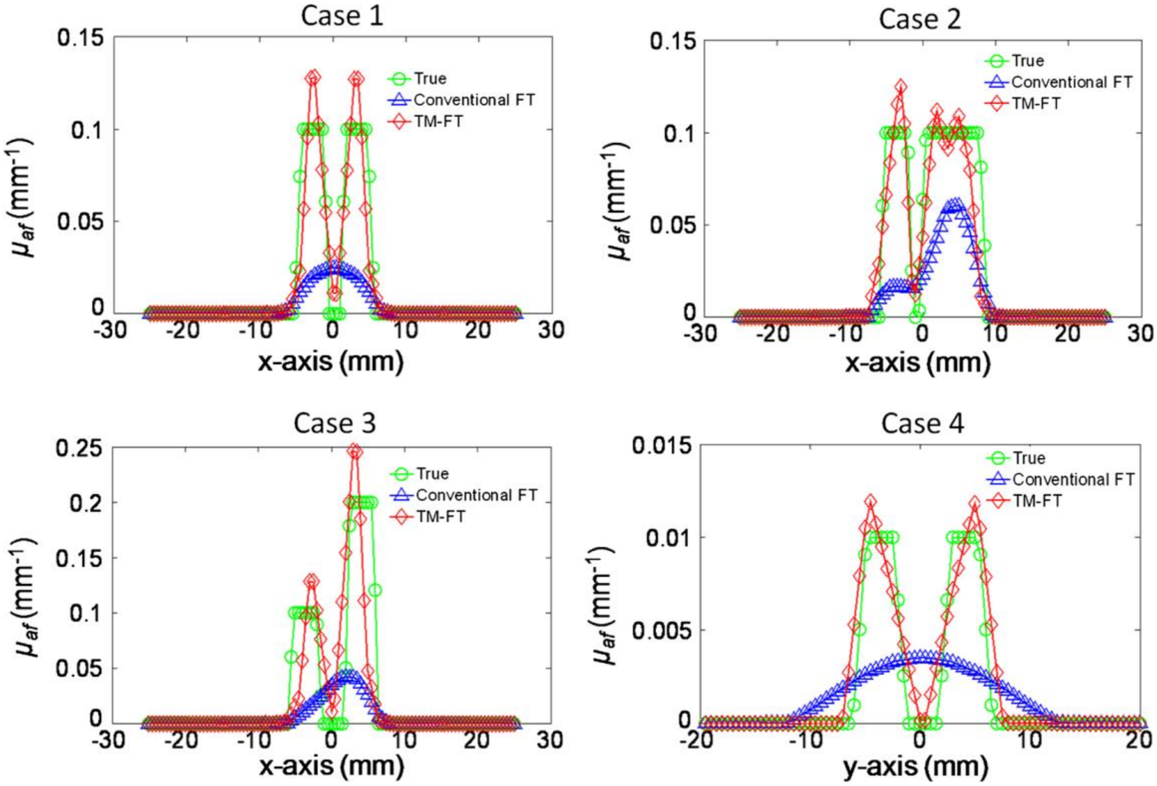

Figure 4. 6 Profile of the results for the second simulation study. The profiles are carried out across the inclusions, along the yellow dashed line, (Figure 4.5).(189)

Table 4. 2 Recovered μ_{af} for Second Simulation Study. (189)

				Two Objects Resolved		Conventional FT		TM-FT	
Case No.	**Obj. No.**	**Inclusion Size (mm)**	**True μ_{af} (mm^{-1})**	**FT**	**TM-FT**	**μ_{af} (mm^{-1})**	**FWHM (mm) *x / y***	**μ_{af} (mm^{-1})**	**FWHM (mm) *x / y***
1	1	4	0.01	✗	✓	0.0020	8.7/9.9	0.0092	4.4/5.0
	2	4	0.01					0.0098	4.4/5.0
2	1	4	0.01	✗	✓	0.0049	6.1/12.5	0.0093	5.2/5.2
	2	8	0.01					0.0092	8.1/8.3
3	1	4	0.01	✗	✓	0.0033	6.9/10.9	0.0095	4.4/5.0
	2	4	0.02					0.0178	4.6/5.2
4	1	4	0.01	✗	✓	0.0028	4.5/14.7	0.0086	4.2/5.1
	2	4	0.01					0.0085	4.3/5.3

The first case shows that TM-FT successfully recovered two individual inclusions that are 2 mm apart, while conventional FT fails. When one inclusion is larger in size, it is recovered dominantly with conventional FT as the smaller inclusion is hardly visible. However, TM-FT recovers the true size and location of both inclusions regardless of their sizes, as shown in case 2. The third case shows that if one inclusion has twice the source strength than the other, TM-FT can still recover 1.9 times contrast between the two inclusion, while conventional FT shows that the higher concentration inclusion dominates the reconstructed μ_{af} map and the inclusion with lower concentration is hardly visible.

Due to the transmission geometry, the spatial resolution in the vertical direction is expected to be lower than in the horizontal direction. Accordingly, the two inclusions are separated 4 mm away in the fourth case but in the vertical direction. Conventional FT is not able to separate them due to its poor spatial resolution in this direction. However, TM-FT is not affected by the optical source-detector geometry because the spatial resolution is primarily determined by the HIFU scan. In all cases, the error in the recovered object size changes between 5% and 30% when TM-FT is used, while the errors in the recovered μ_{af} values are always less than 15%.

4.3.3 Presence of Background Fluorescence

There is likely to be residual fluorescence and/or autofluorescence from the tissue surrounding the target in realistic *in vivo* experiments. In this study, the contribution of background fluorescence is taken into account to investigate the performance of TM-FT in the presence of background fluorescence. Two cases with object to background contrast of 10 and 2 were evaluated, as shown in Table 4.3.

Table 4. 3 Recovered μ_{af} for Third Simulation Study*.(189)

Case No.	**True $\mu_{af}(mm^{-1})$: Inclusion/Background**	**Conventional FT: $\mu_{af}(mm^{-1})$**	**TM-FT: $\mu_{af}(mm^{-1})$**
1	0.01/0.005	0.0055 (45%)	0.0091 (9%)
2	0.01/0.001	0.0021 (79%)	0.0088 (12%)

* Percent error is shown in the parenthesis

For conventional FT and TM-FT, the inclusion could be localized on the fluorescence map, as shown in Figure 4.7. For conventional FT, the recovered fluorescence absorption coefficient is 0.0055 (45% error) and 0.0021 (79% error) for the contrast of 10 and 2, respectively. The recovered value is significantly improved to 0.0091 (9% error) and 0.0088 (12% error) using TM-FT, indicating the accuracy and robustness of TM-FT in recovering the fluorescence source strength independent of object to background contrast.

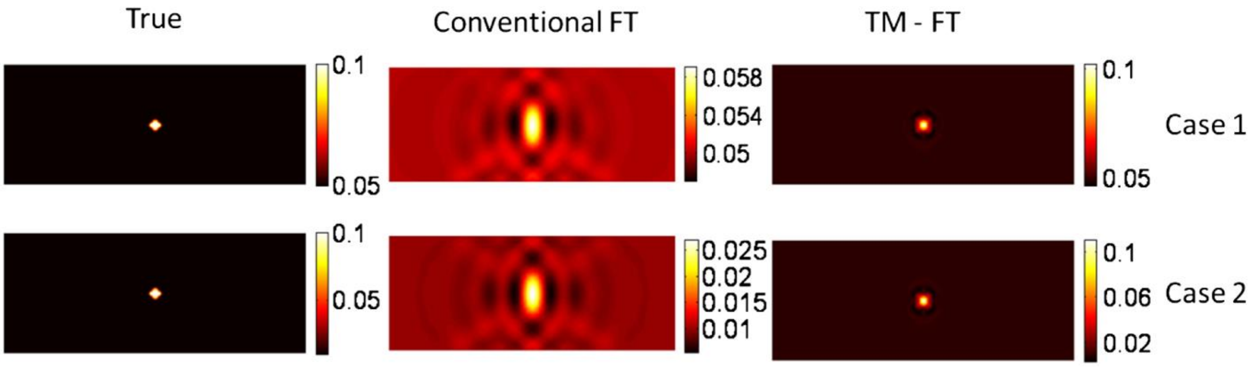

Figure 4. 7 Results for the third simulation study. These results show the effect of background fluorescence, present in the phantom, on the quality of reconstructed image.(189)

4.3.4 Various Heating Profile

As seen in the previous simulations, TM-FT does not always work perfectly, although it is superior to conventional FT for all cases. To further improve the TM-FT performance, the HIFU resolution needs to be considered because it is directly related to the spatial resolution of TM-FT. For this purpose, in this last simulation study, we evaluated the effect of the HIFU focal size and the spatial sampling rate on the spatial resolution of this method. Similar to the first phantom study, a 4mm diameter inclusion is embedded in the same rectangular phantom. The HIFU is scanned through an 8 mm×8 mm area with 0.5, 1.5, 2, and 3 mm step size (cases 1–4). Then, for the same phantom, the same area is scanned with a 1.0 mm step using a HIFU with a focal size of 0.8, 2.5, and 3.5 mm (cases 5–7). The reconstructed fluorescence absorption maps are shown in Figure 4.8, and the recovered absorption coefficient and fluorescence source size for each inclusion is listed in Table 4.4. When the 0.5 mm scanning step is used, the source strength can be accurately recovered to 0.01 mm^{-1}, and the value decrease to 0.0076 mm^{-1} (24% error) when the scanning step increases to 3 mm. Cases 1–4 shows that with TM-FT, the finer the scanning step, the better the spatial resolution and quantitative accuracy. This is logical because TM-FT relies primarily on the HIFU spatial resolution. When the 0.8 mm focal spot HIFU is used (case 5), the source strength is recovered as 0.0089 mm^{-1} (11% error), and the error increases to 32% as the focal size increases to 3.5 mm (case 7).

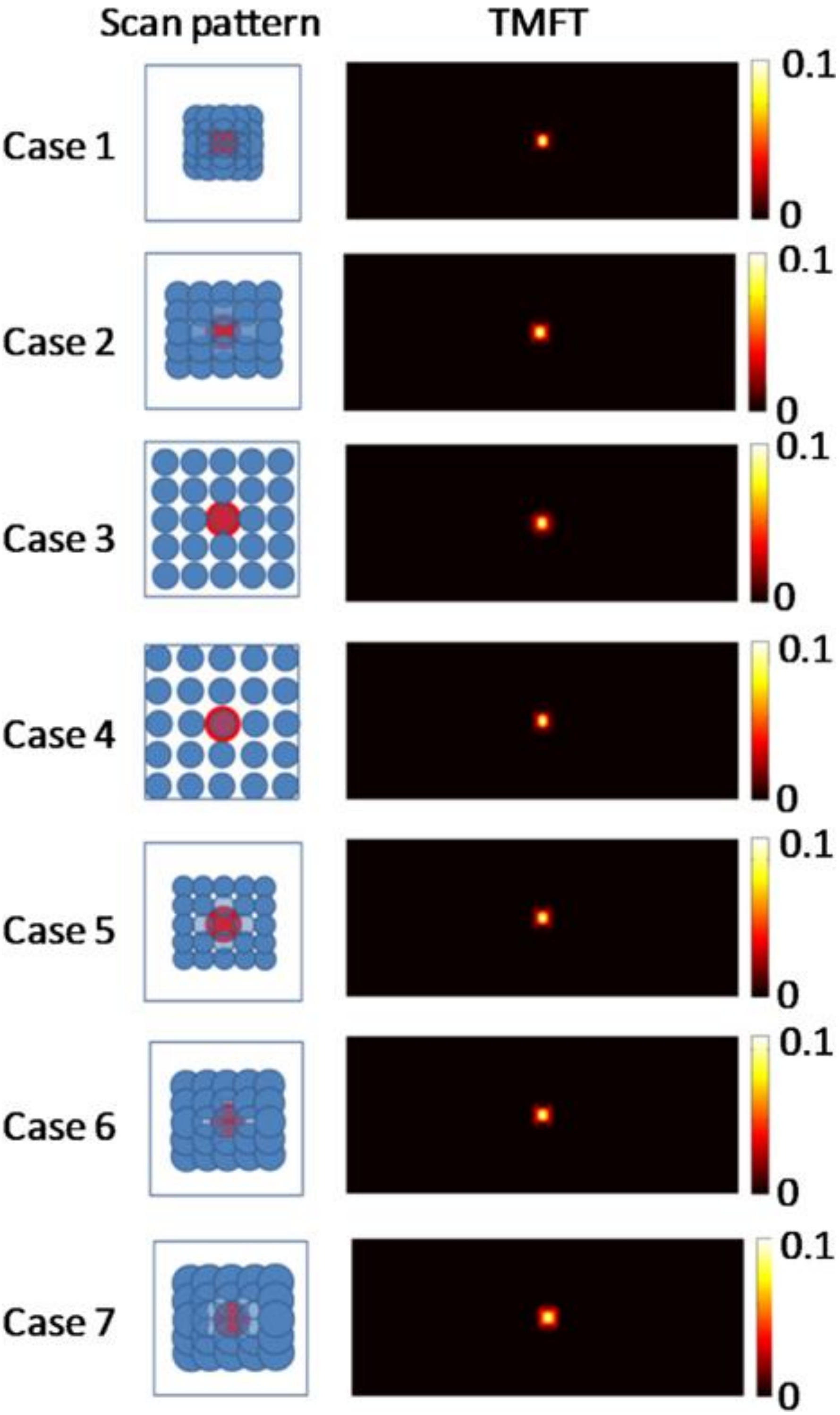

Figure 4. 8 Results of the fourth simulation study showing the dependence of spatial resolution of TM-FT on the HIFU resolution.(189)

Table 4. 4 Recovered μ_{af} for Fourth Simulation Study.(189)

				TM-FT	
Case No.	**Scanning step (mm)**	**HIFU Focal Spot Size (mm)**	**True μ_{af} (mm^{-1})**	**μ_{af} (mm^{-1})**	**FWHM (mm) x / y**
1	0.5	1.5	0.01	0.01	3.2/4.2
2	1.5	1.5	0.01	0.0085	3.8/4.4
3	2	1.5	0.01	0.0078	3.6/4.6
4	3	1.5	0.01	0.0076	3.6/4.5
5	1	0.8	0.01	0.0089	3.6/4.4
6	1	2.5	0.01	0.0083	3.8/4.2
7	1	3.5	0.01	0.0068	4.8/5.0

Finally, cases 5–7 show that the smaller the HIFU focal spot, the better the spatial resolution and quantitative accuracy of TM-FT, especially for small objects.

4.4 Discussion and Conclusion

This study investigates the performance of our new imaging modality termed “temperature modulated fluorescence tomography,” which can provide high-resolution fluorescence images with superior quantitative accuracy. TM-FT is based on the change of fluorescence quantum efficiency in correspondence to a temperature change. In practice, the relationship between the two parameters can be measured using fluorescence spectroscopy together with a temperature control and measuring device. In TM-FT, the location and structure of the fluorescence source can be directly determined from HIFU scan. This geometric information from TM-FT can serve as structural *a priori* information to guide the image reconstruction via the conventional image-guided approach. Please note that, unlike traditional image-guided FT, structural information offered by the HIFU scan accurately indicates the position of the fluorescence sources. By constraining and guiding the FT reconstruction algorithm, TM-FT can obtain high-resolution and quantitatively accurate fluorescence concentration maps. It is important to note here that the resolution of TM-FT directly depends on the HIFU resolution. Therefore, the HIFU resolution and its scanning pattern play a crucial role in TM-FT. Accordingly, our simulation studies not only demonstrated that TM-FT is superior to conventional FT for many different cases, including objects buried in a fluorescence background, but they also confirmed that the HIFU resolution and selected scanning pattern are critical. In the practical application of this technique, a scanning pattern selection would depend on the time available for imaging (i.e., more overlapping patterns would require more time) and selection of the HIFU transducer would depend on the application (i.e., the imaging depth for a HIFU with smaller focal spot would be limited).

In conclusion, TM-FT combines the superior sensitivity of fluorescence imaging and spatial resolution of focused ultrasound. These simulation studies demonstrated the feasibility of this TM-FT approach. The results showed that TM-FT can robustly recover the fluorescence source with high spatial resolution and quantitative accuracy for a number of cases. Overall, this ability to provide higher resolution and superior quantitative accuracy, makes TM-FT an ideal candidate for *in vivo* preclinical and clinical imaging.

Chapter 5: ThermoDots

"There are no such things as applied sciences, only applications of science."
– Louis Pasteur

5.1 Contrast agents for fluorescence imaging

5.1.1 Introduction and overview

Fluorescent molecular imaging has the potential to provide personalized patient-specific diagnosis and individually tailored treatments based on specific biological attributes identified by an exogenous fluorescent contrast agent also known as a fluorophore or fluorescent molecular probe. Fluorescent probes are molecules that absorb light at a specific wavelength and emit light at a longer wavelength. FT can identify molecular biomarkers labeled by a fluorescent molecular probe. The specificity of the probes determines the sensitivity of fluorescent imaging (64). With the recent developments of molecular probes, the applications for FT are increasing. Indeed, *in vivo* small animal imaging with fluorescence contrast agents has become an important tool in preclinical biological research. FT has been used to investigate disease processes, evaluate responses to therapy, and to develop new drugs (192-196).

When choose a fluorescent molecular probe, there are a few key points to consider. The first is choosing the right fluorophore to obtain the desired wavelength, brightness, and stability. Secondly, the probe should be biologically stable *in vivo*, overcome biological delivery barriers to penetrate tissue and cells, and collect in significant amounts to produce the desired contrast. Lastly, in order for the probes to provide information about the location or specific characteristic of a disease, the probes should only produce contrast at the desired target. The types of fluorescent contrast agents can be divided into three main categories which are summarized in Table 5.1: non-specific, targeted, and activatable molecular probes.

Table 5. 1 Categories of fluorescent contrast agents.

Probe Types	**Commercial availability**	**FDA approval**	**Specificity**	**Signal to background ratio**	**Targeting**
Non-specific	Yes	Yes (ICG and Methylene blue)	Low	Low	Passive Targeting
Targeted	No	No	High	Medium	Active Targeting
Activatable	No	No	High	High	Passive Targeting

5.1.2 Non-specific probes

The first and most commonly used probe in FT imaging is the non-specific fluorescent contrast agent. A non-specific fluorescent probe consist of a fluorescent dye, but lacks the reactive groups for selective recognition and conjugation(197). Non-specific probes are the most readily available of the three probe types and are produced commercially for a wide range of wavelengths and applications(198). In particular, the most popular of the two FDA approved NIR optical contrast dyes in the United States is Indocyanine green (ICG). As far back as 1956, this FDA-approved fluorophore has been used as a diagnostic aid for determining cardiac output, hepatic function, and liver blood flow (199). In the 1970s, ICG angiography was also FDA approved for ocular studies (199). In addition, non-specific probes such as ICG have also gained attention as a probe to study hypervascularization for detection of solid tumors due to the increased vascular permeability of cancer blood vessels compared to normal tissue through the enhanced permeability and retention (EPR) effect (200). The newly formed and highly porous tumor blood vessels exhibit enhanced vascular permeability which ensures a sufficient supply of nutrients to the tumor tissue for rapid growth but also allows for passive accumulation of the fluorophore in the cancerous tissue. In addition, the impaired lymphatic drainage due to the poorly developed lymphatics in the tumor results in an increased retention (201, 202). Studies have shown the feasibility of ICG enhancement for detection of solid tumors in many cancers including breast, pancreas, and colon cancer (194, 198, 202-204). Additionally, ICG has also shown clinical potential for sentinel lymph node mapping in breast cancer patients (198, 205). In general, a non-specific fluorescent contrast agent such as ICG can be used as a physiological indicator of malignant lesions but has poor specificity as it relies on passive accumulation through the EPR effect. Low target to background signal ratio or SNR is typical for non-specific probes due to the circulating fluorescent probes producing background fluorescence in the blood.

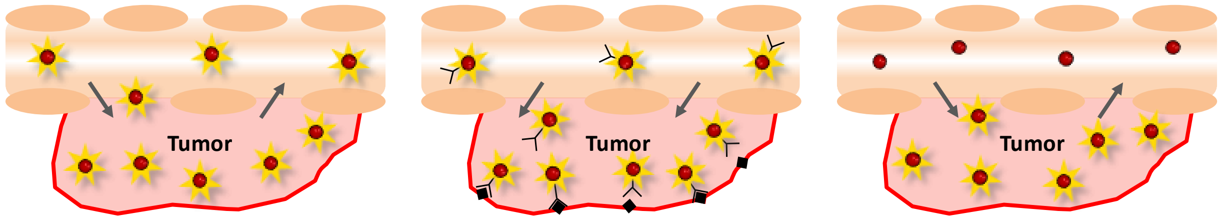

Non-specific probes
Passive targeting
(a)

Targeting probes
Active targeting
(b)

Activatable probes
Passive targeting
(c)

Figure 5. 1 Illustration for the three types of fluorescent imaging strategies. (a) Non-specific probes diffuse and accumulate in the tumor tissue due to the leaky tumor blood vessel through the EPR effect. This passive targeting has low specificity and low target to background signal due to the amount of fluorescent probes circulating in the blood. (b) Smart or activatable probes are designed to emit a signal and "turned on" under certain conditions such as binding to a target tissue or could occur from conformational changes due to environmental factors. Activatable probes display high specificity and sensitivity. Although not shown, activatable probes can be engineered to be targeted.

(c) Targeted probes can be engineered to target a certain receptor. Active targeting improves the specificity and can improve the sensitivity by allowing a length of time before imaging for the background signal to be washed out so that the enhancement in diseased tissue can be observed.

5.1.3 Targeted probes structure

Instead of relying on passive targeting, a popular method to improve the selectivity of the fluorophore to the target site is by active targeting. This also has the added potential of enhancing the contrast between the diseased and normal tissue. In this method, a NIR fluorophore which emits a detectable signal is conjugated to a specific targeting moiety (i.e. antibodies, antibody fragments, proteins, peptides, etc.) that exhibits a strong affinity and binds specifically to a certain receptor (206). This allows the targeted fluorescent probe to recognize and bind to a specific molecular target, thereby improving the contrast and retention time by thus confining the fluorophore in the targeted region for a sufficient length of time. The degree of specificity and sensitivity achieved is dependent on the choice of biomarker and targeting moiety (207).

To develop targeted contrast agents, a key factor is to identify one or more molecular targets that is uniquely different in diseased cells compared to normal cells. Targeted contrast agents have become popular for cancer imaging as overexpression of various receptors in the diseased tissue is characteristic of many cancers. This allows for targeted contrast agents to be used to selectively identify cancer and specific tumor types. For example, targeted contrast agents have shown potential in targeting tumor related angiogenesis. The cell adhesion molecule integrin $\alpha_v\beta_3$ plays an integral role in tumor angiogenesis and metastasis (22, 208). Integrin $\alpha_v\beta_3$ is a promising target as it is known to be significantly upregulated in most cancers including glioblastoma, melanoma, breast, ovarian, and prostate cancers compared to normal tissue and its expression level is correlated to the aggressiveness of the disease (22, 209, 210). Chen et al. showed the feasibility of an integrin $\alpha_v\beta_3$ targeted fluorescent dye created by conjugating cyanine dye 5.5 to an arginine-glycine-aspartic acid (RGD) peptide which is known to target integrin $\alpha_v\beta_3$(22). Clear signal enhancement of the targeted fluorescent dye was visualized in subcutaneous U87MG glioblastoma tumors ($\alpha_v\beta_3$ positive) xenografted mice and demonstrated potential as for tumor and metastasis diagnosis (208, 211).

In addition, Cai et al. showed replacing Cy 5.5 with quantum dots (QD) as the fluorescence agent can improve the efficiency and contrast of the integrin $\alpha_v\beta_3$ targeted fluorescent contrast agent *in vivo* (212). Quantum dots are semiconductor nanoparticles (2-10 nm diameter) that have much potential in targeted probes. QDs exhibit many advantages compare to organic fluorophores including a size- and composition- tunable fluorescence emission, large absorption over a wide spectral ranges, a narrow emission spectrum, higher photostability, and a brighter fluorescent signal due to their higher extinction coefficients (212). When coated with an aqueous-compatible organic layer, QDs can be attached to different molecular targets and be used as fluorescence targeted probes (207, 213). Gao et al. demonstrated the use of an ABC triblock copolymer coated QD conjugated to a monoclonal antibody with a strong affinity to prostate-specific membrane antigen (PSMA) in subcutaneous C4-2 tumor xenografted mice (213, 214).

Another interesting advancement has been the use of lipid or polymer based nanoparticles which can improve the efficiency of targeted contrast agents. Nanoparticles are generally defined in the nanometer size range 1 to 100 nm and have gained popularity as a drug delivery vessel and more recently for biomedical imaging (215, 216). The nanoparticles consist of amphiphilic molecules that can self-assemble in aqueous solution and encapsulate fluorescent contrast enhancers such as ICG or QDs (216-218). The three main advantages of the nanoparticle is that it provides a surface which can be functionalized with one or more targeting moieties without affecting the performance of the fluorescent contrast agents (18). The surface can also be modified to increase the plasma circulation time. Hydrophilic polymer such as polyethylene glycol (PEG) has been commonly used for this purpose in several studies (218-220). Lastly, nanoparticles allow for contrast agents to be included at predetermined ratios either in the interior or on the surface (18). Although application of these particles for imaging purposes is relatively new, studies have shown promise (216). Portnoy et al. developed a new liposome-based near-infrared probe using ICG and the cetuximab monoclonal antibody for epidermal growth factor receptor (EGFR). Not only did the probe show selective binding to A431 colon carcinoma cells overexpressing EGFR, they also found that the ICG encapsulated liposomes exhibited a higher fluorescent signal and quantum yield than free ICG (221). Zhang et al. showed that inclusion of a liposomal nanodelivery system improved the targeting ability of their phosphotidylserine (PS)-targeted optical imaging probe, PGN-L-800CW, which contains NIR dye, (IRDye® 800CW) (222). Schroeder demonstrated the feasibility of targeting quantum dots entrapped in a lipid micelle to folate in mice bearing J6456-FR tumors which upregulate folate *in vivo* (218).

Although the specificity is high, to enhance the target to background signal ratio, a washout period must be observed before imaging to decrease the background fluorescent signal of the unbound fluorescent probes in the bloodstream. Often times this waiting period can be 24 hours or more (222). While this process can be easily achieved *in vitro* by washing out the unbound fluorescent probes in a dish, it is much more complicated *in vivo* and results in many unbound fluorophores contributing to the background signal.

5.1.4 Smart activatable probes function

An alternative strategy to improve the specificity and signal to background noise ratio (SNR) by reducing the background signal and maximizing the target signal is the use of smart or activatable molecular probes (223). Unlike the previous probes discussed which are “always on”, these probes are designed to "turned on" and emit a signal only after the probes have been specifically activated by a target. Consequently, activatable probes can attain high target-to-background signals as these probes in their original injected state are relatively undetectable. These probes are based on the controlled manipulation of the fluorescent dyes quantum yield causing the probes to switch from a weakly fluorescent state to strong emission after interacting with the intended target and undergoing a chemical reaction or structural conformational change (197, 224).

Weissleder et al. introduced the first activatable NIR probes for *in vivo* imaging of proteolytic enzyme activity in 1999 (38). Proteolytic enzymes represent an attractive target for cancer imaging as they are present in elevated levels in tumors (225). Their enzyme-activatable probes contained NIR fluorophore Cy5.5 conjugated to a macromolecular carrier (poly-lysine backbone) with multiple methoxypolyyethylene glycol polymers (PLL-MPEG) (38). The fluorescence of the probes is essentially undetectable in the quenched state due to the close proximity of the fluorophores to each other due to the polymer backbone. After the cleavage of the polymer backbone by proteolytic enzyme activity, the fluorophores are separated from the polymer backbone to restore the fluorescence emission. *In vivo* imaging demonstrated the high signal to background ratio yielding a 12-fold increase in NIRF signal after activation (38). Indeed, this has led to a number of activatable probes developed using enzyme activation of NIR fluorescent dyes mediated by tumor associated proteases such as cathepsins (cathepsin D), caspases and matrix metalloproteinas(MMP2) (195, 226-229). The high sensitivity and ability of activatable fluorescent probes to detect gene expression has much potential for early cancer diagnosis (230).

Activation can also occur from conformational changes due to environmental factors such as temperature or pH and oxygenation which has the potential to provide important functional information about the tumor microenvironment (219, 231-234). Fluorescent thermometers which use fluorescent probes to sense and non-invasively monitor intracellular temperature at the nanoscale have recently attracted much attention in biology and in addition has the potential to play a role in the diagnosis and treatment of cancer (235, 236). Thermal activation is achievable through temperature sensitive polymers such as polyNIPAM derivatives and poloxamers such as Pluronics (237). These polymers show reversible phase transition associated with temperature inducing a switch from hydrophilic behavior at low temperature to aggregation and formation of hydrophobic domains at high temperatures (238). Activation occurs when coupled to a polarity-sensitive fluorescent dye such as ICG or benzofurazan that strongly emitted fluorescence in hydrophobic environments (237). Uchiyama et al. demonstrated a 13.3 fold increase in fluorescence intensity from 29-37°C using the fluorophore benzofurazan and the copolymers of N-isopropylacrylamide (NIPAM)(239). Drs. Chen and Li demonstrated a 6x increase in fluorescent signal from 22 to 40°C using their thermal reversible fluorescent probe in the NIR window using the fluorophore ICG and thermal sensitive polymer Pluronic F-127(219).

The slightly acidic pH in the tumor microenvironment (pH<7.4) compared to healthy tissue (pH~7.4) is well known and has been well researched for anti-tumor therapy (240, 241). Activation by pH level is possible with the use of pH-sensitive dyes such as boron-dipyrromethene (BODIPY) and the near-infrared (NIR) fluorescent dye cyanine (Cy) to create a probe that is almost non-fluorescent in normal tissues but has a strong emittance in acidic pH environments (231, 232, 240). Urano et al. was one of the first to develop a targeted pH-activatable probe using BODIPY. They developed a series of acidic pH sensitive probes targeting the human epidermal growth factor receptor type 2 (HER2) with the monoclonal antibody trastuzumab that when absorbed in the acidic tumor extracellular space becomes protonated and emits a 500 nm signal over 300-fold greater intensity than the background (231). On the other hand, Lee et al. based their targeted activatable probe on the fluorescent dye Cy to create a NIR pH-activatable probe targeting αvβ3 integrin (ABIR), a protein that is highly overexpressed in endothelial cells during tumor angiogenesis (232).

Hypoxia is also a well-known characteristic of solid tumors and has not only been associated with tumor progression and metastasis, but also has implications for treatment and therapy as well (242, 243). Hypoxia is a result when tumor tissue lacks oxygen due to rapid tumor growth. As a result, imaging the low oxygen concentration in the tumor region could be of great significance. A number of studies have shown that phosphorescence quenches in the presence of oxygen and thus, can be used to directly detect oxygen in cells and tissues (244). The phosphorescence lifetime and intensity are inversely proportional to the oxygen concentration in the tissue sample (245). Phosphorescent probes including metalloporphyrin complexes and ruthenium and iridium complexes have shown promise as the low oxygen level in the tumors increases the signal intensity of the oxygen-sensitive activatable fluorescent probes (234, 240, 245, 246). Zhang et al. showed a novel red light emitting iridium complex $Ir(btp)_2(acac)$ (BTP) to detect hypoxia. The hypoxia-sensing probes were injected into five mice bearing five different cancer cells lines (CC-7, human glioma–derived U87, human lymphoma–derived RAMOS, human colon carcinoma–derived HT-29, and mouse lung cancer–derived LL-2), and *in vivo* results showed illumination of the tumors after a mere 5 minutes following injection of the probes (246).

These activatable probes represent an exciting new line of research as not only can they provide functional information about the tumor microenvironment, but many of these probes are reversible and thus have the potential to provide real time monitoring (223). In addition, activatable probes also have the potential for targeting thereby increasing their specificity and sensitivity in the detection of a disease.

5.2 Developments of ThermoDots

5.2.1 Introduction and Overview

This thesis focuses on the development of a novel multi-modality fluorescence tomography system that uses heat to quantitatively resolve the concentration of fluorescent probes with high resolution. In order to accomplish this, a heat-activatable NIR fluorescence probe had to be used. Recently, temperature-sensitive fluorescence contrast agent has been reported with use of ICG-loaded Pluronic micelles (134, 135, 219). As the temperature changes, the interiors of micelles change their hydrophobicity/hydrophilicity, which in turn induces a change in the solvent polarity thus resulting in a change in the quantum efficiency of the loaded ICG micelles (134, 219). The temperature dependence of these contrast agents provides a major opportunity to overcome the spatial resolution limitation of conventional fluorescence imaging by using temperature modulation. This chapter will describe the specially developed thermo-reversible activatable fluorescent probes developed for TM-FT named, ThermoDots. The ThermoDots are based on probes developed by Drs. Yongping Chen and Xingde Li from Johns Hopkins University and its activatable properties are dependent on two main ingredients: ICG and Pluronic polymers(134, 219).

5.2.2 Main components of ThermoDots

5.2.2.1 Fluorescent dye ICG

The first main component of the ThermoDots is the fluorophore Indocyanine Green (ICG). ICG is currently the only FDA approved NIR fluorophore for medical diagnosis and has many advantages for fluorescence tomography. The molecular chemical structure and fluorescence excitation and emission spectrum are shown in Figure 5.2. ICG is a polar molecule composed of two polycyclic parts (benzoindotricarbocyanin) connected by a carbon chain with a sulfate group bound to each polycyclic part. ICG has amphiphilic properties due to the lipophilic polycyclic parts and the hydrophilic sulfate groups (247). ICG has an excitation and emission wavelength of 780 nm and 830 nm in aqueous solution (248). In blood, ICG binds to plasma proteins such as albumin, globulins, and lipoproteins which redshifts absorption spectrum ~25 nm (249). It operates in the NIR region (700-900 nm) which offers several advantages over visible fluorophores including deeper tissue penetration, less autofluorescence, and larger Stoke shifts (250). The lifetime and quantum efficiency of ICG have been shown to be 0.56 ns and 0.016, respectively (85).

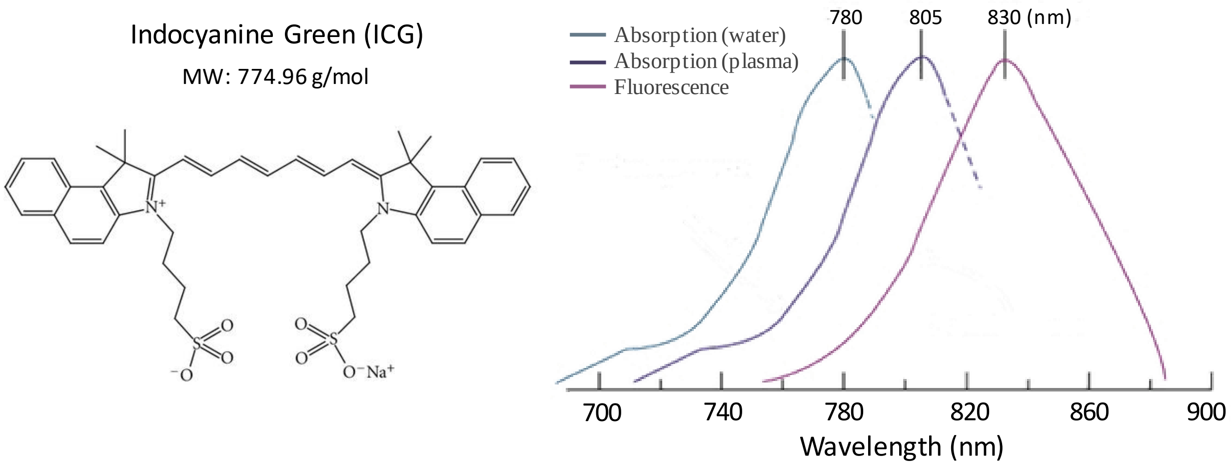

(a) (b)

Figure 5. 2 ICG. (a) Structure of Indocyanine green (ICG). (b) Normalized absorption and fluorescence spectrum of ICG showing the wavelength with the peak absorption of ICG in water (780 nm, green line) and plasma (805 nm, purple line). The peak fluorescence is at 830 nm (pink line). Figure is modified from Journal of Oncology, Vol 2012, Herranz, M. and Ruibal, A., Optical Imaging in Breast Cancer Diagnosis: The Next Evolution, Page No 863747. Copyright (2012) under the Creative Commons Attribution License (251).

ICG is the most widely used FDA approved NIR fluorophore and has an excellent safety record (199, 250). ICG of its own accord is non-specific and has shown promise for optical tumor detection (251). ICG can be used for cancer imaging to study tumor vascular permeability as it strongly binds to plasma proteins in the blood, behaving as a macromolecular contrast agent. ICG is also rapidly cleared from the circulatory system through the liver. A few human studies have demonstrated the feasibility of using ICG for tumor detection in breast cancer. Malignant tumors showed increased absorption due to ICG accumulation and slower rate constants (slower up-take, delayed peak and slower outflow) compared to healthy or benign tissue (101, 203, 252).

For imaging purposes, ICG delivery, accumulation, and retention in the tumor are crucial, however, its applications are limited due to its thermal, photo, and aqueous instability(253). Not only is ICG is amphiphilic and degrades in aqueous solution, it also has a tendency to aggregate and quench with high concentrations in solution leading to a lower fluorescence quantum yield. Therefore, the absorption properties of ICG which are dependent on concentration are not necessarily linear. In addition, ICG tends to degrade with exposure to light. The photo-degradation property is also concentration dependent. Furthermore, it has been reported that higher temperatures along with pH also play an important role in ICG degradation(253). Consequently, there has been much interest in the development of targeted or activatable probes to counteract the limited delivery, accumulation, and retention of ICG alone.

5.2.2.2 Pluronics: temperature dependent material

The second main component of the ThermoDots is the thermo-sensitive micelles made from Pluronic polymers. Pluronics is a commercially available poloxamer trademarked by BASF and are composed of a nonionic, triblock copolymer containing two poly(ethylene oxide) (PEO) blocks linked together by one poly(propylene oxide) (PPO) block, Figure 5.3.a. PEO has been well-studied as it is extremely hydrophilic and the simplest water soluble polymer (254). On the other hand, PPO is hydrophobic but water soluble at low temperatures and concentrations (255). However, it becomes less soluble with increasing temperatures and concentration, such that at ambient temperature, PPO is highly hydrophobic and does not dissolve in water. This amphiphilic nature of the Pluronics results in the formation of spherical micelles with a hydrophobic PPO core and hydrophilic PEO shell (256). This behavior is reversible. Thus, micelle formation is dependent on concentration of the Pluronics as well as temperature since PPO dissolves in water at low temperatures. The temperature and concentration at which micelles are formed are known as the critical micelle formation temperature (CMT) and the critical micelle formation concentration (CMC). Both CMC and CMT vary according to Pluronic type.

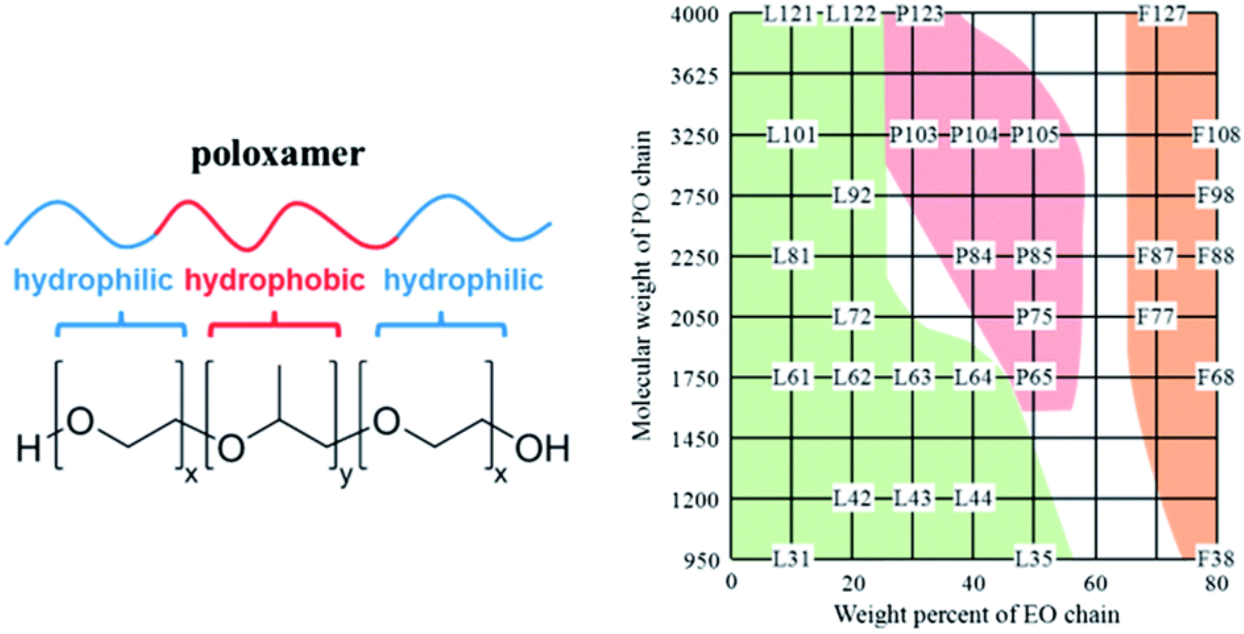

(a) (b)

Figure 5. 3 Poloxamers. (a) Molecular structure of a Pluronics triblock copolymer. (b) Pluronic grid (color code: physical state of copolymers under ambient conditions: green = liquid; red = paste; orange = flake). Reprinted from Polymer Chemistry, Vol 5 Issue 10, Pitto-Barry, A., & Barry, N. P., Pluronic® block-copolymers in medicine: from chemical and biological versatility to rationalisation and clinical advances, Page No 3291-3297. Copyright (2014) under the Creative Commons Attribution License. (257)

The lengths of the polymer blocks can be customized resulting in a variety of Pluronic types with different thermal properties, *in vivo* properties, and biological interactions with cells and cell membranes (257). Figure 5.3b shows the different Pluronic polymers manufactured by BASF. The nomenclature for these polymers consist of a letter indicating the morphism or phase of each copolymer (liquid (L), paste (P), and flake (F)) at room temperature, followed by one or two numbers indicating 1/300th of the molar mass of the PPO block per unimer. The last digit shows the percentage of PEO content per unimer. For example, Pluronic F-127 is solid at room temperature and has a PPO molecular mass of 3,600 g/mol and a 70% PEO content. The CMC and CMT decrease with an increase in the copolymer PPO content (258).

Poloxamers are an important class of surfactants and have widespread industrial and cosmetic applications (227). More recently, Pluronics have become popular in many areas of pharmaceutical research including drug delivery systems, biological response modifiers, and pharmaceutical ingredients (257). A growing number of studies have looked at Pluronic micelles to deliver drugs due to the hydrophobic core which can encapsulate hydrophobic agents and the surrounding hydrophilic shell that provides aqueous stability (259, 260). The first Pluronic micelle formulation to reach clinical trials contained doxorubicin encapsulated in the core of a mixture of Pluronic L61 and F127 micelles (121, 261). Other studies have shown promise using different combinations of Pluronic micelles and drugs (256, 259, 262, 263). The small size of the Pluronic nanoparticles (~10-100 nm) can provide longer circulation times by reducing clearance by the RES system and promote passive targeting to solid tumors through the EPR effect (256). Other advantages include inhibition of drug efflux transporters overcoming Multi Drug Resistance (MDR) and decreased drug interactions with cells and proteins (256, 262, 264, 265). In addition, the hydrophilic shell can be modified to target a specific biological feature which can allow for drugs to be loaded in high concentrations in the micelle for cancer therapy (259, 266).

Recently, pluronic nanoparticles have been gaining popularity in the field of fluorescent imaging by incorporating hydrophobic fluorescent contrast dyes. In particular, encapsulation of ICG in the Pluronic micelle core has shown much promise (134, 267). Indeed, encapsulation of ICG has been shown to provide increased stability, protection from nonspecific plasma protein binding, enhanced circulation times, and longer shelf-life (267). They can also be functionalized for active targeting and to prolong circulation time (267). In addition, not only are the polymeric nanoparticles promising delivery vehicles, they can also be activatable with the use of the thermo-sensitive Pluronic polymers. The thermal responsive behavior of the polymer is due to the change of hydrophobicity/hydrophilicity property as the temperature changes. ICG is also amphiphilic and its fluorescence yield is dependent on solvent polarity. As the temperature increases, the PPO blocks of the Pluronic polymer become more hydrophobic decreasing the size of the ICG encapsulated micelles and increasing the hydrophobicity within the micelle core (233). This in turn results in the enhancement of ICG fluorescence. This change in fluorescence is reversible and is the basis for the activatable thermos-reversible NIR fluorescent nanoprobes, ThermoDots, used in this study.

5.2.3 ThermoDots preparation

The ThermoDots were prepared by encapsulating ICG in Pluronic polymeric micelles by our industrial collaborator, InnoSense LLC (Torrance, CA). A solvent evaporation method was employed to encapsulate ICG into the micelles as seen in Figure 5.4. ICG was first complexed in chloroform with triethylamine (TEA) or Tetraoctylammonium bromide (TOAB) and incorporated drop-wise into the Pluronic micelle solution. The nanocapsules of Pluronic-ICG were then evaporated, isolated by centrifugation, and washed with deionized water (64). A small sample was used to characterize the ThermoDots solution to determine their activation temperature range. Then, the ThermoDots were stored in the dark and refrigerated at 4°C. They were kept in glass vials sealed with parafilm to prevent exposure to moisture from the environment and wrapped in aluminum foil to prevent light exposure.

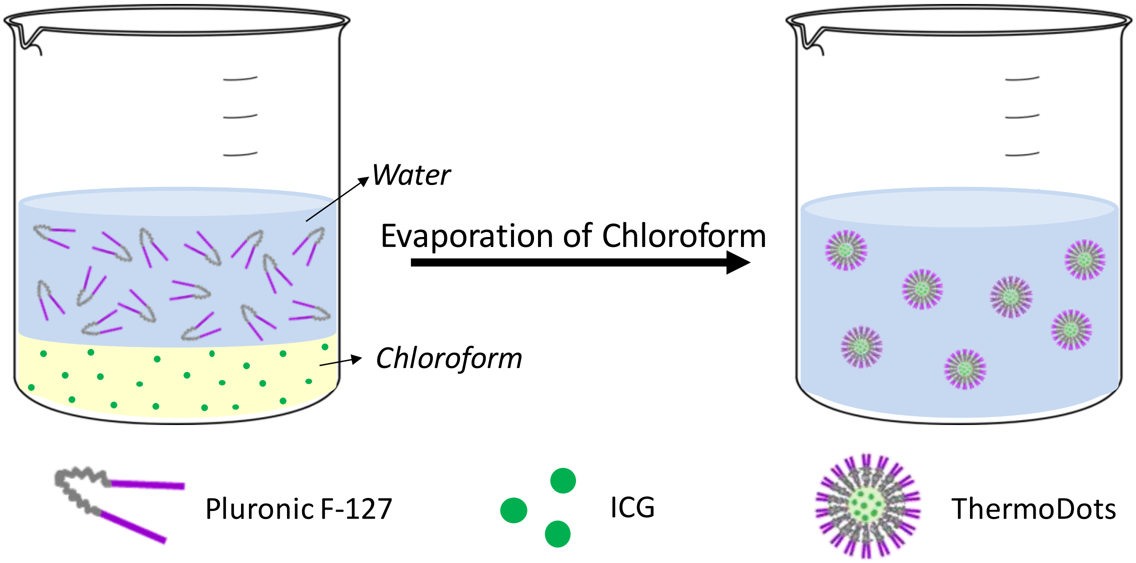

Figure 5. 4 Schematic illustration of solvent evaporation method used to engineer the ICG encapsulated Pluronic micelles.

5.3 Characterization and Optimization of ThermoDots

5.3.1 Introduction and overview

In this work, five different polaxamers were studied: F-127, F-68, F-88, F-108, and Po-237. Pluronic F-127 was mainly studied as it is FDA approved. Although the combination is not approved, choosing two materials (ICG, Pluronic F-127) which are FDA approved individually improves the likelihood of clinical transition in the future. With the overall goal being clinical translation, three different formulations of the ThermoDots were studied for phantom, animal, and future human applications.

5.3.2 Characterization

5.3.2.1 Characterization system

To characterize the ThermoDots, a frequency domain fluorescence system was constructed. The Thermodots were first characterized to determine their responsiveness in relation to temperature. For this process, the ThermoDots sample was heated and cooled in a controlled manner using two thermoelectric coolers (TEC). The change in fluorescence intensity and phase were recorded along with the temperature of the ThermoDots solution sample. A diagram of the customized temperature characterization system is shown in Figure 5.5a. A custom-made copper holder was used to hold the glass NMR tube (3mm diameter, 8 cm long). Two detector fibers were placed opposite of each other and at a 90° angle from the excitation source fiber as seen in Figure 5.5b. A fiber-optic temperature sensor (FTC-DIN-ST-GE, Photon Control, Inc. British Columbia, Canada) was inserted in the sample tube to monitor the sample temperature. The temperature of the sample was controlled by two TECs located beneath the copper holder. A heat sink was used to dissipate heat from the TECS. A maximum 3 A of current was provided to the TEC through a power supply.

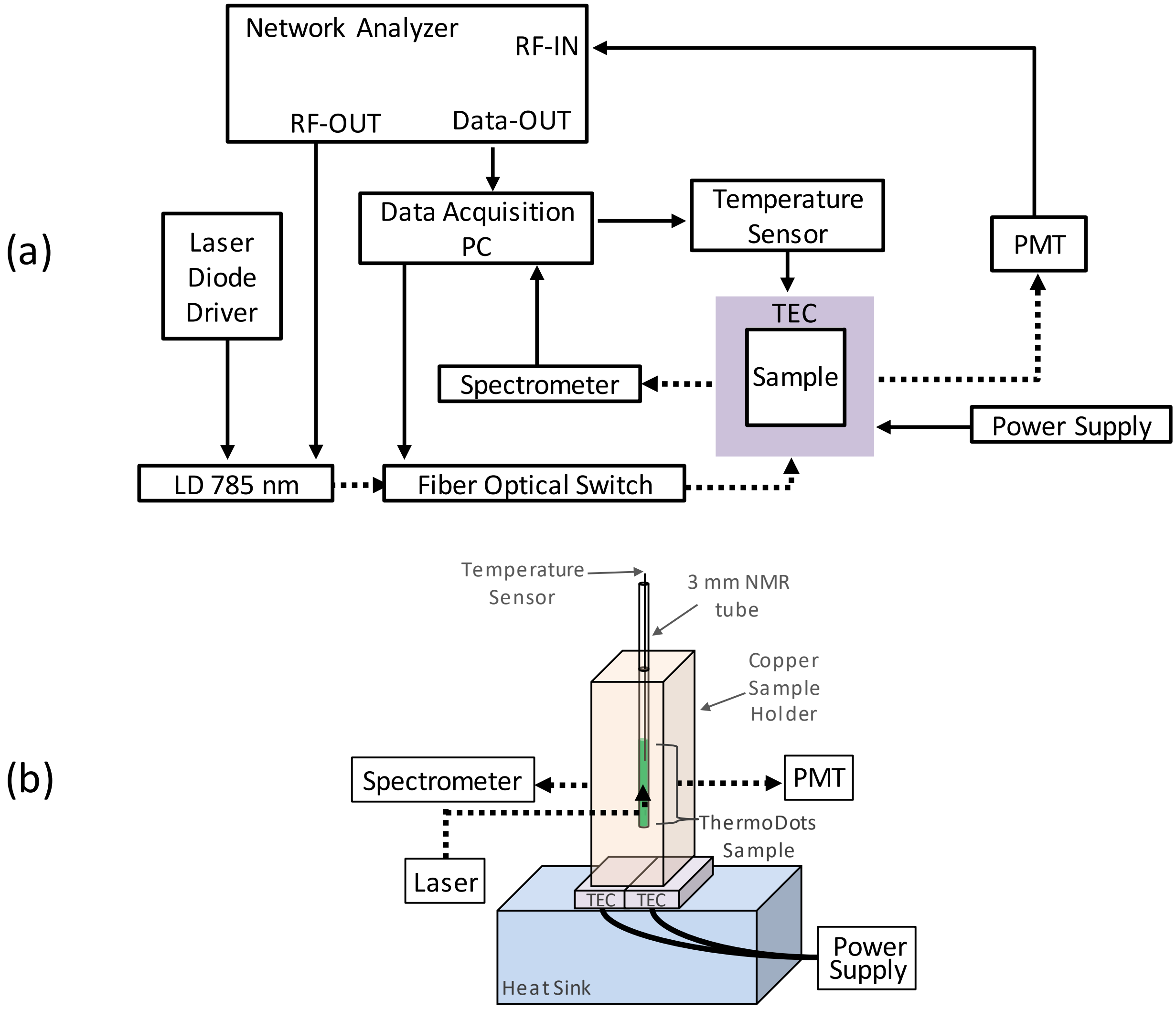

Figure 5. 5 ThermoDots characterization. (a) Schematic diagram of the frequency domain system to characterize ThermoDots dependence on temperature. The temperature dependent fluorescence is characterized with a spectrometer and PMT simultaneously. (b) Close up of customized sample holder including the copper sample holder whose temperature is controlled by two thermoelectric coolers (TEC). The laser enters the sample holder 90° from two fluorescence emissions fibers which are opposite of each other. A fiber optic temperature sensor is used to measure the sample agent temperature.

A 785-nm laser diode (300 mW, Thorlabs, Newton, New Jersey, USA) was utilized for fluorescence excitation, while a fiber optic switch was used to switch the laser on and off. A photomultiplier tube (PMT) and spectrometer (USB2000, Ocean Optics, Florida, USA) were used simultaneously for fluorescence light detection. More details on the PMT can be found in Chapter 6. A network analyzer (Agilent Technologies, Palo Alto, California) provides a 100 MHz RF signal for the laser-diode amplitude modulation and also measures the amplitude and phase of the detected fluorescence signal.

The changes in amplitude and phase indicate variations in fluorescence quantum efficiency and fluorescence lifetime, respectively. To characterize the thermos-responsiveness of the ThermoDots, the sample is heated slowly (1 degree/minute) until the fluorescence intensity plateaus. The measured temperature range is set to include a minimum of five degrees above and below the ThermoDots activatable temperature range. For the PMT detection, each fluorescence measurement is averaged three times and completed in 2 sec. The spectrometer has an integration time of 200 milliseconds and is averaged twice. The sample is characterized twice and averaged to ensure accuracy.

5.3.2.2 Fluorescence dependence on temperature

The ThermoDots were first characterized to determine their responsiveness in relation to temperature. The fluorescence signal dependence on local temperature is shown in Figure 5.6 using a ThermoDots formulation of 4% Pluronic F-127 micelle/20 μM. As indicated by the increased ICG fluorescence yield, the fluorescence signal amplitude increases about 31 dBm (intensity increases ~36 times) as the temperature is elevated by only 4°C from 18-22°C indicating an increased ICG fluorescence quantum yield. At the same time, the phase decreases about 31 degrees indicating an increased ICG lifetime. These results agree with previously published studies on the dependence of fluorescence quantum efficiency and lifetime to solvent polarity (81, 84). With increased temperatures, the interior of the micelles becomes more hydrophobic, resulting in an increase in both fluorescence quantum efficiency and lifetime. For both phase and amplitude, outside of the activation temperature range/CMT (18-22°C) the signal plateaus as the hydrophobicity of the micelle core is not changing.

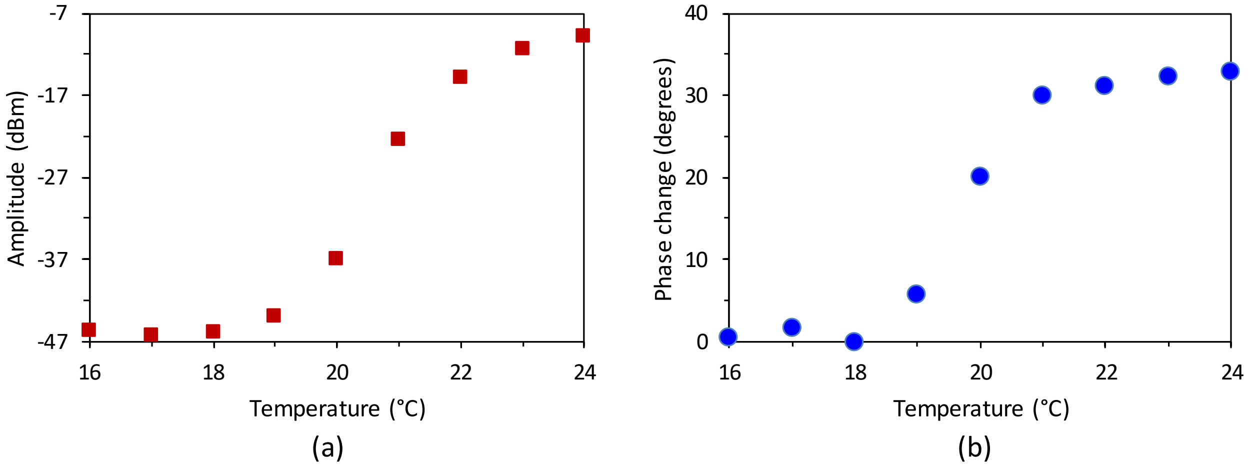

Figure 5. 6 Temperature response of 4% Pluronic F-127/20 μM ICG ThermoDot formulation. Network analyzer measurements of the amplitude and phase change of the fluorescence signal as the temperature of the sample is increased form 16-24°C. The temperature is measured using a fiber optical temperature sensor.

5.3.2.3 Red-Shift Spectrum

The fluorescence spectra of free ICG was compared to 4% Pluronic F127/20 μM ICG ThermoDots at different temperatures. A concentration of 5 μM free ICG was used for comparison as ICG is known to self-quench at higher concentrations in aqueous solution (268). As seen in Figure 5.7, a red-shift was observed for the emission spectra of the ICG encapsulated micelles compared to the free ICG. The extent to which the peak ThermoDots fluorescence signal was red-shifted increased with temperature as an 8 nm red-shift was observed when the ThermoDots were in their activated state (25°C). In general, the enhanced fluorescent signal of the ICG encapsulated Pluronic F127 micelles has been attributed to the increased fluorescence quantum efficiency which in turn, for amphiphilic dyes, depend on the solvent polarity (233). An increase in the fluorescence emission spectrum was also observed for increased temperatures indicating a more hydrophobic environment.

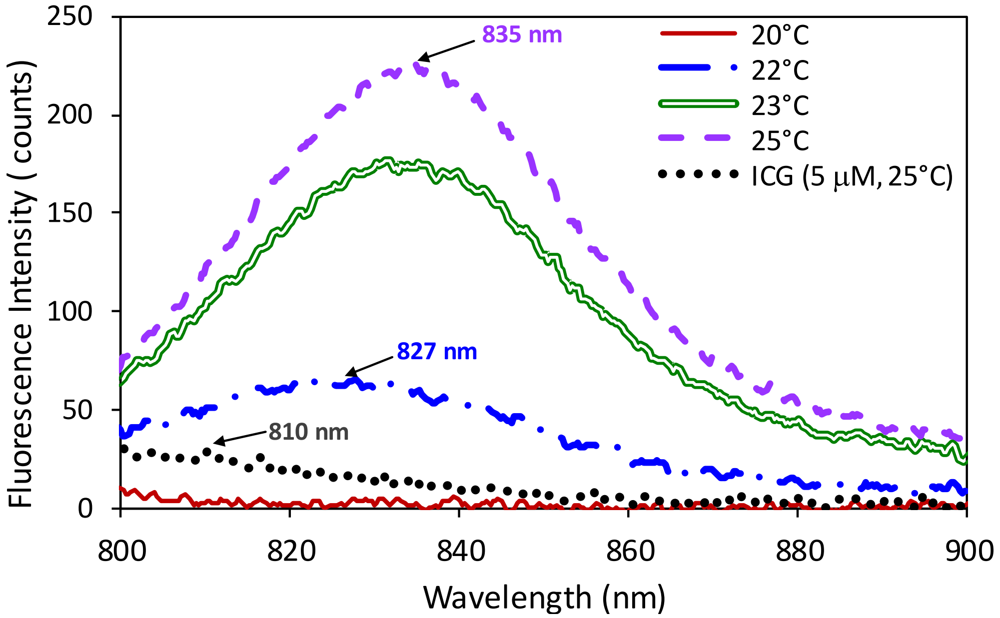

Figure 5. 7 Red-shift of ThermoDots. Emission spectrum of free ICG (5 µM, 25°C) and ThermoDots (4% Pluronic F127/ 20µM ICG) plotted at different temperatures in the activation range (20-25°C). The small red shift of the peak fluorescence was observed with increasing temperatures and highlighted by the arrows.

5.3.2.4 Reversibility

In addition, the ThermoDots fluorescence response to local temperature is reversible. A study was performed using the characterization system set up described above. Two TECs were used to modulate the temperature which was measured by a fiber optic temperature probe. A spectrometer was used to record the fluorescence signal. During each cycle of the temperature modulation, the ThermoDots were held at thermal equilibrium at each temperature (20, 22, and 25°C) for 3 minutes. The ThermoDots used in this study contain 2% Pluronic F-127/20 μM ICG and have an activation range from 20-25°C. Figure 5.8 shows the reversibility and repeatability of the ThermoDots fluorescence response to temperature. This reversible behavior is consistent with other studies (233). This reversible change is a result of the encapsulated ICG response to the changing hydrophobic/hydrophilic environment in the Pluronic micelle core with temperature. The fluorescence response was very repeatable at the endpoints at 36.5 ± 2.8 counts at 20°C and 1137.0 ± 16.3 counts at 25°C. However, inside the activation temperature range, there was a slight difference in the ThermoDots fluorescence response to increasing and decreasing temperatures. Thus, as the agents are being developed for TM-FT, the ThermoDots response to temperature is characterized for heating.

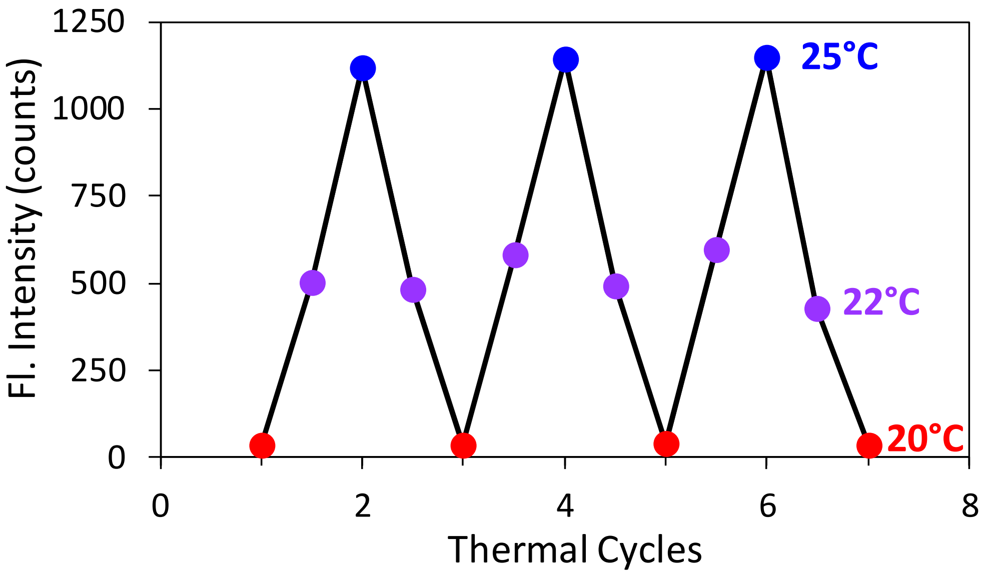

Figure 5. 8 Reversible response of the ThermoDots fluorescence response to temperature. The ThermoDots were held at thermal equilibrium for 3 minutes at each degree plotted. The fluorescence response is consistent at the endpoint of the thermal cycle but shows a slight difference when in the heating and cooling phase.

5.3.2.5 Size (DLS)

The size and the temperature dependent swelling/shrinking behavior of the ThermoDots were characterized by dynamic light scattering (DLS). Above the CMT, the size of the Pluronic micelles are expected to shrink due to increasing hydrophobicity of the Pluronic PPO block with temperature. This thermosensitive size behavior of the ThermoDots can be seen in Figure 5.9 where the size and the fluorescence intensity of ThermoDots consisting of 0.8% Pluronic F-127 and 20 μM ICG were measured with increasing temperatures. DLS measurements were performed at different temperatures using a Brookhaven instrument (Brookhaven, NY) at a 632.8 nm wavelength with the help of Dr. Sumi Lee from the Dr. Jered Haun lab at UCI. Figure 5.9a shows the sensitivity of the ThermoDots size to changing temperatures as the diameter of the ThermoDots drastically decreased almost 17-fold from 27-31°C. The average sizes of the ThermoDots at 27, 28, 29, 30, and 31°C were 158.05 ± 27.41 nm, 150.80 ± 27.74, 100.93 ± 15.02, 75.17 ± 17.751, and 9.541 ± 0.6329 nm, respectively. Above and below the activation temperature range (27-31°C), the size of the ThermoDots remained stable. The small size of the ThermoDots is optimal to passive or actively target tumor as the ThermoDots are much smaller than 400-600 nm which is the reported maximum pore size cutoff in tumors (269). This allows room for possible further modifications to the ThermoDots such as a PEG layer for enhanced circulation and targeting ligands. Figure 5.9b shows the corresponding increase in fluorescence intensity for the active temperature range. As mentioned by Chen et al., a unique property of the Pluronic micelles is the fact that the core becomes increasing hydrophobic as the size decreases when the temperature is increased (233). This in turn results in enhanced fluorescent signal for the encapsulated ICG (233).

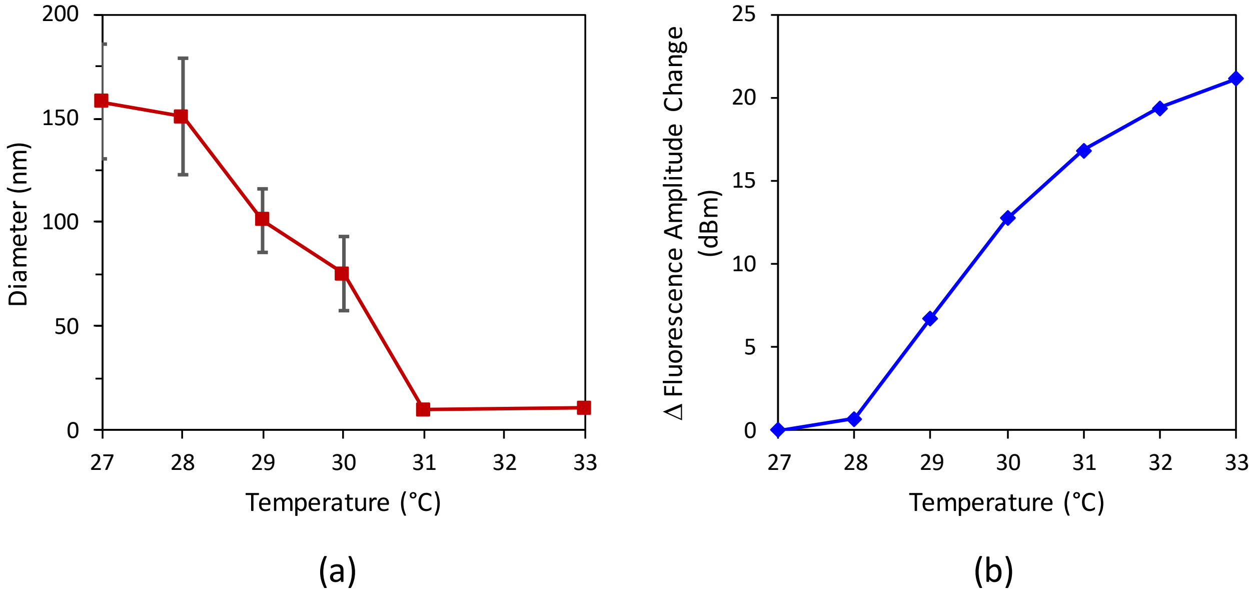

Figure 5. 9 ThermoDots size response to temperature. (a) Size of ThermoDots (0.8% Pluronic F-127/20 μM ICG) measured by DLS and (b) corresponding fluorescence signal intensity change from 27-33°C.

5.3.2.6 Stability and Shelf-life of ThermoDots

The shelf life of ICG alone in aqueous media consist of ~6 hours before degradation can be seen in the fluorescence quantum efficiency (270). Indeed, Saxena et al. found that the degradation half-life of ICG in aqueous solution, in the dark at room temperature, is 16.8 ± 1.5 hrs (271). This greatly limits the preclinical and clinical applications for ICG. In the presence of water, ICG degrades to form leucoforms, however, encapsulation of ICG inside the hydrophobic region of the micelle has been shown to have a stabilizing effect (219, 271). As seen in Figure 5.10, the peak fluorescence intensity of the ThermoDots (Pluronic F-127, 0.5% TOAB, and 20 μM ICG) at 830 nm remained stable with only a slight degradation in fluorescence signal for a minimum of 3 weeks when stored in a sealed glass vial at 4°C in the refrigerator and covered with aluminum foil to prevent any exposure to light. For comparison, the degradation half-life of free ICG is shown by the blue dashed line. Further studies with different type and concentrations of Pluronics as well as ICG concentration have also shown increased stability. The average "shelf-life" of the different Pluronic solutions varied between 1-3 weeks depending on the type and concertation of Pluronic micelle. This is consistent with other literature studies which reported little effect on the ICG stability when varying ICG concentration compared to varying the type and concentration of Pluronic (219, 253). Furthermore, Kim et al. reported increasing ICG micelles solution stability with higher concentration of Pluronic F-127 (219).

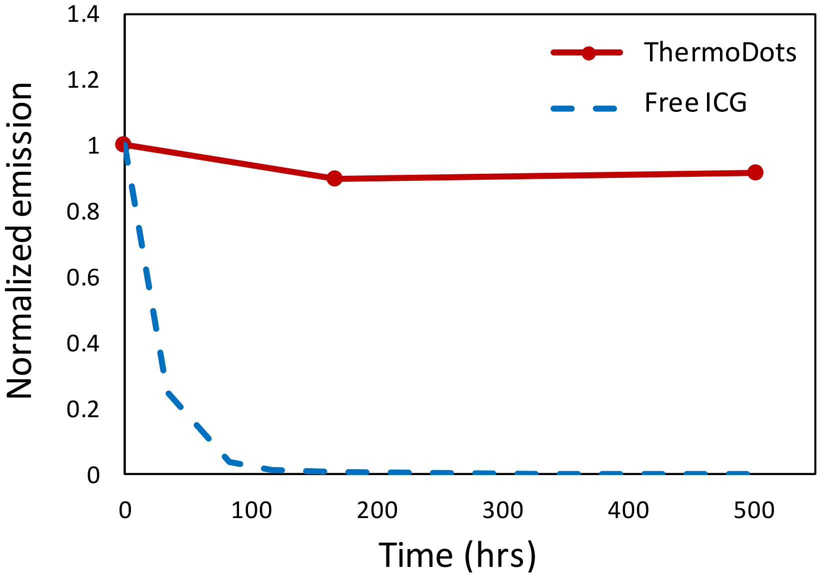

Figure 5. 10 Fluorescence stability of ThermoDots. Relative fluorescence emission of ThermoDots (red solid line) over 3 weeks at room temperature. The degradation half-life of free ICG is shown by the blue dashed lines.

While the fluorescent signal intensity is important for most imaging contrast agents, for the ThermoDots, the key feature is their response to temperature resulting in a drastic increase in signal with increasing temperature. Therefore, the shelf-life of the ThermoDots mainly relies on whether the ThermoDots are activatable. The change in the fluorescence signal was studied to determine whether the amount of time the ThermoDots are activatable. The change in fluorescent signal is equal to the ratio of fluorescence signal at temperature 2 (T2) divided by the fluorescent signal at temperature 1 (T1), (fluorescence signal change=F_{T2}/F_{T1}). Four different Pluronic solutions were plotted below, Figure 5.11. Part (a) shows three different concentration of Pluronic F-127 micelle solutions using TOAB as a solvent. The activation temperature range is unique for different concentration and formulations of ThermoDots. The maximum change occurs when the ThermoDots are first made and shows a decrease in signal over 3-4 weeks. A larger increase in fluorescent signal is also seen for larger concentrations of Pluronic F-127. Figure 5.11b shows the change in fluorescent signal for 2% Pluronic F-127/20 μM ICG using TEA as a solvent from 20-25°C compared to free ICG. Although a decrease in the maximum fluorescence signal change over time, this batch of ThermoDots exhibited remarkable stability and longevity, remaining active for 59 weeks.

These stability results show that the ThermoDots are more stable than ICG. Compared to ICG which must be used within hours, the shelf-life of the ThermoDots are on the order of weeks, up to a year, making it more feasible for future clinical transition.

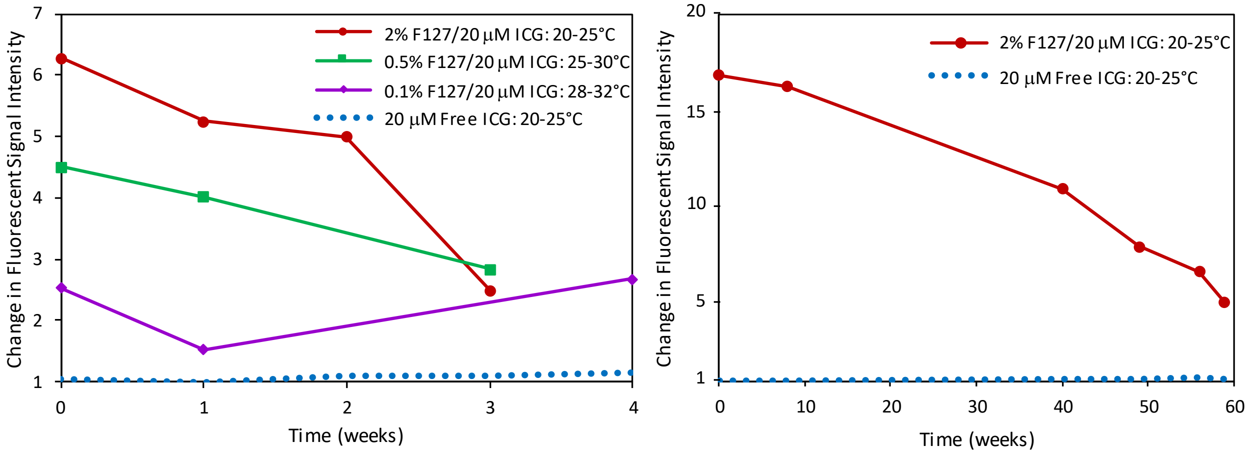

(a) (b)

Figure 5. 11 ThermoDots activation shelf-life. Relative change in fluorescence emission of the ThermoDots over time for different concentrations of Pluronic F127/20 µM ICG solutions. The change corresponds to the ratio between the fluorescence signal intensity at the endpoints of the active temperature range: F_{temp2}/F_{temp1}. (a) The change in fluorescence signal for three different concentrations of ICG encapsulated Pluronic solutions using TOAB as a solvent are shown: 2% (20-25°C, red line), 0.5% (25-30°C, green), and 0.1% (28-32°C, purple) were plotted over time. The change in fluorescence for 20 µM free ICG from 20-25°C is shown by the blue dotted line. (b) Ratio of 2% Pluronic F127/20 µM ICG with TEA as a solvent (red solid line) and 20 µM free ICG (blue dotted line) at 25°C versus 20°C over time. This agent remained activatable for a record 59 weeks.

5.3.3 Temperature and fluorescence signal optimization

5.3.3.1 Introduction

After the ThermoDots were shown to be stable and exhibit the characteristic temperature dependent fluorescence signal for TM-FT, the ThermoDots were optimized and developed for small animal and human imaging. The ultimate goal of TM-FT is for *in vivo* human imaging, and thus, an attempt was made to see whether ThermoDots could be made for this temperature range. Overall, three different formulations of the ThermoDots were developed for phantom, small animal, and human studies. This involved maximizing the fluorescence signal change and optimizing the activation temperature range for their specified application. For convenience, the phantom formulation was designed to work with room temperature (20-25°C). The small animal version (mice and rat) ideal temperature range is between 30-37°C which is within the temperature window (27-41°C) to avoid detrimental effects of hypothermia and hyperthermia (272). In general, other studies have also shown lowering the body temperature of these hardy animals to be beneficial and a means to protect the brain, heart, and other organs when subjected hypoxia and ischaemia (273). For the *in vivo* human formulation, the target activation temperature lies between 35-41°C to avoid moderate hypothermia and tissue damage. Different methods were studied to optimized the fluorescence change and shift the activation temperature.

5.3.3.2 Concentration

The concentration of the Pluronic micelles greatly affects the activation temperature range as seen in Figure 5.12.a. In this study, eight different formulations of ThermoDots containing the same ICG concentration (20 μM) but different concentrations of Plutonic F127 micelles were compared at different temperatures to study how the concentration of Pluronic F-127 micelles affects the activation temperature and fluorescence. From Figure 5.12a, lowering the concentration of the Pluronic micelles shifts the activation temperature range to higher temperatures. It can also be seen that the max fluorescence signal increases with larger concentrations of Pluronic F-127 and begins to plateau after 2%. Figure 5.12b shows the change in the fluorescence signal from a four-degree temperature increase in the activation range for different concentrations of Pluronic F-127 micelles. A trend was observed as the amplitude of the fluorescence change increased with larger concentrations of Pluronic F-127 with the exception of the 7% concentration. The 7% Pluronic F-127 concentration formulation exhibits a high fluorescence signal in the inactivated and activated state. In Figure 5.12b, unlike the other seven formulations, the 7% exhibits a fluorescence signal brighter than the ICG control which has a concentration of 5 μM in the inactivated state. This high minimum fluorescence signal results in a smaller change in fluorescence.

These results show that the ThermoDots can be tuned to different temperature ranges, however, shifting the activation temperature to *in vivo* ranges leads to a smaller fluorescence change and lower peak fluorescence signal. In addition, the effect that the ICG concentration has on the activation temperature and fluorescence was also studied. Unlike Pluronic micelle concentration, ICG concentration did not greatly affect the activation temperature range. The fluorescence change was maximized for ICG concentrations (~20-30 μM) but exhibited a decreased above and below this optimal range. The peak fluorescence signal also followed the same trend.

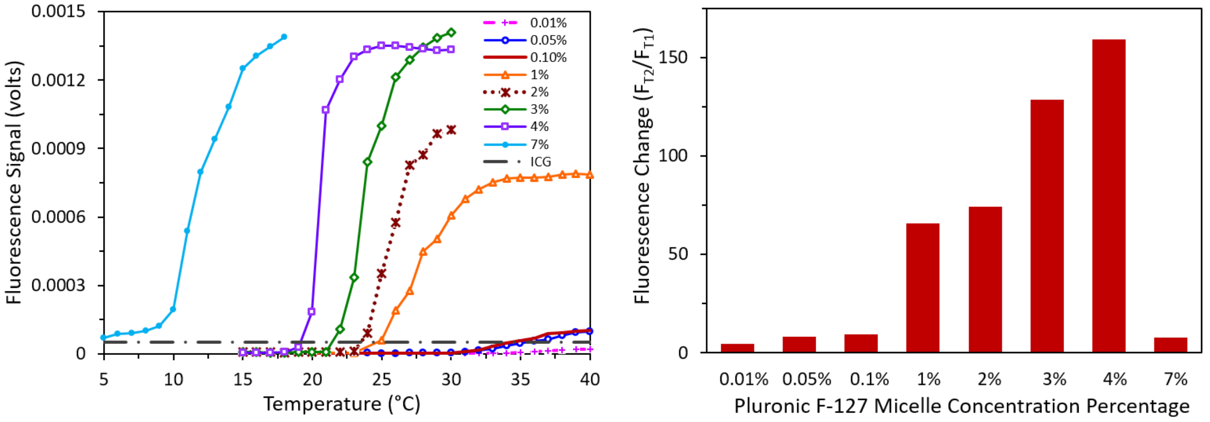

(a) (b)

Figure 5. 12 Pluronic F-127 micelle concentration effect on fluorescence change and activation temperature range. (a) The fluorescence signal (volts) of eight concentrations of Pluronic F-127 micelles (0.01%, 0.05%, 0.1%, 1%, 2%, 3%, 4%, 7%) with 20 μM ICG were plotted against temperature (°C). Lower Pluronic F-127 micelle concentrations showed a higher activation temperature but lower fluorescence change. (b) Max fluorescence change for four degree increase in temperature over the eight different concentrations of Pluronic F-127 micelle.

5.3.3.3 Polaxamer Material

Although decreasing the concentration of the Pluronic F-127 micelle was found to shift the activation temperature of the F-127 ThermoDots towards the *in vivo* biological temperature window, the agents were not stable and exhibited a limited fluorescence signal change. Therefore, other polymers were investigated to shift the activation temperature range of the ThermoDots to small animal and human *in vivo* temperatures. Pluronic F-108 showed much promise for small animal temperatures exhibiting a 17 times increase from 30-34°C and nearly a 50 times increase in fluorescent signal over the activation temperature range from 30-37°C. Two other polymers, Pluronic F-88 and polaxamer Po-237, also showed potential for human *in vivo* temperatures. Figure 5.13 shows an 8x change for 1% Po-237/20μM ICG while a 18x change in fluorescent signal was seen for 1.7% F88/20 μM ICG from 35-41°C. These results show that *in vivo* optimized temperature ranges can be achieved with high signal temperature.

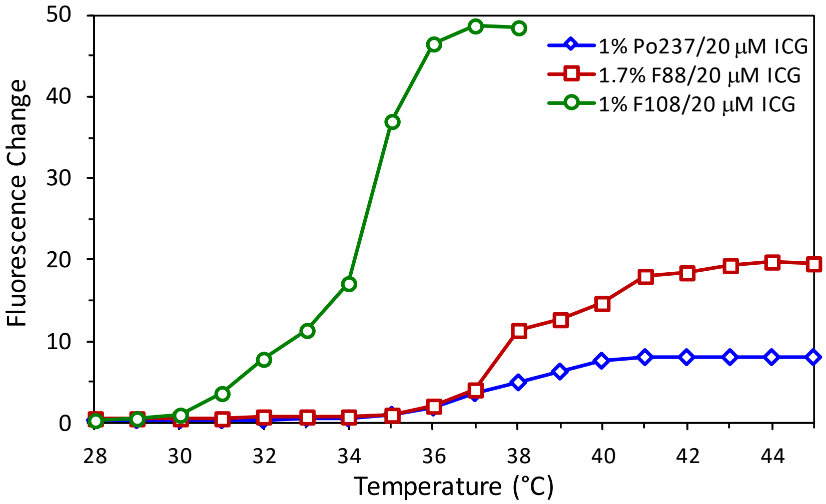

Figure 5. 13 Effect of ThermoDots composition on activation temperature range. Fluorescence intensity change in response to temperature for 1% concentration F108 (green, circle marker) and *in vivo* optimized 1% concentration Poloxamar 237 (blue, diamond marker) and 1.7% concentration Pluronic F88 (red, square marker).

5.4 *In vivo* animal studies

5.4.1 Introduction and overview

Due to the complex biology of humans and animals, a fluorescent agent that shows a certain type of behavior in the laboratory may exhibit a completely different behavior *in vivo*. In addition, biological interactions and reactions, such how a certain drug or dye is metabolized or binds to plasma proteins, require *in vivo* studies. Thus, an important aspect of the ThermoDots is understanding how the agents behave *in vivo*. Namely, how do they distribute through the body, whether they display the required temperature dependent behavior, and whether they are safe for animals. In this section, several *in vivo* studies were performed to investigate these unknown variables.

All animal procedures in this section were approved by the Institutional Animal Care and Use Committee at University of California, Irvine. A combination of mice and rats were used in these studies. Prior to imaging, the animal is shaven to remove hair around the imaging area. Anesthesia was performed using Ketamine (0.17 ml per 200 g rat) through an intraperitoneal (i.p) injection. After the experiment, the animal is placed on the electronic heating pad to conserve its body temperature and prevent hyperthermia complication during recovery.

5.4.2 In vivo bio-distribution studies

In these bio-distribution studies, the ThermoDots were investigated to gain insight on how the ThermoDots distribute in the body and shed light on their potential use for *in* *vivo* TM-FT. The *in vivo* pharmacokinetics and bio-distribution of several ThermoDots formulations were studied and compared to ICG which is the only FDA-approved NIR fluorescent dye.

Once the agents were characterized and optimized, a 1 mL solution of the various ThermoDots solutions were injected intravenously through the tail vein of a Fisher rat bearing breast cancer tumor models. Five to six weeks old Fisher rats with 180 g average weight were used in this study. The pharmacokinetics of the rat injected with the ThermoDots was performed using a custom designed system featuring a cooled charge-coupled device (CCD) camera (Perkin Elmer, Cold Blue, Massachusetts) for detection coupled with a macro-lens focused at the object. A 785-nm laser diode (80mW, Thorlabs, Newton, New Jersey) along with an 800 nm bandpass filter was used to excite the fluorophore and clean up the excitation signal. Images were acquired sequentially with a 30 second integration time in a dynamic fashion to study the pharmacokinetics of the ThermoDots.

Immediately following the tail vein injection of a 4% F127 ThermoDots solution, a high fluorescent signal is seen concentrated in the tumor after 1 minute, Figure 5.14(a). However, as seen from the images, the ThermoDots are not only present in the tumor but in the surrounding tissue due to unspecific uptake. Following images show a decrease in fluorescent signal indicating the removal of ThermoDots from the circulatory system within 10 minutes. Figure 5.15. shows the pharmacokinetics of 4% F127 ThermoDots are very similar to ICG. Both fluorescent agents show a diffusion in the tumors where they accumulate for a short time before being cleared out steadily afterwards.

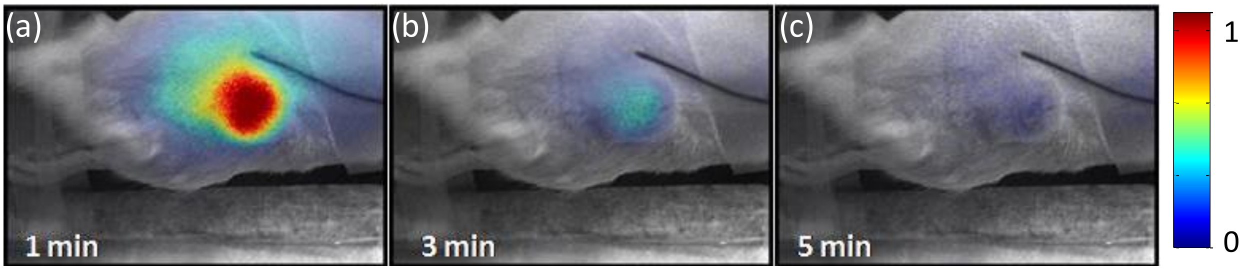

Figure 5. 14 Pharmacokinetics of ThermoDots *in vivo*. Time-lapsed fluorescent images of PEG layer coated 4% F127 ThermoDots injected to a tumor bearing rat (b)1 minute, (c) 3 minute, and (d) 5 minute after ThermoDots injection. Fluorescence images are acquired every 30 seconds and superimposed on the anatomic image acquired under room light. The fluorescent ThermoDots accumulated in the tumor very quickly (~1min) and are rapidly cleared out by the liver. A temperature probe was used to monitor the temperature of the rat.

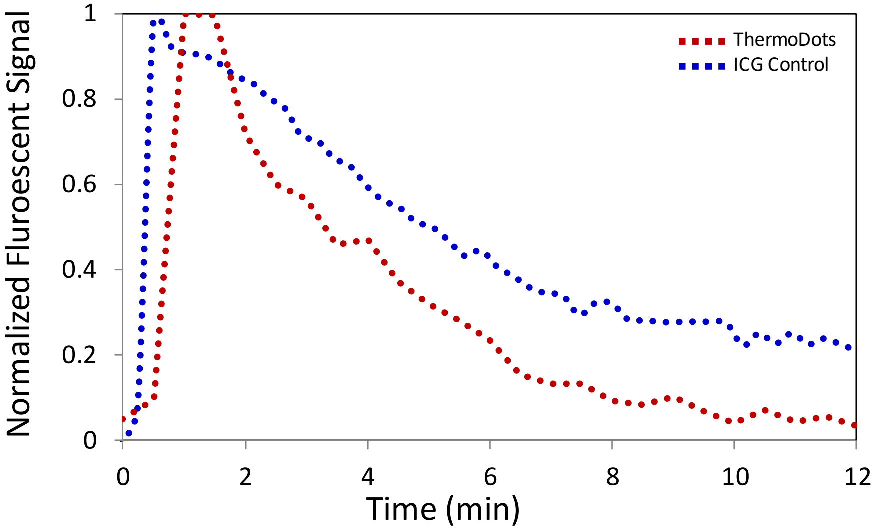

Figure 5. 15 Graph of pharmacokinetics of 4% F127 ThermoDots (red line) injected to a tumor bearing rat comparing normalized fluorescent signal with time (minutes) compared to FDA approved ICG (blue line). Just like ICG, the agents wash in to the tumor due to leaky tumor vessels just after the injection but wash out in approximately 10 minutes due to extraction from the blood circulation by the kidney and liver.

Figure 5.16 shows the pharmacokinetics of four ThermoDots formulations. The ThermoDots wash in to the tumor due to leaky tumor vessels just after the injection but wash out in approximately 10 minutes due to extraction from the blood circulation by the kidney and liver. As expected, all ThermoDots formulations show similar pharmacokinetics to FDA approved ICG.

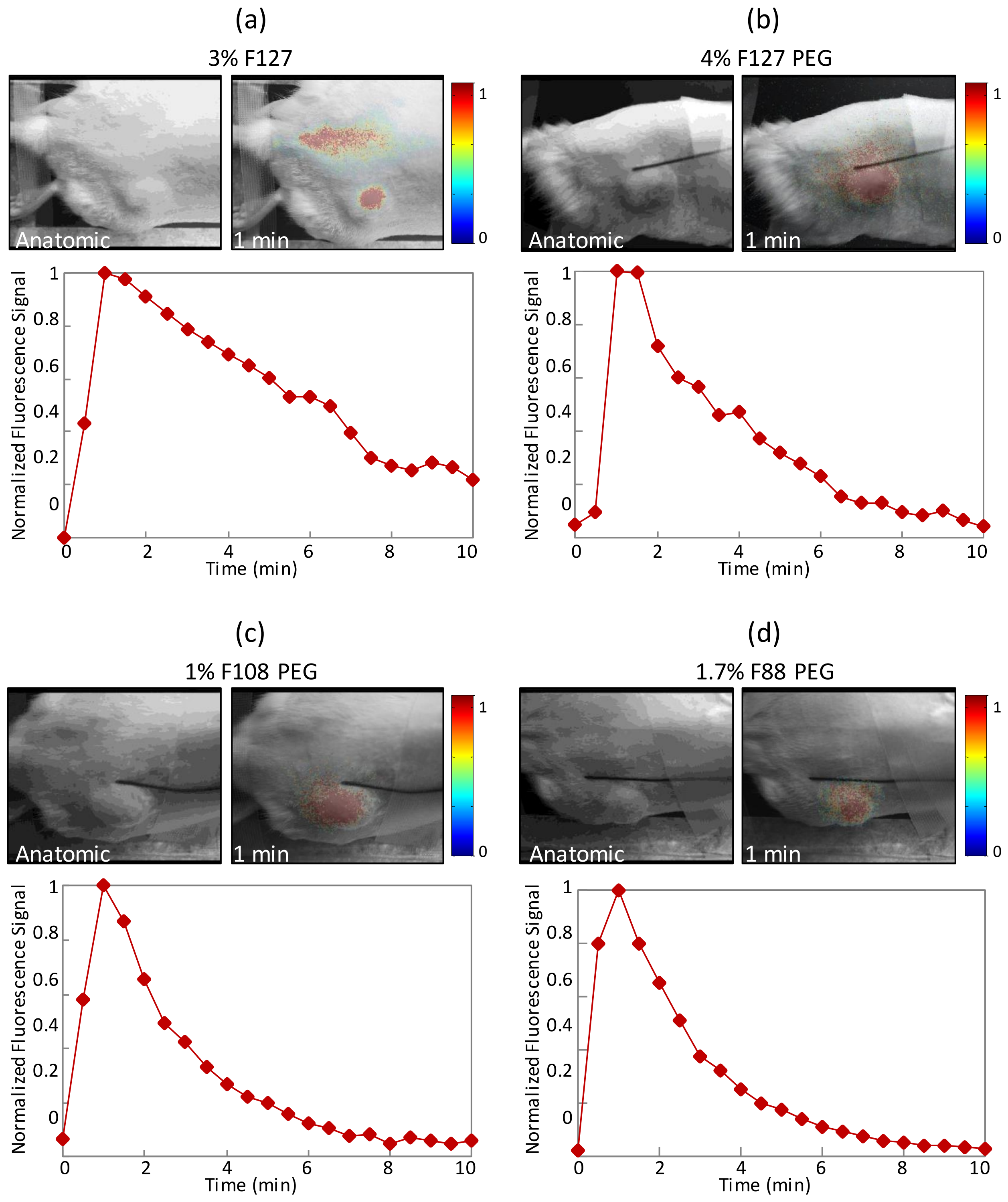

Figure 5. 16 The pharmacokinetics of four versions of ThermoDots including (a) one of the first version of the agents 3% F127 with 30μM ICG, and three optimized and PEGlyated ThermoDot formulations: (b) 4% F127, (c) 1% F108, and (d) 1.7% F88. Fluorescence images are acquired every 30 seconds and superimposed on the anatomic image acquired under room light. Fluorescent image shown is at 1 min, or max intensity. The plot shows the fluorescence intensity in the tumor during

the study. The agents wash in to the tumor due to leaky tumor vessels just after the injection but wash out in approximately 10 minutes due to extraction from the blood circulation by the kidney and liver.

As seen in the previous figures, the ThermoDots accumulate in the tumor and quickly wash out in 10 minutes, however, when imaging was performed 24 hours later, traces of the agent were found only in the tumor as seen in Figure 5.17. The image acquired 24-hours after the injection reveals that ThermoDots are still present in the tumor but in very low amounts due to the impaired lymphatic drainage from the EPR effect. The CCD camera settings were changed due to the low levels of light. The integration time was increased from 30 s to 2 min and the gain was increased 5x. Thus, the fluorescent signal in image Figure 5.17b is 20x lower than part (a). Since the concentration of the ThermoDots is much lower after 24 hours, it is hard to utilize them for imaging using EPR effect.

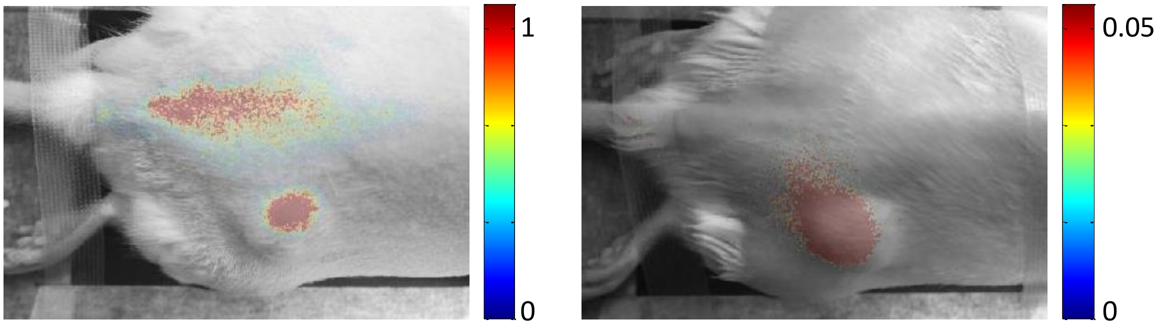

(a) (b)

Figure 5. 17 24 hour comparison of ThermoDots signal. Comparison of images immediately taken after 3% F127 ThermoDots injection versus image taken next day. Normalized fluorescent image overlaid on an anatomical image taken: a) 1 minute after injection with 30 second integration time, and b) 24 hours after injection with 2-minute integration time. The color bars show the normalized fluorescent signal intensity which indicate a 20x higher signal in image (a).

Once in the circulatory system, the ThermoDots are expected to behave very similar to ICG. Due to the enhanced permeability of cancer blood vessels, the ThermoDots are expected to leak into extravascular space in the tumor due to their small size, 10-20 nm, through the enhanced permeability and retention (EPR) effect (233). Here, they are expected to accumulate in the tumor during this diffusion process but clear out rapidly through the liver. *In vivo* studies using initial ThermoDots versions confirmed this result based on their enhancement kinetics, Figures 5.14-5.16.

Although the untargeted Thermodots accumulates in the tumor with high contrast, they also show uptake in surrounding tissue. In addition, after 1 min, the ThermoDots are quickly cleared from the tumor and circulatory system and thus the agent concentration, and hence, fluorescent signal levels are very low, Figure 5.14. Therefore, in order for the ICG-loaded micelles to be viable for *in vivo* TM-FT studies, the ThermoDots need to be optimized to improve the retention time and concentration of ThermoDots inside the tumor. Targeting the ThermoDots to the tumor could solve these problems by binding the micelles of the ThermoDots to tumor receptors thus increasing the accumulation and retention time of the ThermoDots in the tumor. This will provide higher signal and lead to fast imaging, which will allow utilization of them for the TM-FT technique. EGFR- and PSMA- targeted ThermoDots which are expected to accumulate in the tumor with much higher concentration are discussed in section 5.5.

5.4.3 In vivo Temperature dependence

As seen in the previous section, the low concentration and rapid clearance of the ThermoDots from the tumor are not optimal to test the thermos-responsive behavior of the ThermoDots *in vivo*. The ThermoDots do not stay in the tumor long enough to measure the difference in fluorescence signal due to temperature. However, in this special case where the

ThermoDots collected and stayed in the body of the mouse, the thermos-responsive behavior of the ThermoDots could be seen *in vivo*.

For this study, Pluronic-F127 ICG-loaded micelles (150 μL) were injected intravenously through the tail vein of a 7-8 week old balb/c mouse bearing 4T1 cancer tumor model at a dose of 10 μg ICG. To achieve prolonged plasma circulation, a second dose was injected 30 min after the first dose of ICG-loaded micelles. Imaging was performed on the same system described in the previous section, 4.4.2. Data analysis was performed using ImageJ and MATLAB. A heating pad was placed beneath the mouse and turned on 12 minutes after the second injection. Prior to heating, the external temperature of the mouse was close to room temperature at 22°C and was increased to 27 °C with the heating pad. A fiber-optic temperature sensor (FTC-DIN-ST-GE, Photon Control, Inc. BC, Canada) was fixed next to the tumor and used to monitor the external temperature of the mouse as seen in Figure 5.18 a.

Figure 5.18 (a) and (b) shows the pharmacokinetics of the ICG-loaded micelles following the second injection. As expected, the ThermoDots diffuse into the tumor due to the leaky vasculature from the EPR effect, and begin clearing from the tumor within 2 minutes. However, unlike the previous cases where all the ICG-loaded micelles were completely cleared from the tumor, a large portion of the micelles stayed in the body as seen by the high fluorescent signal immediately above the tail in Figure 5.18a. As seen in Figure 5.18b, the normalized fluorescent signal stabilizes around 8 minutes after injection. This anomaly is most likely from a complication in the tail vein intravenous setup resulting in the ICG-loaded micelles being injected into both the muscle and tail vein of the mouse. Taking advantage of the high concentration of ThermoDots residing in the muscle, a heating pad was used to increase the body temperature of the mouse to determine if the ICG-loaded micelles showed a dependence on temperature. From Figure 5.18c, we can see that there is a small temperature dependence. Increasing the temperature 3 degrees Celsius from 24-27°C resulted in a 15% increase in the normalized fluorescent signal.

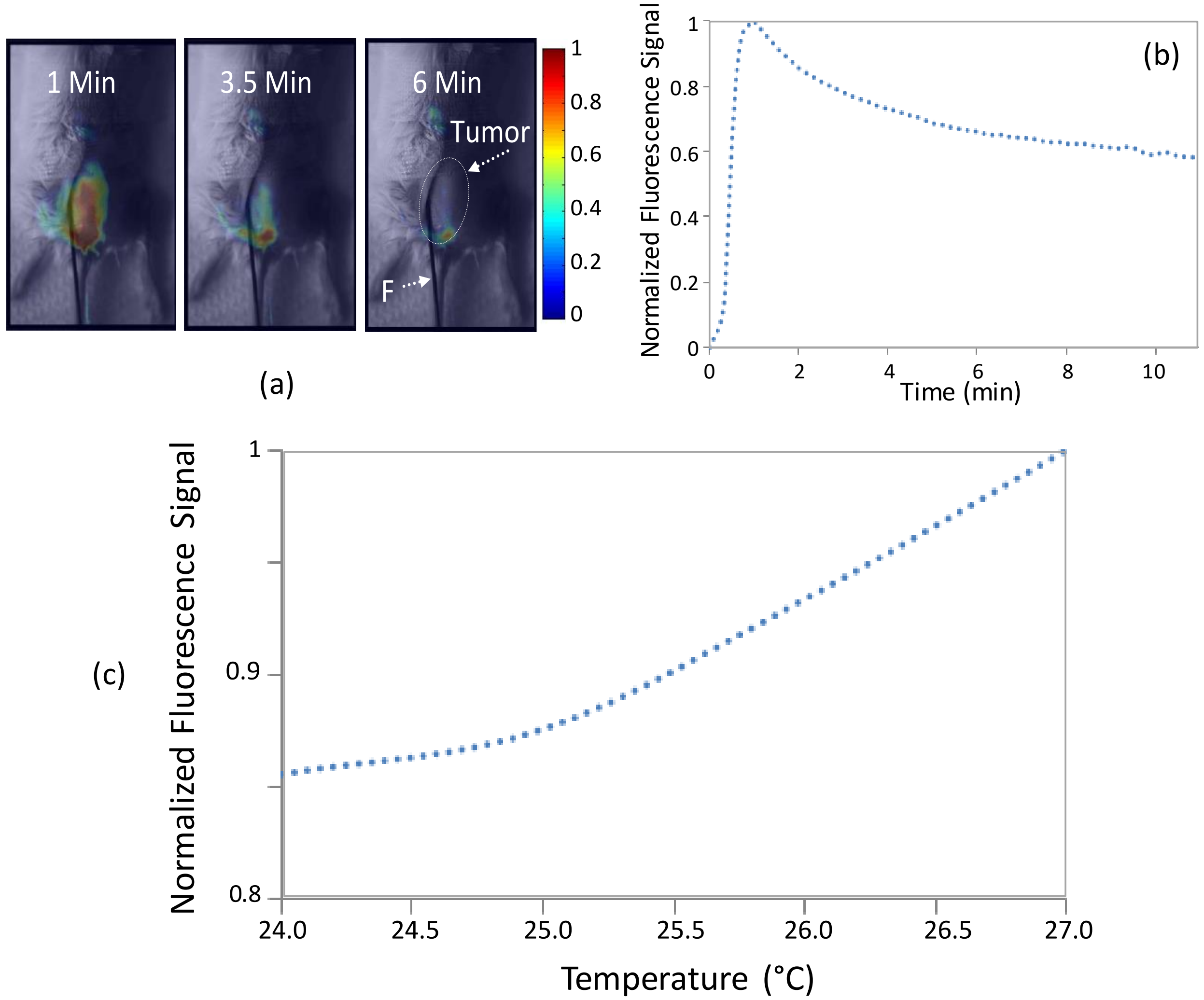

Figure 5. 18 *In vivo* temperature dependence. (a)Time lapsed images of 4% F127 ThermoDots injected to a tumor bearing mouse. The fluorescent nanoprobes accumulate in the tumor very quickly (~1 min) and are cleared out by the liver, excluding the portion of ThermoDots stuck in the tail vein as seen in the 6-minute image. A temperature probe was used to monitor the temperature of the mouse. The tumor region (delineated by the dashed line) and the fiber optic temperature sensor is indicated with "Tumor" and "F" in the images. (b) Graph of pharmacokinetics of 4% F127 ThermoDots injected to a tumor bearing mouse of fluorescence signal with time (minutes). Due to the portion of ThermoDots stuck in the tail vein, the fluorescence is relatively stable after 8

minutes. (c) Plot of temperature dependent fluorescence behavior of the 4% F127 ThermoDots *in vivo* 10 minutes after injection. A heating pad was used to heat the body temperature of the mouse. Fluorescence images were taken with a 30 second integration time.

The results show that the ThermoDots demonstrate their thermo-responsive fluorescent behavior *in vivo*. Although these preliminary results show the feasibility of the temperature dependent fluorescence quantum yield *in vivo*, much more rigorous testing and optimization of the ThermoDots need to be completed before translation to *in vivo* small animal TM-FT. This will require targeting of the ThermoDots to increase the retention time and concentration of the ThermoDots in the tumor.

5.4.4 In vivo toxicity studies

After the imaging studies in section 5.4.2, to shed some light on how the animals metabolize the ThermoDots and their toxicity level, the spleen, kidney, and liver of the rats, were excised and sent out for histology studies. The freshly harvested organs were fixed overnight in 10% neutral buffered formalin, processed, sectioned at 6 microns and stained with hematoxylin and eosin. Tissue slices were obtained from each organ and analyzed by the Experimental Tissue Shared Resource Facility of Chao Family Cancer Center at UCI. The histology report prepared by the Director of the facility, Dr. Robert Edwards showed that there was a trivial degree of generalized vascular congestion in all the sampled organs, however, this is likely a normal consequence of the euthanasia mechanism. Most importantly, there was no sign of any endothelial damage or activation, and the liver, kidney and spleen sections do not reveal any abnormalities. In particular, the ThermoDots-treated liver reveals monotonous cords of hepatocytes without reactive change and an absence of any visible sinusoidal endothelial injury or Kupffer cell reaction. Furthermore, the Thermodots-treated spleen reveals unremarkable red pulp and preservation of the perivascular white pulp. Figure 5.19 shows some sample images from each organ. All images were taken at 20x magnification on an Olympus BX45 microscope fitted with a DP-25 camera. These encouraging results confirmed that the ThermoDots injection was safe for the animals.

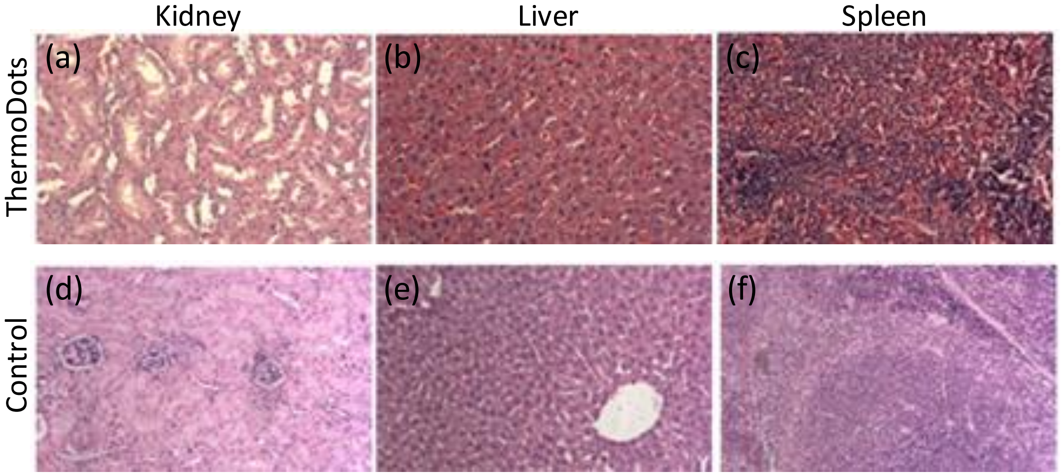

Figure 5. 19 Histology results. Comparison of H&E-stained sections from multiple organs of rats injected with i.v. ThermoDots (a-c) and analogous control organs for comparison: (d) kidney, (e) liver, and (f) spleen. (a) Sections of the ThermoDots-treated kidney reveals an absence of any glomerular and tubular injury. (b) The ThermoDots-treated liver reveals monotonous cords of hepatocytes without reactive change and an absence of any visible sinusoidal endothelial injury or Kupffer cell reaction. (c) The ThermoDots-treated spleen reveals unremarkable red pulp and preservation of the perivascular white pulp.

5.5 Targeting studies

5.5.1 Introduction and overview

As mentioned in the previous section, in order to perform TM-FT *in vivo*, the concentration and retention time of the ThermoDots in the tumor must be increased. To accomplish this, we looked into the feasibility of targeting the ThermoDots with the help of our collaborators. Due to their suitable structure for labeling, the temperature-responsive fluorescent nanocapsules can effectively act as targeting probes for various molecular pathways. To increase the retention time of the agents, a poly(ethylene glycol) PEG coating was added to the agents. PEG is a hydrophilic biocompatible polymer that has been used in numerous biomedical applications such as suppositories, contraceptive sponges, and wound-healing membranes(274). PEG has been extensively used for formulations requiring increased circulation time by acting as a shield against adsorption of opsonin biomolecules to the surface of temperature-responsive fluorescent nanocapsules and their consequent rapid recognition and removal by the reticuloendothelial system(64, 275).

5.5.2 EGFR

The first step was determining if the ThermoDots were targetable. Epidermal growth factor receptor (EGFR) was chosen as the first targeting mechanism due to its long history and popularity as a pharmaceutical target. Overexpression of EGFR, which are receptors located at the surface of the cell, has long been associated with many cancers (276). In 1978, it was the first of the ninety discovered receptor tyrosine kinases (277, 278). EGFR has become a popular pharmaceutical target for cancer therapies due to its influence on cell proliferation, division, and survival (276, 279). This has led to a number of EGFR-targeted therapeutic drugs such as Gefitinib and Cetuximab(276).

The EGFR-targeted ThermoDots were made by our collaborators at InnoSense Inc. and the Dr. Jered Haun lab at UCI. Fluorescence-activated cell sorting was used to investigate the specificity of the EGFR-targeted ThermoDots and performed by Dr. Maha Rahim from the Dr. Haun lab. Skin cancer A431 cells which overexpress EGFR were used to test the targeting ability of the EGFR-bound ThermoDots. The A431 cells (500,000 cells/sample) were labeled with non-targeted and EGFR-targeted ThermoDots at varying concentrations and incubated with a secondary anti-body. The fluorescence intensities were assessed by flow cytometry and analyzed using FACSDiva software. Cells treated with the non-targeted ThermoDots were used for controls. The mean fluorescence intensity from cells incubated only with secondary antibody was subtracted from all other samples to remove background signal.

The results of our first successful targeted ThermoDots formulation are shown below in Figure 5.20. This figure measured the fluorescence signal from the A431 cells using flow cytometry with three different concentrations of the EGFR-bound ThermoDots: 0.2, 2.0, and 3.0 g/mL. As seen in the figure, the two larger concentrations of the EGFR-targeted ThermoDots exhibited a much higher fluorescent signal than non-targeted ThermoDots which indicate that the EGFR-targeted ThermoDots can target EGFR. This initial study confirmed that the ThermoDots are able to be targeted.

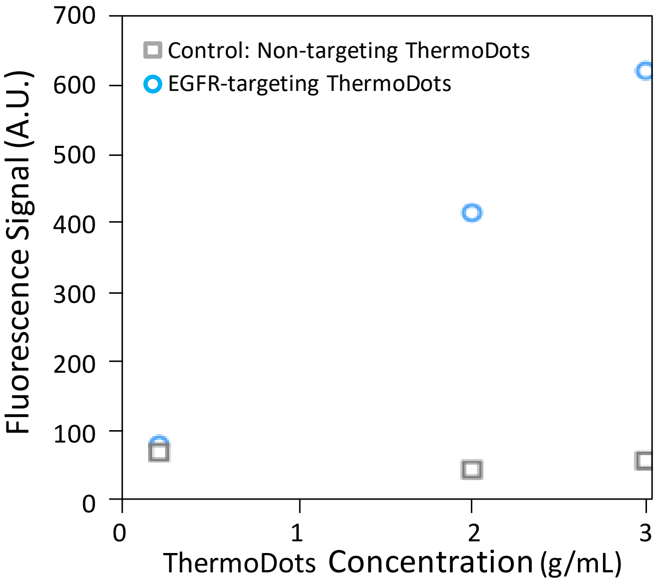

Figure 5. 20 EGFR targeted ThermoDots. Graph of fluorescence signal versus concentration of ThermoDots comparing non-targeted (gray) and EGFR-targeted (blue) ThermoDots. Three different concentration of the ThermoDots were used: 0.2, 2.0, and 3.0 g/mL. Fluorescence-activated cell sorting using skin cancer A431 cells was used to test the targeting ability of the EGFR-targeted ThermoDots made by our collaborators.

5.5.3 PSMA

After confirming that the ThermoDots were targetable, we also looked into prostate specific membrane antigen (PSMA) as a possible targeting mechanism. According to the American Cancer Society, excluding skin cancer, prostate cancer is the most common cancer and second leading cause of cancer-related deaths in men in the United States (280). PSMA is a highly-restricted prostate cell-surface antigen that is expressed in all types of prostate tissue but significantly overexpressed in prostate cancer cells (281). The level of PSMA expression increases with tumor aggressiveness, metastasis, and progression making it a highly promising pharmaceutical target not only for therapy but imaging as well (282, 283). In fact, ProstaScint™ which was FDA approved in 2004 is a well-known radiopharmaceutical used in prostate cancer diagnosis.

The PSMA-targeted ThermoDots were also made by our collaborators at InnoSense Inc. and the Dr. Haun lab. Fluorescence-activated cell sorting and immunofluorescence was used to investigate the specificity of the PSMA-targeted ThermoDots and performed by Dr. Rahim. For the flow cytometry, the PSMA-targeted ThermoDots were screened against three different prostate cancer cell lines expressing different levels of PSMA: low (PC-3), medium (C42B), and high (LNCaP). Cells were grown using standard culture conditions and suspended using trypsin-EDTA treatment. The cells (500,000 cells/sample) were labeled with the antibody-modified PSMA ThermoDots and incubated with a fluorescein-modified monoclonal rat anti-mouse IgG2a/b secondary antibody. The fluorescence intensities were assessed by flow cytometry and analyzed using FACSDiva software. Cells treated with the non-targeted ThermoDots were used for controls. The mean fluorescence intensity from cells incubated only with secondary antibody was subtracted from all other samples to remove background signal. For the immunofluorescence study, C42B and PC-3 prostate cancer cell lines were grown on Lab-Tek glass chamber slides, labeled with antibody-modified PSMA ThermoDots, and incubated with fluorescein-modified monoclonal rat anti-mouse IgG1 secondary antibody. The cells were imaged using an inverted laser scanning confocal microscope (FV1000, Olympus) with a 60× water immersion lens, and data was acquired with Fluoview software (Olympus).

Figure 5.21 looks at the specificity of the PSMA-bound ThermoDots over three different prostate cells lines with different levels of PSMA expression using flow cytometry. The low expressing PSMA PC-3 cells showed little difference from the control, while the C42B cells which do express some PSMA showed an affinity for the PSMA-bound ThermoDots over the control. Following this trend, the PSMA-targeted ThermoDots exhibited a clear preference for the highly expressing PSMA LNCaP cells. These results demonstrate the specific targeting of PSMA.

In addition, immunofluorescence was used to visualize the distribution of the PSMA-targeted ThermoDots in the cells and further confirm the specific PSMA targeting from the antibody-modified ThermoDots. As you seen in Figure 5.21b, the C42B cells, which express moderate levels of PSMA, displayed clear targeting of membrane bound PSMA after incubation with the PSMA-targeted ThermoDots followed by detection with the fluorescein-modified secondary antibody. The PSMA-targeted ThermoDots yielded higher fluorescent signals than the control which consisted of ThermoDots modified with a nonbinding control antibody. Moreover, low PSMA expressing PC-3 cells exhibited minimal membrane staining after labeling with the PSMA-targeted ThermoDots compared to control. Overall, these results showed that the ThermoDots are targetable which will hopefully lead to an increase in the concentration and retention time of the ThermoDots in tumor, thereby opening the door for future *in vivo* TM-FT studies.

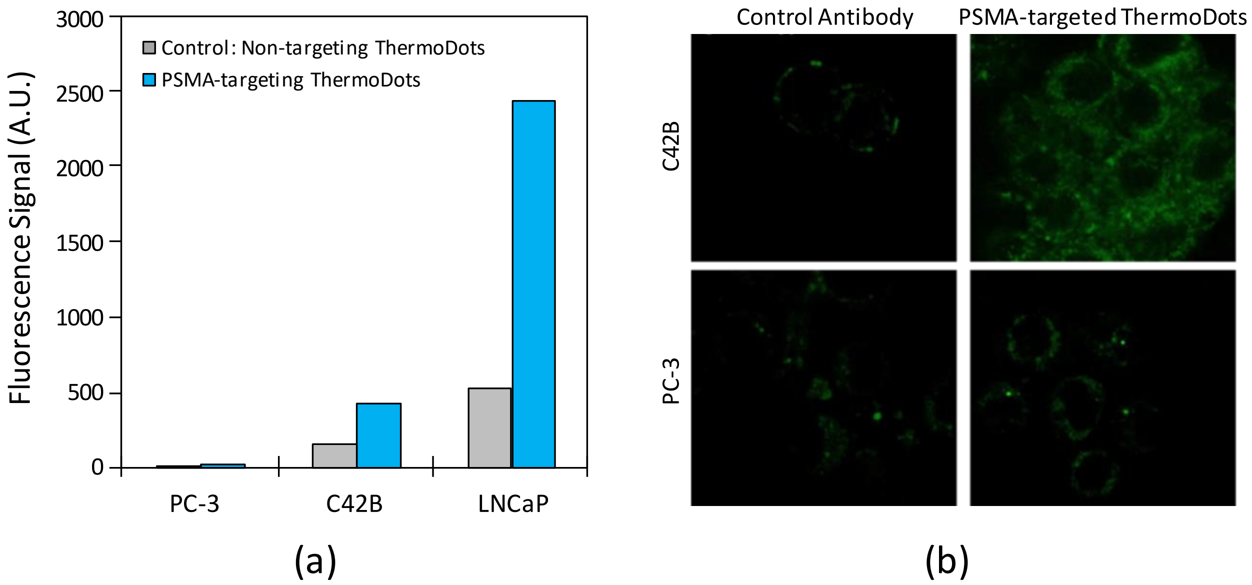

Figure 5. 21PSMA targeted ThermoDots. (a) FACS analysis showing the specific binding of the PSMA-targeted ThermoDots. The PSMA-targeted (blue) and non-targeted (gray) ThermoDots were screened over three different cell lines expressing different levels of PSMA: low (PC-3), medium (C42B), and high (LNCaP). (b) Immunofluorescence images showing the distribution of the ThermoDots in C42B and PC-3 prostate cancer cell lines using fluorescein-modified anti-IgG1 antibody. PSMA-targeted ThermoDots exhibited a high fluorescent signal and clear targeting of the membrane bound PSMA of the C42B cells compared to the ThermoDots modified with a nonbinding control antibody and the low expressing PC3 cells.

Chapter 6: System Development and Experimental Details

"If we knew what it was we were doing, it would not be called research, would it?"

– Albert Einstein

6.1 Introduction

TM-FT combines the resolution of focused ultrasound with the sensitivity of FT to produce images of unprecedented spatial resolution in deep tissue. Unlike other multimodality imaging systems/methods which work independently and must then be co-registered, TM-FT is a true multi-modality as both FT and focused ultrasound work simultaneously, in harmony, to directly measure the position of the temperature-sensitive fluorophore with high resolution. This required the construction of a new hybrid TM-FT system. This involved several trials to optimize the system from a simple manual prototype to test the feasibility of this new method to its current state which is fully automated and capable of incorporating DOT data as optical functional *a priori* information to improve the FT reconstruction.

This chapter will report on the development and optimization of the TM-FT system and scanning process. In addition, it will also describe experimental details such as image reconstruction and phantoms used in this work.

6.2 Instrumentation

6.2.1 Detectors

A photomultiplier tube (PMT) (R7400U-20, Hamamatsu, Japan) was chosen to detect the fluorescence signal due to its low noise and high sensitivity to low light signals. PMTs use a photocathode to convert light into electronic signal. PMTs apply an electric field to amplify the number of electrons by accelerating the electrons through a chain of dynodes. Consequently, PMTs have the highest gain (up to 10^6) compared to photodiodes or avalanche photodiodes. This specific model is one of the world's smallest PMTs and was chosen due to its compact size (< 1 inch) and spectral range (300-920 nm)(284).

6.2.2 Laser source

As the ThermoDots are based on the fluorophore ICG which has an absorption peak at 785 nm, a 785 nm laser (75 mW, Thorlabs, Newton, NJ) was used for the first TM-FT prototype. Later a second laser was bought to increase the photon signal and was centered at 790 nm (300 mW, Thorlabs, Newton, NJ). The laser was operated in frequency domain mode and a network analyzer was used to modulate (100 MHz) the laser power. A fiber optic switch was used to deliver the light to one of the multiple optical source fibers. To make sure the laser output power was stable, the laser was turned on well before beginning the experiment. The laser was allowed to stabilize for one hour prior to beginning the experiment and was kept on until the end of the experiment.

6.2.3 Focused ultrasound

Focused ultrasound is an emerging modality that can transport energy in the form of ultrasound (US) waves through a medium to produce multiple biological effects through thermal or mechanical means specifically at a target depth and location (285, 286). This non-invasive technique has become increasingly popular in many types of diseases and has shown great potential for tumor ablation as well as targeted drug delivery, thrombolysis, and hemostasis (285, 286). Although the biological effects of focused ultrasound were first recognized in 1927, clinical translation and approval has been slow (287). Indeed, while focused ultrasound is commonly used in Europe and Asia for a variety of diseases, in the USA, only four treatment applications have FDA approval. From the first FDA approval in 2004 for treatment of uterine fibroids, to relief of pain in bone metastases (2012), to prostate tissue ablation (2015) and treatment of essential tremors in 2016, there is no denying the increasing popularity of focused ultrasound in clinical medicine and its potential for other clinical applications. Figure 6.1 shows a figure from the Focused Ultrasound Foundation describing the different applications being studied.

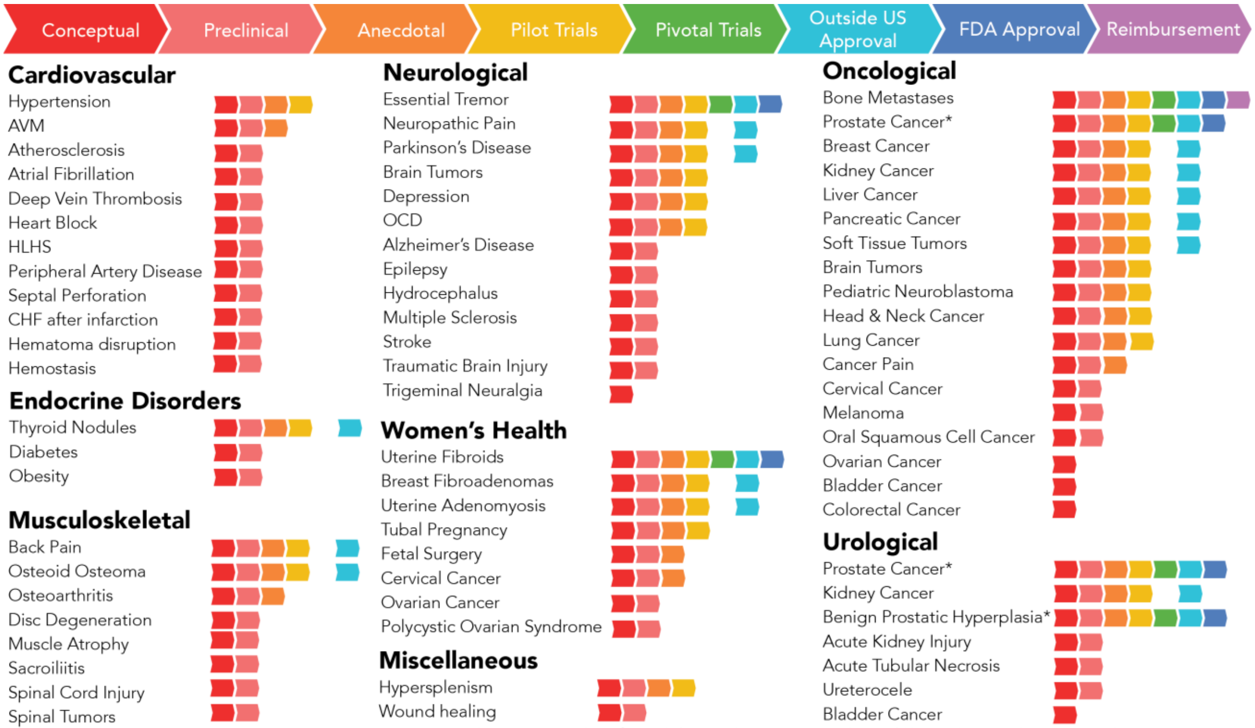

*the FDA approved two focused ultrasound systems in 2015 that could be used to treat these prostate diseases

Figure 6. 1 Summary of the state of research and regulatory approval of focused ultrasound for over 50 medical conditions in the US categorized by disease. Copyright (2015) with permission from the Focused Ultrasound Foundation.(285)

Focused ultrasound can provide localized heating by focusing acoustic waves to create a zone of intense pressure and heat also known as a "hot spot". This allows for heating in a targeted area, with minimal effect to surrounding tissue, which can range from a few degrees to over 90° C commonly seen in ablative therapy. The level and duration of this temperature elevation is known as the tissue's "thermal dose." The thermal dose is affected by the nature of the tissue (muscle vs. bone) and the ultrasound parameters (power, duration, and mode—continuous versus pulsed). Figure 6.2b shows the biological significance of the thermal dose and its dependency on temperature and exposure time. TM-FT is safe as it utilizes the focused ultrasound in a low power mode, to heat the tissue a few degrees (max temp < 42°C) for a short period of time (t ≤ 2 sec).

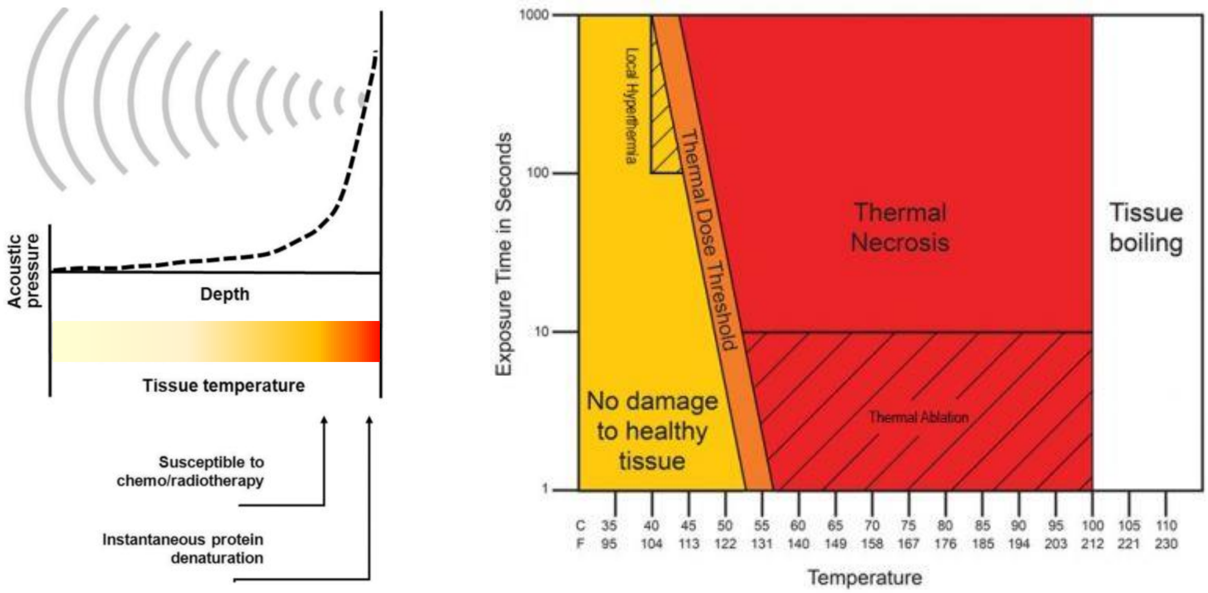

(a) (b)

Figure 6. 2 Focused ultrasound. (a) Basic concept of HIFU-induced tissue change by hyperthermia. As acoustic waves are focused onto small spot, the acoustic pressure is rapidly elevated near focus where tissue temperatures are also raised to level that is sufficient for thermotherapeutic effects, resulting in coagulation necrosis. (b)Different levels of thermal dose and their biological outcome. Part (a) is reprinted from Korean Journal of Radiology, Vol 9 Issue 4, Kim, Y. S., et al., High-Intensity Focused Ultrasound Therapy: an Overview for Radiologists, Page No 291-302. Copyright (2008) under the Creative Commons Attribution Non-commercial License. Part (b):Copyright (2015) with permission from the Focused Ultrasound Foundation.(285, 286)

In this work, a spherically curved transducer (H-102 transducer, MR-compatible, Sonic Concepts, Inc., WA, USA) was chosen to focus the acoustic waves at a fixed point. Compared to the other types of focusing methods, this self-focusing method is the simplest, least expensive, and often most accurate method (286). The location and size of the focal zone depends on the frequency and geometry of the transducer. In particular, tissue absorption of the US waves (and resultant tissue heating) is directly proportional to the US frequency. Higher frequencies are absorbed more readily along the US beam path thus decreasing the possible depth penetration due to prefocal absorption (288). Similarly, a decrease in frequency increases the penetration depth of the beam but makes it more difficult to create a sharply defined thermal focus (289). Thus, the choice of frequency is application specific and ranges from 0.5 MHz for deep treatments to 8 MHz for shallow treatments (289, 290). For the TM-FT experiments described in this work, a 1.0 MHz US frequency was chosen as frequencies near 1 MHz have been found to be most useful for heat deposition (289). In addition, the focused ultrasound transducer has a cylindrical focal zone of 1.33 mm in diameter and 1 cm in length located at a focal depth of 6 cm.

MR thermometry was performed to validate these parameters. Figure 6.3 shows the MRI thermal mapping results when the focused ultrasound is turned on for a duration of 10 seconds at a power of 50 W in chicken breast. This MR thermometry was performed inside a Philips 3 Tesla Achieva system and has a 5 second temporal resolution. As seen from the figure, the temperature distribution and the FWHM of the profile (1.4 mm) match with the specifications of the HIFU transducer focal spot size provided by the manufacturer (1.33 mm). As the FWHM of the heating spot size is 1.4 mm, this in turn becomes the spatial resolution limitation for this set-up. Since the spatial resolution directly depends on the focused ultrasound transducer, in the future, this could be improved as there are commercially available focused ultrasound transducers with focal spots smaller than 1 mm.

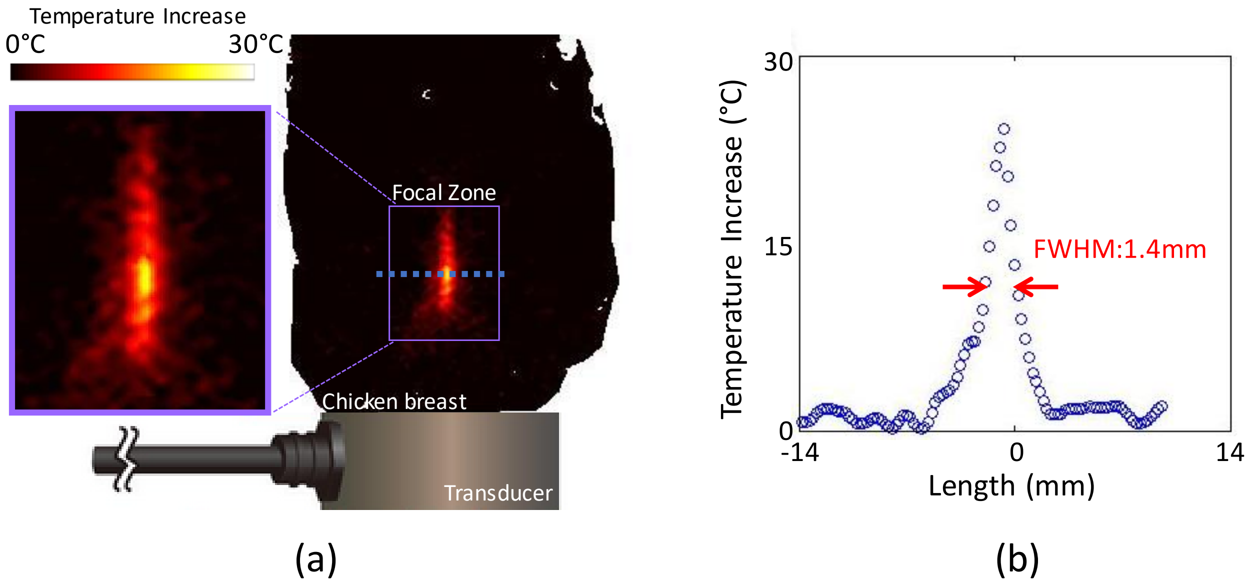

Figure 6. 3 Validation of HIFU parameters in biological tissue using MR thermometry. (a) Focal zone of the Sonic Concepts H-102 focused ultrasound transducer (50 W, 10 seconds) in chicken breast. MR thermometry results show the localized heating and sharp increase in temperature at the center of the focal zone. (b) Profile of focal zone taken from blue dotted line in MR thermometry data shows the FWHM is 1.4 mm.

6.3 Experimental Set up

6.3.1 Introduction

TM-FT combines the spatial resolution of focused ultrasound with the sensitivity of FT. Therefore, a new system had to be custom made for this new technique to seamlessly meld the two separate modalities together into one system. Most multi-modality methods consist of two or more techniques operating independently and separately, and then are combined using co-registration (19, 51, 54, 190). Unfortunately, this can cause complications and errors can occur when the structural boundaries provided by the anatomical imaging modality do not exactly coincide with the true fluorescent distribution (185). However, TM-FT blends focused ultrasound and FT into the same system and they work together to generate the *exogenous functional a priori* information. This negates the need and complications that arise from co-registration.

The first step in building this multi-modality system was to build a bench-top TM-FT prototype to test the feasibility of this novel technique. After the feasibility of this method was validated, the next step was to optimize the scanning time of the system for the future goal of *in vivo* animal imaging. Therefore, the goal of the second TM-FT system was to fully automate the system and optimized the focused ultrasound scan time for animal studies focused ultrasound scan. These two systems used agar phantoms which do not represent the true optical and acoustic properties of biological tissue. Therefore, the system had to be modified in order to validate the feasibility of TM-FT in *ex vivo* animal tissue before transitioning to *in vivo* animal studies. The final step was to add DOT to the automated TM-FT system to obtain *endogenous a priori* information to estimate the optical properties of the tissue and guide the TM-FT reconstruction algorithm.

6.3.2 System 1: Manual Prototype

A schematic diagram of the first TM-FT prototype can be seen in Figure 6.4. The TM-FT system can be divided into two parts: FT and focused ultrasound. For the FT portion, a 785 nm laser diode (75 mW, Thorlabs, Newton, NJ) illuminated the object under investigation in transillumination mode. A fiber optic switch was used to deliver the laser light to one of eight source optical fibers (625 μm). A network analyzer (Agilent Technologies, Palo Alto, CA) was utilized to simultaneously provide RF modulation (100 MHz) for the laser-diode while also measuring the amplitude of the detected signal. The transmitted light was collected by one of eight optical fibers (1 mm) and passed through a series of lens (Newport Corporation, CA) and band-pass filters (830 nm, MK Photonics, Albuquerque, NM) which collimated, filtered out excitation light, and focused the transmitted photons to the detector. A photomultiplier tube (PMT) (R7400U-20, Hamamatsu, Japan) was chosen to detect the fluorescence signal. The signal was then amplified by an RF amplifier before being recorded by the network analyzer. The aspherical lens, filters, PMT, and RF amplifier were kept inside an RF shielding container to maximize the SNR.

The focused ultrasound components are outlined in blue in Figure 6.4. The focused ultrasound transducer (H-102, Sonic Concepts, Inc. WA) had a center frequency of 1.1 MHz. The lateral FWHM of the focal spot was 1.4 mm. The transducer was driven by a sinusoidal signal from by a functional generator (PTS 500, Programmed Test Sources, Inc. WA) and amplified by a power amplifier (155LCRH, Kalmus, USA). The optical fibers, phantom, and focused ultrasound transducer were submerged in water to prevent reflection of the acoustic waves. Finally, to perform spatial scanning, the transducer was mounted on three (x, y, z) manual translational stages (25 mm, Newport Corporation, CA) and placed above the phantom to be imaged.

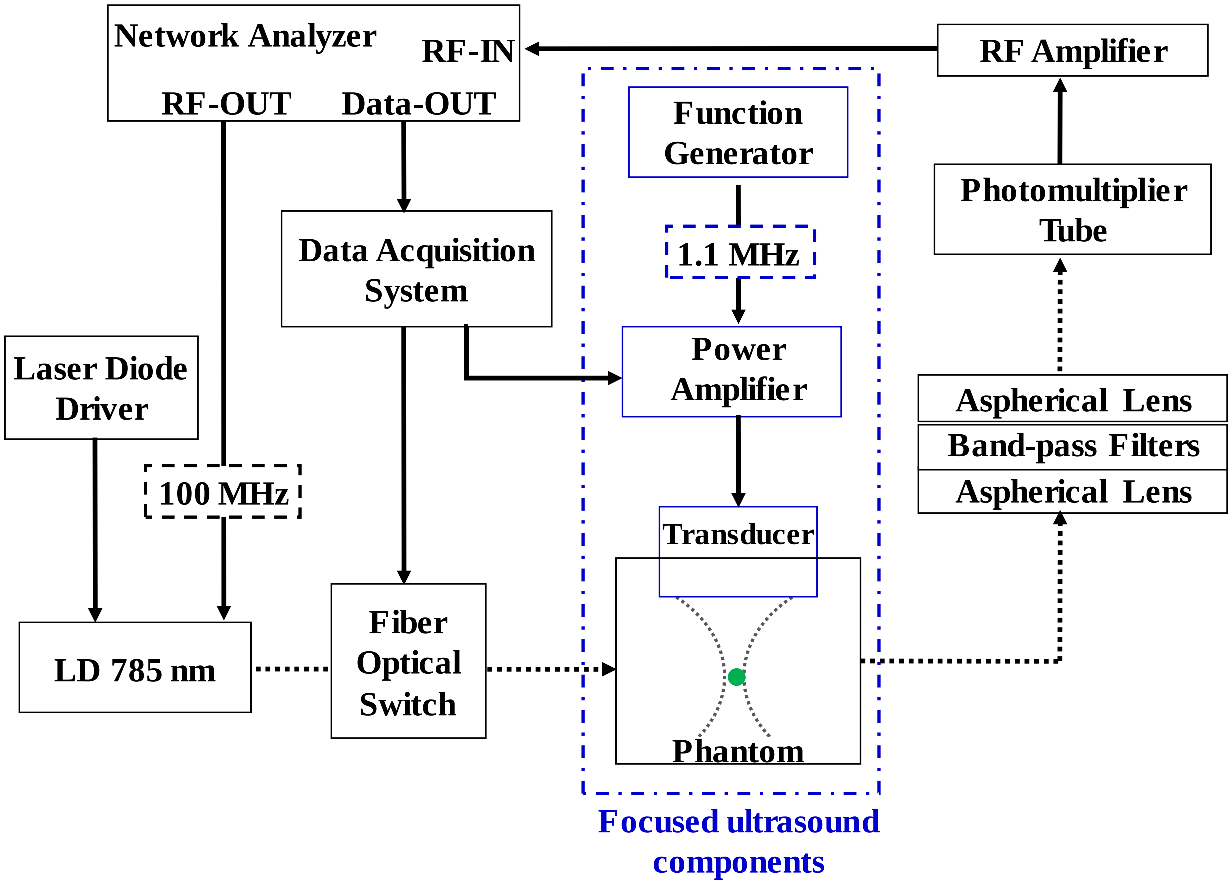

Figure 6. 4 Schematic of first generation frequency domain TM-FT system. The transducer is driven by a combination of a signal generator and an RF power amplifier. Using a xyz translational stage, it is scanned over the probed medium that is simultaneously irradiated with modulated laser light. The intensity variations are detected using a photomultiplier tube and measured by a network analyzer.

6.3.3 System 2: Automated TM-FT

For the second-generation system, two major updates were made to the first TM-FT prototype, described in section 5.3.1.2. To combat the high acquisition time of the step and shoot method, two motorized translational stages (NLS4, 8 inch, Newmark Systems) were incorporated to automate the system and procedure. The focused ultrasound transducer was mounted on two computer-controlled linear stages, chosen for their precision, and placed above the phantom to be imaged. The focused ultrasound used in this system was also a H-

102 transducer from Sonic Concepts, Inc. but operated at 1.0 MHz. For imaging, the *xy* focused ultrasound scan was programmed to be fully automated using LabVIEW CVI (National Instruments, USA).

Transitioning from the step and shoot mode to a continuous scanning method (described in section 5.4.3.2) decreases the SNR and sensitivity of the system. Therefore, to combat this problem, components of TM-FT system was updated to improve the SNR and sensitivity. The laser diode was upgraded from 75 mW to 300 mW (Thorlabs, NJ, USA), a power increase of 4-fold. This new laser was centered at 790 nm. In addition, the 1 mm detectors fiber from the previous were replaced by six fiber bundles (6 mm) which greatly increased the amount of fluorescent light detected (~6x). A picture of the fully automated TM-FT system can be seen in Figure 6.5.

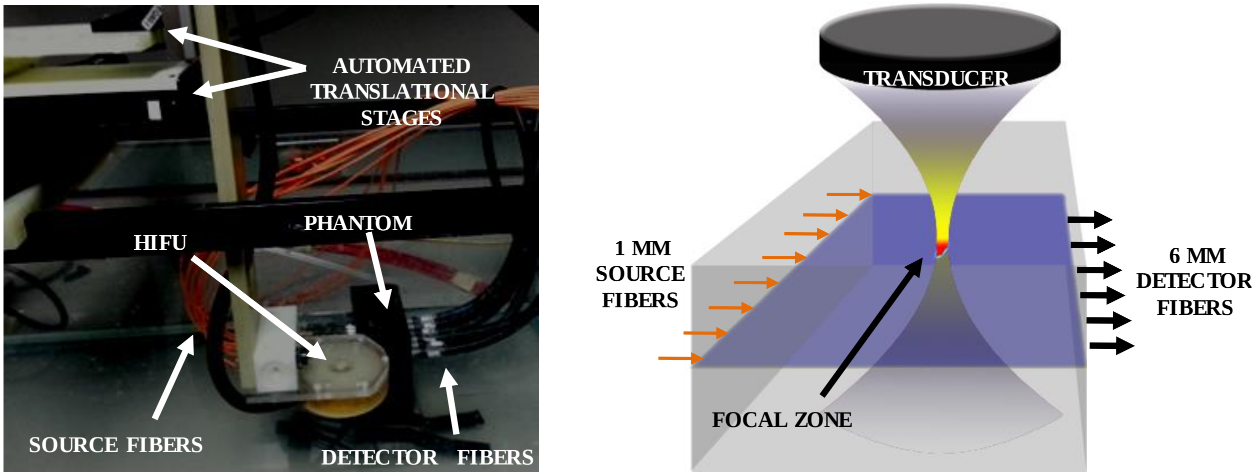

(a) **(b)**

Figure 6. 5 TM-FT System Set Up and close up of phantom with HIFU. 1(a) Picture of TM-FT System which includes HIFU positioned on top of the phantom and controlled by automated translational stages. Eight source fibers (1 mm diameter) and six detector fibers (6 mm diameter) are positioned opposite of each other for transillumination measurements. 1 (b) Close up of phantom. Here you can see that the HIFU focal zone is in the same plane (blue plane) as the 1 mm source fibers and 6 detector fibers.(65)

6.3.4 System 3: TMFT-DOT

The previous systems used agar phantoms which did not represent the true heterogeneous nature of the optical properties of biological tissue. In addition, agar phantoms are made with specific optical properties. Therefore, when transitioning to animal tissue where the optical properties are unknown, the final step was to add DOT to this automated multi-modality system to better estimate the optical properties of the medium. Figure 6.6 shows how DOT (outlined in red) is incorporated into the existing TM-FT system. In addition to the *exogenous functional a priori* from the ThermoDots and focused ultrasound scan, DOT can provide *endogenous functional a priori* information to constrain the TM-FT image reconstruction algorithm. The DOT components consisted of a second PMT detection system, nearly identical to the existing FT detection system, in which the transmitted light could be diverted for DOT measurements. The transmitted light was focused (aspherical lens, Newport Corporation, CA) into the PMT (R7400U-20, Hamamatsu, Japan) before being amplified (RF amplifier) and measured by the network analyzer. This system allows for both FT and DOT measurements as the transmitted light can be easily diverted into the correct detection box using a switch.

The previous two systems only allowed for agar phantoms with known optical properties. Incorporation of DOT is the next step to *in vivo* animal studies as it transitioned TM-FT from agar phantoms and allows *ex vivo* animal studies. Chapter 6.3 shows the results of a study using this system to test the feasibility of TM-FT in animal tissue.

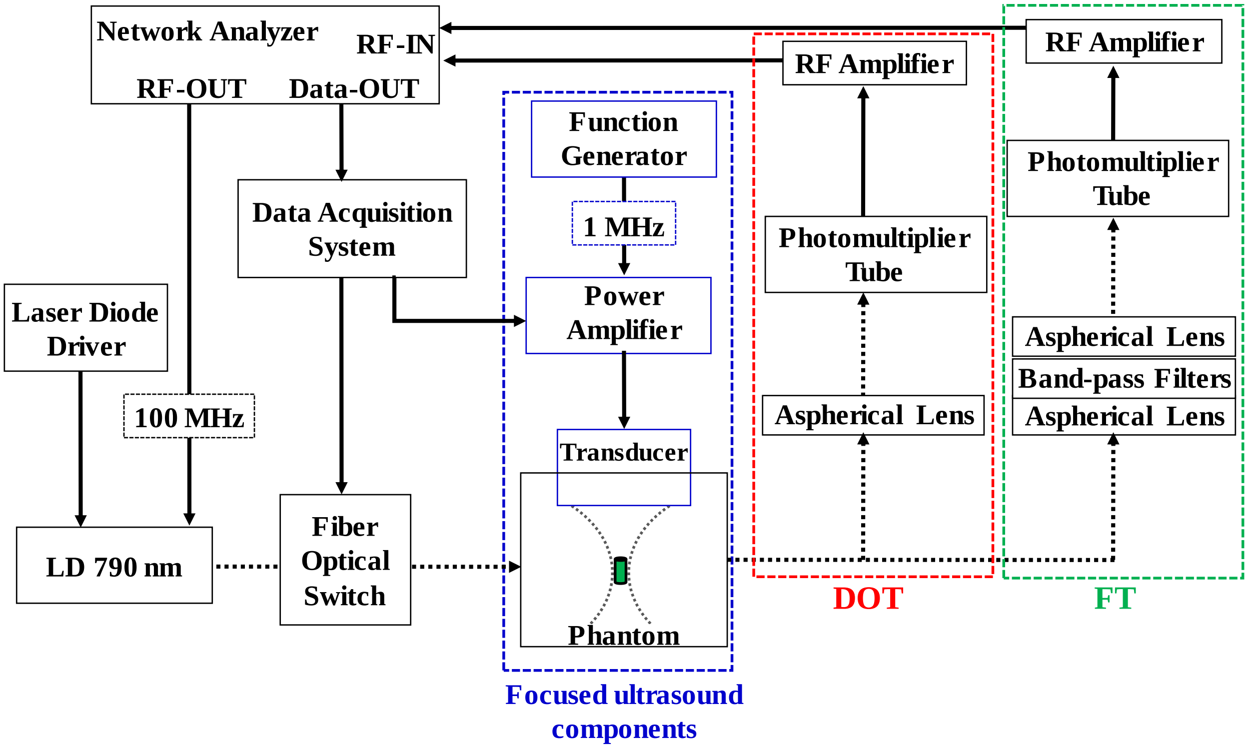

Figure 6. 6 Schematic of DOT/TM-FT system. The focused ultrasound components are outlined in blue, the FT components in green, and the newly integrated DOT components are outlined in red.

6.4 Optimization of focused ultrasound scan

6.4.1 Introduction

Optimization of the system and scanning method are critical for TM-FT potential and future applications. The scanning method went through several iterations before its current state. Initially, a step and shoot method was used to test the feasibility of TM-FT. In this method, the focused ultrasound would shoot in a raster scan pattern and the increased fluorescent signal following the temperature modulation would be used to generate a map of the ThermoDots position with high resolution. This system was controlled manually and although this system was the simplest to use, the long acquisition time (> hours) made it impractical for real world applications. Thus, automated translational stages were introduced to speed up the scanning time. A continuous scanning method was introduced where the focused ultrasound is turned on and scanned across the medium in a line while continuous measurements are taken. Thus, a new method was introduced where the system would scan the tissue in two scans (forward and reverse) and convolve the two scans to make a binary map of the position of the temperature dependent fluorescence fluorophore with focused ultrasound resolution. However, although the spatial resolution was high in the direction parallel to the scanning lines, this method lacked resolution in the perpendicular direction. Thus, the current scanning method was introduced in which two addition scans were added in the perpendicular direction for a total of 4 scans. The four scans are combined to generate the high resolution binary map. This method sped up the TM-FT acquisition method from over 8 hours to a mere 29 minutes which is feasible for *in vivo* animal studies. The two published scanning methods are described below.

6.4.2 Pulsed scanning method

6.4.2.1 Scan

The first TM-FT scanning method used a raster scan (step and shoot) technique to map the position of the temperature dependent fluorescent ThermoDots. The HIFU transducer was mounted on an *xyz* translational stage and placed above the phantom, Figure 6.7. The transducer was scanned laterally in both *x* and *y* directions in 0.5 mm steps. At each step, the laser was turned on and the maximum fluorescent signal was recorded after a 2 second focused ultrasound pulse (10 W). A cooling period was observed before the next focused ultrasound pulse as the fluorescent signal returned to the baseline signal. The measurement at each scan position was averaged four times, which yields 2 second acquisition time for each point. The fluorescence data collected from the source/detector pair with the highest signal-to-noise ratio (SNR).

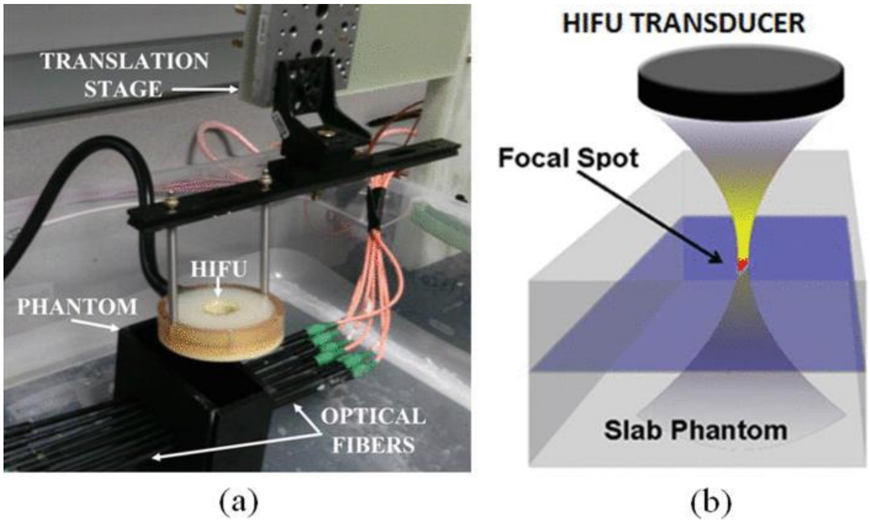

Figure 6. 7 Experimental set-up. (a) TM-FT system. The HIFU transducer is mounted on an xyz translational stage with the source and detector fibers placed on opposing sides of the phantom to acquire transmission mode fluorescence measurements. (b) Diagram of HIFU transducer. During the HIFU scan, the transducer generates a localized temperature increase on the focal spot (~1.4 mm size) which changes the measured fluorescence signal only the focal spot is on the fluorescence source.(62)

In order to know the point spread function (PSF) of the temperature profile generated by the focused ultrasound for this method, a fiber-optic temperature sensor was inserted in an agarose phantom and the temperature change was recorded when the focused ultrasound was scanned through a 5 mm × 5 mm area with 0.5 mm steps. The normalized temperature increase in each scanning point is shown in Figure 6.8a. The profile across the sensor tip (Figure 6.8b) shows the temperature increase as a function of x-position of the focused ultrasound scan step. The FWHM of the heating spot size was 1.8 mm and corresponds to point spread function of our system, which in turn becomes the spatial resolution limitation for this specific set-up.

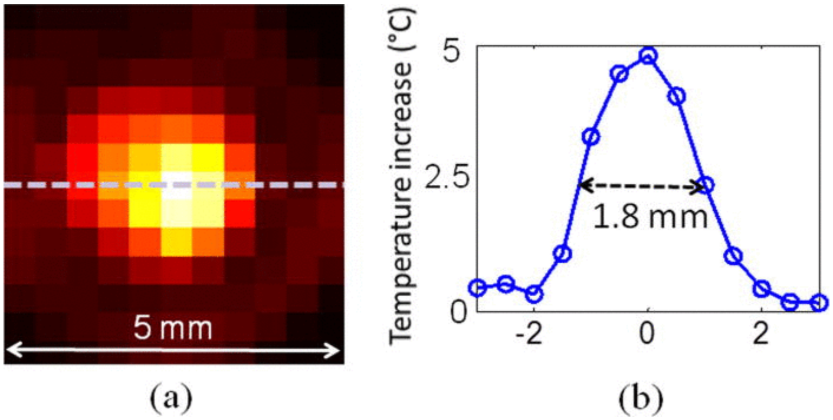

Figure 6. 8 The point spread function measurement. (a) An optical temperature sensor is inserted in the phantom and the temperature change is recorded when the HIFU is scanned through a 5 mm × 5 mm area with 0.5 mm steps. (b) The profile shows that the FWHM of the heating spot size is 1.8 mm.(62)

6.4.2.2 Experimental procedure

The TM-FT experimental procedure is shown below in Figure 6.9. The first step is to take conventional FT measurements with the 8 sources and detectors for a total of 64 measurements. The second step is to then run the measurements through a conventional FT reconstruction program to give a general location of the inclusion, or region of interest (ROI). Next, the focused ultrasound is scanned through this ROI (8mm x 8mm area) in 0.5 mm steps for a total of 256 measurement positions (step 3). For each position, the focused ultrasound gives a 2 second pulse on low power to modulate the temperature at the hot spot a few degrees (~4°C). The fourth step is to use this information to generate the binary map of the position of the fluorescence distribution with high spatial resolution. The fluorescence signal variation is mapped to each scanning position and a measurement is taken after the HIFU pulse. Therefore, a significant change is observed only when the hot spot is scanned through the fluorescence object resulting in a much improved spatial resolution. The FWHM is used as a threshold for the binary map. The final step (step 5) is to combine the binary map from step 4 with the conventional FT measurements from step 1 and use it as *a priori* information to guide and constrain the TM-FT reconstruction algorithm to map the position of the fluorescent ThermoDots with high spatial resolution.

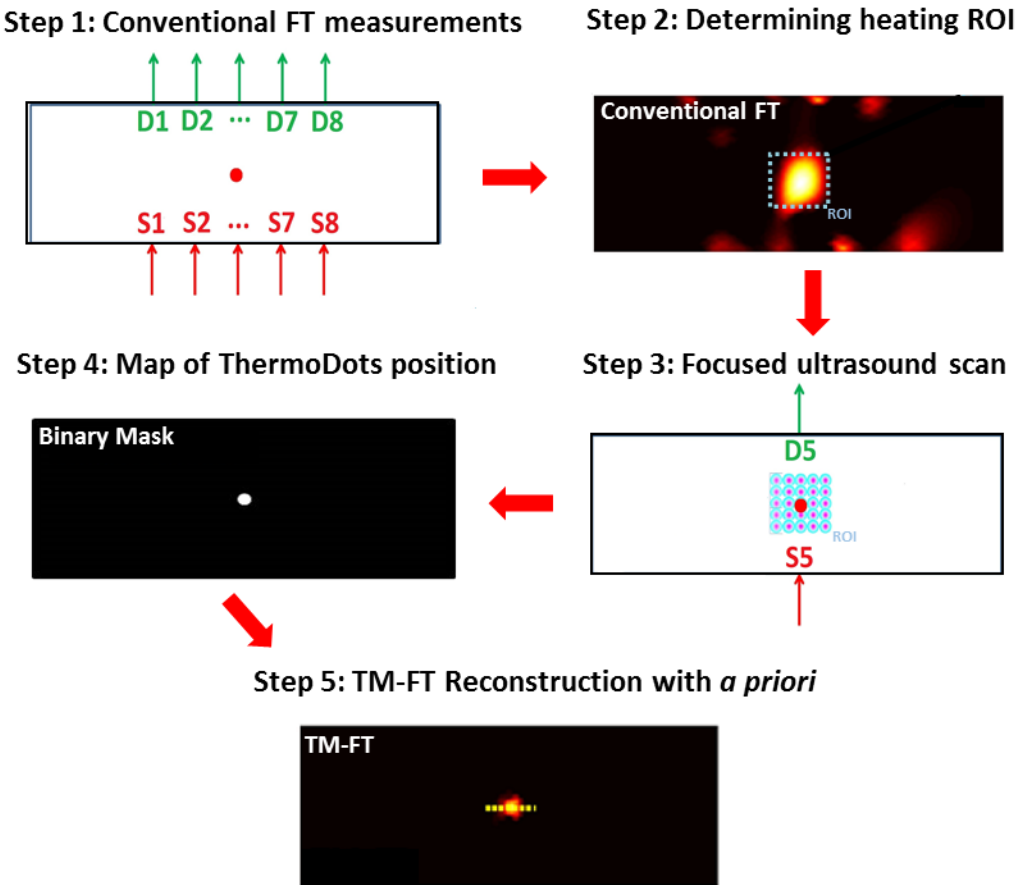

Figure 6. 9 Diagram of experimental procedure for first TM-FT prototype.

6.4.2.2 Summary

This prototype system and scanning procedure were designed to test the feasibility of this novel technique. This system featured a step and shoot (focused ultrasound pulse) method in which the focused ultrasound was moved in 0.5 mm sized steps by three manual translational stages in a raster scanning pattern. The advantages of method and system are the low cost, quick construction, and simplicity (allows for simple mapping of the fluorescent signal according to position to generate binary mask). However, the main disadvantage was the length of time required to scan an 8 mm x 8 mm area. A background fluorescent signal (which is related to the temperature of the ThermoDots without heating) was taken before the focused ultrasound scan and used a baseline. During the scan, a waiting period was observed to let the fluorescent signal returned to the baseline before the next focused ultrasound pulse measurement. Due to the fact that the focused ultrasound only generated a 4°C increase in temperature, the average waiting period was quite long, approximately 2 minutes per step, resulting in a scanning time of more than 8 hours. In addition, the system was manually operated which required a person to manually move the focused ultrasound transducer to the next step, wait for the ThermoDots to cool back to room temperature, and then take the next measurement. Although this system successfully proved that TM-FT was feasible, the practicality of TM-FT still needs to be addressed.

6.4.3 Continuous scanning method

6.4.3.1 Introduction

Although the phantom study showed the feasibility of this system, the practicality of the scan was an issue as step by step HIFU pulse scans are hindered by long cooling times. Before each step, the temperature of the phantom had to return to its baseline temperature before proceeding. Previously, a 7 x 7 mm scan with a 1 mm step size with a two second pulse at every millimeter would require a 2 minute cooling time before measuring the next adjacent point which results in a 1 hour and 40 minute cooling time. By implementing automatic stages and programming them to scan in a jumping pattern which instead of heating adjacent parts of the phantom, jumps to an area far away from the previous point, the cooling time was cut down to 25 minutes. Nevertheless, the time required for a 7mm x 7 mm is not practical for imaging live animals. Therefore, a new, fast scanning method was introduced which reduces the imaging time 40-fold. By continuously scanning the ultrasound beam over a 50 mm by 25 mm field-of-view, high-resolution fluorescence images are obtained in less than 29 min, which is critical for *in vivo* small animal imaging.

Transitioning from a pulsed, step and shoot method to a continuous fast scan mode brought new complications such as the effect of heat diffusion to consider. In addition, a new method had to be used to analyze the focused ultrasound scanning data and generate the binary mask compared to the simple fluorescent mapping of position from the previous step and shoot mode. This new method was published in Optics Letters and is reproduced in parts in the following section (185).

6.4.3.2 Scan[3]

Unlike structural *a priori* information which reveals the boundaries of anatomic structures, this method directly delineates the boundary of the fluorescent target. Therefore, it is important to note that the TM-FT binary mask alone reveals a high-resolution image of

---

[3] This section (6.4.3.2 Scan) was reproduced from Optics Letters, Vol 40 Issue 21, Nouizi, Farouk. et al., Implementation of a new scanning method for high-resolution fluorescence tomography using thermo-sensitive fluorescent agents. Page No 4991-4995 Copyright (2015) with permission from Optical Society of America. (156)

the fluorescent agent distribution prior to any complex reconstruction process. However, recovering quantitative fluorescence concentration and lifetime parameters requires solving the inverse problem of FT. Our previous results demonstrated the superior performance of TM-FT compared to conventional FT. However, data acquisition time was the main weakness of this technique due to utilization of the HIFU step-and-shoot mode (62, 63). Here, we introduce a fast scan method that drastically accelerates the acquisition speed without sacrificing the spatial resolution of this imaging technique. These preliminary experimental results show the ability of our fast scan TM-FT method to resolve small fluorescent inclusions embedded several centimeters deep in a scattering medium.

The phantom used in this experiment is a 100 (x) × 40 (y) × 100 mm (z) agarose phantom. Its absorption and reduced scattering coefficients are set to 0.008 and 0.86 mm^{-1}, respectively. A 3 mm diameter, 10 mm long cylindrical inclusion filled with ThermoDots is embedded at the center of the phantom along the z-axis, 50 mm below the top surface (Figure 6.10). The ThermoDots concentration used in this experiment generates a fluorescence signal equivalent to 0.8 μM of ICG at low temperature.

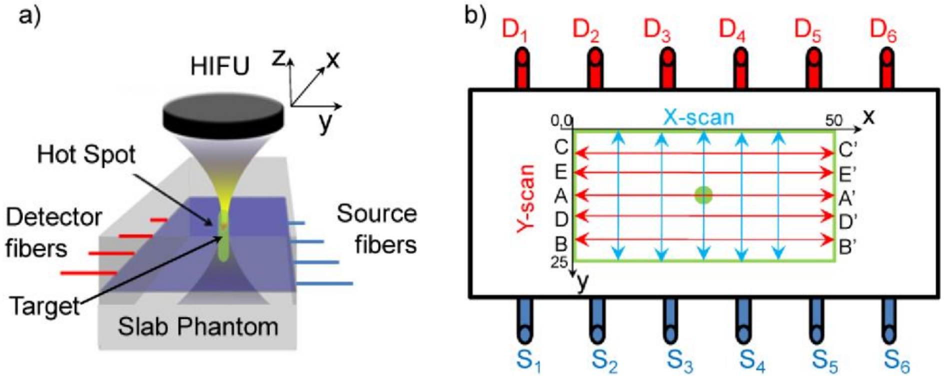

Figure 6. 10 HIFU continuous scan set up. (a) HIFU transducer is positioned at the top of the agar phantom while six source (blue) and six detector (red) fibers are placed at both sides of the phantom. (b) Cross section of the phantom at the fiber plane, 50 mm below the top surface [the blue

plane in (a)]. HIFU beam is scanned in two orthogonal directions, X-scan (blue) and Y-scan (red), over the phantom (bold black). The cylindrical fluorescent target is positioned at the center of the phantom along the z-axis.(185)

The previous step-and-shot technique requires more than an hour to scan an 8×8 mm ROI. In this new method, the imaging time is considerably reduced by keeping the HIFU on continuously at low power, while scanning in both x and y directions (Figure 6.10b). Considering the size of the HIFU hot spot (~1.33 mm), 37 scanning lines cover an area of 49.21×25 mm^2 for the X-scan, while 18 scanning lines cover an area of 50×23.94 mm^2 for the Y-scan. The centers of both scanned areas are aligned at the center of the phantom.

While HIFU is generally used therapeutically at high power to burn tissue, here it is used diagnostically in a low power mode to induce a slight temperature change to generate a measurable increase in fluorescence signal (291). However, the thermal diffusion and the effect of residual heat still need to be taken into account. A typical thermal diffusivity value for most soft tissues is 14×10^{-4} cm^2/s (292). The thermal diffusion length during the pulse period can be estimated by the following equation: $\partial_T = 2\sqrt{D_T \cdot \tau_p}$, where D_T is the thermal diffusivity and τ_p is the pulse width. Using this equation, the calculated thermal diffusion length for a one second pulse is 0.75 mm. For this reason, during a line scan, the HIFU beam is scanned faster, with a speed of 4.16 mm/s, to prevent the effect of heat diffusion from the portion of the line previously scanned. The network analyzer acquires 200 measurements in a 50 mm line scan yielding a sampling rate of one measurement per 0.25 mm. Thus, considering the size of the hot spot of the HIFU (1.33 mm), a filtering window width of five data points is used to smooth the measured signals.

We assign $\Phi_{pp'}$ to be the fluorescence signal measured while performing a linear scan from the point P to the point P', where P represents a particular scanning line denoted by letters A to E according to their scan sequence (Figure 6.10b). Meanwhile, $\varphi_{pp'}$ represents the first derivative of $\Phi_{pp'}$. In the absence of ThermoDots along the scanning line, no change in the fluorescence signal is induced by the HIFU ($\Phi_{BB'}$) (Figure 6.11). However, a sudden jump in the fluorescence signal is detected when the HIFU is scanned over the target ($\Phi_{AA'}$) (Figure 6.11). As soon as the HIFU beam leaves the target, the fluorescence signal starts decreasing at a lower rate due to cooling. Hence, the first derivative of the signal can only be used to identify the first encountered boundary of the fluorescence target ($\varphi_{AA'}$). Therefore, a second scan is performed in the opposite direction ($\Phi_{A'A}$), and its derivative ($\varphi_{A'A}$) is used to identify the boundary of the target from the opposite side. Each of these four scans is achieved in just over 7 min, which makes the total HIFU scanning time approximately 29 min. We observed that ζ_A, the sum of the derivatives obtained on line AA' in opposite directions ($\varphi_{AA'}{}'$ and$\varphi_{A'A}$), reveals the boundaries of the inclusion on that particular line (Figure 6.11). An interleaved scanning pattern is used to avoid waiting for the signal to decrease to the baseline before performing the scan in the opposite direction or crosstalk due to the heat diffusion in adjacent lines. While performing the Y-scans, the HIFU is sequentially scanned from point A to A', B' to B, C to C', and then A' to A…etc. (Figure 6.10). A 2D image I_Y can be formed over the Y-scan by assembling all the sums (ζ_A, ζ_B, ζ_C,…) with respect to their spatial coordinates (Figure 6.12b). Similarly, I_X can be formed over the X-scan (Figure 6.12a).

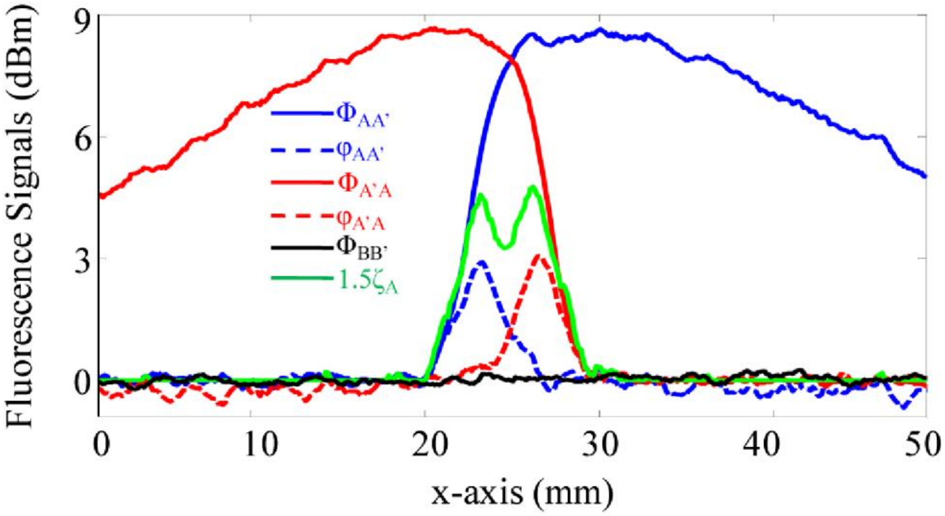

Figure 6. 11 Analysis of TM-FT HIFU scan measurements. Measured fluorescence signals on a single Y-scan (AA') in opposite directions (blue and red solid lines) for the phantom with single target. The derivatives (blue and red dashed lines) reveal the boundaries of the target for this particular Y-scan (AA') when summed together (green solid line).(185)

An elongation in the shape of the inclusion is indeed noticed along the scanning direction, y-axis for I_Y and x-axis for I_X (Figures 6.12a and 6.12b). Figure 6.12c shows the image I_{XY} resulting from the product of pixel to pixel of I_X and I_Y. It demonstrates that the circular shape of the target is recovered better using a combination of both scans I_X and I_Y. This correction of the target shape is clearly observed by the FWHM values of the profiles of I_X, I_Y, and I_{XY} along both the x- and y-axis, across the target given at the top of each individual map in Figure 6.12. They show that each scan improves the spatial resolution of the final image in its orthogonal direction. The binary mask used as *a priori* information to constrain the FT reconstruction algorithm is obtained by simply segmenting the I_{XY} at half-maximum.

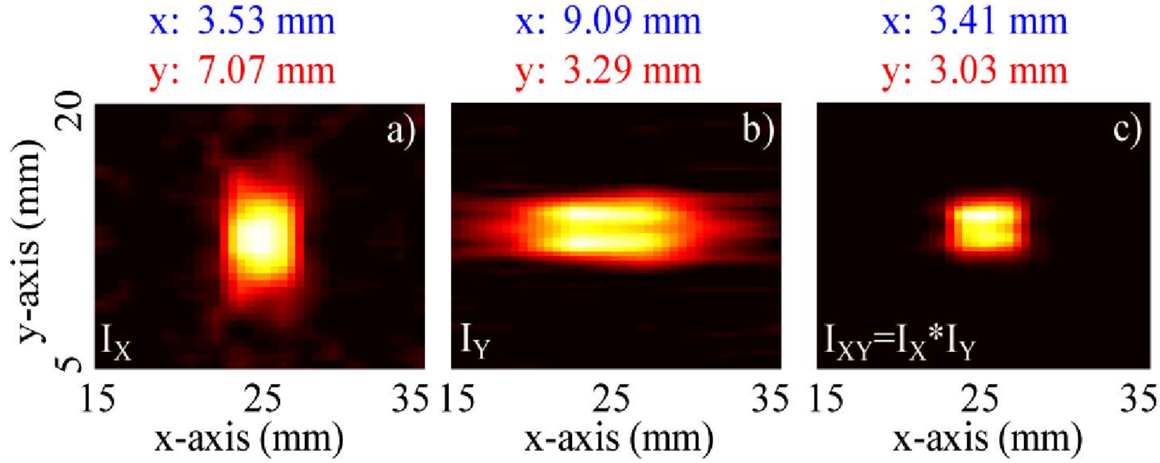

Figure 6. 12 Processing of HIFU scan measurements. Assembling the sum of the derivatives for all of the lines provides the approximate location and shape of the target, $\boldsymbol{I_X}$(a) and $\boldsymbol{I_Y}$(b). However, combination of these maps obtained by the product of *X*- and *Y*-scans provides a better extraction of the real boundary of the fluorescence target, $\boldsymbol{I_{XY}}$(c). The FWHM values along the *x*- and *y*-directions are provided above.(185)

In the first experiment, the 3 mm diameter inclusion is shifted by 6 mm to the left of the center of the phantom. A very good agreement is obtained between the mask generated using our new, fast TM-FT method and the real inclusion size and position (Figures 6.13a and 6.13b). The irregularities on the shape of the inclusion are only due to the interpolation of the segmented I_{XY} on the FEM mesh. Furthermore, the TM-FT method (Figure 6.13d) recovers the object better than conventional FT, where no *a priori* information is used (Figure 6.13c). In fact, conventional FT recovered the size of the target more than four times its original size (Figures 6.13e and 6.13f). However, our method accurately localized the target size and position. Moreover, TM-FT recovered the fluorescence absorption with high quantitative accuracy with less than 3% error.

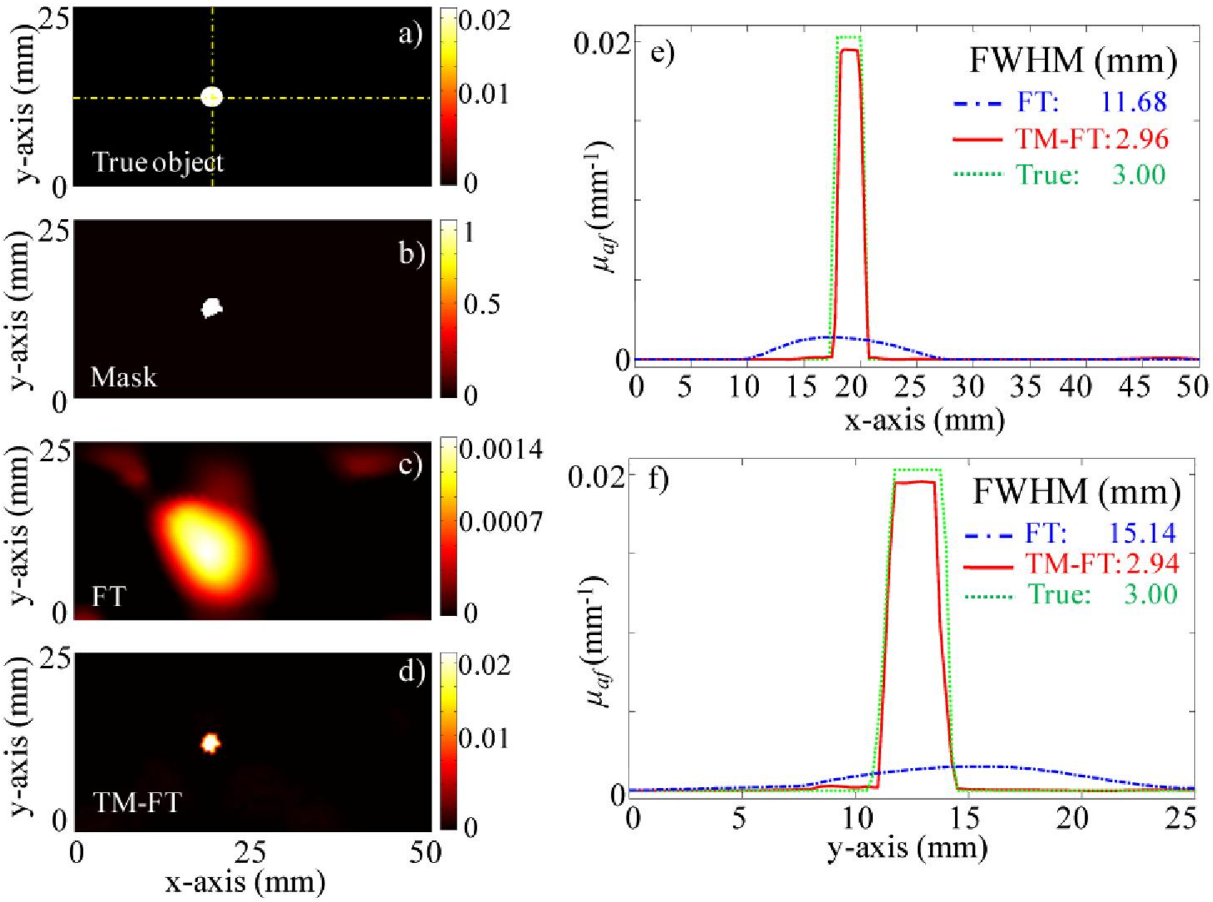

Figure 6. 13 Experiment results for the first phantom with a single 3 mm diameter target. (a) True ThermoDots distribution in the optical fiber plane. (b) Binary map obtained using TM-FT. (c) Reconstructed fluorescence map using conventional FT with no *a priori* information. (d) Reconstructed fluorescence map using TM-FT. The profiles across the fluorescence target along (e) x- and (f) y-directions show that the size of the fluorescence target is accurately recovered.(185)

Next, a second identical target is embedded to test the limits of our method in distinguishing two nearby inclusions. The minimum distance between the two inclusions successfully resolved by our method is ~1.4 mm (Figure 6.14a). This distance is approximately equal to the size of the hot spot of our HIFU (~1.33 mm). Figure 6.14c shows that conventional FT completely fails to resolve the two inclusions. On the other hand, the TM-FT mask represents a high-resolution distribution of the fluorophore prior to any reconstruction process (Figure 6.14b). Using this mask, TM-FT is able to resolve both targets successfully (Figure 6.14d). Moreover, TM-FT overestimates the fluorescence absorption by only ~9%, while conventional FT underestimates it by more than 90%. This small quantitative error of TM-FT is due to the slight underestimation of the target size in the mask (2.87 mm) (Figure 6.14f). The improvement in the spatial resolution is clearly visible on the profiles carried out along the inclusions (Figures 6.14e and 6.14f). In fact, despite the limited source-detector configuration, the spatial resolution is improved not only in the x-axis, but also along the y-axis.

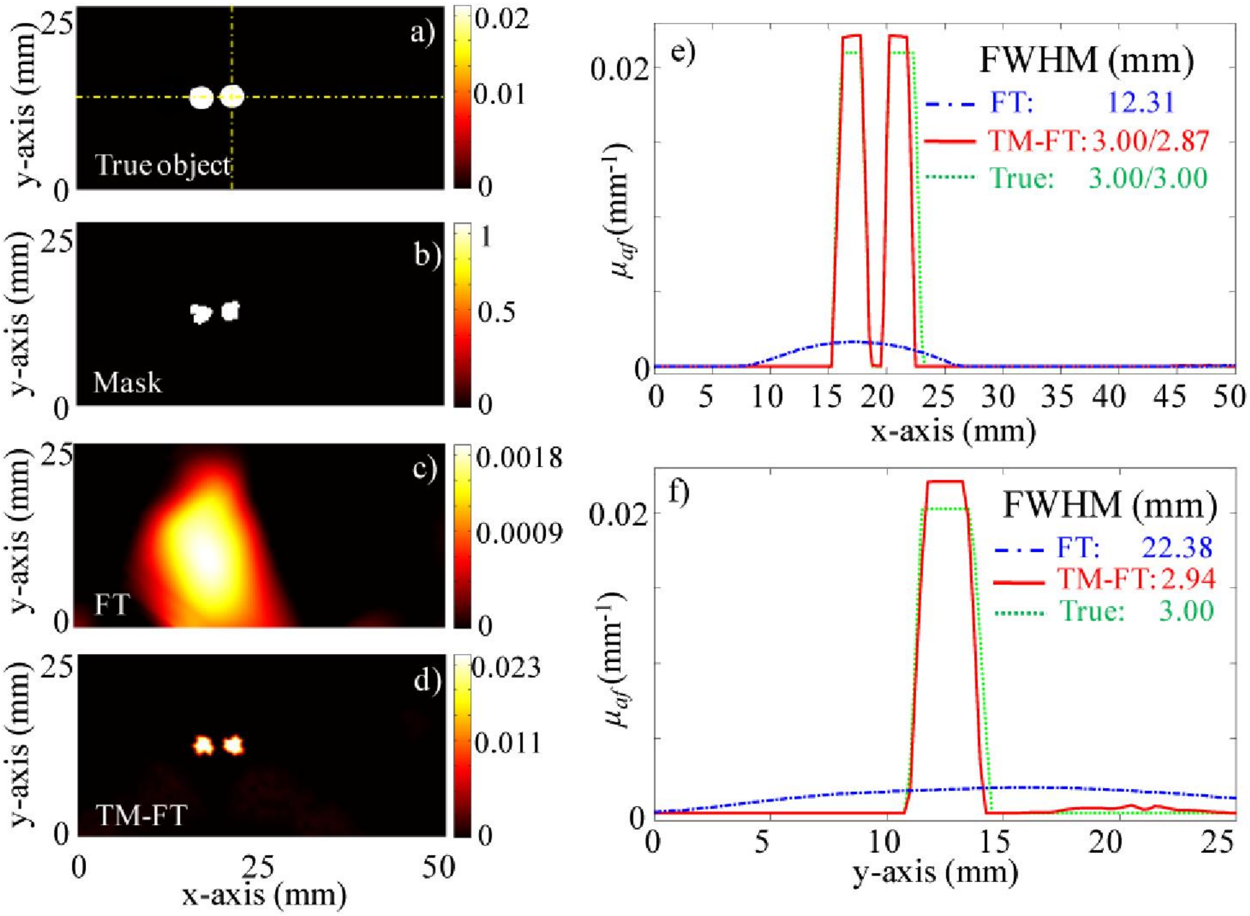

Figure 6. 14 Experiment results for the second phantom with two identical targets separated by 1.4 mm. (a) True ThermoDot distribution in the optical fiber plane. (b) Binary map obtained using TM-FT. (c) Reconstructed fluorescence map using conventional FT with no *a priori* information. (d) Reconstructed fluorescence map using TM-FT. The profiles along the dashed yellow lines (e) x- and (f) y-directions show that the sizes of the fluorescence targets are accurately recovered.(185)

In conclusion, we have demonstrated a new continuous-scan approach that drastically reduces the TM-FT imaging time. This opens the possibility for high-resolution whole-body *in vivo* small animal imaging as this continuous scanning method can image a field-of-view of 50×25 mm in less than 29 min and, hence, reduces the overall imaging time 40 fold compared to the previous step-and-shot mode. Please note that this time reduction is obtained by sacrificing the sensitivity since performing derivative reduces the overall signal to noise ratio by six times for this particular experimental setting. As for any imaging modality, the performance of TM-FT degrades when background fluorescence is present. However, using targeted ThermoDots has the potential to alleviate this effect by selectively accumulating in diseased tissue and increase the performance of TM-FT.

6.5 Experimental procedure

In general, the process for TM-FT consists of the following steps:

1. Data acquisition
2. Calibration and pre-processing of the data
3. Forward modelling of light transport
4. Inverse problem
5. Post-processing
6. Interpretation of parameters

In summary, data acquisition consists of collecting amplitude and phase measurements of the emission signal for the HIFU, FT, and DOT scan. For calibration purposes, an addition FT/DOT measurement is obtained using a homogenous phantom with known optical properties. These measurements are compared with the simulated values obtained from forward modelling and a calibration factor is then obtained for each measurement to convert the experimental data into simulation space to be compared with the simulated data in the inverse problem. The HIFU scan and DOT information are processed and used as *a priori* data to guide and constrain the image reconstruction algorithm. From this image, the optical properties of the medium can be used to extract the location as well as the concentration of the ThermoDots.

6.6 Image Reconstruction

The couple diffusion method (frequency domain) was used to model the propagation of light in tissue to recover the fluorescence parameter μ_{af} which is related to fluorophore concentration. These equations were altered to reflect the temperature dependence of the ThermoDots quantum efficiency as seen below:

$$\begin{cases} -\nabla[D_x \nabla \Phi_x] - [\mu_{af} + \mu_{ax}]\Phi_x = -q_0 \\ -\nabla[D_m \nabla \Phi_m[\eta(T)]] - \mu_{am}\Phi_m[\eta(T)] = -\Phi_x \eta(T)\mu_{af} \end{cases} \quad [6.1]$$

Unlike ICG which has a quantum efficiency of 0.016, η(T) denotes the temperature-dependent fluorescence quantum yield of the ThermoDots. η(T) is obtained by characterizing the ThermoDots prior to the experiment to obtain the fluorescence dependence on temperature. More detains can be found in chapter four. The image reconstruction is described in detail in chapter two.

When DOT was available, both absorption and reduced scattering maps were reconstructed and incorporated into the FT reconstruction algorithm as *endogenous functional a priori*. The *exogenous functional a priori* information is used as 'Laplacian-type *a priori'* to find the fluorophore concentration for the inclusion and the background. In this work, unless otherwise noted, the scattering constant is fixed and only the fluorophore concentration reconstructed. For the FT and TM-FT algorithm, a homogeneous μ_{af} distribution is assumed as the initial guess for the reconstruction. μ_{af} is found by minimizing the difference between the forward solver solution and the measurements. The forward solver solution is obtained by solving the coupled diffusion, (equation [6.1]) with the finite element method using a mesh that consists of N=6034 and 11,775 triangular elements.

6.7 Phantoms

6.7.1 Overview of tissue-mimicking phantoms for optical imaging

Tissue mimicking phantoms are important for biomedical imaging system design, testing, optimization, and validation. An imaging phantom is a specially designed object that can be scanned or imaged to test the performance of an imaging system. Phantoms which can be made from commercially available materials to mimic the properties of living tissue without risk to live subjects. In addition, phantoms can also serve as calibration standards for quality control as they are less complex and produce more consistent results than live biological tissue.

For optical imaging, the main goal is to add absorbers, scatterers, and fluorophores to match the optical properties of the phantom with biological tissue. There are generally three types of tissue-mimicking phantoms for optical imaging: solid, liquid, and agarose gel phantoms. However, with TM-FT, the addition of focused ultrasound makes it necessary to simulate the thermal and mechanical properties of biological tissue as well. Solid phantoms lack the water content to simulate the thermal and mechanical properties of biological tissue. Thus, the phantoms used for TM-FT are mostly liquid and agarose gel phantoms.

6.7.2 TM-FT experimental phantoms

Liquid and agarose gel phantoms are simple and quick to produce. They are quite similar as they both utilize clinical grade Intralipid (Intralipid® 10%, Fresenius Kabi, Uppsala, Sweden) as an optical scatterer, which is inexpensive, widely available, and biocompatible. Commercially Indian ink (Winsor and Newton, UK) is used as an optical absorber. Fluorophores can also be added. The fluorophores could be water soluble (ie, ICG and water soluble quantum dots) or non-water soluble (ie, DTTCI). However, agarose gel phantoms utilize agarose powder (OmniPur® Agarose Gel, EM Science, Gibbstown, NJ) to change the viscosity of the phantom and can be used to tune the mechanical and thermal properties of the agarose gel phantom. This addition of agarose powder requires the phantom to be heated and additional time to cool and set. Thus, liquid phantoms are much faster to make (few minutes versus hours). Just like the liquid phantoms, the agarose gel phantoms require the use of container as they lack a defined shape as the amount of agarose powder is quite low (<1%). This container is shown in Figure 6.15, and holds a

100 mm×40 mm×100 mm sized phantom. The source and detector fibers are placed opposite of each other in the center of the phantom (50 mm below the surface).

In this thesis work, the fluorescence inclusion unfortunately cannot be made from agarose powder due to the small inclusion size. Therefore, thin wall glass and plastic tubes were used to hold the liquid solution containing the ThermoDots as shown in Figure 6.15. However, for optical calibration purposes, a liquid phantom with homogeneously distributed ICG is used.

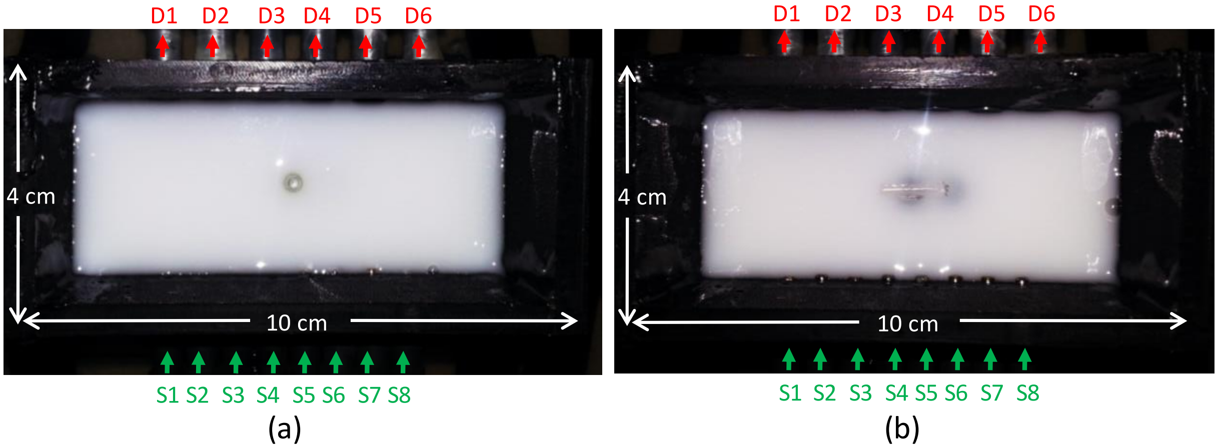

Figure 6. 15 TM-FT phantom holder and liquid phantoms with fluorescent inclusions: (a) glass 3 mm diameter tube inclusion and (b) soft acoustically transparent plastic tube (1 cm length and 2.5 mm diameter). Optical fiber sources are denoted by green arrows and detector fiber bundles by red arrows.

6.8 Summary

In summary, we built a non-contact TM-FT system in which FT and focused ultrasound work together to provide a map of the fluorescence distribution with high spatial resolution. As the focused ultrasound is combined in the same setting as the FT components, this map can easily be used as *soft a priori* to guide the TM-FT reconstruction system. In addition, DOT was also added to the system to recover the background absorption and scattering parameters of the medium. TM-FT is a true multimodality technique relying on both optic and acoustic interaction with the medium under investigation. Before *in vivo* studies, TM-FT must first be validated in *ex vivo* animal tissue. With agar phantoms, the optical parameters were known, however, the addition of DOT opens up the possibility of *ex vivo* tissue samples which better represent the true heterogenous nature of the optical and acoustic properties of live animal tissue.

Chapter 7: Experimental Results

"The fundamental principle of science, the definition almost, is this: the sole test of the validity of any idea is experiment." –Richard P. Feynman

7.1 Feasibility Phantom Studies

7.1.1 Proof of concept[4]

7.1.1.1 Introduction

The ill-posed and underdetermined nature of the inverse problem does not permit optical imaging in thick tissue with high resolution. The main reason is the strong tissue scattering, making direct light focusing infeasible beyond one transport mean free path(49). As one of the optical imaging techniques, fluorescence tomography (FT) utilizes laser light to excite the fluorescence sources located deep in a medium. Once excited, these sources relax to their ground state in nanoseconds by emitting lower energy photons. While propagating towards the surface of the medium, these photons are subject to a vast amount of scattering events along the way. This makes the FT inverse problem exceptionally difficult, which is defined as the problem of recovering the fluorescence source distribution from the measured light intensities on the tissue surface. Accordingly, the resolution and quantitative accuracy of

---

[4] This section (7.1.1 Proof of concept) was reproduced from Applied Physics Letters, Vol 100 Issue 7, Lin, Yuting. et al., Temperature-modulated fluorescence tomography in a turbid media. Page No 073702 Copyright (2012) with permission from AIP Publishing. (34)

the reconstructed images are very low (293). An intriguing solution to this problem is to induce periodic displacement of scattering particles and variation of the refractive index in the medium using a focused ultrasound field. Using this approach and scanning the focused ultrasound field over the probed medium, ultrasound modulated fluorescence tomography (UMFT) can enhance the resolution (137, 138). However, only a small fraction of the photons that travels through the focused ultrasound column can be modulated at a time. The low modulation efficiency and extremely low signal to noise ratio (SNR) are the two main factors that make its implementation difficult. Recently, micro-bubbles that are surface-loaded with self-quenching fluorophores are used to enhance the contrast of UMFT (141, 294). However, the main disadvantage of microbubbles are their instability, low circulation residence times, low binding efficiency to the area of interest especially in the fast-flow conditions, and possible side effects of their destruction during the imaging session (264, 295).

In this thesis, we present an approach that we termed "temperature-modulated fluorescence tomography (TM-FT)." TM-FT also utilizes focused ultrasound, which is rather used to heat the medium, only a couple of degree Celsius but with a high spatial resolution. A key element of the TM-FT is the recently emerged temperature-sensitive fluorescence contrast agents using ICG loaded pluronic nanocapsuless that pave the way for this technique (219, 291). The quantum efficiency of these nanocapsules was shown to be very sensitive to the temperature. For example, when heated from 22 to 40 °C, the fluorescence light intensity emitted by these nanocapsules increases two- to four-fold, and more importantly, this process is reversible. Our TM-FT technique leverages the temperature dependence of these contrast agents to overcome the spatial resolution limitation of conventional FT by using temperature modulation/tagging. In this technique, the medium is irradiated by both excitation light and a high intensity focused ultrasound (HIFU) wave. The crucial benefit of HIFU is that the temperature of the medium is modulated with very high spatial resolution (~1.5 mm) due to the absorption of acoustic power in the ultrasound focal zone. When the temperature sensitive fluorescence agents are present within the HIFU focal zone, local temperature increase affects their quantum efficiency. As a result, the emitted fluorescence light intensity has a substantial change. The difference in the detected fluorescence signal following the HIFU temperature modulation can render the position of these nanocapsules with high spatial resolution. Furthermore, this can be achieved without using a complex reconstruction algorithm as in the case for conventional FT.

7.1.1.2 Methods

7.1.1.2.1 Mathematical framework

To illustrate the TM-FT process for high resolution fluorescence tomography, the light propagation and heat transfer is modeled using a finite element method frame work. With diffusion approximation as the light propagation model in turbid medium, the TM-FT process is formulated with the following equations. Let us assume that the scanning area consists of discrete locations $[\vec{x_i}, i \leq N]$. Equations [7.1] and [7.2] describe conditions before and after the application of the HIFU beam to obtain selectively localized heating in the medium, respectively,

$$-\nabla\cdot(\mathrm{D}\nabla\varphi_0^{\mathrm{m}}) + \mu_{\mathrm{a}}\varphi_0^{\mathrm{m}} = \eta(\mathrm{T}_0)\mu_{\mathrm{af}}\varphi^{\mathrm{x}}$$
[7.1]

$$-\nabla\cdot(D\nabla\varphi_i^m) + \mu_a\varphi_i^m = \eta(T_i)\partial(\vec{x}-\overrightarrow{x_\iota})\mu_{af}\varphi^x\,, 1 \le i \le N—j$$
[7.2]

with the diffusion coefficient D, the absorption coefficient μ_a, the photon density at excitation φ^x and emission wavelength φ^m, and the fluorescence absorption coefficient μ_{af}. The ideal focused heating at $\overrightarrow{x_\iota}$ corresponds to a delta function in equation [7.2], which can be approximated by a compactly supported and fast decaying function in practice. Letting $d_i = \varphi_i^m - \varphi_0^m$ and $c = \eta(T_i)-\eta(T_0)$, we have:

$$-\nabla\cdot(\mathrm{D}\nabla\mathrm{d_i}) + \mu_{\mathrm{a}}\mathrm{d_i} = \mathrm{c}\,\partial(\vec{\mathrm{x}}-\overrightarrow{\mathrm{x_\iota}})\mu_{\mathrm{af}}(\overrightarrow{\mathrm{x_\iota}})\varphi^{\mathrm{x}}, 1 \le \mathrm{i} \le \mathrm{N}$$
[7.3]

The difference measurement d_i, only has values when the scanning step $\overrightarrow{x_\iota}$ is nonzero for $\mu_{af}(\overrightarrow{x_\iota})$. Therefore, when the HIFU scans over the probed medium, the TM-FT could produce high resolution fluorescence images even without any reconstruction process.

7.1.1.2.2 System details

We performed experimental studies to demonstrate that the TM-FT could penetrate several centimeters thick scattering tissue, still at ultrasound resolution (submillimeter to millimeter). The resolution of TM-FT mainly depends on the ultrasound transducer and achieving sub-millimeter resolution is possible using commercially available transducers. The schematic of the system is shown and described in detail Chapter 6, Figure 6.6. A 785 nm laser diode (80 mW) was used for fluorescence excitation and a PMT was used to detect the fluorescence signal due to its high sensitivity. A network analyzer not only provided the RF modulation for the laser-diode but also measured the amplitude of the detected signal at the same time. The commercially available HIFU transducer used had a center frequency of 1.1 MHz and was mounted on a *xyz* translational stage. The lateral FWHM of the focal spot was 1.33 mm and located 6 cm from the transducer surface.

7.1.1.2.3 ThermoDots

The temperature sensitive agent Pluronic ICG was provided by our collaborator from Innosense, LLC. In order to verify the responsiveness of the pluronic-ICG to temperature increase, we recorded the fluorescence intensity and the contrast agent solution temperature at the same time. The pluronic-ICG is placed in a 1 cm wide cuvette, and the fluorescence intensity was measured using the photomultiplier tube with source and detector fibers placed in orthogonal directions. A thermoelectric cooler was used to heat the ThermoDots solution in the cuvette. The temperature of the ThermoDots solution was monitored by a fiber-optic temperature sensor that was inserted in the cuvette while heating. The amplitude signal increased around 5 dB (intensity increases 1.8 times) as the temperature increases only 3-4 °C as shown in Figure 7.1, indicating an increased ICG fluorescence yield.

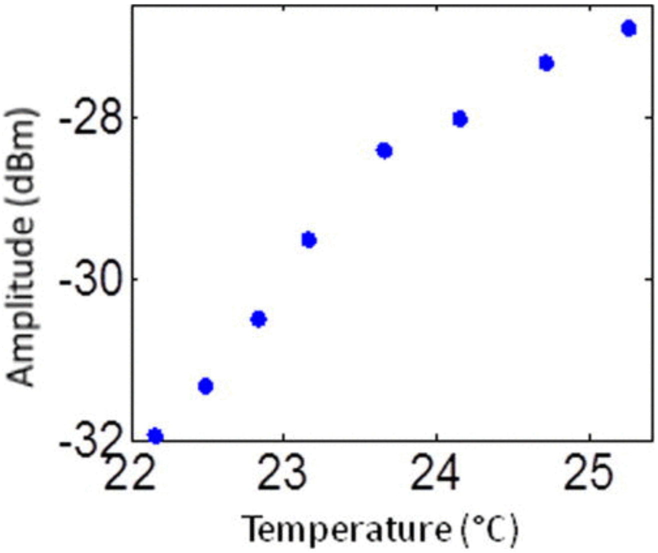

Figure 7. 1 Temperature response of Pluronic ICG. The amplitude signal is recorded with the network analyzer, and the temperature is measured using a fiber optical temperature sensor.(62)

7.1.1.2.4 Phantom set up

A 4 cm × 10 cm × 10 cm slab gel phantom made from agarose is immersed in a water tank. The HIFU transducer is mounted on a xyz translational stage and placed on top of the phantom. The transducer is scanned laterally in both *x*- and *y*-directions. The measurement at each scan position is averaged four times, which yields a 2 second acquisition time for each point. The PSF of the system was measured using a fiber optic temperature sensor and corresponds the FWHM of the heating spot size is 1.8 mm which in turn becomes the spatial resolution limitation for this set-up. The experimental set up can be seen in Chapter 6, Figure 6.7.

7.1.1.3 Results

A 3 mm fluorescence inclusion filled with Pluronic-ICG (Innosense Inc.) is embedded in the middle of the phantom. Intralipid (0.5%) and Indian Ink are added as scatterer and absorber, making the scatter and absorption coefficient of the phantom 0.6 mm^{-1} and 0.005 mm^{-1}, respectively. The actual size, position, and concentration of the inclusion are shown in Figure 7.2a and 7.2b. First, conventional FT measurements are acquired. Figure 7.2c shows the conventional FT reconstruction(133, 190). A region of interest is determined from this image (ROI_{TM}) and then the HIFU is scanned through it (8 mm × 8 mm area) with 0.5 mm steps, Figure 7.2d. For each step, the HIFU power is turned on for 2 seconds, and the resulting temperature in the inclusion is kept below 40 °C. The fluorescence signal variation is mapped to each scanning position, and significant change is observed only when the HIFU hot spot is scanned through the fluorescence object (Figure 7.2e), resulting in a much improved spatial resolution. The comparison of the experimentally measured fluorescence intensity change and those predicted by the theoretical model is shown in Figure 7.2f. Excellent agreement between the theory and the experiment is obtained for this case. There is some deviation observed, which is likely attributed to the contribution of residual heating from the previous scanning step. The profiles plot across the fluorescence source for the true object and the object recovered from the TM-FT is shown in Figure 7.2g. The FWHM of the recovered object size from the TM-FT is 3.2 mm, which is really close to 3.0 mm true object size.

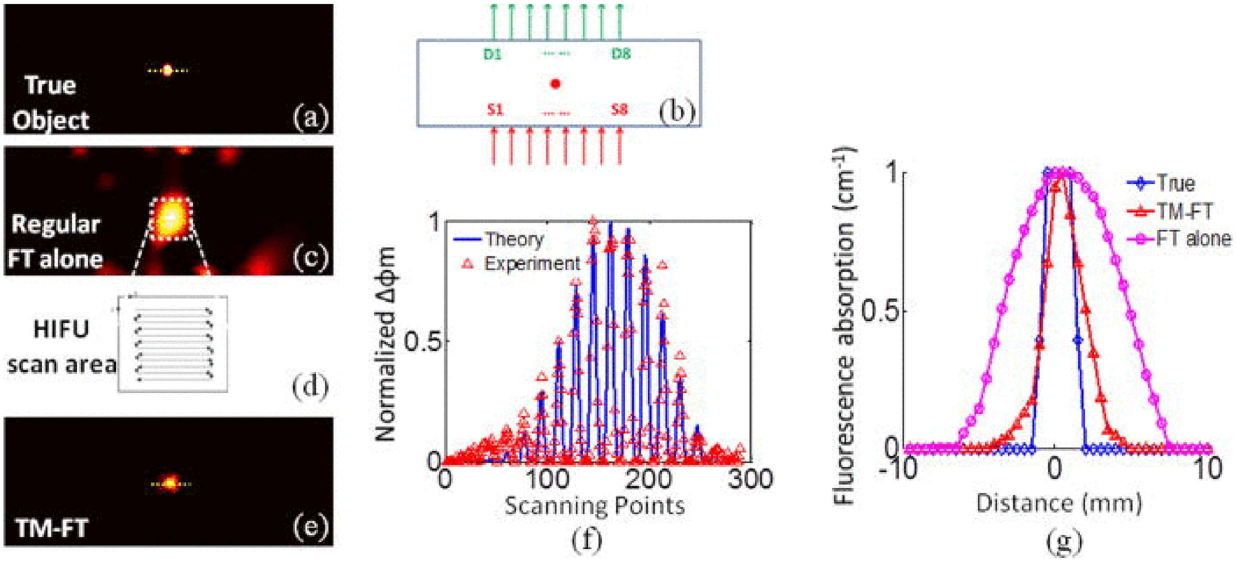

Figure 7. 2 Phantom experiment results. (a) The true size and position of inclusion is shown. (b) The position of the sources and detectors is indicated in 'S' and 'D' numbers. They are placed in opposite side of the phantom to acquire fluorescence measurements in transmission mode. (c) The reconstructed fluorescence map using conventional fluorescence tomography. Meanwhile, the scanning area is determined as indicated by dashed lines. (d) The HIFU transducer is scanned through an 8 mm × 8 mm area while fluorescence measurements are taken. (e) The fluorescence signal only significantly changes when the HIFU hot spot is scanned through the fluorescence object, which reveals the high resolution fluorophore distribution map. (f) The comparison of the experimentally measured fluorescence intensity change and those predicted by the theoretical model. The theoretical prediction is shown in solid lines, while the experimental data is plotted in triangles. (g) The normalized profiles plot across the fluorescence source shows that the size of the fluorescence source is accurately recovered.(62)

7.1.1.4 Discussion

In this study, we have observed the temperature modulated fluorescence signal in scattering medium with HIFU resolution. This technique combines the high sensitivity of fluorescence molecular imaging and high spatial resolution of ultrasound to overcome the ill-posedness of the fluorescence tomography in scattering medium. In the past, there has been extensive effort to improve the resolution of FT. One approach is to integrate FT with other anatomic imaging modalities such as x-ray, MRI, and ultrasound (25, 51, 54, 190, 296, 297). However, the weakness of this approach is that it does not perform well if the fluorescent target cannot be localized in the anatomical image. The low modulation efficiency and extremely low signal to noise ratio make the implementation of ultrasound modulation of fluorescence signals difficult (137, 138). Meanwhile, an intriguing combination of optical and ultrasound techniques has led the development of photo-acoustic tomography (PAT) that can provide the optical absorption maps with much higher resolution (~1 mm) and a depth penetration of 3 to 5 cm(49, 144, 298). PAT has been applied to recover spatially resolved tissue intrinsic contrast maps with very high resolution. Recently, it has demonstrated to provide distribution of exogenous contrast agents using multiple-wavelength measurements, and an enhanced contrast of PAT signal is achieved through fluorescence quenching (145, 146, 299, 300). However, PAT is inherently sensitive to absorption and detects differential increase in absorption due to molecular probes compared to background absorption. In contrast, the TM-FT method that we have demonstrated here is directly sensitive to the fluorescence contrast. Besides obtaining fluorescence images at focused ultrasound resolution, the TM-FT can also render quantitatively accurate images using a proper reconstruction algorithm. This will be an avenue that we will pursue in the near future.

7.1.2 Lifetime and scattering[5]

7.1.2.1 Introduction

Fluorescence imaging is becoming an important molecular imaging tool to identify biomarker distributions *in vivo (10, 13, 48, 301, 302)*. It can potentially play an important role

---

[5] This section (7.1.2 Lifetime and scattering) was reproduced from the Journal of Applied Optics, Vol 17 Issue 5, Lin, Yuting. et al., Temperature-modulated fluorescence tomography based on both concentration and

in preclinical and clinical studies because of its high sensitivity to exogenous contrast agent. There are essentially two fluorescence parameters that can be spatially resolved with this technique, namely fluorescence concentration and lifetime. Most fluorescence imaging systems, especially commercial ones, focus on the measurement of the fluorophore concentration alone. On the other hand, fluorescence lifetime imaging holds promise in investigating the micro-environment of a lesion as demonstrated in the fluorescence lifetime imaging microscope (86, 303, 304). To resolve the lifetime information, a time-dependent measurement technique such as a frequency-domain or a time-domain system is required. Recently, there has been a great interest in developing fluorescence imaging systems based on lifetime contrast (31, 126, 305). Despite the exciting development of highly sensitive and versatile fluorescence probes, the main barrier in widespread use of fluorescence imaging *in vivo*, including in tomographic mode, is the low spatial resolution caused by strong tissue scattering. The recovered fluorescence parameters highly depend on the size and depth of the fluorescence source. For that reason, a fluorescence imaging system that can resolve both fluorescence concentration and lifetime with high resolution in deep tissue is highly desired.

Recently, temperature-sensitive fluorescence contrast agent has been reported with use of indocyanine green (ICG)-loaded pluronic nanocapsules (219, 291). As the temperature changes, the interiors of nanocapsules change their hydrophobicity/hydrophilicity, which in turn changes the quantum efficiency of the loaded ICG. It has been reported that fluorescence lifetime is also sensitive to the solvent polarity

---

lifetime contrast. Page No 0560071-0560074. Copyright (2012) with permission from the Society of Photo Optical Instrumentation Engineers. (106)

(84). Therefore, it is expected that the lifetime of pluronic-ICG is also responsive to temperature change. Such temperature dependence of these contrast agents provides a major opportunity to overcome the spatial resolution limitation of conventional fluorescence imaging by using temperature modulation. In this second experimental study, we demonstrate a temperature-modulated fluorescence tomography (TM-FT) system, which utilizes the temperature dependence of ICG-loaded pluronic nanocapsules and achieves fluorescence imaging at focused ultrasound resolution. The medium is irradiated by both excitation light and a high intensity focused ultrasound (HIFU) wave. The HIFU scans through the medium with low power and sequentially generates a hot spot to elevate the temperature of a small area a few degrees. When the temperature-sensitive fluorescence agent presents within a HIFU focal zone, the local temperature increase in turn changes the fluorescence quantum efficiency and lifetime inside the focal zone. We have previously demonstrated a similar system that only monitors the change in quantum efficiency; however, the TM-FT system presented here operates in the frequency domain, which is essential for lifetime imaging (62). In this work, we experimentally demonstrate imaging fluorescence objects in scattering tissue through several centimeters based on both fluorescence intensity and lifetime contrast, yet both parameters can be resolved at focused ultrasound resolution (~ 1 mm) with our TM-FT system.

7.1.2.2 Methods

7.1.2.2.1 Instrumentation

A frequency-domain system was constructed to measure both fluorescence intensity and lifetime as a function of temperature. As a first step to verify the responsiveness of the

ThermoDots to temperature change, the sample was heated and cooled in a controlled manner by a thermoelectric cooler. The change in fluorescence signal was recorded, together with the temperature of the contrast agent solution. A diagram of the measurement system and experimental setup can be seen in Figure 5.5.

A 785-nm laser diode (80 mW) was utilized for fluorescence excitation, while a fiber optic switch was used to switch the laser on and off. For fluorescence light detection, a photomultiplier (PMT) detection unit was used. A network analyzer provided a 100 MHz RF signal for the laser-diode amplitude modulation and also measures the amplitude and phase of the detected fluorescence signal. The change in amplitude and phase indicates variation in fluorescence quantum efficiency and fluorescence lifetime, respectively (178, 306, 307). More details on the experimental set up can be found in section 6.3.2.

For the phantom experiment, a high intensity focused ultrasound (HIFU), utilized in a low power mode, was used to heat the ThermoDots which were embedded in an agarose tissue-simulating phantom. The HIFU transducer had a center frequency of 1.1 MHz and was mounted on a *x*, *y*, *z* translational stage and used to generate a focused hot spot. The lateral FWHM of the focal spot was 1.33 mm, located 6 cm from the transducer. The transducer was driven by a function generator and power amplifier. More details can be found in section 6.3.2.

7.1.2.2.2 ThermoDots

The thermo-responsive ThermoDots were provided by our collaborators from InnoSense LLC. To characterize the temperature dependent response of the ThermoDots, the agent was characterized using the system described in section 5.3.2. The sample was heated slowly for about 1 min, and the temperature increase is kept below 5°C. Each fluorescence measurement was averaged eight times and completed in 2 seconds. The temperature and fluorescence measurements were sampled and recorded with a temporal resolution of 10 seconds. The results are shown in Figure 7.3. The amplitude increases about 5 dBm (intensity increases 1.8 times) as the temperature is elevated by only 3°C, indicating an increase in the ICG fluorescence quantum yield. At the same time, the phase decreases about 6 degrees, indicating an increased ICG lifetime. These results are in agreement with the previously published study on the dependence of fluorescence quantum efficiency and lifetime to solvent polarity (62, 81, 84, 178, 267, 306-309). With increased temperature, the interior of micelles becomes more hydrophobic, resulting in an increase in both fluorescence quantum efficiency and lifetime.

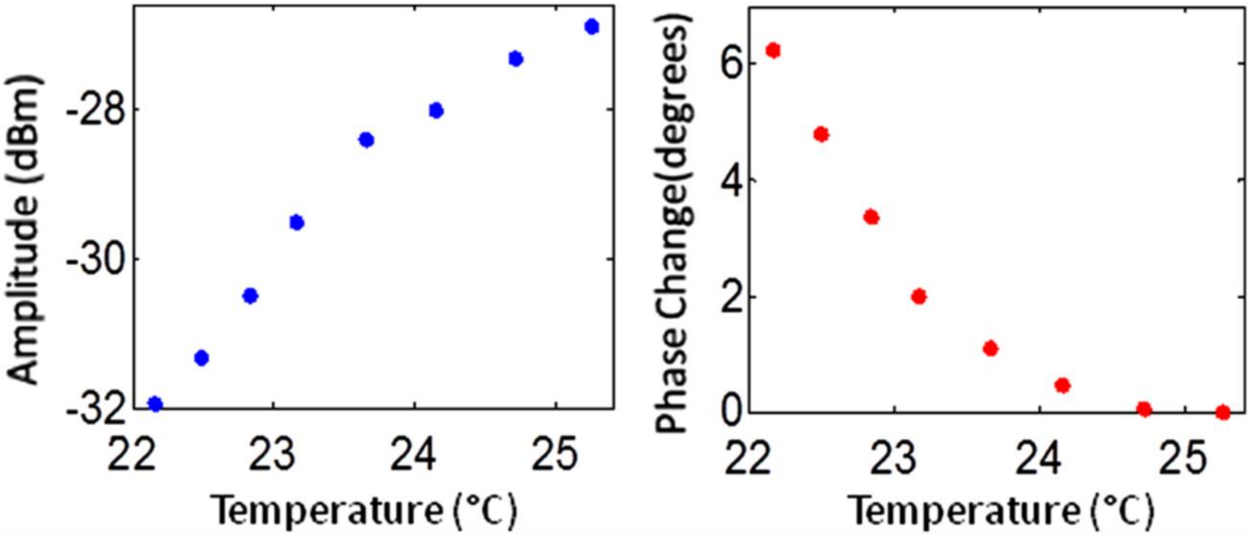

Figure 7. 3 Network analyzer measurements of the amplitude and phase change of the fluorescence signal as the sample temperature increases several degrees.(63)

7.1.2.2.3 Phantom setup

A 4 x 10 x 10 cm slab agar phantom was immersed in a water tank. The transducer was scanned laterally in both the *x*- and *y*-directions above the phantom. The measurement was averaged four times, yielding an acquisition time of 2 seconds for a particular transducer position. A 3-mm fluorescence inclusion filled with the ThermoDots were embedded in the middle of the phantom. Additions of 0.5% Intralipid and Indian Ink were used to set the reduced scattering and absorption coefficient of the phantom to 0.005 mm^{-1} and 0.6 mm^{-1}, respectively. The actual size, position, and concentration of the inclusion are shown in Figure 7.4a. During the measurements, the focused ultrasound was scanned over an 8 x 8 mm area at 1-mm steps (Figure 7.4b). At each step, the focused ultrasound was turned on for 2 seconds, and the power was adjusted to keep the temperature at the focal spot below 40°C. The change in both fluorescence signal amplitude and phase was mapped to each scanning position.

7.1.2.3 Results

A phantom study was performed to demonstrate the feasibility of a TM-FT system for resolving a temperature-sensitive fluorescence agent at high spatial resolution based on both intensity and lifetime contrast. Figure 7.4 shows the phantom study results. Both amplitude and phase only significantly vary when the HIFU hot spot is scanned through the fluorescence object [Figure 7.4 (c) and 7.4 (d)], resulting in a much improved spatial resolution. As seen from the profiles across the fluorescence inclusion [Figure 7.4 (e) and 7.4 (f)], the FWHM of the inclusion recovered from both intensity and lifetime maps is the same, 3.2 mm.

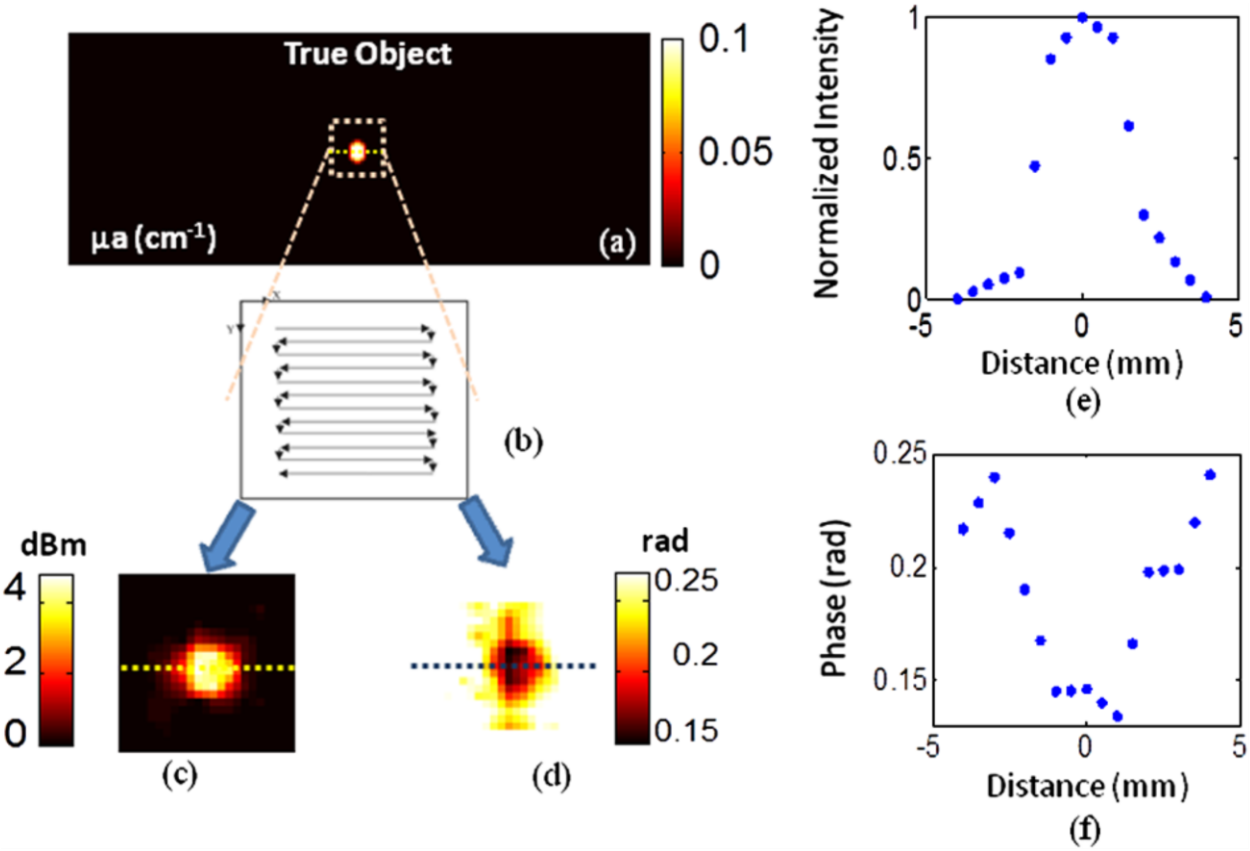

Figure 7. 4 Phantom experiment results. (a) The true size, position, and concentration of the inclusion are shown. A 3-mm inclusion filled with Pluronic-ICG is embedded in the middle of a 4 × 10 cm phantom. (b) HIFU is scanned through an 8 × 8 mm area while fluorescence measurements are taken. (c), (d) The fluorescence intensity and lifetime signal only change significantly when the HIFU hot spot is scanned through the fluorescence object, which reveals the high resolution fluorophore distribution map. (e), (f) The normalized profiles plotted across the fluorescence inclusion show that the size of the object is accurately recovered based on both intensity and lifetime contrast. (63)

7.1.2.4 Discussion

This study successfully observed a temperature-modulated fluorescence signal in scattering medium with HIFU resolution. Especially the lifetime contrast mechanism, which is independent of fluorescence intensity, could be robustly recovered with high resolution. A frequency-domain TM-FT system was constructed and used to acquire time-resolved fluorescence measurements. The frequency-domain system was chosen because of its relatively low cost and fast acquisition time. A time-domain system can also be integrated into a TM-FT system to extract lifetime information (117, 305). Furthermore, it is feasible to use a tomographic approach to quantify the fluorescence concentration and lifetime if the actual temperature change can be predicted through proper modeling of the HIFU pressure field and bio-heat transfer equation (187). However, this is beyond the scope of this study and will be investigated in the future.

TM-FT combines the optical contrast of fluorescence imaging and the spatial resolution of focused ultrasound, which is also the nature of another technique called ultrasound modulated fluorescence tomography (UMFT) (138, 139). The main difference is that TM-FT measures the direct amplitude and phase change caused by the temperature elevation in the focal zone, while UMFT utilizes direct ultrasound modulation of the optical signal in the focal zone. Therefore, the spatial resolutions of both TM-FT and UMFT are limited by the focused ultrasound spot size and thus are expected to be similar. On the other hand, UMFT has low modulation efficiency and an extremely low signal-to-noise ratio, which are the two main factors that make its implementation difficult. Another intriguing technique is photo-acoustic tomography (PAT), which can provide optical absorption maps at ultrasound resolution (~1 mm) and a depth penetration of 3 to 5 cm (49, 144, 298). It has been demonstrated to provide distribution of exogenous contrast agents using multiple-wavelength measurements (145, 146, 299). However, the main difference is that PAT is inherently based on absorption contrast and detects differential increase in absorption from comparing molecular probes to background, whereas TM-FT measures the exogenous fluorescence signal directly.

In conclusion, this study demonstrated a temperature-modulated fluorescence tomography system that effectively obtains fluorescence intensity and lifetime contrast at ultrasound resolution. This novel technique can potentially contribute to the development of new temperature-sensitive contrast agents. Future work includes establishing a mathematical framework for TM-FT, extensively investigating the sensitivity and spatial resolution, and performing verification through *in vivo* studies.

7.2 Tissue simulating phantom studies [6]

7.2.1 Introduction

The previous study showed the feasibility of TM-FT and used a step and shoot scanning method. However, the small size of the scan and the length of time was not optimal. To optimize the system for animal studies, the new faster scanning method was introduced to reduce the data acquisition time drastically (185). In this approach, the focused ultrasound transducer is moved continuously while the fluorescence signal is monitored as opposed to the slow step-and-shoot approach previously employed (62). This method is described in detail in Chapter 6, section 6.4.3. In this study, the performance of this new fast TM-FT system was investigated with an extensive experimental phantom study using the

---

[6] This section (7.2 Tissue simulating phantom studies) was reproduced from Applied Optics, Vol 56 Issue 3, Kwong, T. C. et al., Experimental evaluation of the resolution and quantitative accuracy of temperature-modulated fluorescence tomography. Page No 521-529. Copyright (2017) with permission from Optical Society of America. (285)

new scanning method. The experimental studies were used to evaluate the effect that size, depth, and concentration of the fluorescence target has on the performance of TM-FT.

Four phantom studies were performed to test the performance of the TM-FT system to accurately recover the correct absorption. In the first part of this study, the linearity of the system response was tested using inclusions filled with various dilutions of the activatable and thermo-reversible ThermoDots. Next, the depth and size dependence of the fluorescent inclusion on the recovered ThermoDots concentration was evaluated for TM-FT and compared to conventional FT. Finally, the spatial resolution limit of the system was studied. In all cases, utilization of the focused ultrasound *functional a priori* information from TM-FT resulted in a significant improvement in the spatial resolution and quantitative accuracy compared to conventional FT.

7.2.2 Methods

7.2.2.1 Instrumentation

All experiments were performed with a custom-built system developed for TM-FT described in Chapter 6, section 6.3.3. This system integrated focused ultrasound with a conventional frequency-domain FT system. A 790 nm laser modulated by a 100 MHz signal was used to illuminate the object under investigation in transillumination mode. A PMT was used to detect and amplify the filtered fluorescent light. A focused ultrasound transducer with a focal spot (~1.33 mm in diameter and 10 mm in length) located 60 mm below the transducer was used to provide localized heating; see Figure 7.5a. The transducer was set to produce a 4°C increase in temperature and mounted on two computer-controlled automatic translational stages in the xy-plane. A third manual translational stage allowed height adjustments for the transducer above the phantom. Both the transducer and the optical interface that held the fibers together with the phantom were submerged in water.

The fully automated focused ultrasound scanning procedure covered a 50 mm x 25 mm area, as shown in Figure 7.5b. This procedure consists of two x-scans, as indicated by the dashed blue lines, and two y-scans, as indicated by the dashed red lines, with one scan moving in a forward direction and the other scan moving in the reverse direction. The distance between each scanning line was 1.35 mm, nearly the diameter of the focal spot of the transducer, in both x- and y-directions. To avoid the effect of heat diffusion from adjacent lines, a jumping pattern was utilized instead of scanning lines in a consecutive fashion. During these scans, the transducer was turned on continuously while the network analyzer recorded the fluorescence data collected from the source/detector pair with the highest signal-to-noise ratio (SNR). A filtering window of five data points wide, which roughly corresponded to the size of the focal spot (~1.33 mm) of the transducer was used to smoothen the measured signals. The FWHM was used as a threshold to create a binary map of the position of the ThermoDots with high spatial resolution. This binary map was used as *functional a priori* to constrain the reconstruction algorithm. A more detailed explanation of the focused ultrasound continuous scanning method can be found in Chapter 6, section 6.4.3.

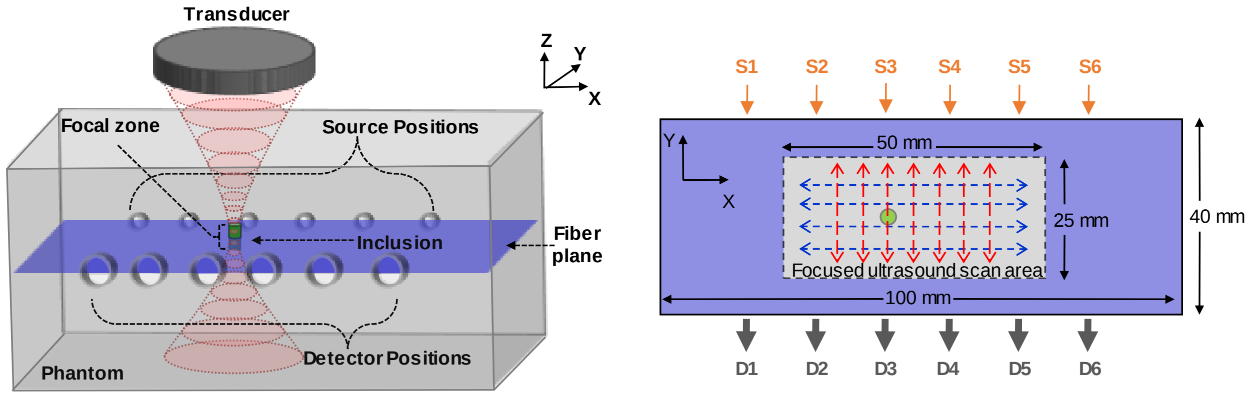

(a) (b)

Figure 7. 5 Experimental set up. (a) Three-dimensional schematic of the phantom and focused ultrasound transducer. The transducer produces a focal zone of ~1.33 mm in diameter and 10 mm in length. The centers of the focal zone as well as the ThermoDots inclusion (green cylinder) are in the same plane (blue plane) as the source and detector optical fibers. (b) Cross-sectional view of the phantom at the fiber plane [blue plane in Figure 1(a)] located 50 mm below the surface. The transducer is scanned over the focused ultrasound scan area (gray) in orthogonal directions forming the xx-scan (blue dashed lines) and the yy-scan (red dashed lines). Six source fibers (1 mm diameter, orange arrows) and six detector fibers (6 mm diameter, gray arrows) are positioned at opposite ends of the phantom for transillumination measurements. (310)

7.2.2.2 Optical image reconstruction algorithm

Since the quantum efficiency of the ThermoDots is temperature dependent, the coupled diffusion equation at the emission wavelength is altered to account for this dependence on temperature:

$$\begin{cases} -\nabla[D_x \nabla \Phi_x] - [\mu_{af} + \mu_{ax}]\Phi_x = -q_0 \\ -\nabla[D_m \nabla \Phi_m[\eta(T)]] - \mu_{am}\Phi_m[\eta(T)] = -\Phi_x \eta(T)\mu_{af} \end{cases} \quad [7.4]$$

where $\eta(T)$ denotes the temperature-dependent fluorescence quantum yield, and q_0 is the isotropic excitation light source. For the following variables, the subscripts x and m represent the excitation and emission wavelengths, respectively. $\Phi(W \cdot mm^{-2})$ is the photon density, and D describes the diffusion coefficient, $D = 1/3(\mu_a + \mu_s')$. The absorption and reduced scattering coefficients of the medium are represented by μ_a and μ_s', respectively. μ_{af} is the absorption coefficient of the fluorophore and is directly related to its concentration. The synthetic fluorescence signal for the source (s) and detector (d), $S_{s,d}$ (s,d=1,2,…,6), are obtained by solving the coupled diffusion equation [7.4] with the finite element method using a mesh that consists of N=6034 nodes and 11,775 triangular elements.

The absorption coefficient of the fluorescence map, μ_{af}, is recovered by iteratively minimizing the quadratic error between these synthetic signals and the fluorescence ones, $F_{s,d}$, measured on the surface of the phantom. The update to the absorption coefficient of fluorescence, $\Delta\mu_{af}$, is obtained using the Levenberg–Marquardt minimization algorithm after incorporating the binary mask provided by TM-FT as soft *a priori* (129, 133):

$$\Delta\mu_{af} = (J^T J + \lambda L^T L)^{-1} J^T \left(F_{s,d} - S_{s,d}\right)^2 \tag{7.5}$$

where J represents the Jacobian matrix (M×N), with M=36 being the number of measurements. λ is the inversion regularization factor. L (N×N is the Laplacian-type *a priori* matrix used to incorporate the binary mask and constrain the reconstruction process. The value of L for a couple of nodes i and j is given by

$$L_{i,j} = \begin{cases} 0 & i,j \text{ in different regions} \\ -1/N_r & i,j \text{ in the same region} \\ 1 & i = j \end{cases} \tag{7.6}$$

with N_r being the number of nodes in a given region. More details on this method have been published previously and can be found in Chapter 3 (129, 185, 189).

7.2.2.3 ThermoDots

The ThermoDots were prepared by our industrial collaborator, InnoSense LLC (USA) and consist of 20 μM ICG encapsulated in 4% Pluronic-F127 polymeric micelles. The ThermoDots were characterized to determine their thermo-responsiveness and active temperature range. For these phantom studies, the ThermoDots were optimized to perform at room temperature (20°C) for convenience and measured a 23 dBm (~15x) increase in the signal amplitude between 20°C and 24°C. The phantom experiments are performed at 20°C and the focused ultrasound is set to heat the medium by 4°C at its focal spot to maximize the fluorescence signal change. More details on the ThermoDots preparation and characterization can be found in Chapter 5, sections 5.2 and 5.3.

7.2.2.4 Phantom Studies

The experiments carried out in this phantom study were performed using a 100 mm x 40 mm x 100 mm phantom-mimicking biological tissue. The phantoms were prepared using intralipid (0.5%) and India ink (Winsor and Newton, UK) to respectively simulate the tissue scattering and absorption optical properties. The absorption and reduced scattering of the phantom were the same for both excitation and emission wavelengths and set to μ_a=0.008 mm^{-1} and μ'_s=0.86 mm^{-1}, respectively.

The inclusions were made from optically transparent glass tubes of varying diameters cut down to 10 mm in length. For the first set of experiments, a 3 mm diameter tube was filled with various concentrations of the ThermoDots to measure the linearity of the system. To investigate the size dependence, tubes with different diameters were utilized (5, 4, 3, and 2 mm) and filled with an 837 nM ThermoDots solution. Following that, a single 3 mm diameter inclusion at the same concentration was positioned at various depths to explore the depth dependence. Finally, two identical 3 mm diameter inclusions were positioned in the center with different separations to evaluate the spatial resolution and performance of TM-FT. In all cases, the axis of the tube was aligned with the focused ultrasound column in the z-direction and centered in line with the optical fiber plane.

7.2.3 Results

7.2.3.1 Phantom study I: Linearity

For this study, a single 3 mm glass tube is imbedded in the tissue mimicking phantom as described previously in Figure 7.6. The tube is consecutively filled with four concentrations of the ThermoDots to investigate the performance of TM-FT in accurately recovering different concentrations. Dilutions are performed on the ThermoDots solution (100%, 90%, 75%, and 50%) to achieve four different concentrations: 837 nM, 782 nM, 516 nM, and 358 nM. Fluorescence absorption coefficient images of the ThermoDots are reconstructed without and with the functional *a priori* information provided by the focused ultrasound. The ThermoDots concentration maps were obtained from the fluorescence absorption images and are shown in Figure 7.6.

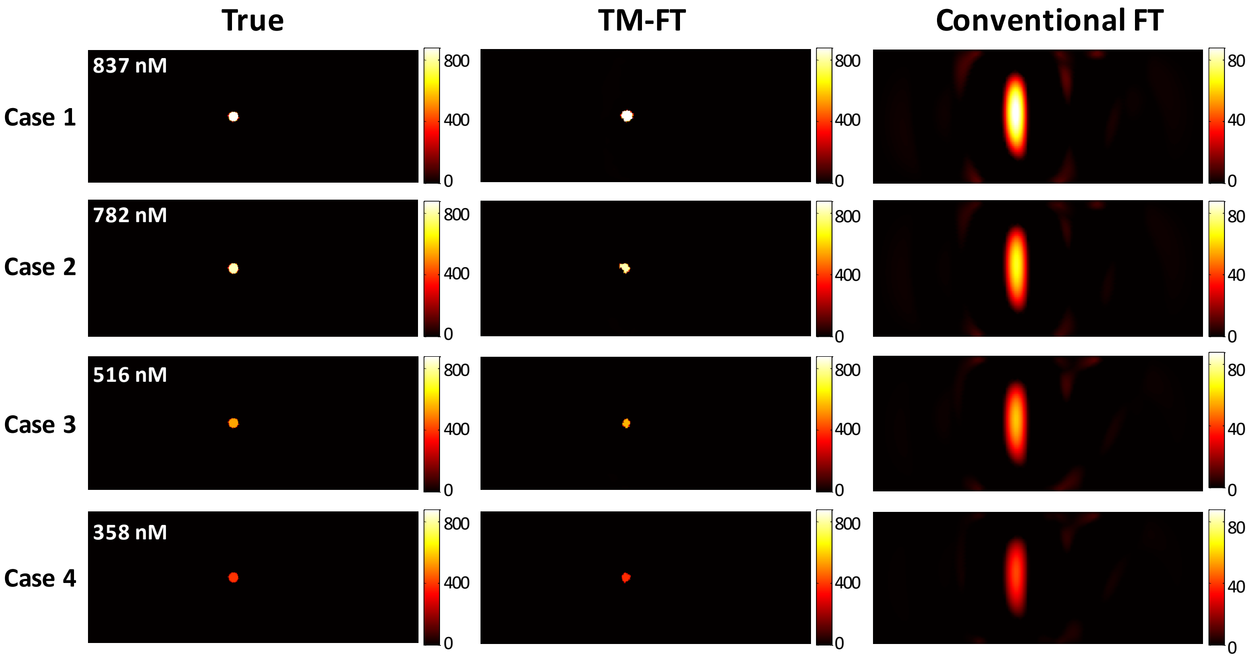

Figure 7. 6 Experimental results 1: linearity. Reconstructed ThermoDots concentration maps comparing TM-FT (middle column) and conventional FT (right column) to the true value (left column) for four different ThermoDots concentrations. Case 1: 837 nM; Case 2: 782 nM; Case 3: 516 nM; and Case 4: 358 nM. The color bars all have units of nM.(310)

Figure 7.6 shows the ThermoDots concentration images reconstructed without and with the *functional a priori* information provided by the focused ultrasound. As seen from this figure, the ThermoDots concentration is accurately recovered with TM-FT and has less than a 4% error for all four cases compared to conventional FT, which greatly underestimates all four concentrations (factor of 10). In addition, although the size of the inclusions is overestimated using conventional FT, the addition of the focused ultrasound *functional a priori* information of TM-FT considerably improves the recovered size of the inclusion. The results of the concentration and inclusion size recovered from TM-FT and conventional FT are summarized in Table 7.1.

Table 7. 1 Recovered ThermoDots Concentration and Size of Inclusions with TM-FT and Conventional FT for Phantom Study 1: System Response Linearity.(310)

	True		**TM-FT**			**Conventional FT**		
Case	Concentration (nM)	FWHM (mm) x/y	Concentration (nM)	% error Concentration	FWHM (mm) x/y	Concentration (nM)	% error Concentration	FWHM (mm) x/y
1	836.5	3.00/3.00	838.2	0.2%	3.00/3.25	86.9	89.6%	5.75/19.25
2	782.4	3.00/3.00	777.1	0.7%	2.50/3.00	65.0	97.7%	5.75/19.25
3	516.0	3.00/3.00	536.2	3.9%	2.25/2.50	55.5	89.2%	5.50/18.25
4	357.9	3.00/3.00	366.3	2.3%	2.75/2.75	39.4	89.0%	5.0/18.00

Figure 7.7 shows that the recovered ThermoDots concentration is linear with respect to the true concentration for both TM-FT and FT alone. The correlation coefficient for TM-FT and stand-alone FT fitted curves is 0.998 and 0.863, respectively. Although linear, the recovered ThermoDots concentration is severely underestimated with FT alone. However, the accuracy of the recovered ThermoDots concentration is greatly improved for all cases when the functional *a priori* information of TM-FT is utilized. This can be seen as the slope as TM-FT is close very close to 1 with a slope of 0.968 compared to 0.081using conventional FT.

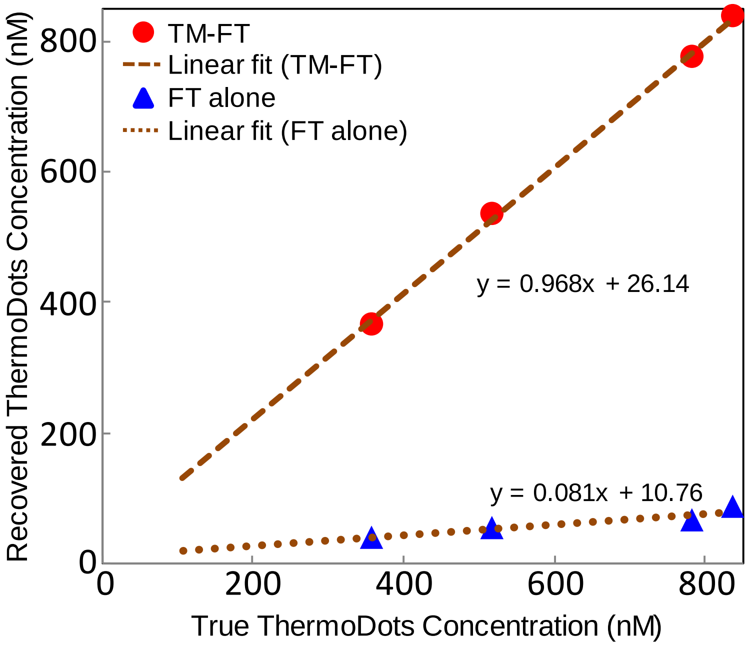

Figure 7. 7 Plot of the recovered versus true ThermoDots concentrations. The red circles and blue triangles represent the recovered values with TM-FT and FT, respectively. The dashed and dotted lines represent the least squares linear fit for both cases. Although both TM-FT and FT alone show a linear response with respect to the true ThermoDots concentration, only TM-FT recovers the correct concentrations. The correlation coefficient for the TM-FT and stand-alone FT fitted curves is 0.998 and 0.863, respectively.(310)

Indeed, the recovered concentration accuracy directly depends on the spatial resolution of the system. For the conventional FT, the spatial resolution in the *y* direction is expected to be lower than the *x* direction due the transillumination configuration of the system. This can be seen by comparing the recovered size of the inclusion in orthogonal directions. For all four cases, the recovered object size in conventional FT images is significantly larger in the *y* direction (~6x) compared to the *x* direction (~1.6x). Accordingly, as the ThermoDots fluorescent signal is attributed to a larger area, this resulted in a large percent error in the recovered concentration (≥89%).

TM-FT uses the focused ultrasound scan to create a binary map of the ThermoDots distribution with high spatial resolution. With the addition of this *functional a priori* data, TM-FT is able to recover quantitatively accurate concentration values for the ThermoDots with less than 4% error. TM-FT is not affected by the source–detector geometry as the spatial resolution of TM-FT is primarily determined by the focused ultrasound. The error in the recovered size of the ThermoDots is even in both the *x* and *y* directions and varies between 0–25% in the recovered size of the object for the four concentrations.

A slight trend is observed with the higher concentrations of the ThermoDots (Case 1 and 2) having a smaller percent error than Cases 3 and 4. This is reasonable as the lower concentrations would result in a lower fluorescent signal and lead to a lower SNR, which makes recovering the concentration more challenging.

7.2.3.2 Phantom study II: Size dependence

The performance of TM-FT in recovering inclusions of different sizes is studied using four different sized inclusions: 5 mm, 4 mm, 3 mm, and 2mm. The inclusions are positioned equidistance between the source and detector fibers as seen in Figure 7.8. The recovered absorption maps of the ThermoDots obtained with TM-FT and conventional FT are presented in Figure 7.8.

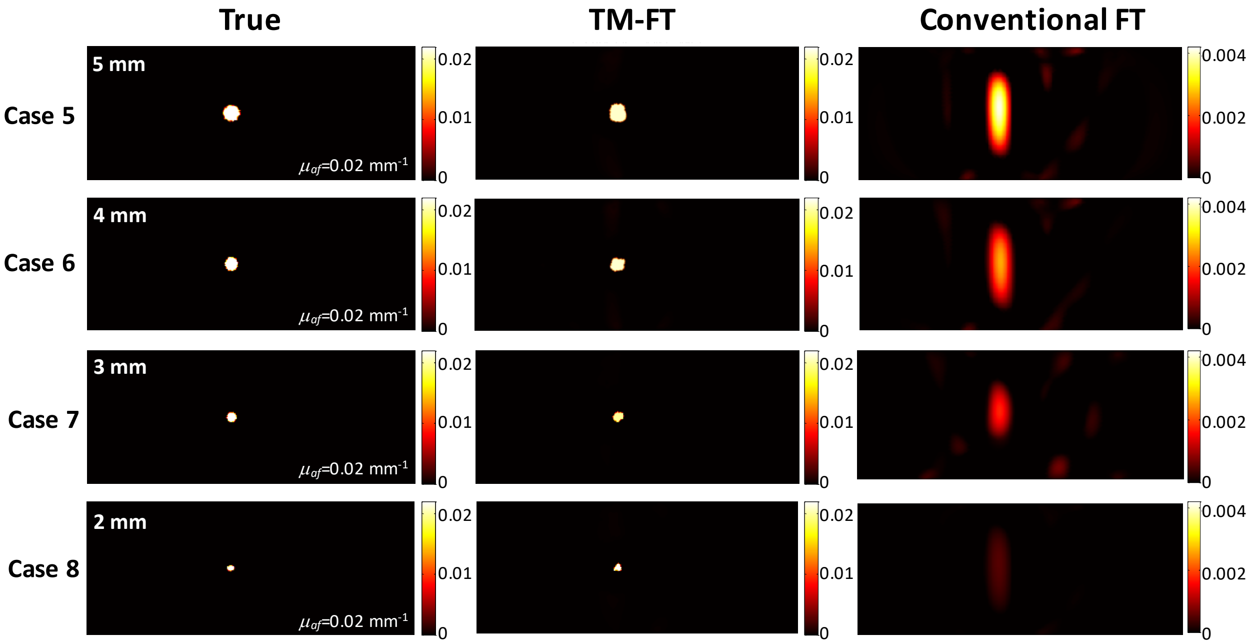

Figure 7. 8 Experimental results 2: size dependence. Reconstructed ThermoDots absorption maps comparing TM-FT (middle column) and conventional FT (right column) to the true values (left column) for the different sized inclusion diameters. Case 5: 5 mm; Case 6: 4 mm; Case 7: 3 mm; and Case 8: 2 mm. As seen in the images, the reconstructed absorption depends on the size of the inclusions for conventional FT. However, when the *functional a priori* is used for TM-FT, the true value can be reconstructed with less than 12% error for all cases. The color bars all have units of mm^{-1}.(310)

The effect that the size of the inclusion has on the accuracy of the recovered absorption for all four phantoms can be seen in Table 7.2. For conventional FT, the inclusion is overestimated in both length and width and greatly underestimated the absorption of the ThermoDots for all four sizes. The error in the recovered absorption is over 90% for all four cases. The error in the recovered size and absorption also increased as size of the inclusion decreased. This trend can be seen for conventional FT as the recovered absorption increases from 0.000649 mm^{-1} to 0.004065 mm^{-1} compared to the true value of 0.02 mm^{-1}, as the size of the inclusion increases from 2 mm to 5 mm. As expected, the accuracy of the recovered ThermoDots absorption is higher when the inclusion is of larger size. This follows as a larger sized inclusion filled with the same ThermoDots concentration, will emit a higher fluorescent signal and result in a higher SNR.

However, the addition of the *functional a priori* information using TM-FT improved the size and quantitative accuracy considerably. For the larger size inclusion, 5 mm and 4 mm, the inclusion was accurately recovered in the *x*-direction (length) but slightly overestimated the width for Case 1 and underestimated the width for Case 2 with an error of 5% and 6.25%, respectively. The recovered absorption for both cases was close to the true value of 0.02 mm^{-1} at 0.01898 mm^{-1} and 0.01899 mm^{-1}, respectively. For the 3mm object, the size of the inclusion was slightly overestimated at 3.25 mm in both the width and length. The recovered absorption was very close to the true value at 0.01977 mm^{-1} with a 1.15% error. For Case 8 with the smallest inclusion (2 mm diameter), the object size was close to the true value but slightly overestimated in *y*-direction (width) at 2.25 mm. The recovered absorption was 0.0224 mm^{-1} with an error of 12%.

Table 7. 2 Recovered ThermoDots Fluorescence Absorption and Size of Inclusions with TM-FT and Conventional FT for Phantom Study 2: Size Dependence. (310)

	True		**TM-FT**			**Conventional FT**		
Case	μ_{af} (mm^{-1})	FWHM (mm) x/y	μ_{af} (mm^{-1})	% error μ_{af}	FWHM (mm) x/y	μ_{af} (mm^{-1})	% error μ_{af}	FWHM (mm) x/y
5	0.02	5.00/5.00	0.0190	5.1%	5.00/5.25	0.0041	91.3%	5.75/19.25
6	0.02	4.00/4.00	0.0190	5.1%	4.00/3.75	0.0026	94.4%	5.75/19.00
7	0.02	3.00/3.00	0.0198	1.2%	3.25/3.25	0.0018	94.7%	5.75/13.00
8	0.02	2.00/2.00	0.0224	12.0%	2.00/2.25	0.0007	96.8%	5.25/20.25

For all four cases, the recovered size of the ThermoDots inclusion is off by only ± 0.25 mm and is not size dependent. With TM-FT, there is only a slight size dependence as the recovered concentration for cases 5-7 are close to the true value and have similar error. The percent error in the recovered absorption for the 2 mm case is more than double the error of cases 5-7 but still acceptable at 12%. Overall, the recovered size and absorption of the ThermoDots inclusion using TM-FT is within a 12.5% and 12% error respectively, indicating that size dependence of TM-FT is minimal as long as the object is equal to or larger than the focused ultrasound focal spot.

7.2.2.3 Phantom Study III: Depth dependence

To study the effect the position of the inclusion has on the recovered fluorescence absorption, a 3 mm inclusion is filled with the same ThermoDots concentration and positioned at four different distances from detector 3: 20 mm, 15 mm, 10 mm, and 5 mm as seen in the left column of Figure 7.9. The ThermoDots fluorescence absorption maps are reconstructed with and without *functional a priori* information and compared in Figure 7.9. The results of all four cases are summarized in Table 7.3.

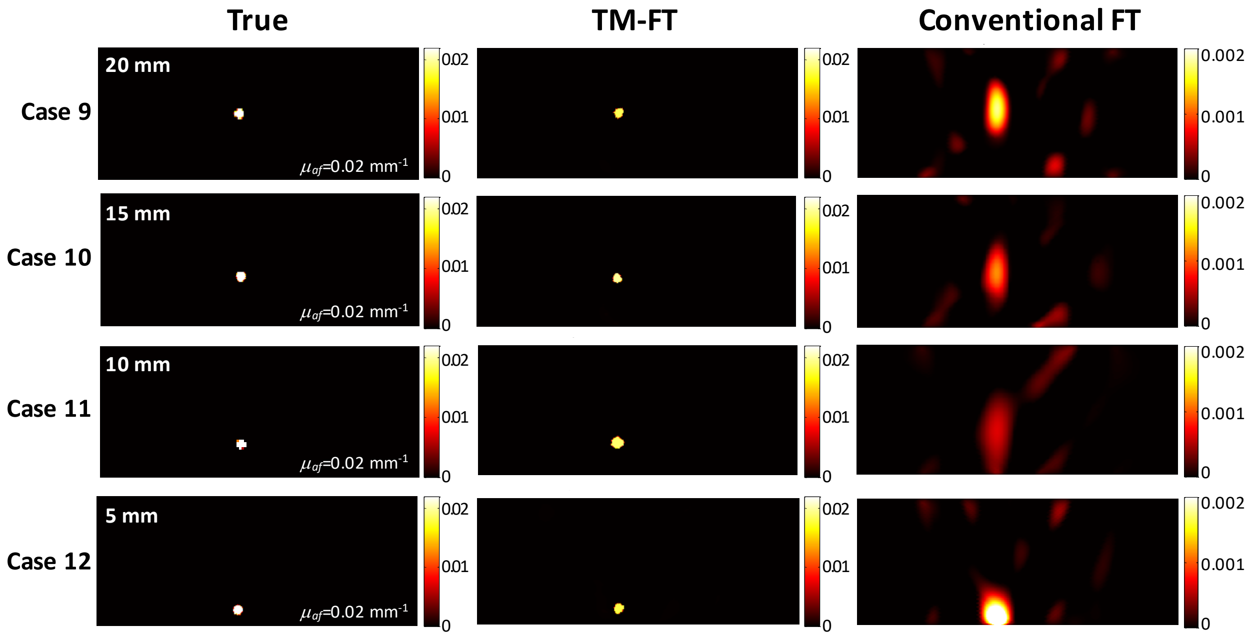

Figure 7. 9 Experimental results 3: depth dependence. Reconstructed ThermoDots fluorescence absorption maps comparing TM-FT (middle column) and conventional FT (right column) to the true value (left column) for different ThermoDots inclusion depths. Case 9: 20 mm; Case 10: 15 mm; Case 11: 10 mm; and Case 12: 5 mm. The reconstructed fluorescence absorption depends on the depth. Conventional FT is unable to resolve the inclusion at 5 mm depth (Case 12). However, when the *functional a priori* is used for TM-FT, the true value can be reconstructed with less than 10.5% error for all cases. The color bars all have units of mm^{-1}.(310)

When the inclusion is positioned equidistance from source 3 and detector 3, the recovered ThermoDots fluorescence absorption coefficient is 0.01823 mm^{-1} yielding an 8.85% error for TM-FT. When the inclusion is moved closer to the detectors at 15 mm, 10 mm, and 5 mm away, the fluorescence absorption coefficient is recovered with 0.8%, 6%, and 10.2% errors, respectively. Contrarily, for conventional FT without the use of *a priori* information, the fluorescent inclusion is overestimated in size and underestimated in the recovered absorption by more than a factor of 10. The fluorescence absorption coefficient is recovered with over 90% error for cases 9-11. Meanwhile, when the inclusion is positioned only 5 mm away from detector 3, the reconstruction program fails to separate the inclusion from the detector.

Table 7. 3 Recovered ThermoDots fluorescence absorption and size of inclusions with TM-FT and conventional FT for phantom study 3: Depth dependence.(310)

	True			**TM-FT**			**Conventional FT**		
Case	Depth (mm)	μ_{af}(mm^{-1})	FWHM (mm) x/y	μ_{af}(mm^{-1})	% error μ_{af}	FWHM (mm) x/y	μ_{af}(mm^{-1})	% error μ_{af}	FWHM (mm) x/y
9	20	0.02	3.00/3.00	0.0182	8.9%	2.75/3.00	0.0018	91.3%	5.75/13.25
10	15	0.02	3.00/3.00	0.0199	0.8%	3.00/3.00	0.0011	94.4%	6.00/13.50
11	10	0.02	3.00/3.00	0.0188	6.0%	3.75/3.00	0.0007	94.7%	7.25/21.75
12	5	0.02	3.00/3.00	0.0180	10.2%	3.00/3.00	na	na	na

The reconstructed fluorescence absorption is expected to be dependent on the location of the inclusion due to the trans-illumination configuration of the system (116). The recovered absorption uses a reconstruction algorithm to model the propagation of photons through the medium from the 36 signals acquired from the source-detector pairs. The accuracy of the recovered ThermoDots absorption is dependent on the sensitivity which is highest in the center of the phantom when the inclusion lies within multiple source-detector pair paths. This is seen in the conventional FT cases as the error in the recovered absorption increases as the inclusion moves away from center toward the edge of the phantom. The percent error increased from 91.3% to 94.7% for cases 9-11. For case 12, positioned 5 mm away from the detector, the inclusion is located in an area of low sensitivity as it does not fall within multiple source-detector pair paths which describes the placement of the inclusion on the y-axis and thus conventional FT was unable to resolve the inclusion.

However, TM-FT utilizes the functional *a priori* information from the focused ultrasound to establish the position of the fluorescence during the initialization of the reconstruction algorithm and is not affected by the optical source-detector configuration. As seen in Figure 7.9, TM-FT resolves all the inclusions, including the one located at the depth of 5 mm and recovers the ThermoDots fluorescence absorption with a maximum of 10.2% error for all depths.

7.2.3.4 Phantom study IV: Resolution limit

In the last study, the spatial resolution of the TM-FT system is investigated using multiple inclusions. In this study, two identical 3 mm inclusions filled with the same ThermoDots concentration are placed at decreasing distances from each other in order to find the resolution limit of our system as seen in Figure 7.10. Four cases are studied: 1.4 mm, 3 mm, 6.3 mm, and 9 mm separation between the adjacent edges of the two objects. Figure 7.11 shows the ThermoDots fluorescence absorption maps reconstructed with TM-FT and conventional FT.

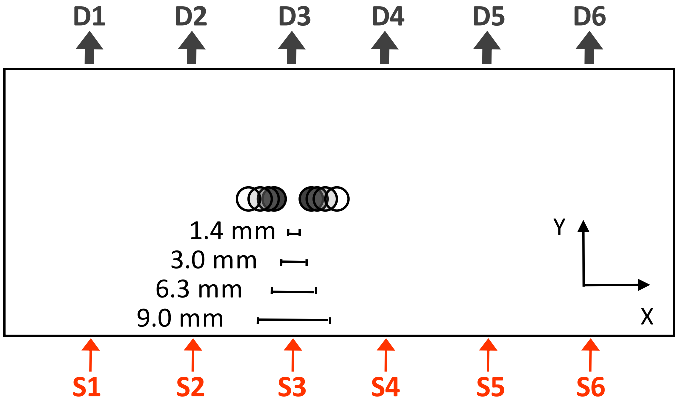

Figure 7. 10 Experimental setup for phantom study 4: spatial resolution. Cross-sectional view of the phantom and ThermoDots inclusions separated by different distances. (310)

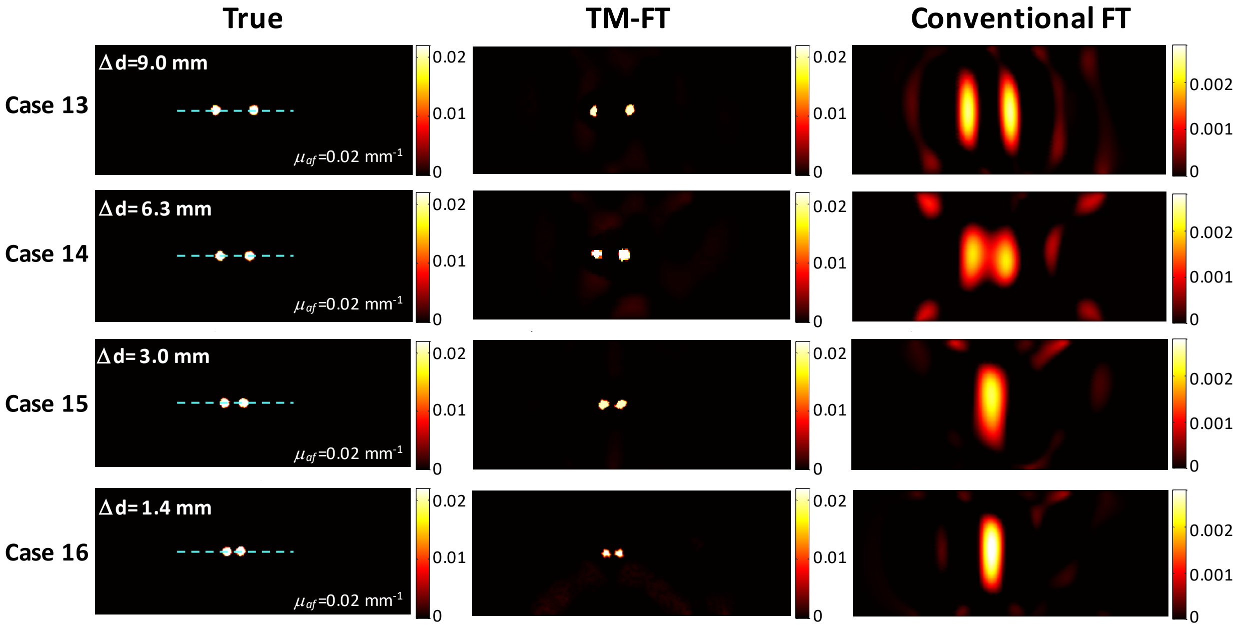

Figure 7. 11 Experimental results 4: resolution limit. Reconstructed ThermoDots fluorescence absorption maps comparing TM-FT (middle column) and conventional FT (right column) to the true value (left column). Δd is the distance separation between the two objects. Case 13: 9 mm; Case 14: 6.3 mm; Case 15: 3 mm; and Case 16: 1.4 mm. Conventional FT is only able to fully separate the two objects for Case 13 when the separation distance is 9 mm. However, when the *functional a priori* is used for TM-FT, two separate objects can be seen for all four cases and the recovered ThermoDots fluorescence absorption is obtained with less than 11% error for all cases. The blue dashed lines in the right column indicate the plot profiles in Figure 7.12. The color bars all have units of mm^{-1}.(310)

The inherent limited spatial resolution of FT is clearly seen in the recovered ThermoDots fluorescence absorption maps in Figure 7.11. Conventional FT is only able to resolve the two objects for the largest separation of 9 mm. The two inclusions are overestimated in size and severely underestimated in the recovered ThermoDots fluorescence absorption with over an 87% error. Excluding this case, FT is unable to resolve the two inclusions as separate entities and thus the two inclusions are calculated as one inclusion in Table 7.4. Although the two objects are almost resolved for Case 14, when the inclusions are separated by 6.3 mm, the profiles of the two objects overlap and cannot be resolved using the FWHM as the threshold. Figure 7.12 shows the plot profiles along the yellow dashed line as indicated in the first column of Figure 6.2.3.4.2 for the true inclusions and the reconstructed inclusions from conventional FT and TM-FT.

Table 7. 4 Recovered ThermoDots Fluorescence Absorption and Size of Inclusions with TM-FT and Conventional FT for Phantom Study 4: Spatial Resolution.*(310)

	True			TM-FT				FT			
Case	Δd (mm)	μ_{af} (mm^{-1})	FWHM (mm) x/y	μ_{af} (mm^{-1})	% Error μ_{af}	Left FWHM (mm) x/y	Right FWHM (mm) x/y	μ_{af} (mm^{-1})	% Error μ_{af}	Left FWHM (mm) x/y	Right FWHM (mm) x/y
13	9.0	0.02	3.00/3.00	0.0191	4.6%	2.25/2.50	3.00/3.00	0.0025	87.6%	5.00/17.75	5.00/18.25
14	6.3	0.02	3.00/3.00	0.0219	9.3%	2.75/2.50	3.75/3.0	0.0020	90.0%	17.25/14.25	17.25/13.25
15	3.0	0.02	3.00/3.00	0.0188	6.3%	3.25/3.00	2.75/2.50	0.0022	88.8%	7.50/17.50	7.50/18.00
16	1.4	0.02	3.00/3.00	0.0222	10.8%	2.50/2.50	2.50/2.50	0.0015	92.6%	5.50/18.50	5.50/17.50

*Δd is the distance separating the two objects.

Both TM-FT and conventional FT are able to resolve two separate objects for case 13 as seen in Figure 7.12 with 9 mm separation. This is the only case where conventional FT is able to resolve two separate objects. However, the two inclusions are overestimated in size and severely underestimated in the recovered ThermoDots fluorescence absorption with over an 87% error. Conversely, TM-FT is able to recover the absorption at 0.0191 with only a 4.6% error and closely match to the true absorption of 0.02 mm^{-1}. The size of the objects recovered was much closer to the true size compared to conventional FT. The left inclusion was underestimated in size at 2.25 mm and 2.5 mm for the x- and y-axis, respectively, while the inclusion located to the right was found to be an exact match at 3 mm in length and width. While TM-FT is able to accurately recover the correct location of the inclusions, for conventional FT, the right inclusion is shifted slightly by +0.25 mm while the left inclusion is more severely shifted by -2 mm in the x-axis.

For cases 14-16, conventional FT was unable to separate the two inclusions and thus recovers a large single inclusion in the middle of the two inclusions as seen in Figure 7.12. Although the two objects are almost resolved in case 14, the profiles of the two objects overlap and cannot be resolved using the FWHM as the threshold. However, TM-FT does not have this problem but is able to recover the absorption, position, and size with high accuracy. For case 14, the recovered absorption was only slightly overestimated at 0.0219 mm^{-1} with an error of 9.3% using TM-FT. The position and size of left inclusion was very close to the true value. However, the right inclusion was overestimated in size at 3.75 mm /3 mm (x-axis/y-axis) and shifted by -1 mm in the x-direction. Case 15 had the two inclusions separated by 3 mm, which matched the size of the diameter of the inclusions. The recovered absorption was close to the true value at 0.0188 mm^{-1} with a 6.25% error. TM-FT accurately recovered the position of the inclusion, although the left inclusion was slightly overestimated in the x-direction at 3.25 mm while the right inclusion was underestimated at 2.75 mm and 2.5mm for x- and y-axis, respectively. For the final case which had a separation of 1.4 mm, TM-FT recovered the true location of the inclusions and recovered two identically sized objects that were slightly underestimated at 2.5 mm for both x- and y-directions. The recovered absorption was slightly overestimated at 0.0222 mm^{-1} with a 10.8% error.

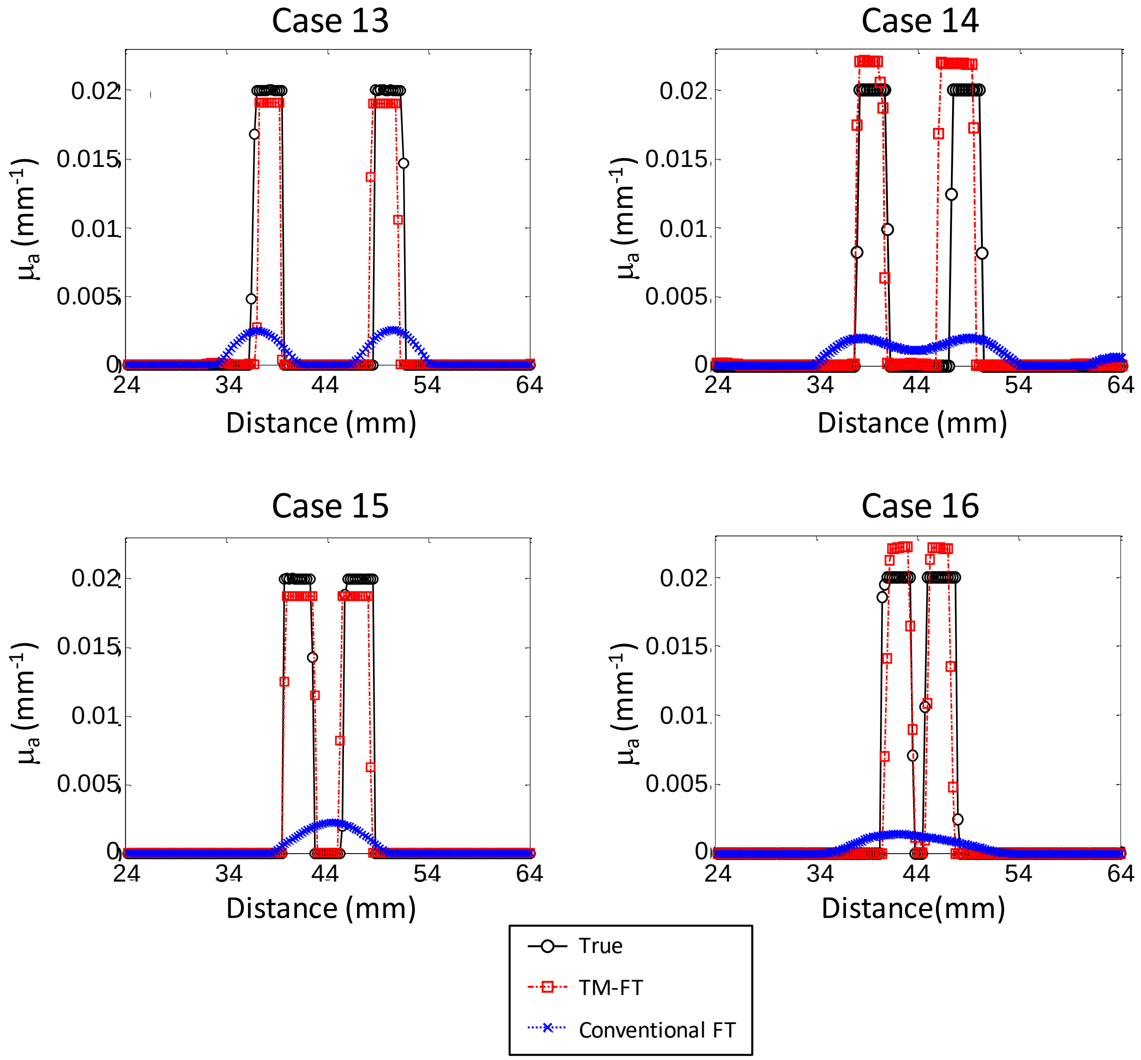

Figure 7. 12 Plot profiles of inclusions from resolution study. The profiles are taken along the blue dashed line in Figure 7.11.

The inherent limited spatial resolution of FT is clearly seen in the recovered ThermoDots fluorescence absorption maps in Figure 7.11. The recovered absorption is expected to improve when the objects are clearly distinguished. With the exception of case 14 which has a larger error than case 15, there is a trend as the separation between the two object decreases, the error in the recovered absorption increases for both conventional FT and TMFT. For conventional FT, when the two inclusions are in close proximity, the error is highest for 1.4 mm separation at 92.6%. This follows as the reconstruction program is unable to separate the two objects and attributes the signals originating from a single entity. However, TM-FT is able to reconstruct two separate objects for all cases, including the 1.4 mm separation case, and is able to recover the correct size with a maximum error of 25%. For all cases, the error in the recovered fluorescence absorption is less than 11%. This experiment shows that TM-FT can resolve two objects separated by 1.4 mm, which is approximately equal to the size of the focal spot of the focused ultrasound and the distance between the line scans. Consequently, the spatial resolution limit for TM-FT relies on the focal spot size of the focused ultrasound. While choosing a focused ultrasound with a smaller focal spot will increase the spatial resolution, it will also require an increase in the number of scan lines, resulting in a longer scan time.

7.2.4 Discussion

This experimental study investigates the performance of the TM-FT system using tissue-mimicking phantoms in resolving the concentration, size, and location of embedded fluorophore inclusions. The high scattering of light combined with the inherently limited spatial resolution of FT can be seen in the low spatial resolution and quantitative accuracy of the FT reconstructed absorption and concentration maps. In addition, the dependence on the source and detector configuration can also be seen from the lower resolution in the y direction and more specifically from phantom study 2. Depth dependence, as the quantitative accuracy and resolution of the ThermoDots inclusion, decreases as the inclusion is moved away from the center of the phantom. On the other hand, extensive phantom studies show that TM-FT provides superior spatial resolution and quantitative accuracy and does not depend on the geometry of the optical sources and detectors. TM-FT uses the thermo-sensitive quantum yield of the temperature-dependent ThermoDots and the localized heating from focused ultrasound to directly map the location and structure of the ThermoDots distribution with high spatial resolution. This information is used as *a priori* data and incorporated into the FT reconstruction program to provide high spatial resolution and quantitatively accurate images.

The spatial resolution study investigated the resolution limit of the TM-FT system. The spatial resolution is dependent on two factors: the focused ultrasound scanning pattern and the focal spot size. However, as the distance between the line scans is equal to the focal spot size, the resolution of TM-FT is ultimately determined by the focal spot size (~1.33 mm). Consequently, the focal spot size can be reduced by choosing a transducer with a smaller focal spot or by increasing the frequency. However, this will require additional line scans to cover the same area and will result in a longer data acquisition time. In addition, while increasing the frequency of the transducer will reduce the size of the focal spot, this will also lead to a decrease in the penetration depth (311).

For FT reconstructions, when using *structural a priori* information, the accuracy of this *a priori* information can be a source of error. Errors can occur when the fluorescence is not exactly aligned or confined uniformly within the specified region from anatomical imaging modalities, such as MRI, CT, or ultrasound, as it is assumed that the fluorophore distribution is homogenous within the defined region, such as a tumor boundary. However, this is not the case for TM-FT as it uses the temperature dependence of the fluorophore to provide high spatial resolution *functional a priori* that is not based on anatomical information. As TM-FT heavily depends on the accuracy of the fluorescence *a priori* binary map, it follows that this could be a source of error if the accuracy of the binary map is compromised. Regardless, the results show that this error is minimal compared to the improvement in size and quantitative accuracy of TM-FT. The error in ThermoDots fluorescence absorption recovered is at most 12% compared to conventional FT alone, which averaged an error above 90%.

TM-FT has many applications from preclinical small animal imaging to the clinical treatment of cancer. The future lies in targeting these ThermoDots to provide tumor-specific imaging. Optical devices have become one of the highest growth areas in preclinical imaging due in large part to their use in the development and assessment of new drugs for pharmaceutical research (13). As a small animal imaging device, TM-FT has the potential to provide *in vivo* fluorescence images with superior spatial resolution and sensitivity than commercial fluorescence systems. TM-FT is not only competitive with the spatial resolution of photoacoustic tomography (PAT) but has superior sensitivity as PAT has an inherent sensitivity to absorption and not the exogenous fluorescence contrast (62). Future work includes expanding the current TM-FT prototype and adapting ThermoDots for *in vivo* animal imaging studies.

7.3 *Ex vivo* Studies: Chicken Breast

7.3.1 Introduction

TM-FT is a true multimodality technique that relies on both optic and acoustic interaction with the imaged medium. Although agar phantoms have been used to simulate the optical and mechanical properties of biological tissue, the true potential of TM-FT for preclinical and clinical applications remains unknown as it has not been evaluated in biological tissue. Consequently, it is necessary to demonstrate the feasibility of this technique in biological tissue. In this study, chicken breast, a common substitute for biological tissue in optical and ultrasound studies was chosen due to its similarity to the optical and acoustic properties of human breast tissue (312, 313). In addition, as the optical properties of chicken breast are unknown, diffuse optical tomography (DOT) was incorporated into the existing TM-FT system and used to provide optical functional *a priori* information to constrain the FT image reconstruction algorithm. The obtained *ex vivo* chicken breast tissue results demonstrate the ability of TM-FT to resolve a small fluorescent inclusion embedded several centimeters deep in biological tissue.

7.3.2 Methods

7.3.2.1 Chicken breast preparation

For the chicken breast study, a chicken breast was cut into a 30 mm x 40 mm x 90 mm slab and centered in the middle of the sample holder (100 mm x 40 mm x 100 mm). The middle of the chicken breast slab was aligned with the optical fiber plane using a tissue mimicking agar slab as seen in Figure 7.13. The chicken breast was surrounded with an optical matching fluid and sealed with a clear acoustically-transparent plastic to reduce reflection of the focused ultrasound waves.

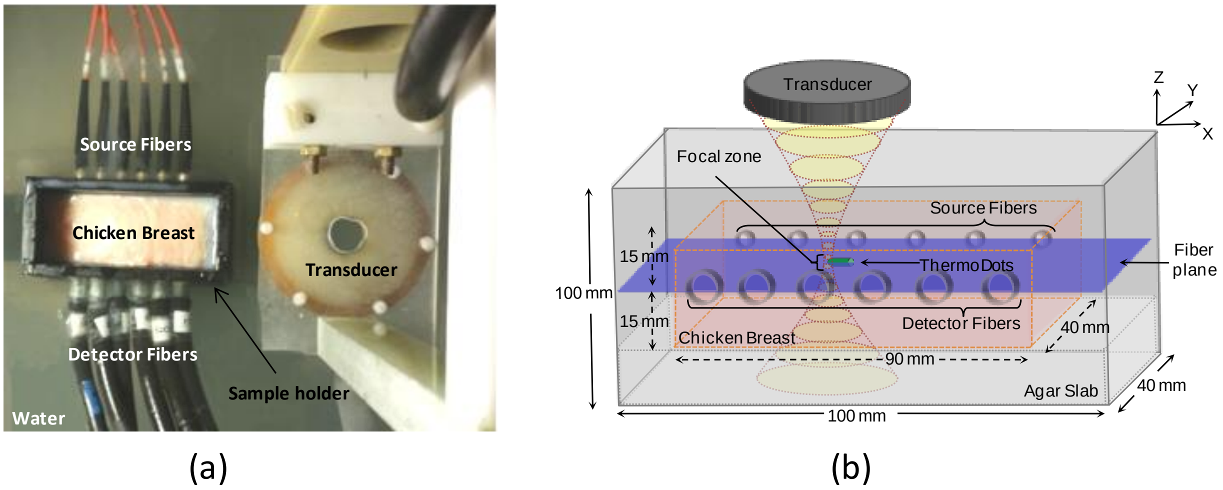

Figure 7. 13 Experimental set up. (a) 3D schematic showing the sample holder and the focused ultrasound transducer. The transducer produces a focal zone of ~1.33 mm diameter (xy) and 10 mm in length (z). The center of the focal zone, ThermoDots inclusion (green tube), and chicken breast slab (pink box) are aligned in the fibers plane (blue plane) defined by the source and detector optical fibers. The chicken breast rested on an agar slab and surrounded by an optical matching fluid. (b) Picture of TMFT system including the sample holder and transducer which are immersed in a tank filled with water.

The agar slab and matching fluid were prepared using intralipid (0.5%) and Indian ink (Winsor and Newton, UK) to respectively mimic the tissue reduced scattering and absorption properties: μ_s'= 0.6 mm^{-1}and μ_a=0.008 mm^{-1}. A small clear acoustically-transparent plastic tube (1.5 mm x 5 mm) was filled with the ThermoDots solution, μ_a=0.02 mm^{-1}, and embedded inside the chicken breast slab. The tube was aligned along the fiber plane and centered between the source and detector located third from the left as seen in Figure 7.14. The ThermoDots consisted of 20 μM Indocyanine Green (ICG) encapsulated in 4% Pluronic-F127 polymeric micelles. The ThermoDots were formulated for room temperatures and exhibited a 15x increase in fluorescence signal for a 4 °C change in temperature from 20-24°C.

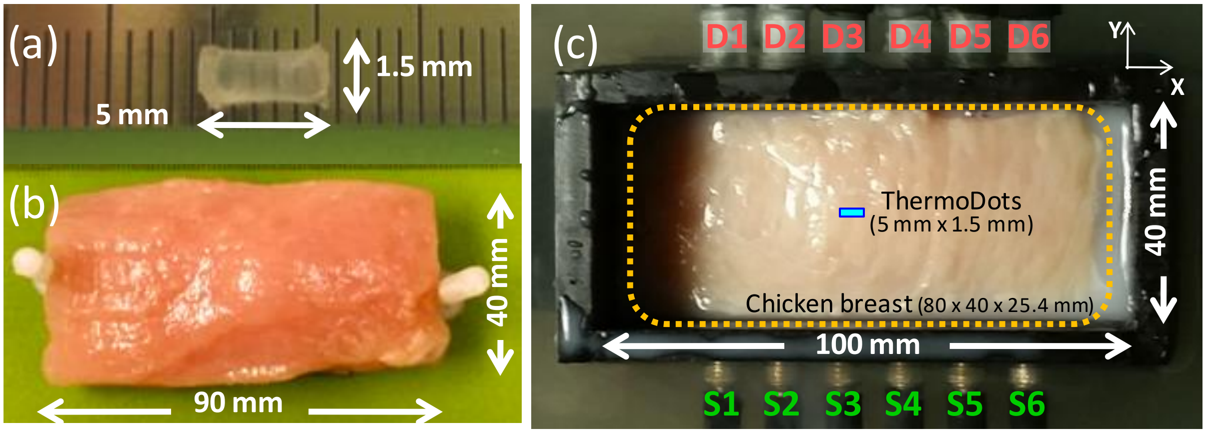

Figure 7. 14 Experimental details (a) 1.5 mm diameter by 5 mm long tube filled with ThermoDots solution that was embedded inside the (b) chicken breast slab which was 40 mm x 90 mm x 30 mm. (c) Picture of chicken breast and ThermoDots tube in the fiber plane. The inclusion is centered between source 3 and detector 3.

6.3.2.2 Experimental procedure: DOT

The experiment was performed on a custom built TM-FT system (310). However, as the optical properties of chicken breast are unknown, diffuse optical tomography (DOT) was incorporated into the existing TM-FT system and used to provide *optical functional a priori* information to constrain the FT image reconstruction algorithm. The system was modified in order to divert the detected light into a second identical PMT to collect DOT measurements when needed. A detailed description and schematic of the DOT/TM-FT system can be found in section 6.3.4. To generate the *fluorescence functional a priori* information, the transducer was turned on to induce a 4 °C temperature increase at the focal zone and scanned over a 50 mm x 25 mm area in 29 minutes (185). The FWHM was used as a threshold to create a binary map of the position of the ThermoDots with high spatial resolution.

Prior to the FT reconstruction, DOT was used to recover the absorption and reduced scattering coefficients of the chicken breast as described previously (128). As the absorption and reduced scattering coefficients of the *ex vivo* chicken breast at the excitation and emission wavelengths are nearly equal (~1% difference), in this study, μ_a and μ_s' were acquired at the excitation wavelength, 785 nm (314). In addition, due the low optical contrast (<2x) and small size (<5%) of the ThermoDots tube compared to the background chicken breast, the obtained optical maps were mostly homogeneous. The averaged optical properties of the chicken breast obtained were μ_a=0.0139 mm^{-1} and μ_s'= 0.5165 mm^{-1}. Following the DOT, conventional FT measurements were acquired. Then, the reconstructed DOT optical properties were used as *optical functional a priori* information in the conventional FT reconstruction program to identify the location of the ThermoDots. Next, the focused ultrasound scan was used to create a binary map of the position of the fluorescence tube with focused ultrasound spatial resolution. Finally, this binary map was implemented as a *soft a priori* with the previous fluorescence data to reconstruct the concentration of the ThermoDots (129).

7.3.3 Results

To test the feasibility of TM-FT in imaging biological tissue, we investigated the performance of TM-FT to accurately recover the size, shape, position, and concentration of the ThermoDots tube embedded inside the chicken breast slab. The ThermoDots absorption maps recovered with FT and TM-FT were compared to the true concentration value of the tube.

7.3.3.1 Concentration

Figure 7.15 shows the recovered fluorescence absorption maps (obtained using the DOT *optical functional a priori*) comparing conventional FT and TM-FT with the true fluorescence absorption value in the tube. As seen in the conventional FT absorption map (Figure 7.15.b), conventional FT recovers a fluorescent distribution 3x larger in the x-axis and 5.5x larger in the y-axis direction compared to the true size of the tube. Consequently, since the recovered fluorescence is spread upon a larger area, it results in an underestimated fluorescence absorbance of 0.005521 mm^{-1}, which is 4x smaller than the true fluorescence absorbance set to 0.02 mm^{-1}. The binary mask generated from the focused ultrasound scan in Figure 7.15.c localizes the ThermoDots position prior to any reconstruction process. Consequently, in order to find the concentration of the ThermoDots, this binary mask is used as *fluorescence functional soft a priori* and combined with the DOT *optical functional a priori* information to solve the FT inverse problem. The resultant TM-FT fluorescence absorption map (Figure 7.15.d) illustrates the improved spatial resolution and quantitative accuracy compared to conventional FT. Not only did TM-FT recover a fluorescent distribution very similar to the size, shape, and position of the true fluorescent distribution, it also reconstructed the exact fluorescence absorption (0.0201 mm^{-1}, <0.5% error).

The accuracy of FT and TM-FT strongly depends on the accuracy of their forward problem to model the light propagation within the medium. When the optical properties of chicken breast were taken from literature and assumed (μ_a=0.01 mm^{-1} and μ_s'= 0.3 mm^{-1}), there was a 30% error in the recovered fluorescence absorption (314) . However, when the correct absorption and reduced scattering values found from the DOT measurements were used, the error decreased to 0.45%. Therefore, the addition of DOT to TM-FT is integral to obtain quantitatively accurate fluorescence images when the optical properties are unknown.

(a) True

(c) Binary mask

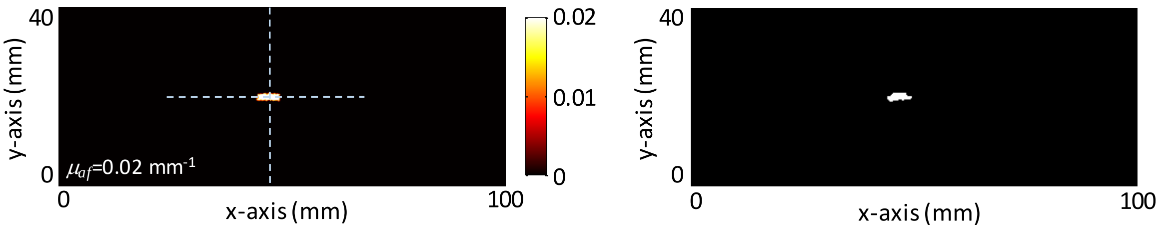

(b) Conventional FT

(d) TM-FT

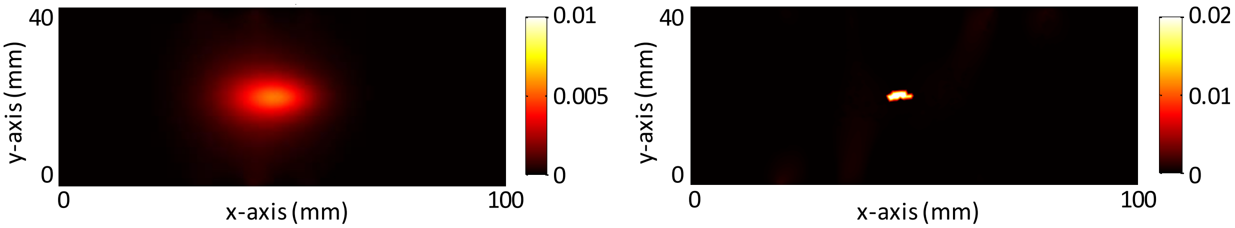

Figure 7. 15 *Ex vivo* experimental results. ThermoDots fluorescence absorption maps in the fiber plane. (a) True ThermoDots distribution. (b) Conventional FT fluorescence map with DOT optical functional *a priori*. (c) Binary mask used to outline the fluorescence tube to generate the (d) TM-FT fluorescence absorption map with DOT optical functional *a priori*. The color bars have units of mm^{-1}.

7.3.3.2 Size and position

When considering the size of the recovered object, TM-FT nearly recovers the exact size of the 1.50 mm in diameter by 5.00 mm long tube. TM-FT reconstructs the exact length of the tube in the x-axis and slightly overestimated the diameter by a mere 0.25 mm. Although irregularly shaped, Figure 7.16a and b shows the profiles of the ThermoDots distribution in the x- and y-axis which were carried out where the fluorescent distribution was the largest. This can also be visualized by the blue dashed lines in Figure 7.16a. As seen from Figure 7.16, the fluorophore distribution recovered by TM-FT in the x-axis is shifted slightly to the left by 0.25 mm. For the y-axis, the tube is marginally overestimated by 0.25 mm and shifted upwards by a mere 0.125 mm. This might be the result of the interpolation from the mesh to the Cartesian grid image. Nevertheless, with only 0.25 mm or less difference in position, TM-FT can accurately recover the correct position of the ThermoDots in biological tissue.

In comparison, for conventional FT, the center of the recovered fluorophore distribution is shifted 1.25 mm to the right in the x-axis and exactly aligned in the y-direction although it is greatly overestimated in size. The recovered size of the ThermoDots distribution is 15.75 mm in the x-axis and 8.25 mm in the y-axis. In general, the spatial resolution of conventional FT in the y-axis is expected to be lower than the x-axis due to the transillumination configuration of the system. However, TM-FT is not affected by the source-detector geometry as the spatial resolution of TM-FT is primarily determined by the spatial resolution of focused ultrasound.

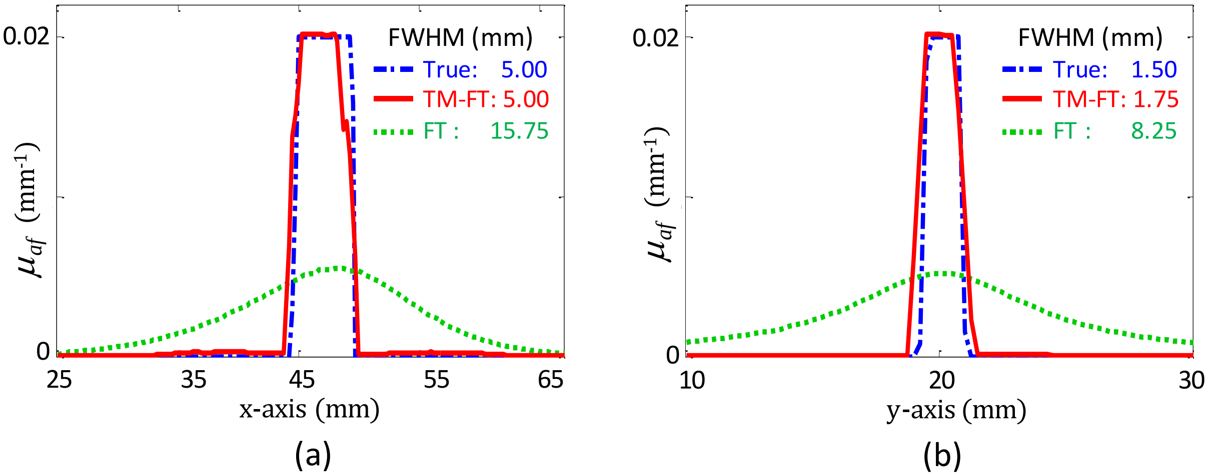

Figure 7. 16 Profiles of inclusions from chicken breast study. Profiles of the ThermoDots recovered fluorescence absorption maps along the blue dashed lines in Fig. 3.a. The profiles along the (a) x-axis and (b) y-axis show that the size of the fluorescent target is accurately recovered using TM-FT (red line). Conventional FT (green dots line) is severely overestimated in size and underestimated in absorption value compared to the true value (blue dot-dashed line).

7.3.3.3 Shape

Figure 7.17 shows a zoomed-in version of the recovered absorption maps of TM-FT and conventional FT. When considering the shape of the recovered object, conventional FT recovered an ellipsoid shaped fluorescence distribution compared to the true rectangular distribution of the ThermoDots tube. However, TM-FT relies on the acoustics waves from the focused ultrasound transducer and is therefore not constrained by the same scattering and absorption limitations as optical waves. This can be seen in the superior spatial resolution of the TM-FT results. Consequently, TM-FT is more accurate at recovering the correct shape and position of the ThermoDots. As seen in Figure 7.17a, although irregularly shaped, the TM-FT fluorescence distribution is mainly confined within the known boundary (green line) and corresponds well with the true ThermoDots distribution. The irregularities in the outline are a result of the shape of the mesh elements.

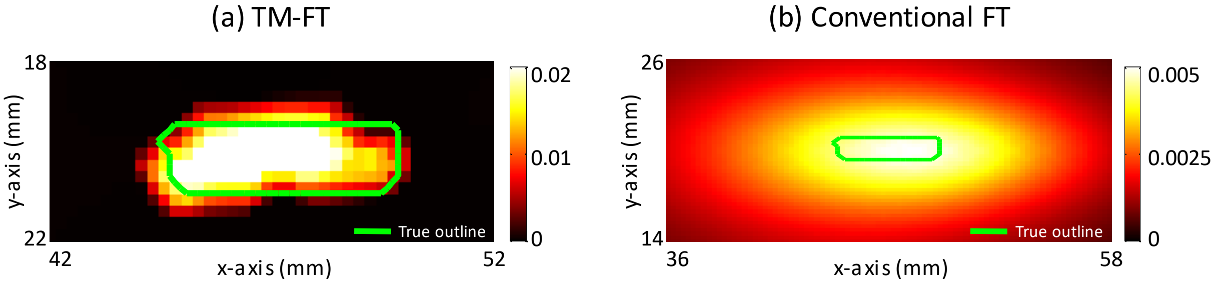

Figure 7. 17 Close up of ThermoDots inclusion. Recovered fluorescence absorbance map with the true ThermoDots boundary outlined in green. (a) TM-FT and (b) conventional FT. A very good agreement is obtained between the shape, size, and position of the ThermoDots recovered with TM-FT and the true value. Conventional FT recovers an ellipsoid shaped fluorescence distribution much larger than the true size of the tube and with much lower absorbance. The color bars have units of mm^{-1}.

7.3.4 Discussion

In conclusion, this *ex vivo* chicken breast study demonstrates the ability of TM-FT to accurately recover the correct size, shape, position, and concentration of the ThermoDots in biological tissue. Previous studies were performed on agar phantoms that although similar, did not perfectly model the optical and mechanical properties of biological tissue. As this technique heavily relies on both optical and acoustic waves, a more accurate model is needed to verify the feasibility of TM-FT in biological tissue. Chicken breast was chosen as it is commonly used as a substitute for human breast tissue in optical and ultrasound studies (312, 313). Consequently, this study was the first to demonstrate that TM-FT can be used in biological tissue. Compared to previous studies which used homogeneous phantoms with known optical properties, DOT was added to the system in order to correct for the optical background heterogeneity. The results show that TM-FT was able to recover the correct size and position of the ThermoDots with sub millimeter error and recovered the true ThermoDots absorption with less than 0.5% error. These promising results demonstrate the feasibility of TM-FT in biological tissue and opens up the possibility for high spatial resolution whole body *in vivo* small animal imaging in the future.

Chapter 8 Summary and Future Work

"A complex system that works is invariably found to have evolved from a simple system that works." – John Gall

8.1 Conclusion

In conclusion, this thesis introduces a novel multi-modality imaging technique capable of combining the sensitivity of FT with the resolution of focused ultrasound to produce quantitatively accurate fluorescent imaging with high spatial resolution in thick tissue (> 6 cm). The feasibility of this method to provide superior spatial resolution and high quantitative accuracy was validated in phantoms and *ex vivo* animal tissue. In this thesis, the motivation, mathematical framework, system design and description, ThermoDots probe development, simulation studies, phantom studies as well as *ex vivo* studies are presented. The instrumentation and ThermoDots probes developed in this work represent the preliminary steps to develop an *in vivo* small animal TM-FT system.

The poor spatial resolution and quantitative accuracy of FT, especially in thick tissue, is the main obstacle preventing the widespread use in clinical applications. However, FT has found its niche in preclinical applications, as it has the capacity for *in vivo* molecular imaging. Indeed, small animal FT systems have found great popularity in biomedical and pharmaceutical research to study molecular and cellular events to further our understanding of biology and search for new molecular pathways to treat diseases. In addition, *in vivo* small animal FT systems allow low cost development of new drugs, therapies, devices, and probes using NIR light that is safe for the animals, unlike CT or nuclear imaging, allowing longitudinal monitoring to study long term effects.

An ideal FT system should not only allow visualization of the fluorophore distribution in tissue, but also provide quantitatively accurate concentration values in a heterogeneous medium. Although, planar florescence imaging has been extensively applied for molecular imaging of mice, a tomographic approach is required to resolve depth and fluorescence concentration information. While prototype FT systems have been demonstrated in the literature, the high scattering of light in biological tissues makes it difficult to obtain quantitatively accurate fluorescent images with optical techniques alone. Consequently, multimodality techniques and hybrid imaging systems have been used to overcome this obstacle by incorporating spatial information derived from a high resolution imaging modality. However, this method requires highly accurate information which is challenging to obtain as the high resolution imaging modalities (CT, MR, ultrasound) are not sensitive to the fluorescent contrast. Thus, errors arise when the true fluorescent distribution does not exactly match the segmented region defined by the anatomical image. TM-FT can overcome this limitation as focused ultrasound and FT work together by using temperature activatable fluorescent probes, ThermoDots, to directly map the true fluorescent distribution with high spatial resolution to improve the FT reconstruction. Furthermore, TM-FT can reconstruct quantitatively accurate fluorescence parameter images which will have great potential in a number of applications covering a broad range of topics from stem cells to cancer research. In addition, the increased sensitivity and specificity of TM-FT can offer opens up the door to study diseases in their beginning stages and monitor early treatment response.

TM-FT also has much promise for clinical applications as it can offer molecular information without the use and complications arising from harmful radiation and radiopharmaceuticals. With its high resolution and quantitative accuracy, TM-FT has great potential to play significant role from diagnosis to the therapy planning and treatment. TM-FT could significantly contribute to the development and effective assessment of molecular imaging probes for clinical imaging by speeding up investigations of orthotopic pre-clinical tumor models and development of novel temperature responsive optical probes. The development of these molecular probes could provide opportunities for personalized diagnosis and treatment (10, 315-317). Indeed, the high sensitivity and specificity of TM-FT could offer new ways to provide personalized treatment for human patients, by providing early treatment results with the use of mouse drug avatars, or to improve the specificity of ultrasound guided HIFU therapy (318, 319). The long-term goal will be translating this TM-FT technique to clinics to provide high resolution and quantitative fluorescent imaging in a safe, low cost, and portable system to increase the accessibility of molecular imaging. Thus, the aim of this work is to test the feasibility of this new technique and build the foundation for developing a system that can eventually be used in the clinics.

8.2 Future work

The future lies in further developing this technique for small animal imaging by expanding our current 2D TM-FT system to 3-D whole body small animal imaging and targeting the ThermoDots for *in vivo* imaging. Understanding the capabilities and limitations of our method is the first step in developing this technique for *in vivo* animal imaging. The instrumentation and ThermoDots probes developed in this thesis represent the preliminary steps to develop an *in vivo* small animal TM-FT system. In this work, two key steps to translate TM-FT to *in vivo* animal imaging were accomplished, namely, optimizing the method and scan time for live animals, and adding DOT capabilities for heterogeneous animal tissue. Thus, we are currently working on an *in vivo* small animal TM-FT system (Figure 8.1). To make this system more compatible to animals, a membrane was introduced to separate the animal from the water which was used as an acoustic matching fluid for the HIFU. In addition, the PMT was replaced with a CCD detection method to capture images. Although this method is less sensitive, this current setup can be further improved by replacing the current cooled integrated CCD with an intensified CCD (ICCD) to amplify the photon signal before it is recorded by the CCD so that high gain (10^5) can be achieved. In addition, a filter wheel can be used to easily switch between DOT and FT measurements. Once this system is built, and we can validate the feasibility of TM-FT *in vivo,* the next step will be to develop this system for 3D whole body small animal imaging.

In addition, prior to any *in vivo* imaging, the ThermoDots need to be further optimized for in vivo animal imaging by developing a targeted small animal ThermoDots version for *in vivo* temperatures with a substantial change in fluorescent signal over a narrow temperature range. Indeed, the studies performed in this work show much promise. Not only are we able to manipulate the temperature range, the preliminary studies also show the potential for the ThermoDots to be used *in vivo*. Furthermore, the preliminary targeting studies show that the ThermoDots are able to be targeted. Although these preliminary studies show promise, further work needs to be done to fully optimize the ThermoDots for *in vivo* imaging.

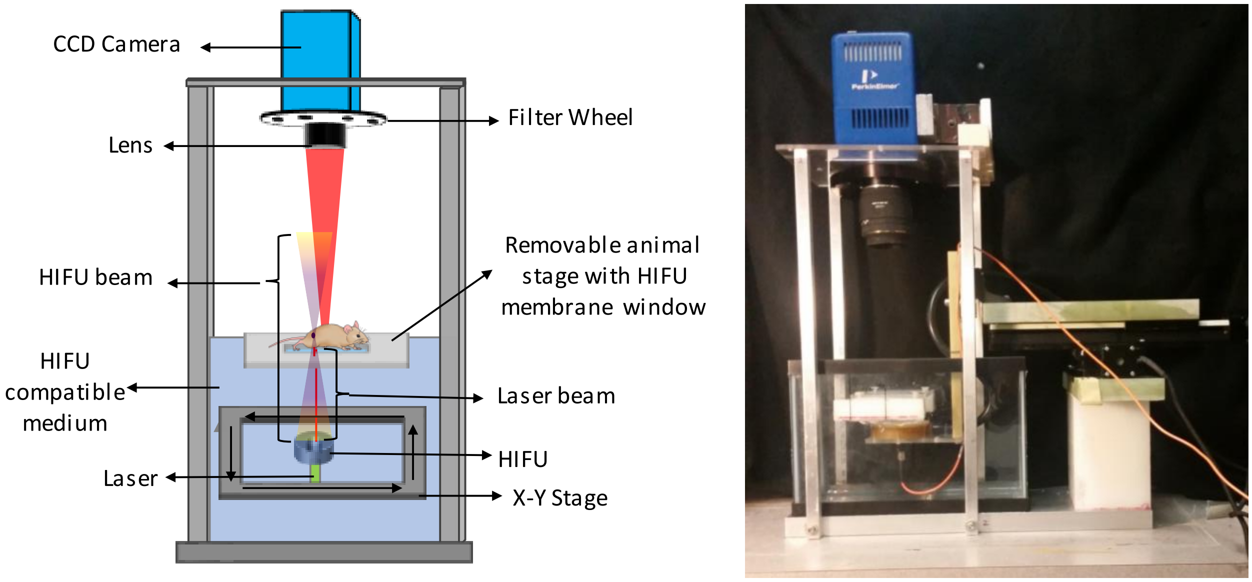

(a) (b)

Figure 8. 1 (a) Schematic for the *in vivo* small animal TM-FT system. (b) TM-FT prototype.

Once the ThermoDots are optimized for *in vivo* temperatures, the first step will be to test the feasibility of the TM-FT *in vivo* first using surgically embedded tubes filled with the ThermoDots solution and then with the targeted ThermoDots in a mouse tumor model. Once this technique is validated *in vivo*, we will explore the different potential applications for TM-FT. As TM-FT is fluorescence-based, it has great clinical translational potential due to the rapid development of targeted molecular probes towards human imaging such as breast and brain imaging. Moreover, the synthesis material used in this study, ICG and Pluronic-127 polymers are both FDA approved. In addition to cancer diagnosis, TM-FT has the potential to be used to monitor the drug delivery process in the future as it has already been shown that a therapeutic drug can be incorporated with ICG in the Pluronic micelle (320). Furthermore, since a HIFU is used in our set-up, TM-FT can also be used for therapeutic planning and real-time HIFU hyperthermia treatment monitoring for different types of cancers, such as prostate and breast.

REFERENCES

1. W. C. Rontgen, "On a new kind of ray, a preliminary communication," *Wurzburg Physico-Médical Society on December* **28**((1895).
2. G. Bansal, "Digital radiography. A comparison with modern conventional imaging," *Postgraduate medical journal* **82**(969), 425-428 (2006).
3. S. N. Reske, and J. Kotzerke, "FDG-PET for clinical use," *European Journal of Nuclear Medicine and Molecular Imaging* **28**(11), 1707-1723 (2001).
4. B. D. H. M. E. L. D. C. A. K. M. G. R. J. Boas D A, and Q. Zhang, "Imaging the body with diffuse optical tomography," *IEEE Sig. Proc. Mag.* **18**(6), 57 (2001).
5. A. Cerussi et al., "In vivo absorption, scattering, and physiologic properties of 58 malignant breast tumors determined by broadband diffuse optical spectroscopy," *Journal of Biomedical Optics* **11**(4), 044005-044016 (2006).
6. R. Choe et al., "Differentiation of benign and malignant breast tumors by in-vivo three-dimensional parallel-plate diffuse optical tomography," *J Biomed Opt* **14**(2), 024020 (2009).
7. D. W. Townsend et al., "Grand challenges in biomedical physics," *Frontiers in Physics* **1**(1 (2013).
8. T. F. Massoud, and S. S. Gambhir, "Molecular imaging in living subjects: seeing fundamental biological processes in a new light," *Genes & development* **17**(5), 545-580 (2003).
9. J. Capala, and K. Bouchelouche, "Molecular imaging of HER2-positive breast cancer: a step toward an individualized 'image and treat' strategy," *Current Opinion in Oncology* **22**(6), 559-566 510.1097/CCO.1090b1013e32833f32838c32833a (2010).
10. E. M. Sevick-Muraca, and J. C. Rasmussen, "Molecular imaging with optics: primer and case for near-infrared fluorescence techniques in personalized medicine," *Journal of Biomedical Optics* **13**(4), 041303-041316 (2008).
11. P. A. Valdés et al., "Quantitative fluorescence in intracranial tumor: implications for ALA-induced PpIX as an intraoperative biomarker," *Journal of Neurosurgery* **115**(1), 11-17 (2011).
12. A. de Gramont et al., "From Chemotherapy to Targeted Therapy in Adjuvant Treatment for Stage III Colon Cancer," *Seminars in Oncology* **38**(4), 521-532 (2011).
13. F. Leblond et al., "Pre-clinical whole-body fluorescence imaging: Review of instruments, methods and applications," **98**(1), 77–94 (2010).
14. K. M. Tichauer et al., "Computed tomography-guided time-domain diffuse fluorescence tomography in small animals for localization of cancer biomarkers," *J Vis Exp* 65), e4050 (2012).
15. E. E. Graves, R. Weissleder, and V. Ntziachristos, "Fluorescence molecular imaging of small animal tumor models," *Curr Mol Med* **4**(4), 419-430 (2004).
16. V. Ntziachristos, "Fluorescence molecular imaging," *Annu Rev Biomed Eng* **8**(1-33 (2006).
17. G. Zacharakis et al., "Fluorescent protein tomography scanner for small animal imaging," *IEEE Trans Med Imaging* **24**(7), 878-885 (2005).

18. S. M. Janib, A. S. Moses, and J. A. MacKay, "Imaging and drug delivery using theranostic nanoparticles," *Advanced drug delivery reviews* **62**(11), 1052-1063 (2010).
19. D. Hyde et al., "Hybrid FMT-CT imaging of amyloid-beta plaques in a murine Alzheimer's disease model," *Neuroimage* **44**(4), 1304-1311 (2009).
20. F. Stuker et al., "Hybrid small animal imaging system combining magnetic resonance imaging with fluorescence tomography using single photon avalanche diode detectors," *IEEE Trans Med Imaging* **30**(6), 1265-1273 (2011).
21. Y. Lin et al., "In vivo validation of quantitative frequency domain fluorescence tomography," *J Biomed Opt* **17**(12), 126021 (2012).
22. X. Chen, P. S. Conti, and R. A. Moats, "In vivo Near-Infrared Fluorescence Imaging of Integrin αvβ3 in Brain Tumor Xenografts," *Cancer Research* **64**(21), 8009 (2004).
23. Y. Chen et al., "Metabolism-enhanced tumor localization by fluorescence imaging: in vivo animal studies," *Opt Lett* **28**(21), 2070-2072 (2003).
24. J.-M. D. S. L. Troy T, and B. Rice, "Quantitative comparison of the sensitivity of detection of fluorescent and bioluminescent reporters in animal models," *Mol. Imaging* **3**(1), 9 (2004).
25. Y. Lin et al., "Quantitative fluorescence tomography using a trimodality system: in vivo validation," *J Biomed Opt* **15**(4), 040503 (2010).
26. S. V. Patwardhan et al., "Quantitative small animal fluorescence tomography using an ultrafast gated image intensifier," *Conf Proc IEEE Eng Med Biol Soc* **1**(2675-2678 (2006).
27. C. Kim et al., "Sentinel lymph nodes and lymphatic vessels: noninvasive dual-modality in vivo mapping by using indocyanine green in rats--volumetric spectroscopic photoacoustic imaging and planar fluorescence imaging," *Radiology* **255**(2), 442-450 (2010).
28. F. Gao et al., "Simultaneous fluorescence yield and lifetime tomography from time-resolved transmittances of small-animal-sized phantom," *Appl. Opt.* **49**(16), 3163-3172 (2010).
29. T. P. Gade et al., "Targeted elimination of prostate cancer by genetically directed human T lymphocytes," *Cancer Res* **65**(19), 9080-9088 (2005).
30. C. Li et al., "Three-dimensional fluorescence optical tomography in small-animal imaging using simultaneous positron-emission-tomography priors," *Opt Lett* **34**(19), 2933-2935 (2009).
31. A. T. N. Kumar et al., "A Time Domain Fluorescence Tomography System for Small Animal Imaging," *Medical Imaging, IEEE Transactions on* **27**(8), 1152-1163 (2008).
32. X. Montet et al., "Tomographic fluorescence mapping of tumor targets," *Cancer Res* **65**(14), 6330-6336 (2005).
33. V. Ntziachristos et al., "Visualization of antitumor treatment by means of fluorescence molecular tomography with an annexin V-Cy5.5 conjugate," *Proc Natl Acad Sci U S A* **101**(33), 12294-12299 (2004).
34. G. Zacharakis et al., "Volumetric tomography of fluorescent proteins through small animals in vivo," *Proc Natl Acad Sci U S A* **102**(51), 18252-18257 (2005).

35. C. Bremer, V. Ntziachristos, and R. Weissleder, "Optical-based molecular imaging: contrast agents and potential medical applications," *European Radiology* **13**(2), 231-243 (2003).
36. V. Ntziachristos et al., "Fluorescence molecular tomography resolves protease activity in vivo," *Nat Med* **8**(7), 757-760 (2002).
37. B. N. Giepmans et al., "The fluorescent toolbox for assessing protein location and function," *Science* **312**(5771), 217-224 (2006).
38. W. R et al., "In vivo imaging of tumors with protease-activated near-infrared fluorescent probes," *Nat. Biotechnol.* **17**(375 (1999).
39. R. Weissleder, "Scaling down imaging: molecular mapping of cancer in mice," *Nat Rev Cancer* **2**(1), 11-18 (2002).
40. Bruker, "In-Vivo Xtreme II," Bruker, https://www.bruker.com/products/preclinical-imaging/opticalx-ray-imaging/in-vivo-xtreme-ii/overview.html (2017).
41. LI-COR, "Pearl Triology Small Animal Imaging System," LI-COR, https://www.licor.com/bio/products/imaging_systems/pearl/index.html?utm_source=SeminarBrochure&utm_medium=brochurelink&utm_content=Pearl&utm_campaign=Seminars (2017).
42. A. E. H. C. analytikjena, "iBox Explorer Imaging Microscope," analytikjena, An Endress + Hauser Company, http://uvp.com/iboxexplorer2.html?gclid=CMSLn6e30tMCFRSDfgodBbkOsg (2017).
43. A. E. H. C. analytikjena, "iBox Scientia Small Animal Imaging System," analytikjena, An Endress + Hauser Company https://www.uvp.com/ibox.html (2017).
44. C. Darne, Y. Lu, and E. M. Sevick-Muraca, "Small animal fluorescence and bioluminescence tomography: a review of approaches, algorithms and technology update," *Physics in medicine and biology* **59**(1), R1 (2013).
45. T. Imaging, "InSyTe FLECT True 260 Tomographic Optical Preclinical Imaging," TriFoil Imaging http://www.trifoilimaging.com/products-services/imaging-modalities/optical.
46. PerkinElmer, "FMT In Vivo Imaging System," PerkinElmer, http://www.perkinelmer.com/searchresult/instruments/_/N-0ZshnixxZzd1mwyZ1hittkgZ1x6xq59Z10bne4tZ1ywt7px?searchName=fluorescence&No=0&Ns=Best%20Match (2017).
47. PerkinElmer, "IVIS Lumina In Vivo Imaging System," PerkinElmer, http://www.perkinelmer.com/searchresult/instruments/_/N-0ZshnixxZzd1mwyZ1hittkgZ1x6xq59Z10bne4tZ1ywt7px?searchName=fluorescence&No=0&Ns=Best%20Match (2017).
48. V. Ntziachristos, "Fluorescence Molecular Imaging," *Annual Review of Biomedical Engineering* **8**(1), 1-33 (2006).
49. H.-I. W. Lihong V. Wang *Biomedical Optics: Princoples and Imaging*, 1 ed., Wiley-Interscience, New Jersey (2007).
50. D. Kepshire et al., "A microcomputed tomography guided fluorescence tomography system for small animal molecular imaging," *Review of Scientific Instruments* **80**(4), 043701-043710 (2009).

51. S. C. Davis et al., "Magnetic resonance--coupled fluorescence tomography scanner for molecular imaging of tissue," *Review of Scientific Instruments* **79**(6), 064302-064310 (2008).
52. Y. Lin et al., "Quantitative fluorescence tomography using a trimodality system: in vivo validation," *Journal of Biomedical Optics* **15**(4), 040503-040503 (2010).
53. D. G. Josiah et al., "High-Frequency Ultrasound-Guided Fluorescence Tomography of Protoporphyrin IX in Subcutaneous Tumors," in OSA Technical Digest (CD) BMB5 (2010).
54. J. D. Gruber et al., "System development for high frequency ultrasound-guided fluorescence quantification of skin layers," *Journal of Biomedical Optics* **15**(2), 026028-026025 (2010).
55. V. Ntziachristos et al., "Looking and listening to light: the evolution of whole-body photonic imaging," *Nature biotechnology* **23**(3), 313-320 (2005).
56. A. Ale et al., "Imaging performance of a hybrid x-ray computed tomography-fluorescence molecular tomography system using priors," *Medical Physics* **37**(5), 1976-1986 (2010).
57. Y. Lin et al., "Quantitative fluorescence tomography using a combined tri-modality FT/DOT/XCT system," *Opt. Express* **18**(8), 7835-7850 (2010).
58. M. Guven, B. Yazici, and V. Ntziachristos, "Fluorescence optical tomography with a priori information," *Biomedical Optics (BiOS) 2007* 643107-643107-643115 (2007).
59. N. Beckmann, "In vivo magnetic resonance techniques and drug discovery," *Brazilian journal of physics* **36**(1A), 16-22 (2006).
60. J. Kandukuri et al., "A Dual-Modality System for Both Multi-Color Ultrasound-Switchable Fluorescence and Ultrasound Imaging," *International Journal of Molecular Sciences* **18**(2), 323 (2017).
61. B. Yuan et al., "High-resolution imaging in a deep turbid medium based on an ultrasound-switchable fluorescence technique," *Applied physics letters* **101**(3), 033703 (2012).
62. Y. Lin et al., "Temperature-modulated fluorescence tomography in a turbid media," *Applied physics letters* **100**(7), 073702 (2012).
63. Y. Lin et al., "Temperature-modulated fluorescence tomography based on both concentration and lifetime contrast," *Journal of biomedical optics* **17**(5), 0560071-0560074 (2012).
64. T. C. Kwong et al., "Activatable thermo-sensitive ICG encapsulated pluronic nanocapsules for temperature sensitive fluorescence tomography," *SPIE BiOS* 93390C-93390C-93396 (2015).
65. T. C. Kwong et al., "Validation of temperature-modulated fluorescence tomography in vivo," *SPIE BiOS* 89370H-89370H-89377 (2014).
66. V. Tsenova, and E. V. Stoykova, "Refractive index measurement in human tissue samples," *12th International School on Quantum Electronics Laser Physics and Applications* 413-417 (2003).
67. V. V. Tuchin, and V. Tuchin, *Tissue optics: light scattering methods and instruments for medical diagnosis*, SPIE press Bellingham (2007).

68. A. E. Cerussi et al., "Spectroscopy enhances the information content of optical mammography," *J Biomed Opt* **7**(1), 60-71 (2002).
69. T. Durduran et al., "Diffuse optics for tissue monitoring and tomography," *Reports on Progress in Physics* **73**(7), 076701 (2010).
70. S. Srinivasan et al., "In vivo hemoglobin and water concentrations, oxygen saturation, and scattering estimates from near-infrared breast tomography using spectral reconstruction," *Acad Radiol* **13**(2), 195-202 (2006).
71. J. Ruiz, "Breast Density Quantification Using Structured-light Diffuse Optical Tomography," in *UC Irvine: Biomedical Engineering*, p. 142, Dissertation, UC Irvine, Retrived from: http://escholarship.org/uc/item/8gx3v6tv (2016).
72. J. S. L. Wang L, and L. Zheng, "MCML-Monte Carlo modeling of light transport in multi-layered tissues," *Comput. Methods Programs Biomed.* **47**(2), 131 (1995).
73. L. Wang, and S. L. Jacques, "Hybrid model of Monte Carlo simulation diffusion theory for light reflectance by turbid media," *J. Opt. Soc. Am.* **10**(8), 1746 (1993).
74. S. L. Jacques, "Optical properties of biological tissues: a review," *Physics in medicine and biology* **58**(11), R37 (2013).
75. R. C. Mesquita, and A. G. Yodh, "Diffuse optics: fundamentals and tissue applications," *Nano optics and atomics: transport of light and matter waves* **173**((2011).
76. I. S. Saidi, S. L. Jacques, and F. K. Tittel, "Mie and Rayleigh modeling of visible-light scattering in neonatal skin," *Applied optics* **34**(31), 7410-7418 (1995).
77. S. L. Jacques, "Fractal nature of light scattering in tissues," *Journal of Innovative Optical Health Sciences* **4**(01), 1-7 (2011).
78. B. Valeur, *Molecular Fluorescence: Principles and Applications*, Wiley-VCH Verlag GmbH, Germany (2001).
79. J. McEwen, "Jablonksi Diagram," Chemistry LibreTexts, Retrieved from: https://chem.libretexts.org/Core/Physical_and_Theoretical_Chemistry/Spectroscopy/Electronic_Spectroscopy/Jablonski_diagram (2016).
80. J. W. Lichtman, and J.-A. Conchello, "Fluorescence microscopy," *Nature methods* **2**(12), 910-919 (2005).
81. I. D. Johnson, and M. W. Davidson, "Jablonski Energy Diagram," in *Optical Microscopy Primer Specialized Techniques* M. W. Davidson, Ed., Molecular Expressions, Accessed from:http://micro.magnet.fsu.edu/primer/java/jablonski/jabintro/ (2003).
82. J.-M. I. Maarek, and D. P. Holschneider, "Estimation of indocyanine green concentration in blood from fluorescence emission: application to hemodynamic assessment during hemodialysis," *Journal of biomedical optics* **14**(5), 054006-054006-054012 (2009).
83. B. Hollins, B. Noe, and J. Henderson, "Fluorometric determination of indocyanine green in plasma," *Clinical chemistry* **33**(6), 765-768 (1987).
84. J. R. Lakowicz, *Principles of Fluorescence Spectroscopy*, Third Ed ed., Springer US, Boston, MA (2006).
85. A. Godavarty, E. M. Sevick-Muraca, and M. J. Eppstein, "Three-dimensional fluorescence lifetime tomography," *Med Phys* **32**(4), 992-1000 (2005).
86. S. V. Patwardhan et al., "Time-dependent whole-body fluorescence tomography of probe bio-distributions in mice," *Optics Express* **13**(7), 2564-2577 (2005).

87. S. Keren et al., "A comparison between a time domain and continuous wave small animal optical imaging system," *IEEE transactions on medical imaging* **27**(1), 58-63 (2008).
88. D. A. Boas, C. Pitris, and N. Ramanujam, *Handbook of biomedical optics*, CRC press (2011).
89. T. K. Meyvis et al., "Fluorescence recovery after photobleaching: a versatile tool for mobility and interaction measurements in pharmaceutical research," *Pharmaceutical research* **16**(8), 1153-1162 (1999).
90. R. S. Bradley, and M. S. Thorniley, "A review of attenuation correction techniques for tissue fluorescence," *Journal of the royal society Interface* **3**(6), 1-13 (2006).
91. V. Pansare et al., "Review of long-wavelength optical and NIR imaging materials: contrast agents, fluorophores and multifunctional nano carriers," *Chemistry of materials: a publication of the American Chemical Society* **24**(5), 812 (2012).
92. N. Ramanujam, "Fluorescence spectroscopy of neoplastic and non-neoplastic tissues," *Neoplasia* **2**(1-2), 89-117 (2000).
93. G. A. Wagnieres, W. M. Star, and B. C. Wilson, "In vivo fluorescence spectroscopy and imaging for oncological applications," *Photochemistry and photobiology* **68**(5), 603-632 (1998).
94. B. N. Giepmans et al., "The fluorescent toolbox for assessing protein location and function," *science* **312**(5771), 217-224 (2006).
95. T. Durduran et al., "Bulk optical properties of healthy female breast tissue," *Phys Med Biol* **47**(16), 2847-2861 (2002).
96. D. R. Busch et al., "Optical malignancy parameters for monitoring progression of breast cancer neoadjuvant chemotherapy," *Biomed Opt Express* **4**(1), 105-121 (2013).
97. S. van de Ven et al., "Diffuse optical tomography of the breast: initial validation in benign cysts," *Mol Imaging Biol* **11**(2), 64-70 (2009).
98. A. Gibson, J. Hebden, and S. R. Arridge, "Recent advances in diffuse optical imaging," *Physics in medicine and biology* **50**(4), R1 (2005).
99. M. G. Pakalniskis et al., "Tumor angiogenesis change estimated by using diffuse optical spectroscopic tomography: demonstrated correlation in women undergoing neoadjuvant chemotherapy for invasive breast cancer?," *Radiology* **259**(2), 365-374 (2011).
100. B. W. Pogue et al., "Quantitative hemoglobin tomography with diffuse near-infrared spectroscopy: pilot results in the breast," *Radiology* **218**(1), 261-266 (2001).
101. V. Ntziachristos et al., "Concurrent MRI and diffuse optical tomography of breast after indocyanine green enhancement," *Proc Natl Acad Sci U S A* **97**(6), 2767-2772 (2000).
102. R. Choe et al., "Diffuse optical tomography of breast cancer during neoadjuvant chemotherapy: a case study with comparison to MRI," *Med Phys* **32**(4), 1128-1139 (2005).
103. O. Falou et al., "Diffuse optical spectroscopy evaluation of treatment response in women with locally advanced breast cancer receiving neoadjuvant chemotherapy," *Translational oncology* **5**(4), 238-246 (2012).

104. P. L. Choyke, A. J. Dwyer, and M. V. Knopp, "Functional tumor imaging with dynamic contrast-enhanced magnetic resonance imaging," *Journal of Magnetic Resonance Imaging* **17**(5), 509-520 (2003).
105. K. T. Kotz et al., "Inspiratory contrast for in vivo optical imaging," *Optics express* **16**(1), 19-31 (2008).
106. Y. Lin et al., "Tumor characterization in small animals using magnetic resonance-guided dynamic contrast enhanced diffuse optical tomography," *J Biomed Opt* **16**(10), 106015 (2011).
107. H. Dehghani et al., "Three-dimensional optical tomography: resolution in small-object imaging," *Appl Opt* **42**(16), 3117-3128 (2003).
108. B. W. Pogue et al., "Implicit and explicit prior information in near-infrared spectral imaging: accuracy, quantification and diagnostic value," *Philos Transact A Math Phys Eng Sci* **369**(1955), 4531-4557 (2011).
109. A. H. Hielscher, "Optical tomographic imaging of small animals," *Curr Opin Biotechnol* **16**(1), 79-88 (2005).
110. Q. Fang et al., "Combined optical and X-ray tomosynthesis breast imaging," *Radiology* **258**(1), 89-97 (2011).
111. N. C. Biswal, Y. Xu, and Q. Zhu, "Imaging tumor oxyhemoglobin and deoxyhemoglobin concentrations with ultrasound-guided diffuse optical tomography," *Technology in cancer research & treatment* **10**(5), 417-429 (2011).
112. B. Brooksby et al., "Imaging breast adipose and fibroglandular tissue molecular signatures by using hybrid MRI-guided near-infrared spectral tomography," *Proc Natl Acad Sci U S A* **103**(23), 8828-8833 (2006).
113. Q. Zhu et al., "Ultrasound-guided optical tomographic imaging of malignant and benign breast lesions: initial clinical results of 19 cases," *Neoplasia* **5**(379 - 388 (2003).
114. M. L. Flexman et al., "Monitoring early tumor response to drug therapy with diffuse optical tomography," *Journal of biomedical optics* **17**(1), 0160141-0160148 (2012).
115. Y. Tan, and H. Jiang, "Diffuse optical tomography guided quantitative fluorescence molecular tomography," *Applied optics* **47**(12), 2011-2016 (2008).
116. B. W. Pogue et al., "Comparison of imaging geometries for diffuse optical tomography of tissue," *Optics Express* **4**(8), 270-286 (1999).
117. A. T. Kumar et al., "Fluorescence-lifetime-based tomography for turbid media," *Opt Lett* **30**(24), 3347-3349 (2005).
118. R. S. B. B. B. J. Kumar A T N, and D. A. Boas, "Comparison of frequency-domain and time-domain fluorescence lifetime tomography," *Opt. Lett.* **33**(5), 470 (2008).
119. I. Nissilä et al., "Comparison between a time-domain and a frequency-domain system for optical tomography," *Journal of biomedical optics* **11**(6), 064015-064015-064018 (2006).
120. M. Gurfinkel et al., "Near-infrared fluorescence optical imaging and tomography," *Dis Markers* **19**(2-3), 107-121 (2003).
121. J. Collet, "Poloxamers," *Handbook of Pharmaceutical Excipients* (2003).
122. C. H. Schmitz et al., "Instrumentation for fast functional optical tomography," *Review of Scientific Instruments* **73**(2), 429-439 (2002).

123. B. Chance, Cope, M., Gratton, E., Ramanujam, N., Tromberg, B., "Phase measurement of light absorption and scatter in human tissue," *Rev. Sci. Inst.* **69**(10), 3457-3481 (1998).
124. R. B. Schulz et al., "Hybrid System for Simultaneous Fluorescence and X-Ray Computed Tomography," *Medical Imaging, IEEE Transactions on* **29**(2), 465-473 (2010).
125. D. S. Kepshire et al., "Imaging of glioma tumor with endogenous fluorescence tomography," *J Biomed Opt* **14**(3), 030501 (2009).
126. Y. Lin et al., "A photo-multiplier tube-based hybrid MRI and frequency domain fluorescence tomography system for small animal imaging," *Phys Med Biol* **56**(15), 4731-4747 (2011).
127. S. C. Davis et al., "Image-guided diffuse optical fluorescence tomography implemented with Laplacian-type regularization," *Opt Express* **15**(7), 4066-4082 (2007).
128. Y. Lin et al., "Fluorescence diffuse optical tomography with functional and anatomical a priori information: feasibility study," *Phys Med Biol* **52**(18), 5569-5585 (2007).
129. P. K. Yalavarthy et al., "Structural information within regularization matrices improves near infrared diffuse optical tomography," *Opt. Express* **15**(13), 8043-8058 (2007).
130. S. C. Davis et al., "MRI-coupled fluorescence tomography quantifies EGFR activity in brain tumors," *Acad Radiol* **17**(3), 271-276 (2010).
131. M. Nahrendorf et al., "Hybrid in vivo FMT-CT imaging of protease activity in atherosclerosis with customized nanosensors," *Arterioscler Thromb Vasc Biol* **29**(10), 1444-1451 (2009).
132. L. Hervé et al., "Noncontact fluorescence diffuse optical tomography of heterogeneous media," *Applied optics* **46**(22), 4896-4906 (2007).
133. Y. Lin et al., "Quantitative fluorescence tomography with functional and structural a priori information," *Appl Opt* **48**(7), 1328-1336 (2009).
134. C. Yongping, and L. Xingde, "Thermo/pH-Responsive and Reversible NIR Fluorescent Probes for Optical Molecular Imaging," in OSA Technical Digest (CD) JMA105 (2010).
135. J. J. Escobar-Chávez et al., "Applications of thermo-reversible pluronic F-127 gels in pharmaceutical formulations," *J Pharm Pharm Sci* **9**(3), 339-358 (2006).
136. T. H. Kim et al., "Evaluation of temperature-sensitive, indocyanine green-encapsulating micelles for noninvasive near-infrared tumor imaging," *Pharm Res* **27**(9), 1900-1913 (2010).
137. M. Kobayashi et al., "Fluorescence tomography in turbid media based on acousto-optic modulation imaging," *Applied Physics Letters* **89**(18), 181102-181102-181103 (2006).
138. B. Yuan et al., "Microbubble-enhanced ultrasound-modulated fluorescence in a turbid medium," *Applied Physics Letters* **95**(18), 181113-181113-181113 (2009).
139. B. Yuan, and Y. Liu, "Ultrasound-modulated fluorescence from rhodamine B aqueous solution," *Journal of Biomedical Optics* **15**(2), 021321-021326 (2010).
140. C. Schutt, "Ultrasound-modulated fluorescent contrast agent for optical imaging through turbid media," *Proc. SPIE* **8165**(1), 81650B (2011).

141. B. Yuan, "Ultrasound-modulated fluorescence based on a fluorophore-quencher-labeled microbubble system," *Journal of Biomedical Optics* **14**(2), 024043-024011 (2009).
142. A. L. Klibanov, "Ligand-Carrying Gas-Filled Microbubbles: Ultrasound Contrast Agents for Targeted Molecular Imaging†," *Bioconjugate Chemistry* **16**(1), 9-17 (2004).
143. A. M. Takalkar et al., "Binding and detachment dynamics of microbubbles targeted to P-selectin under controlled shear flow," *Journal of Controlled Release* **96**(3), 473-482 (2004).
144. L. V. Wang, "Prospects of photoacoustic tomography," *Medical Physics* **35**(12), 5758-5767 (2008).
145. L. Meng-Lin et al., "Simultaneous Molecular and Hypoxia Imaging of Brain Tumors In Vivo Using Spectroscopic Photoacoustic Tomography," *Proceedings of the IEEE* **96**(3), 481-489 (2008).
146. R. Ma et al., "Multispectral optoacoustic tomography (MSOT) scanner for whole-body small animal imaging," *Opt. Express* **17**(24), 21414-21426 (2009).
147. W. J. Akers et al., "Noninvasive photoacoustic and fluorescence sentinel lymph node identification using dye-loaded perfluorocarbon nanoparticles," *Acs Nano* **5**(1), 173-182 %@ 1936-0851 (2010).
148. C. Kim, C. Favazza, and L. V. Wang, "In vivo photoacoustic tomography of chemicals: high-resolution functional and molecular optical imaging at new depths," *Chemical reviews* **110**(5), 2756-2782 %@ 0009-2665 (2010).
149. H. H. Sung et al., "Seven years of experience with high-intensity focused ultrasound for prostate cancer: Advantages and limitations," *The Prostate* **72**(13), 1399-1406 (2012).
150. A. B. Barqawi, "Emerging role of HIFU as a noninvasive ablative method to treat localized prostate cancer," *Oncology* **22**(2), 123 (2008).
151. A. Schmitz et al., "Image-guided focused ultrasound ablation of breast cancer: current status, challenges, and future directions," *European Radiology* **18**(7), 1431-1441 (2008).
152. F. Orsi et al., "High intensity focused ultrasound ablation: A new therapeutic option for solid tumors," *Journal of Cancer Research and Therapeutics* **6**(4), 414-420 (2010).
153. F. Orsi et al., "High intensity focused ultrasound ablation: a new therapeutic option for solid tumors," *Journal of cancer research and therapeutics* **6**(4), 414 (2010).
154. F. A. Jolesz, "MRI-Guided Focused Ultrasound Surgery," *Annual Review of Medicine* **60**(1), 417-430 (2009).
155. R. Z, C. ZR, and H. S, "Magnetic resonance imaging-guided, high-intensity focused ultrasound for brain tumor therapy," *Neurosurgery.* **59**(949 (2006).
156. J. FA, and M. N, "Current status and future potential of MRI-guided focused ultrasound surgery," *J. Magn. Reson. Imaging* **27**(391 (2008).
157. A. Sciarra et al., "Advances in Magnetic Resonance Imaging: How They Are Changing the Management of Prostate Cancer," *European Urology* **59**(6), 962-977 (2011).
158. B. Turkbey, P. A. Pinto, and P. L. Choyke, "Imaging techniques for prostate cancer: implications for focal therapy," *Nat Rev Urol* **6**(4), 191-203 (2009).

159. J. K. Kim, Y.-J. Jang, and G. Cho, "Multidisciplinary Functional MR Imaging for Prostate Cancer," *Korean J Radiol* **10**(6), 535-551 (2009).
160. H. Lukka et al., "High-intensity Focused Ultrasound for Prostate Cancer: a Systematic Review," *Clinical Oncology* **23**(2), 117-127 (2011).
161. H. H. Barrett, "Iii the radon transform and its applications," *Progress in Optics* **21**(217-286 (1984).
162. R. C. Haskell et al., "Boundary conditions for the diffusion equation in radiative transfer," *J. Opt. Soc. Am. A* **11**(10), 2727-2741 (1994).
163. K. Ren, G. Bal, and A. H. Hielscher, "Transport- and diffusion-based optical tomography in small domains: a comparative study," *Appl. Opt.* **46**(27), 6669-6679 (2007).
164. S. Arridge et al., "A finite element approach for modeling photon transport in tissue," *Medical physics* **20**(2), 299-309 (1993).
165. F. P. Bolin et al., "Refractive index of some mammalian tissues using a fiber optic cladding method," *Applied optics* **28**(12), 2297-2303 (1989).
166. E. M. C. Hillman, "Experimental and theoretical investigations of near infrared tomographic imaging methods and clinical applications," in *Department of Medical Physics and Bioengineering*, p. 356, University College London, Retrieved from: http://ethos.bl.uk/OrderDetails.do?uin=uk.bl.ethos.268884 (2002).
167. S. Arridge, "Optical tomography in medical imaging," *Inverse Problems* **15**(2), R41-R93 (1999).
168. M. Schweiger et al., "The finite element method for the propagation of light in scattering media: boundary and source conditions," *Med Phys* **22**(11 Pt 1), 1779-1792 (1995).
169. D. W. Marquardt, "An algorithm for least-squares estimation of nonlinear parameters," *Journal of the society for Industrial and Applied Mathematics* **11**(2), 431-441 (1963).
170. K. Levenberg, "A method for the solution of certain non–linear problems in least squares," (1944).
171. M. Schweiger, S. R. Arridge, and D. T. Delpy, "Application of the finite-element method for the forward and inverse models in optical tomography," *Journal of Mathematical Imaging and Vision* **3**(3), 263-283 (1993).
172. H. Dehghani, D. Barber, and I. Basarab-Horwath, "Incorporating a priori anatomical information into image reconstruction in electrical impedance tomography," *Physiological measurement* **20**(1), 87 (1999).
173. A. N. Tikhonov, "Regularization of incorrectly posed problems," (1963).
174. K. D. Paulsen, and H. Jiang, "Spatially varying optical property reconstruction using a finite element diffusion equation approximation," *Med Phys* **22**(6), 691-701 (1995).
175. S. Srinivasan et al., "Improved quantification of small objects in near-infrared diffuse optical tomography," *J Biomed Opt* **9**(6), 1161-1171 (2004).
176. P. K. Yalavarthy et al., "Weight-matrix structured regularization provides optimal generalized least-squares estimate in diffuse optical tomography," *Med Phys* **34**(6), 2085-2098 (2007).

177. S. R. Arridge, and M. Schweiger, "Photon-measurement density functions. Part 2: Finite-element-method calculations," *Applied Optics* **34**(34), 8026-8037 (1995).
178. J. R. Lakowicz, and K. W. Berndt, "Lifetime-selective fluorescence imaging using an rf phase-sensitive camera," *Review of Scientific Instruments* **62**(7), 1727-1734 (1991).
179. H. Dehghani et al., "Numerical modelling and image reconstruction in diffuse optical tomography," *Philos Trans A Math Phys Eng Sci* **367**(1900), 3073-3093 (2009).
180. B. Brooksby et al., "Combining near-infrared tomography and magnetic resonance imaging to study in vivo breast tissue: implementation of a Laplacian-type regularization to incorporate magnetic resonance structure," *J Biomed Opt* **10**(5), 051504 (2005).
181. D. H et al., "Structural a-priori information in near-infrared optical tomography," *Proceedings of SPIE* **6341**(10 (2007).
182. A. H. Golnabi et al., "Comparison of no-prior and soft-prior regularization in biomedical microwave imaging," *Journal of Medical Physics* **36**(3), 159 (2011).
183. W. F. Cheong, S. A. Prahl, and A. J. Welch, "A review of the optical properties of biological tissues," *IEEE Journal of Quantum Electronics* **26**(2166-2185 (1990).
184. V. Peters et al., "Optical properties of normal and diseased human breast tissues in the visible and near infrared," *Physics in medicine and biology* **35**(9), 1317 (1990).
185. F. Nouizi et al., "Implementation of a new scanning method for high-resolution fluorescence tomography using thermo-sensitive fluorescent agents," *Opt Lett* **40**(21), 4991-4994 (2015).
186. K. B. Ocheltree, and L. A. Frizzel, "Sound field calculation for rectangular sources," *Ultrasonics, Ferroelectrics and Frequency Control, IEEE Transactions on* **36**(2), 242-248 (1989).
187. G. Wang et al., "Temperature-modulated bioluminescence tomography," *Opt. Express* **14**(17), 7852-7871 (2006).
188. E. H. Wissler, "Pennes' 1948 paper revisited," *J Appl Physiol (1985)* **85**(1), 35-41 (1998).
189. Y. Lin et al., "Simulation-based evaluation of the resolution and quantitative accuracy of temperature-modulated fluorescence tomography," *Appl Opt* **54**(25), 7612-7621 (2015).
190. Y. Lin et al., "Quantitative fluorescence tomography using a combined tri-modality FT/DOT/XCT system," *Optics Express* **18**(8), 7835–7850 (2010).
191. D. S. Kepshire et al., "Subsurface diffuse optical tomography can localize absorber and fluorescent objects but recovered image sensitivity is nonlinear with depth," *Appl. Opt.* **46**(10), 1669-1678 (2007).
192. S. B. Raymond et al., "Fluorescence tomography in a murine model of Alzheimer's disease," *Biomedical Optics (BiOS) 2007* 64342H-64342H-64348 (2016).
193. V. Ntziachristos et al., "Visualization of Antitumor Treatment by Means of Fluorescence Molecular Tomography with an Annexin V-Cy5.5 Conjugate," *Proceedings of the National Academy of Sciences of the United States of America* **101**(33), 12294-12299 (2004).
194. A. Corlu et al., "Three-dimensional in vivo fluorescence diffuse optical tomography of breast cancer in humans," *Optics Express, Vol. 15, Issue 11, pp. 6696-6716* (2007).

195. C. Bremer, C.-H. Tung, and R. Weissleder, "In vivo molecular target assessment of matrix metalloproteinase inhibition," *Nature Medicine* **7**(6), 743-748 (2001).
196. F. Stuker, J. Ripoll, and M. Rudin, "Fluorescence Molecular Tomography: Principles and Potential for Pharmaceutical Research," *Pharmaceutics* **3**(2), 229-274 (2011).
197. X. Chen, *Molecular Imaging probes for cancer research*, World Scientific (2012).
198. B. E. Schaafsma et al., "The clinical use of indocyanine green as a near-infrared fluorescent contrast agent for image-guided oncologic surgery," *J Surg Oncol* **104**(3), 323-332 (2011).
199. V. L. Dzurinko, A. S. Gurwood, and J. R. Price, "Intravenous and indocyanine green angiography," *Optometry - Journal of the American Optometric Association* **75**(12), 743-755 (2004).
200. J. X. Jiang et al., "Optimization of the enhanced permeability and retention effect for near-infrared imaging of solid tumors with indocyanine green," *Am J Nucl Med Mol Imaging* **5**(4), 390-400 (2015).
201. J. Fang, H. Nakamura, and H. Maeda, "The EPR effect: Unique features of tumor blood vessels for drug delivery, factors involved, and limitations and augmentation of the effect ☆," *Advanced Drug Delivery Reviews* **63**(3), 136–151 (2011).
202. M. Hutteman et al., "Near-infrared fluorescence imaging in patients undergoing pancreaticoduodenectomy," *European Surgical Research* **47**(2), 90-97 (2011).
203. X. Intes et al., "In vivo continuous-wave optical breast imaging enhanced with Indocyanine Green," *Med Phys* **30**(6), 1039-1047 (2003).
204. M. Watanabe et al., "Colonic tattooing using fluorescence imaging with light-emitting diode-activated indocyanine green: a feasibility study," *Surgery today* **39**(3), 214-218 (2009).
205. J. C. Rasmussen et al., "Lymphatic imaging in humans with near-infrared fluorescence," *Current opinion in biotechnology* **20**(1), 74-82 (2009).
206. C.-H. Quek, and K. W. Leong, "Near-Infrared Fluorescent Nanoprobes for in Vivo Optical Imaging," *Nanomaterials* **2**(2), 92-112 (2012).
207. A. Hellebust, and R. Richards-Kortum, "Advances in molecular imaging: targeted optical contrast agents for cancer diagnostics," *Nanomedicine* **7**(3), 429-445 (2012).
208. Zhen Cheng et al., "Near-Infrared Fluorescent RGD Peptides for Optical Imaging of Integrin αvβ3 Expression in Living Mice," *Bioconjugate Chemistry* **16**(6), 1433-1441 (2005).
209. H. Jin, and J. Varner, "Integrins: roles in cancer development and as treatment targets," *British Journal of Cancer* **90**(3), 561-565 (2004).
210. J. D. Hood, and D. A. Cheresh, "Role of integrins in cell invasion and migration," *Nature Reviews Cancer* **2**(2), 91-100 (2002).
211. C. XY, C. PS, and M. RA, "In vivo near-infrared fluorescence imaging of integrin a,alpha(v)beta(3) in brain tumor xenografts," *Cancer Res.* **64**(8009 (2004).
212. W. Cai et al., "Peptide-labeled near-infrared quantum dots for imaging tumor vasculature in living subjects," *Nano letters* **6**(4), 669-676 (2006).
213. X. Gao et al., "In vivo cancer targeting and imaging with semiconductor quantum dots," *Nature Biotechnology* **22**(8), 969-976 (2004).

214. C. Y. L. R. M. C. L. W. Gao X, and S. Nie, "In vivo cancer targeting and imaging with semiconductor quantum dots," *Nat. Biotechnol.* **22**(8), 969 (2004).
215. M. E. Davis, Z. G. Chen, and D. M. Shin, "Nanoparticle therapeutics: an emerging treatment modality for cancer," *Nature Reviews Drug Discovery* **7**(9), 771-782 (2008).
216. S. K. Nune et al., "Nanoparticles for biomedical imaging," *Expert Opin Drug Deliv* **6**(11), 1175-1194 (2009).
217. C. Yongping, J. Toufic, and L. Xingde, "Functional Fluorescent Nanocapsules for Molecular Imaging and Potential Targeted Therapy," in OSA Technical Digest (CD) JME1 (2011).
218. J. Schroeder et al., "Folate-mediated tumor cell uptake of quantum dots entrapped in lipid nanoparticles," *Journal of Controlled Release* **124**(1), 28-34 (2007).
219. T. Kim et al., "Evaluation of Temperature-Sensitive, Indocyanine Green-Encapsulating Micelles for Noninvasive Near-Infrared Tumor Imaging," *Pharmaceutical Research* **27**(9), 1900-1913 (2010).
220. H. Cho et al., "Polymeric micelles for apoptosis-targeted optical imaging of cancer and intraoperative surgical guidance," *PloS one* **9**(2), e89968 (2014).
221. E. Portnoy et al., "Cetuximab-labeled liposomes containing near-infrared probe for in vivo imaging," *Nanomedicine: Nanotechnology, Biology and Medicine* **7**(4), 480-488 (2011).
222. L. Zhang, and D. Zhao, "Liposomal Encapsulation Enhances In Vivo Near Infrared Imaging of Exposed Phosphatidylserine in a Mouse Glioma Model," *Molecules* **18**(12), 14613-14628 (2013).
223. H. Kobayashi, and P. L. Choyke, "Target-cancer-cell-specific activatable fluorescence imaging probes: rational design and in vivo applications," *Accounts of chemical research* **44**(2), 83-90 (2010).
224. D. D. Nolting, J. C. Gore, and W. Pham, "NEAR-INFRARED DYES: Probe Development and Applications in Optical Molecular Imaging," *Curr Org Synth* **8**(4), 521-534 (2011).
225. R. H. Goldfarb, and L. A. Liotta, "Proteolytic enzymes in cancer invasion and metastasis," *Seminars in thrombosis and hemostasis* 294-307 (1986).
226. C.-H. Tung et al., "In vivo imaging of proteolytic enzyme activity using a novel molecular reporter," *Cancer research* **60**(17), 4953-4958 (2000).
227. K. E. Bullok et al., "Biochemical and in vivo characterization of a small, membrane-permeant, caspase-activatable far-red fluorescent peptide for imaging apoptosis," *Biochemistry* **46**(13), 4055-4065 (2007).
228. L. E. Edgington et al., "Noninvasive optical imaging of apoptosis by caspase-targeted activity-based probes," *Nature medicine* **15**(8), 967-973 (2009).
229. R. Weissleder, and V. Ntziachristos, "Shedding light onto live molecular targets," *Nat Med* **9**(1), 123-128 (2003).
230. K. Marten et al., "Detection of dysplastic intestinal adenomas using enzyme-sensing molecular beacons in mice," *Gastroenterology* **122**(2), 406-414 (2002).
231. Y. Urano et al., "Selective molecular imaging of viable cancer cells with pH-activatable fluorescence probes," *Nature medicine* **15**(1), 104-109 (2009).
232. H. Lee et al., "Near-infrared pH-activatable fluorescent probes for imaging primary and metastatic breast tumors," *Bioconjugate chemistry* **22**(4), 777-784 (2011).

233. Y. Chen, and X. Li, "Near-infrared fluorescent nanocapsules with reversible response to thermal/pH modulation for optical imaging," *Biomacromolecules* **12**(12), 4367-4372 (2011).
234. K. Kiyose et al., "Hypoxia-sensitive fluorescent probes for in vivo real-time fluorescence imaging of acute ischemia," *Journal of the American Chemical Society* **132**(45), 15846-15848 (2010).
235. C. D. Brites et al., "Thermometry at the nanoscale," *Nanoscale* **4**(16), 4799-4829 (2012).
236. T. C. Kwong et al., "Temperature-modulated fluorescence tomography: modulating tissue temperature using HIFU for high-resolution in vivo fluorescence tomography," *SPIE BiOS* 857405-857405-857408 (2013).
237. S. Lee et al., "Activatable imaging probes with amplified fluorescent signals," *Chemical Communications* 36), 4250-4260 (2008).
238. Z. Wang et al., "Temperature-sensitive fluorescent organic nanoparticles with aggregation-induced emission for long-term cellular tracing," *ACS applied materials & interfaces* **7**(5), 3420-3425 (2015).
239. S. Uchiyama et al., "Fluorescent molecular thermometers based on polymers showing temperature-induced phase transitions and labeled with polarity-responsive benzofurazans," *Analytical chemistry* **75**(21), 5926-5935 (2003).
240. Y. Wu et al., "Optical imaging of tumor microenvironment," *Am J Nucl Med Mol Imaging* **3**(1), 1-15 (2013).
241. E. Iessi et al., "Tumor acidity and malignancy: novel aspects in the design of anti-tumor therapy," *Cancer Ther* **6**(1), 55-66 (2008).
242. P. Vaupel, "Tumor microenvironmental physiology and its implications for radiation oncology," *Seminars in Radiation Oncology* **14**(3), 198–206 (2004).
243. P. Vaupel, and A. Mayer, "Hypoxia in cancer: significance and impact on clinical outcome," *Cancer and Metastasis Reviews* **26**(2), 225-239 (2007).
244. D. Wilson, and S. Vinogradov, "Tissue oxygen measurements using phosphorescence quenching," *Handbook of Biomedical Fluorescence* **637**(662 (2003).
245. L. S. Ziemer et al., "Oxygen distribution in murine tumors: characterization using oxygen-dependent quenching of phosphorescence," *Journal of Applied Physiology* **98**(4), 1503-1510 (2005).
246. S. Zhang et al., "Phosphorescent light–emitting iridium complexes serve as a hypoxia-sensing probe for tumor imaging in living animals," *Cancer research* **70**(11), 4490-4498 (2010).
247. T. Desmettre, J. Devoisselle, and S. Mordon, "Fluorescence properties and metabolic features of indocyanine green (ICG) as related to angiography," *Survey of ophthalmology* **45**(1), 15-27 (2000).
248. B. Yuan, N. Chen, and Q. Zhu, "Emission and absorption properties of indocyanine green in Intralipid solution," *J Biomed Opt* **9**(3), 497-503 (2004).
249. S. Yoneya et al., "Binding properties of indocyanine green in human blood," *Invest Ophthalmol Vis Sci* **39**(7), 1286-1290 (1998).

250. M. Ogawa et al., "In vivo molecular imaging of cancer with a quenching near-infrared fluorescent probe using conjugates of monoclonal antibodies and indocyanine green," *Cancer research* **69**(4), 1268-1272 (2009).
251. M. Herranz, and A. Ruibal, "Optical imaging in breast cancer diagnosis: the next evolution," *Journal of oncology* **2012**((2012).
252. K. Licha et al., "Hydrophilic cyanine dyes as contrast agents for near-infrared tumor imaging: synthesis, photophysical properties and spectroscopic in vivo characterization," *Photochem Photobiol* **72**(3), 392-398 (2000).
253. V. Saxena, M. Sadoqi, and J. Shao, "Enhanced photo-stability, thermal-stability and aqueous-stability of indocyanine green in polymeric nanoparticulate systems," *Journal of Photochemistry and Photobiology B: Biology* **74**(1), 29-38 (2004).
254. B. Hammouda, and D. L. Ho, "Insight into chain dimensions in PEO/water solutions," *Journal of Polymer Science Part B: Polymer Physics* **45**(16), 2196-2200 (2007).
255. P. Chandaroy et al., "Utilizing temperature-sensitive association of Pluronic F-127 with lipid bilayers to control liposome–cell adhesion," *Biochimica et Biophysica Acta (BBA)-Biomembranes* **1559**(1), 32-42 (2002).
256. E. V. Batrakova, and A. V. Kabanov, "Pluronic block copolymers: Evolution of drug delivery concept from inert nanocarriers to biological response modifiers," *Journal of Controlled Release* **130**(2), 98–106 (2008).
257. A. Pitto-Barry, and N. P. Barry, "Pluronic® block-copolymers in medicine: from chemical and biological versatility to rationalisation and clinical advances," *Polymer Chemistry* **5**(10), 3291-3297 (2014).
258. P. Alexandridis, and T. A. Hatton, "Poly (ethylene oxide)□ poly (propylene oxide)□ poly (ethylene oxide) block copolymer surfactants in aqueous solutions and at interfaces: thermodynamics, structure, dynamics, and modeling," *Colloids and Surfaces A: Physicochemical and Engineering Aspects* **96**(1), 1-46 (1995).
259. A. Russo et al., "Biotin-targeted Pluronic® P123/F127 mixed micelles delivering niclosamide: A repositioning strategy to treat drug-resistant lung cancer cells," *International Journal of Pharmaceutics* **511**(1), 127-139 (2016).
260. S. Thayyil et al., "Cerebral magnetic resonance biomarkers in neonatal encephalopathy: a meta-analysis," *Pediatrics* **125**(2), e382-395.
261. J. Valle et al., "A phase II, window study of SP1049C as first-line therapy in inoperable metastatic adenocarcinoma of the oesophagus," *Journal of Clinical Oncology* **22**(14_suppl), 4195-4195 (2004).
262. V. Y. Alakhov et al., "Hypersensitization of multidrug resistant human ovarian carcinoma cells by pluronic P85 block copolymer," *Bioconjugate chemistry* **7**(2), 209-216 (1996).
263. X. Li et al., "Self-assembly and characterization of Pluronic P105 micelles for liver-targeted delivery of silybin," *Journal of drug targeting* **17**(10), 739-750 (2009).
264. A. M. Takalkar et al., "Binding and detachment dynamics of microbubbles targeted to P-selectin under controlled shear flow," *J Control Release* **96**(3), 473-482 (2004).
265. D. Y. Alakhova, and A. V. Kabanov, "Pluronics and MDR reversal: an update," *Molecular pharmaceutics* **11**(8), 2566-2578 (2014).

266. L. Liu et al., "Bioconjugated Pluronic Triblock-Copolymer Micelle-Encapsulated Quantum Dots for Targeted Imaging of Cancer: In Vitro and In Vivo Studies," *Theranostics* **2**(7), 705-713 (2012).
267. V. B. Rodriguez et al., "Encapsulation and stabilization of indocyanine green within poly(styrene-alt-maleic anhydride) block-poly(styrene) micelles for near-infrared imaging," *Journal of Biomedical Optics* **13**(1), 014025-014010 (2008).
268. R. Rajagopalan et al., "Stabilization of the optical tracer agent indocyanine green using noncovalent interactions," *Photochem Photobiol* **71**(3), 347-350 (2000).
269. F. Yuan et al., "Vascular permeability in a human tumor xenograft: molecular size dependence and cutoff size," *Cancer research* **55**(17), 3752-3756 (1995).
270. A. Inc., "Frequently Asked Questions - IC Green Injection: ophthalmic angiography (indocyanine green for injection, USP) - Akorn," Akorn Inc., http://www.icginjection.com/faqs-2/ (2017).
271. V. Saxena, M. Sadoqi, and J. Shao, "Degradation kinetics of indocyanine green in aqueous solution," *Journal of pharmaceutical sciences* **92**(10), 2090-2097 (2003).
272. A. C. Caro, F. C. Hankenson, and J. O. Marx, "Comparison of Thermoregulatory Devices Used during Anesthesia of C57BL/6 Mice and Correlations between Body Temperature and Physiologic Parameters," *J Am Assoc Lab Anim Sci* **52**(5), 577-583 (2013).
273. C. J. Gordon, "The therapeutic potential of regulated hypothermia," *Emergency Medicine Journal* **18**(2), 81-89 (2001).
274. G. Prencipe et al., "PEG Branched Polymer for Functionalization of Nanomaterials with Ultralong Blood Circulation," *Journal of the American Chemical Society* **131**(13), 4783-4787 (2009).
275. T. V.P, "Which polymer can make nanoparticulate drug carriers long-circulating?," *Advanced Drug Delivery Reviews* **16**(141-155), (1995).
276. C. Yewale et al., "Epidermal growth factor receptor targeting in cancer: a review of trends and strategies," *Biomaterials* **34**(34), 8690-8707 (2013).
277. G. Carpenter, L. King, and S. Cohen, "Epidermal growth factor stimulates phosphorylation in membrane preparations in vitro," (1978).
278. M. K. Paul, and A. K. Mukhopadhyay, "Tyrosine kinase – Role and significance in Cancer," *Int J Med Sci* **1**(2), 101-115 (2004).
279. R. Nishikawa et al., "A mutant epidermal growth factor receptor common in human glioma confers enhanced tumorigenicity," *Proceedings of the National Academy of Sciences* **91**(16), 7727-7731 (1994).
280. "What are the key statistics about prostate cancer?," (2016).
281. S. S. Chang, "Overview of Prostate-Specific Membrane Antigen," *Rev Urol* **6**(Suppl 10), S13-18 (2004).
282. R. C. Mease, C. A. Foss, and M. G. Pomper, "PET Imaging in Prostate Cancer: Focus on Prostate-Specific Membrane Antigen," *Curr Top Med Chem* **13**(8), 951-962 (2013).
283. K. Bouchelouche, P. L. Choyke, and J. Capala, "Prostate Specific Membrane Antigen—A Target for Imaging and Therapy with Radionuclides," *Discov Med* **9**(44), 55-61 (2010).

284. Hamamatsu, "Metal Package Photomultiplier Tube R7400U Series," http://www.alldatasheet.com/datasheet-pdf/pdf/212308/HAMAMATSU/R7400U-20.html.
285. F. U. Foundation, "Mechanisms of Action," Focused Ultrasound Foundation https://www.fusfoundation.org/for-researchers/mechanisms-of-action (2015).
286. Y.-s. Kim et al., "High-intensity focused ultrasound therapy: an overview for radiologists," *Korean journal of radiology* **9**(4), 291-302 (2008).
287. R. W. Wood, and A. L. Loomis, "The physical and biological effects of high-frequency sound-waves of great intensity," *The London, Edinburgh, and Dublin philosophical magazine and journal of science* **4**(22), 417-436 (1927).
288. D. Schlesinger et al., "MR-guided focused ultrasound surgery, present and future," *Medical physics* **40**(8), (2013).
289. G. ter Haar, and C. Coussios, "High intensity focused ultrasound: physical principles and devices," *International Journal of Hyperthermia* **23**(2), 89-104 (2007).
290. C. Hill, "Optimum acoustic frequency for focused ultrasound surgery," *Ultrasound in medicine & biology* **20**(3), 271-277 (1994).
291. Y. Chen, and X. Li, "Near-infrared fluorescent nanocapsules with reversible response to thermal/pH modulation for optical imaging," *Biomacromolecules* **12**(12), 4367-4372 (2011).
292. A. L. McKenzie, "Physics of thermal processes in laser-tissue interaction," *Phys Med Biol* **35**(9), 1175-1209 (1990).
293. F. Leblond et al., "Pre-clinical whole-body fluorescence imaging: Review of instruments, methods and applications," *J Photochem Photobiol B* **98**(1), 77-94 (2010).
294. M. H. M. Benchimol, C. Schutt, and S. Esener, "Ultrasound-Quenchable Fluorescent Contrast Agent: Experimental Demonstration," *Optical Molecular Probes, Imaging and Drug Delivery, OSA Conference* **OSA Technical Digest**((2011).
295. A. L. Klibanov, "Ligand-carrying gas-filled microbubbles: ultrasound contrast agents for targeted molecular imaging," *Bioconjug Chem* **16**(1), 9-17 (2005).
296. D. Kepshire et al., "A microcomputed tomography guided fluorescence tomography system for small animal molecular imaging," *Rev Sci Instrum* **80**(4), 043701 (2009).
297. C. M. Neophytou, and A. I. Constantinou, "Drug delivery innovations for enhancing the anticancer potential of Vitamin E isoforms and their derivatives," *BioMed research international* **2015**((2015).
298. M. Xu, and L. V. Wang, "Photoacoustic imaging in biomedicine," *Review of Scientific Instruments* **77**(4), 041101-041122 (2006).
299. D. Razansky et al., "Multispectral opto-acoustic tomography of deep-seated fluorescent proteins in vivo," *Nat Photon* **3**(7), 412-417 (2009).
300. J. Mérian et al., "Fluorescent nanoprobes dedicated to in vivo imaging: from preclinical validations to clinical translation," *Molecules* **17**(5), 5564-5591 (2012).
301. J. V. Frangioni, "In vivo near-infrared fluorescence imaging," *Current Opinion in Chemical Biology* **7**(5), 626-634 (2003).

302. V. Ntziachristos, C. Bremer, and R. Weissleder, "Fluorescence imaging with near-infrared light: new technological advances that enable in vivo molecular imaging," *Eur Radiol* **13**(1), 195-208 (2003).
303. R. Cubeddu et al., "Time-resolved fluorescence imaging in biology and medicine," *Journal of Physics D: Applied Physics* **35**(9), R61 (2002).
304. E. Kuwana, F. Liang, and E. M. Sevick-Muraca, "Fluorescence lifetime spectroscopy of a pH-sensitive dye encapsulated in hydrogel beads," *Biotechnol Prog* **20**(5), 1561-1566 (2004).
305. R. E. Nothdurft et al., "In vivo fluorescence lifetime tomography," *J Biomed Opt* **14**(2), 024004 (2009).
306. T. Gadella, A. van Hoek, and A. Visser, "Construction and characterization of a frequency-domain fluorescence lifetime imaging microscopy system," *Journal of Fluorescence* **7**(1), 35-43 (1997).
307. A. Godavarty et al., "Fluorescence-enhanced optical imaging in large tissue volumes using a gain-modulated ICCD camera," *Phys Med Biol* **48**(12), 1701-1720 (2003).
308. W.-D. Ma et al., "Pluronic F127-g-poly(acrylic acid) copolymers as in situ gelling vehicle for ophthalmic drug delivery system," *International Journal of Pharmaceutics* **350**(1-2), 247-256 (2008).
309. S. H. Choi et al., "Thermally Reversible Pluronic/Heparin Nanocapsules Exhibiting 1000-Fold Volume Transition," *Langmuir* **22**(4), 1758-1762 (2006).
310. T. C. Kwong et al., "Experimental evaluation of the resolution and quantitative accuracy of temperature-modulated fluorescence tomography," *Applied Optics* **56**(3), 521-529 (2017).
311. G. ter Haar, "Principles of High-Intensity Focused Ultrasound," in *Interventional Oncology: A Practical Guide for the Interventional Radiologist* P. R. Mueller, and A. Adams, Eds., pp. 51-63, Springer, New York, USA (2012).
312. S. F. Sultan, G. Shorten, and G. Iohom, "Simulators for training in ultrasound guided procedures," *Medical Ultrasonography* **15**(2), 125-131 (2013).
313. G. Yao, and L. V. Wang, "Theoretical and experimental studies of ultrasound-modulated optical tomography in biological tissue," *Applied Optics* **39**(4), 659-664 (2000).
314. M. Alhamami, M. C. Kolios, and J. Tavakkoli, "Photoacoustic detection and optical spectroscopy of high-intensity focused ultrasound-induced thermal lesions in biologic tissue," *Medical physics* **41**(5), (2014).
315. C. Bremer, V. Ntziachristos, and R. Weissleder, "Optical-based molecular imaging: contrast agents and potential medical applications," *Eur Radiol* **13**(2), 231-243 (2003).
316. F. A. Jaffer, and R. Weissleder, "Molecular Imaging in the Clinical Arena," *JAMA: The Journal of the American Medical Association* **293**(7), 855-862 (2005).
317. R. Weissleder, "Molecular imaging in cancer," *Science* **312**(5777), 1168-1171 (2006).
318. P. Malaney, S. V. Nicosia, and V. Davé, "One mouse, one patient paradigm: New avatars of personalized cancer therapy," *Cancer letters* **344**(1), 1-12 (2014).

319. E. Garralda et al., "Integrated next-generation sequencing and avatar mouse models for personalized cancer treatment," *Clinical Cancer Research* **20**(9), 2476-2484 (2014).

320. C. Yongping, G. J. Toufic, and L. Xingde, "Bioconjugated ICG/Dox-Micellar Nanocapsules for Optical Molecular Imaging and Targeted Therapy," in OSA Technical Digest (CD) BTuC6 (2010).